The kinematics of the outer Galactic disk from A and F stars

Supervised by:
Prof. J. E. Drew SUPERVISOR
Dr. M. Monguió SUPERVISOR
Dr. T. Gledhill SUPERVISOR

Author:
Amy HARRIS

Centre for Astrophysics Research
School of Physics, Astronomy and Mathematics
University of Hertfordshire

Submitted to the University of Hertfordshire in partial fulfilment of the requirements of the degree of Doctor of Philosophy.

May 2019

Abstract

The kinematics of stars in the outer Galactic disk is poorly known. In addition to constraining the Galactic potential, knowledge of the motions of stars throughout the disk facilitates studies of non-axisymmetric motion, such as streaming motions due to spiral arms. Understanding the kinematics of the disk in full, including the rotation law, will help to map out its structure, and set constraints on its formation and evolution.

I explore the kinematics of A/F stars in two outer-disk pencil beams. I show that A stars in particular are useful probes of outer Galactic disk kinematics. The use of these relatively early-type stars is an alternative to the ISM gas tracers and clump giants that have been commonly used in previous studies. A/F stars offer the advantage of reduced kinematic scatter and asymmetric drift as compared to the older clump giants, and can provide a much denser sampling in the outer disk than ISM gas tracers. They are bright so can be detected out to great distances, and large samples can be efficiently selected from the IPHAS $r-i$, $r-H\alpha$ plane.

The sightlines were chosen to sample the strong shear in Galactic rotation ($\ell = 118^\circ$), and as a control ($\ell = 178^\circ$). Radial velocities (RVs) and extinction-corrected spectro-photometric distances are computed for the sample of > 1300 A/F stars with the aid of MCMC parameter fitting. The rotation law measured at $\ell = 118^\circ$ using the RV data is sharply rising out from $R_G \sim 11$ kpc, going against expectations of a flat or slowly rising law.

Gaia DR2 astrometry, released in April 2018, provided proper motions for the sample. On combining these with the measured RVs and spectro-photometric distances, full space motions are obtained. The Galactocentric radial, azimuthal, and vertical velocity trends are constructed without any prior assumption about the velocity field. The measured rotation curve incorporating proper motion data is flat at $\ell = 178^\circ$, but remains sharply rising at $\ell = 118^\circ$, albeit less so than that determined using only RV data.

I consider the detailed form of the observed Galactocentric trends with specific perturbers in mind, finding no clear interpretation in terms of perturbation from the central bar or spiral arms. The variation of observed trends with longitude and distance is a reflection of the complex dynamics in our Galaxy.

The methods developed in this work and the use of A stars as tracers will be used in the future for fuller exploitation via spectroscopy on forthcoming massively multiplexed wide-field spectrographs. In particular, the PTMCMC method presented will be used to analyse WEAVE survey products. Future use of these young stellar tracers will help us to understand how our Galaxy is, and came to be, how it is now.

Declaration

I declare that no part of this work is being submitted concurrently for another award of the University or any other awarding body or institution. This thesis contains a substantial body of work that has not previously been submitted successfully for an award of the University or any other awarding body or institution.

The following aspects of this submission have been published previously and/or undertaken as part of a previous degree or research programme:

1. The dataset of A and F star spectroscopy that I use was obtained by H. Farnhill as part of their PhD work, and is detailed in their thesis.
2. Parts of the work have been published as Harris et al., 2018, *Monthly Notices of the Royal Astronomical Society*, **475**, 1680, and as Harris et al., 2019, *Monthly Notices of the Royal Astronomical Society*, **485**, 2312.

Except where indicated otherwise in the submission, the submission is my own work and has not previously been submitted successfully for any award.

Acknowledgements

Observations reported here were obtained at the MMT Observatory, a joint facility of the Smithsonian Institution and the University of Arizona.

This study has also benefitted from the service programme (ref. SW2016b05) on the William Herschel Telescope (WHT): the WHT and its service programme are operated on the island of La Palma by the Isaac Newton Group of Telescopes in the Spanish Observatorio del Roque de los Muchachos of the Instituto de Astrofisica de Canarias.

This work has made use of data from the European Space Agency (ESA) mission *Gaia* (`https://www.cosmos.esa.int/gaia`), processed by the *Gaia* Data Processing and Analysis Consortium (DPAC, `https://www.cosmos.esa.int/web/gaia/dpacconsortium`). Funding for the DPAC has been provided by national institutions, in particular the institutions participating in the *Gaia* Multilateral Agreement.

This paper makes use of data obtained as part of the INT Photometric $H\alpha$ Survey of the Northern Galactic Plane (IPHAS, `www.iphas.org`) carried out at the Isaac Newton Telescope (INT). The INT is operated on the island of La Palma by the Isaac Newton Group in the Spanish Observatorio del Roque de los Muchachos of the Instituto de Astrofisica de Canarias. All IPHAS data are processed by the Cambridge Astronomical Survey Unit, at the Institute of Astronomy in Cambridge. The bandmerged DR2 catalogue was assembled at the Centre for Astrophysics Research, University of Hertfordshire, supported by STFC grant ST/J001333/1.

I am grateful to have been able to use data from the WEAVE project during this work, and have been able to use the University of Hertfordshire's high-performance computing facility (`https://uhhpc.herts.ac.uk/`).

I would like to thank the STFC for providing the studentship to fund my studies.

Contents

List of Figures

List of Tables

List of Abbreviations

AL	Along-scan
APOGEE	The Apache Point Observatory Galactic Evolution Experiment
APS	Advanced Processing System
BRAVA	Bulge Radial Velocity Assay
CaT	Calcium triplet
CCF	Cross-correlation function
COMPLETE	Coordinated Molecular Probe Line Extinction and Thermal Emission
CR	Corotation radius
EBHIS	Effelsberg-Bonn HI Survey
ILR	Inner Lindblad Resonance
IMF	Initial mass function
INT	Isaac Newton Telescope
IPHAS	INT Photometric Hα Survey of the Northern Galactic Plane
IRAF	Image Reduction and Analysis Facility
IR	Infrared
ISM	Interstellar medium
LAMOST	Large Sky Area Multi-Object Fibre Spectroscopic Telescope
LSR	Local standard of rest
LSS-GAC	LAMOST Spectroscopic Survey of the Galactic Anticentre
MCMC	Markov Chain Monte Carlo
MS	Main sequence
OLR	Outer Lindblad Resonance
PTMCMC	Parallel Tempering MCMC
RMS	Root mean square
RV	Radial velocity

SCIP	Stellar, Circumstellar and Interstellar Physics
SDSS	Sloan Digital Sky Survey
VLBI	Very long baseline interferometry
WEAVE	WHT Enhanced Area Velocity Explorer
WHT	William Herschel Telescope

Chapter 1

Introduction

1.1 Galactic structure: an overview

Our Galaxy, the Milky Way, is a spiral galaxy that comprises a central bar and bulge, a disk, and a spheroidal halo. The baryonic matter that makes up these components is in the form of gas, dust, and stars, with the majority lying in the flattened disk whose midplane defines the Galactic plane. Table 1.1 details the approximate stellar masses of these Galactic components, the most massive being the disk and the least being the halo. Baryonic matter is believed to make up only a small proportion of the total Galactic mass. Bland-Hawthorn and Gerhard (2016) state the Galactic baryonic mass fraction is just $7 \pm 1\%$. The most major mass component that constitutes nearly all the rest of the Galactic mass is believed to be a dark-matter halo – a component necessary in order to explain the observed rotation curve, and the least well understood.

Component	Stellar mass ($M_\odot$)
Galaxy total	$5 \pm 1 \times 10^{10}$
Thin disk	$3.5 \pm 1 \times 10^{10}$
Thick disk	$6 \pm 3 \times 10^{9}$
Bulge	$(1.4 - 1.7) \times 10^{10}$
Thin bar	$\sim 7 \pm 1 \times 10^{9}$
Superthin bar	$\sim 3 \times 10^{9}$
Halo	$(4 - 7) \times 10^{8}$

TABLE 1.1: *Approximate stellar masses of Galactic components (see Bland-Hawthorn and Gerhard, 2016, and references within).*

z^t	thin disk scaleheight at R_0	$300 \pm 50\,\mathrm{pc}$
z^T	thick disk scaleheight at R_0	$900 \pm 180\,\mathrm{pc}$
R_t	thin disk scalelength	$2.6 \pm 0.5\,\mathrm{kpc}$
R_T	thick disk scalelength	$2.0 \pm 0.2\,\mathrm{kpc}$
f_ρ	local thick-to-thin disk normalisation	$4 \pm 2\,\%$

TABLE 1.2: *Approximate parameters of the Milky Way disk (Bland-Hawthorn and Gerhard, 2016).*

The Galactic disk is the most massive component in terms of stars. It also hosts the majority of the Galaxy's gas and dust. The stellar density profile has been observed to be exponentially declining in both the radial direction, i.e. with Galactocentric radius R_G, and the vertical direction, out from the Galactic midplane. In fact the vertical stellar density profile can be described by the combination of two exponentially declining profiles, which lead to the understanding that the Milky Way disk actually has two components, a thick disk and a thin disk (Gilmore and Reid, 1983). It is thought the thick disk may have been created by an encounter with another smaller galaxy, causing the then-thin disk to be kinematically heated and hence thickened (e.g. Bekki and Freeman, 2003). Table 1.2 details approximate Milky Way disk parameters.

The thick disk, comprising mainly older, lower metallicity stars, has a larger scaleheight than the thin disk. Jurić et al. (2008) use Sloan Digital Sky Survey (SDSS) data of M dwarfs in the Solar neighbourhood to estimate the thick disk scaleheight to be $\sim 900\,\mathrm{pc}$, and Veltz et al. (2008) use G and K type stars within 1.5 kpc to measure a similar scaleheight of $1048 \pm 36\,\mathrm{pc}$. Estimates of the scalelength of the thick disk vary greatly. Bland-Hawthorn and Gerhard (2016) summarise the previous estimates, which range between 1.8 to 4.9 kpc, and conclude that the scalelength is approximately $2.0 \pm 0.2\,\mathrm{kpc}$.

In the midplane, thin disk stars dominate. The local density normalisation ($f_\rho = \rho_T/\rho_t$) has been estimated in many studies, although its value remains fairly uncertain. Gilmore and Reid (1983) first estimated the normalisation to be around 2% using a large sample (> 12500) of stars towards the South Galactic Pole. More recently, Jurić et al. (2008) used SDSS data of ~ 48 million stars, measuring a larger value of $f_\rho = 12\%$. Bland-Hawthorn and Gerhard (2016) analysed all previous measurements and determined a weighted-average value of $4 \pm 2\%$.

The uncertainty of normalisation value is related to the uncertainty of the scaleheights of the two disks. Estimates of the thin disk scaleheight are dependent on the tracer used, since the distance ventured from the midplane is governed by the kinematic temperature of the population – older, kinematically hotter populations will return larger scaleheights. This is confirmed by multiple studies, such as Vallenari et al. (2006) who find a scaleheight near the Solar Circle to be 200 pc for stars aged $1-3$ Gyr, increasing to 350 pc for stars aged $7-10$ Gyr. The G and K stars used in Veltz et al. (2008) resulted in a scaleheight of 225 ± 10 pc, whilst the relatively older M dwarf tracers used in Jurić et al. (2008) returned a thin disk scaleheight of 300 ± 50 pc.

The scaleheight of the thin disk is fairly well constrained using optical and infrared (IR) wavelengths since there is little extinction towards the Galactic poles. However, this is not the case with the scalelength, and hence it is the subject of many studies. If the Galaxy was indeed formed as a result of inside-out growth (e.g. Matteucci and Francois, 1989; Naab and Ostriker, 2006; Brook et al., 2012), the fraction of younger stars will be higher further out in the Galaxy. This means that a scalelength measured using young tracers will generally be larger than one determined using older tracers. This is supported by previous studies, for instance Jurić et al. (2008) find a thin disk scalelength of 2600 pc using M dwarfs, whereas Sale et al. (2010) use younger A-type stars to find a scalelength of ~ 3000 pc.

Dust and gas is concentrated in the thin disk of the Galaxy. The gas is mainly in either the cold molecular phase, such as the H_2 located in dense regions associated with spiral arms, or the warmer atomic phase, such as HI gas. HI gas is spread throughout the disk with a scaleheight of $100-200$ pc in the Solar neighbourhood. The scaleheight of the HI gas strongly increases in the outer regions of the Galaxy, forming what is known as the 'flare'. Kalberla et al. (2007) used Leiden/Argentine/Bonn (LAB) all sky 21-cm line survey data to find the scaleheight of the HI gas disk to increase from just 60 pc at $R_G = 4$ kpc, to 2700 pc at $R_G = 40$ kpc.

Kalberla et al. (2014) present compelling evidence that the stellar disk is also flared. The flare can be understood in terms of a natural phenomenon. As the disk density falls off exponentially with R_G, the gravitational force in the midplane becomes weaker, allowing the gas and stars to migrate further from the plane for the same mean kinetic energy. Other explanations of the flare include kinematic heating from infalling intergalactic medium and satellites (López-Corredoira and Betancort-Rijo, 2009). López-Corredoira and Molgó (2014) use F and G type stars to find the scaleheight at the Solar neighbourhood of the stellar thin-disk to be 240 pc, and of the stellar thick-disk to be 710 pc, with flaring in both the thin and thick disks causing the scaleheight at $R_G = 15$ kpc to be a factor of $3.3\pm^{2.2}_{1.6}$ greater than the Solar neighbourhood value, growing to a factor of $12\pm^{20}_{7}$ at $R_G = 25$ kpc.

The Galactic disk is also warped. Evidence of warping in the Milky Way has been observed in studies of both young and old stars (Reed, 1996; López-Corredoira et al., 2002b; Li et al., 2019a), gas (Kerr, 1957; Levine et al., 2006), and dust (Drimmel and Spergel, 2001). Generally speaking, outside the Solar Circle the north disk ($0^\circ < \ell < 180^\circ$) warps upwards and the south disk ($180^\circ < \ell < 360^\circ$) warps downwards. The kinematic signature of the warp is expected to arise in the form of large-scale systematic velocities perpendicular to the plane, with the strongest signature in the direction of the anticentre. Astrometry from the recent Gaia DR2 release has confirmed this (Poggio et al., 2018). Warping is a common feature amongst spiral galaxies, with a significant fraction ($> 50\%$) showing signs of warping (Sánchez-Saavedra et al., 1990, 2003; Ann and Park, 2006). The cause of the warp in our Galaxy is not settled. The disk bends towards the Magellanic Clouds, indicating that it is perhaps due to gravitational effects (Weinberg and Blitz, 2006). Other suggestions include effects from intergalactic magnetic fields (Battaner et al., 1990) and infalling intergalactic medium (López-Corredoira et al., 2002a).

Spiral structure is a common feature in disk galaxies. The nature of observed structure varies between different galaxies. Flocculent spiral structure is characterised by short, patchy sections of spirals consisting of young stars, gas and dust. Conversely, grand design spiral galaxies have prominent, well-defined spiral arms that contain both young and old stars, along with gas and dust. Some galaxies appear intermediate between the two, with both prominent spirals and less ordered shorter spiral sections. The Milky Way is believed to host intermediate-scale spiral structure, with both prominent spiral arms and smaller spurs (see Figure 1.1). Spiral arms are the sites of increased star formation. This is apparent since they are home to molecular cloud complexes and newly-formed O and early B stars (along with the HII regions they excite). In this context, it is relevant that O and early B stars do not live long enough ($\sim 10\,\mathrm{Myr}$) to travel far from their birthplaces. The precise spiral structure of the Milky Way is still debated due to our obscured view within the disk.

The formation of flocculent spiral structure can be easily understood. If we consider a group of new stars formed due to a local gravitational instability, the differential rotation of the disk will stretch this group out into a spiral shape. This will continue to be sheared, and the most luminous stars will die, leading to the spiral feature fading away. However, the origin and formation of the prominent spiral arms that stretch across entire intermediate-scale or grand design galaxies is less settled.

Two widely discussed concepts are i) density-wave theory, and ii) transient winding arm theory.

Density-wave theory was proposed by Lin and Shu (1964), who stated that the observed spiral structure is a result of a quasi-stationary density wave in the galactic potential. The origin of this density wave is not addressed in the theory, but it is generally believed to be a stable form of spiral structure caused by gravitational instability in the disk. This theory predicts long-lived spiral arms that rotate with the galaxy at a fixed pattern speed that is constant with galactocentric radius. Supporting evidence for this theory would be consistent measurements of the spiral arm pattern speed, Ω_{sp}, at various radii. However, Merrifield et al. (2006) found that the pattern speed of the grand-design spiral structure in NGC 1068 varies significantly with radius, resulting in a very short expected lifetime of the current structure. Studies in the Solar neighbourhood of the Milky Way have returned a range of values for Ω_{sp}, varying between $17-28\,\mathrm{km\,s^{-1}}$ (see Gerhard, 2011, and references within). Dias and Lépine (2005) traced open clusters back to reveal their birthplace, and from this determined $\Omega_{sp} = 24-26\,\mathrm{km\,s^{-1}}$. Further studies at all radii are required to pin down whether the spiral arm pattern speed is constant with radius, and hence whether spiral structure is indeed long-lived as density-wave theory suggests.

The view of spiral arms as transient recurring features has also been long standing. Transient spiral arms are readily produced in N-body simulations (Sellwood and Carlberg, 1984; Grand et al., 2012; Baba et al., 2013), and can survive for up to 10 Gyr (Fujii et al., 2011). Exactly how they recur is unclear, but the Milky Way is not short of mechanisms to excite spiral structure. Locally, gravitational instabillities from perturbations in the stellar distribution may cause structure via swing amplification (Goldreich and Lynden-Bell, 1965; Julian and Toomre, 1966; D'Onghia et al., 2013). Effects from the nearby satellites may also be responsible (Purcell et al., 2011). Transient winding arm theory predicts that the spiral arms rotate with the Galaxy, i.e. the pattern speed decreases with radius, however at present no definitive conclusion has been made from kinematic studies of the spiral arms in our Galaxy. The large amounts of data that come from surveys such as Gaia and WEAVE[1] may help to unpick the nature of the Milky Way's spiral arms.

The dust distribution in the Galaxy largely follows the HI distribution, with dense regions tracing the spiral arms. Since dust absorbs optical light, our view of the Galaxy is obscured by the dust in the disk. However, in the infrared, where dust is more transparent, we can see the bright central region of the Galaxy, compared to the relatively fainter outskirts in the opposite (anticentre) direction. The luminosity profile of the infrared Galaxy reveals that we reside a distance away

---

[1] WHT Enhanced Area Velocity Explorer (Dalton et al., 2016)

from the centre. The centre of our Galaxy is host to a supermassive black hole with an associated bright and compact radio source known as Sgr A*.

The Galactocentric radius of the Sun, R_0, and its motion about the Galactic centre are fundamental parameters in kinematic studies. Measurement of the rotation curve, for example, depends upon these values via both the Galactocentric distance estimation and circular velocity measurement. Consequently, much effort has been put into accurately measuring them. Studies in the last couple of decades return values for R_0 between $7.10 - 8.92\,\mathrm{kpc}$, but the more recent and reliable estimates return a value of around $8.2\,\mathrm{kpc}$ (Bland-Hawthorn and Gerhard, 2016). Most recently, Abuter et al. (2019) used 27 years of astrometric and spectroscopic data to determine the Galactocentric radius of the Sun with an impressive 0.3% uncertainty, finding $R_0 = 8178 \pm 13_{stat} \pm 22_{sys}\,\mathrm{pc}$.

The motion of the Sun can be described in terms of its peculiar motion ($U_\odot$, $V_\odot$, $W_\odot$) with respect to the LSR[2], where $U_\odot$ points towards the Galactic centre, $V_\odot$ in the direction of rotation, and $W_\odot$ upwards from the disk. The motion of the LSR is by definition purely rotational around the Galactic centre with circular speed v_0. The values of $U_\odot$ and $W_\odot$ have been fairly well established, with most recent studies agreeing with $U_\odot = 10 \pm 1$, $W_\odot = 7.0 \pm 0.5$ within their errors (e.g. Schönrich et al., 2010; McMillan, 2017). The $V_\odot$ component is less well constrained, presumably due to unquantified streaming motions in the Solar neighbourhood. Schönrich et al. (2010) used local stellar kinematics to determine $V_\odot = 12.24 \pm 0.47\,\mathrm{km\,s^{-1}}$. A more globally-determined value is found in Bovy et al. (2012), who use APOGEE data to measure $V_\odot = 26 \pm 3\,\mathrm{km\,s^{-1}}$ – significantly larger than that of Schönrich et al. (2010). However, Reid et al. (2014) found a smaller globally-determined value of $14.6 \pm 5.0\,\mathrm{km\,s^{-1}}$ using maser velocities.

It is at the Sun that we define the origin of the Galactic ℓ, b coordinate system. The Galactic longitude, ℓ, is the angle away from the Galactic centre, increasing in the opposite sense to Galactic rotation (see Figure 1.1). The Galactic latitude, b, is the angle away from the midplane, with positive values towards the Northern Galactic Pole. This coordinate system only coincides exactly with the Galactic midplane if the Sun is infact in the midplane, otherwise the $b = 0^\circ$ line is actually slightly tilted relative to the plane. This latter is indeed found to be the case, and the height of the Sun above the midplane is constrained to be around $17 \pm 5\,\mathrm{pc}$ (see Karim and Mamajek, 2017, and references within).

---

[2] Local standard of rest: a point moving on a circular orbit around the Galaxy at the Galactocentric radius of the Sun, R_0

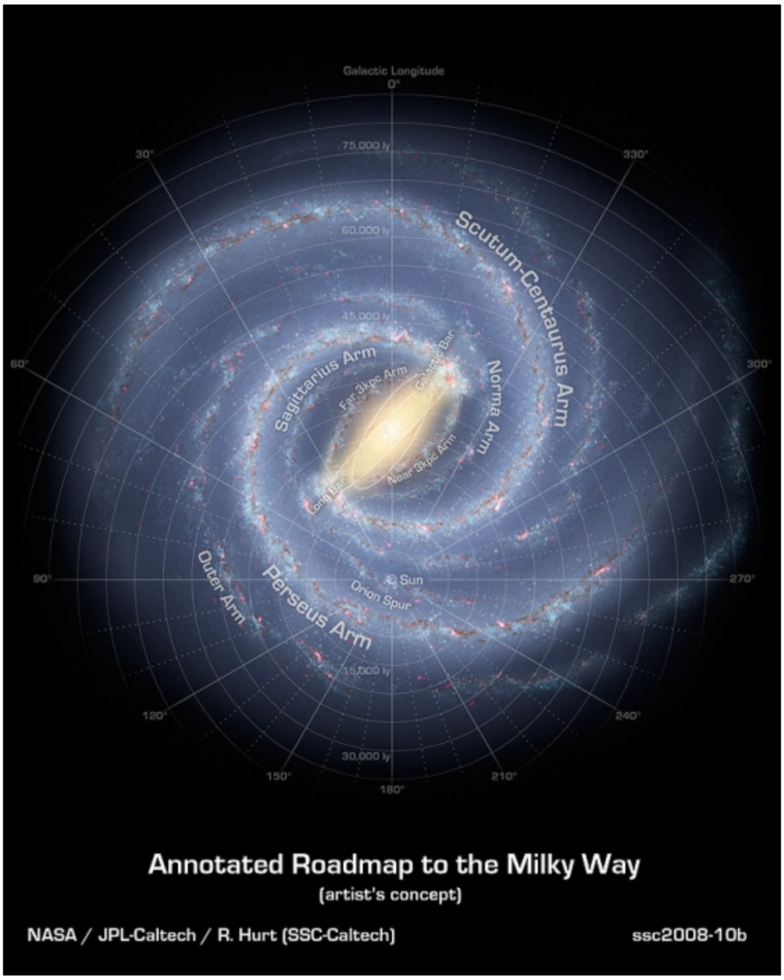

FIGURE 1.1: *An artists impression of the Milky Way. Credit: NASA/JPL-Caltech/ESO/R. Hurt*

Stars in the disk orbit the Galactic centre with differential rotation. Gravitational interactions perturb the orbits of stars in the disk from their equilibrium circular orbit at a radius R_g, known as the guiding radius. The perturbed orbit is pulled back towards its equilibrium circular orbit by an effective restoring force governed by its angular momentum. The star then oscillates around its guiding centre like a harmonic oscillator. This deviation from the circular orbit can be described in terms of epicycles. Projected into the Galactic plane, the epicycle is of the form of an ellipse, with radial-to-tangential axis ratio governed by the gravitational potential. The epicycle is elongated in the tangential direction. A star moves in a retrograde motion along its epicycle with respect to the rotation of the Galaxy. The 3D motion is completed by an oscillation in the vertical direction around the midplane (Sparke and Gallagher, 2007; Binney and Tremaine, 2008).

The non-circular motions of stars result in a distribution of velocities that are described by the velocity dispersion, σ. Older stars have had more opportunity for encounters that perturb their

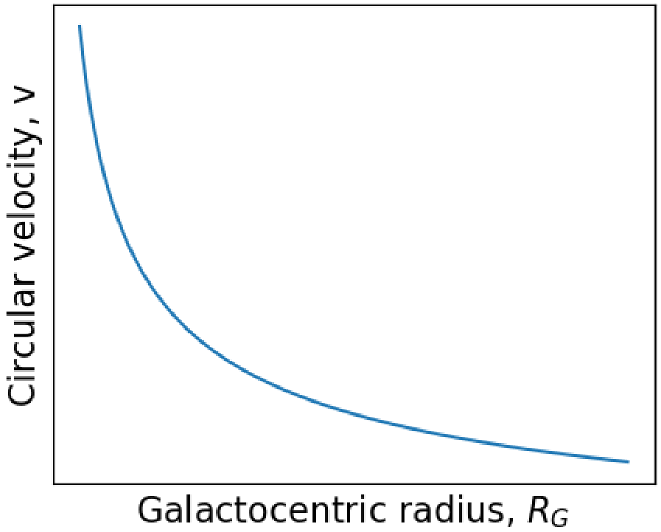

FIGURE 1.2: *Cartoon showing the declining rotation curve of Keplerian motion.*

orbit away from circular, and hence the velocity dispersion of old stars is larger than that of young stars. This is known as the age-velocity dispersion relation (e.g. Yu and Liu, 2018). A typical value of velocity dispersion (of thin disk stars in the Solar neighbourhood) in the Galactocentric radial direction, σ_u, is $\sim 20\,\mathrm{km\,s^{-1}}$ for an A-type star, and $\sim 30\,\mathrm{km\,s^{-1}}$ for an F-type star (Dehnen and Binney, 1998). In general, the velocity dispersion is largest in the radial direction, and least in the vertical direction, i.e $\sigma_u > \sigma_v > \sigma_w$. The ratio of σ_u/σ_v is related to the epicyclic motion of stars, and the magnitude of σ_w has been associated with scattering by giant molecular clouds (Sellwood, 2008). The mean speed at which the stars orbit around the Galactic centre, as a function of the distance from the centre, is known as the rotation curve.

The rotation curve of other disk galaxies has been measured to be approximately flat across its disk (e.g. Bosma, 1978; Rubin et al., 1978; Corbelli et al., 2010). This flat shape goes against Keplerian predictions, which apply to a system in which the majority of the mass is centrally concentrated. For a star in orbit around the Galactic centre at Galactocentric radius R_G, we equate Newton's law of gravitation to the centripetal force to obtain

$$\frac{GM}{R_G^2} = \frac{v^2}{R_G} \tag{1.1}$$

where G is the universal constant of gravitation and M is the mass enclosed within R_G. It then follows that $v \propto R_G^{-1/2}$. Figure 1.2 shows the form of rotation curve from Keplerian motion. The motion of Solar System planets around the Sun follows this form. Considering that in disk galaxies the stars tend to be exponentially distributed with radius, i.e. the majority of them are towards the centre, we might expect a Keplerian-like rotation curve. The observed flat shape of the rotation curve, in stark contrast to the rapidly declining Keplerian rotation law, results in the inference that there is a large amount of mass located in the outskirts of galaxies. This mass, invisible to us, is known as the ‘dark matter halo’.

In our Galaxy the rotation curve is believed to also be approximately flat, but so far coverage of the outer disk in particular has been lacking. Of the few studies of the outer disk, most focus on the anticentre direction only, since this sightline intersects the direction of circular motion and hence only proper motion measurements are required in principle (see Section 1.2). Additionally, accurate distances to the tracers are required in order to measure the rotation curve in the outer disk, which is not an easy feat when faced with the heavy extinction from the interstellar medium (ISM) in the Galactic plane. Knowledge of the exact shape of the rotation curve at all Galactocentric radii will provide constraints on the mass and distribution of the dark matter halo. Our residency in the Milky Way provides us with the opportunity to measure its rotation curve to a higher accuracy than for other galaxies, particularly with the large amounts of data from recent surveys such as Gaia. We describe the methods to do so in Section 1.2.

Another factor to consider in the study of stellar disk kinematics is moving groups. Moving groups, or stellar streams, are groups of stars that share the same velocity, and are observed as overdensities in velocity space. The existence of moving groups in the Solar neighbourhood has long been known, with the discovery of the Pleiades, Hyades and Sirius moving groups dating back to the 19^{th} century. The origin of these groups is thought to be related to kinematic perturbation from, for example, the spiral arms, central bar, or passing or infalling satellites (Antoja et al., 2010). The Hercules moving group, along with others, has been shown to consist of stars with a wide range of metallicities and ages, ruling out the scenario of the groups originating from a particular star formation episode (Bensby et al., 2007; Bovy and Hogg, 2010). Whilst the Hipparcos mission (ESA, 1997) revealed the rich substructure of local kinematics, Gaia DR2 has allowed us to delve deeper into the Galaxy, confirming the persistance of these stellar streams across distances of up to 3 kpc (Ramos et al., 2018). Recently, Antoja et al. (2018) combined both spatial and velocity coordinates to reveal snail shell-like structures in the vertical plane, which they attribute to ongoing phase mixing from an out of equilibrium state caused by kinematic perturbation. Different moving groups are likely imprints of different dynamical processes. Hence, probing the stellar kinematics of the disk, especially in particularly unexplored regions such as the outer disk, will reveal crucial information to aid our understanding of its structure, formation and evolution.

In the central region of the Galaxy is a complex stellar structure known as the bulge. Its main features are a gas-poor body, consisting of old stars with a wide range of metallicities, and a gas-rich inner region which is the site of active star formation. The body is rotating and its shape is described as boxy/peanut-like – viewed side on it resembles a peanut, and viewed from the Sun it appears boxy. The bulge is aligned at an angle of $\sim 20-35^{\circ}$ relative to the Sun-Galactic centre line (López-Corredoira et al., 2005; Wegg and Gerhard, 2013). The origin and formation of the bulge is not well known since observations are hindered by its highly obscured location. Suggested formation mechanisms include i) the initial collapse of the Galaxy, and/or collisions of smaller structures in the early formation of the Galaxy, known as the 'classical bulge' scenario (Eggen et al., 1962; Athanassoula, 2005); ii) buckling of a dynamically evolved barred-disk (Combes et al., 1990); and iii) the migration of star-forming clumps in the young disk (Noguchi, 1999). Athanassoula et al. (2017) compared N-body simulations to observations and suggest that a combination of the above mechanisms are responsible for the Galactic bulge.

Protruding out of the bulge, out to $R_G \sim 5\,\mathrm{kpc}$, is the 'long bar'. Recently, Wegg et al. (2015) combined data from multiple surveys to study the bar using red clump giants, and found it to be aligned at an angle of $28-33^{\circ}$ – consistent with the angle of the bulge. They found the vertical scaleheight of the stars to be decreasing continuously along the bulge and the bar. These observations are consistent with the bulge being the 3D inner component of the long and flat bar. Wegg et al. (2015) also found the vertical stellar density profile of the bar is best fit by two exponential profiles, one with a scaleheight of 180 pc known as the 'thin bar', and the other with a scaleheight of just 45 pc, known as the 'superthin bar'. The smaller scaleheight of the superthin bar indicates its stars are younger than those in the thin bar. The stellar density of the thin bar decreases along the bar, while the stellar density of the superthin bar increases. The increasing density profile of the superthin disk can be interpreted in terms of star formation at the ends of the bar, or the capture of disk stars.

The bar and bulge rotate with a fixed pattern speed, the value of which is still hotly debated. Recently, Portail et al. (2015) used BRAVA[3] data combined with the red clump giant density profile of Wegg and Gerhard (2013) to determine the pattern speed of the bar to be $25-30\,\mathrm{km\,s^{-1}}$. On the other hand, Sormani et al. (2015) modelled the gas flow in a barred potential and compared it

---

[3] Bulge Radial Velocity Assay (Rich et al., 2007)

to observations, favouring a faster pattern speed of around 40 km s^{-1}. Whilst the bar is confined to the central regions of the Galaxy, it has a kinematical impact out into the disk, with strong perturbations related to the resonances of the bar pattern speed. The Galactic bar may well have an impact out to the Solar neighbourhood and possibly beyond (Mühlbauer and Dehnen, 2003; Monari et al., 2014).

The stellar halo contains only about 1% of the stars in the Galaxy. They are old stars with low metallicity. The halo is rich with substructure. It is flecked with globular clusters and wrapped with streams of tidally shredded debris. There has been great interest in tracing the debris streams left by infalling satellites in the recent years, for example the tidal streams of the Sagittarius dwarf spheroidal galaxy (Belokurov et al., 2006; Li et al., 2019b). With a spheroidal shape, the halo has a density profile of $\rho \propto r^{-2.8}$ (Jurić et al., 2008), extending out to of order 100 kpc. It has no net rotation, and is supported by its large stellar velocity dispersion to the tune of 200 km s^{-1} (King et al., 2015; Bird et al., 2019).

1.2 Measuring the rotation curve

Knowledge of the rotation curve at all radii in the disk, both inside and outside of the Solar Circle, ultimately allows for the constraint of the potential of the Galaxy, aiding our understanding of its stucture and history. Non-axisymmetric motions, for example from spiral arms or the central bar, reveal themselves as deviations from the curve. Kinematic distance estimates can be determined with radial velocity (RV) measurements and assuming a rotation curve. This is particularly useful in, for example, studies of ISM gas tracers related to the spiral arms (Roman-Duval et al., 2009), which do not generally offer the alternative distance determination methods that stars do.

First, we describe the cylindrical Galactocentric coordinate system that is used throughout this work. It is defined by: Galactocentric azimuth, ϕ, measured from the centre-anticentre line with ϕ increasing in the direction of Galactic rotation (see Figure 1.3), and given by $\sin\phi = d\cos b \sin\ell / R_G$, where d is the heliocentric distance; Galactocentric radius R_G; and the distance from the mid plane Z. In this frame, the velocities are (u, v, w), with u being the Galactocentric radial velocity, positive towards the Galactic centre, v being the azimuthal velocity, positive in the direction of Galactic rotation, and w being the vertical velocity, positive in the same sense as the Northern Galactic Pole. We also refer to velocities in the heliocentric frame,

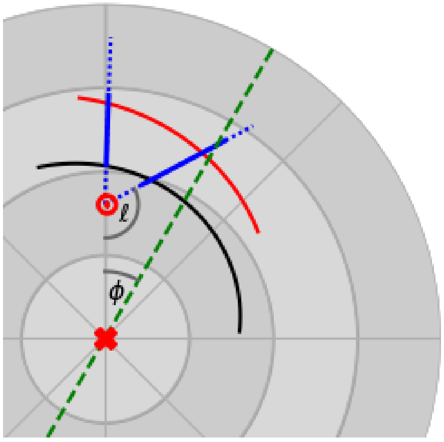

FIGURE 1.3: *A sketch of the Milky Way showing the locations of the sightlines along with segments of the Perseus (black) and Outer (red) Arms (Reid et al., 2014), and an approximate (30°) alignment of the central bar's major axis (green dashed). The Galaxy is rotating clockwise, with the centre shown by the red cross. The Sun is located at* $R_0 = 8$ *kpc (red Sun symbol). Blue dashed lines show the full extent of the sightlines, and solid blue lines represent the actual distance range analysed. The* $\ell = 178°$ *sampling spans* $10.7 < R_G$ *(kpc)* < 14.7*, while the* $l = 118°$ *sightline captures* $9.7 < R_G$ *(kpc)* < 14.0*. The grey circles have radii of 5, 10, 15 and 20 kpc.*

with the radial velocity, v_r, positive when the object is moving away from us, longitudinal or tangential velocity, v_ℓ, positive with increasing longitude, and latitudinal velocity, v_b, positive with increasing latitude.

1.2.1 Analysis

The rotation curve, $v(R_G)$, is the speed at which the Galaxy rotates as a function of Galactocentric distance. In order to determine the rotation curve both the distances to the chosen tracers and the circular velocities of the tracers must be known. The circular motion can be separated into its components projected onto our line of sight, and these projected components follow distinct trends that vary across the sky.

Figure 1.4 shows the pattern of radial velocity, and longitudinal or tangential velocity, in the Galactic plane and with respect to the LSR, expected for stars on circular orbits and with a flat rotation curve of circular velocity of 233 km s^{-1}. The latitudinal velocity is not shown since it is zero in the Galactic plane for the assumptions made. Towards the centre and anticentre, both the radial and longitudinal velocities are zero, since we have adopted a flat rotation curve and circular orbits. In the first ($\ell = 0° - 90°$) and third ($180° - 270°$) quadrants, the radial velocities are generally positive. In the second ($90^{\circ} - 180^{\circ}$) and fourth ($270^{\circ} - 360^{\circ}$), the radial velocities are generally negative. The longitudinal velocity is everywhere negative (or zero) in the region shown. Figure 1.5 is analogous to Figure 1.4, but this time with respect to the Sun, adopting the Solar peculiar motion of (8.6, 13.9, 7.1) $\mathrm{km\,s^{-1}}$ (McMillan, 2017).

Inside the Solar Circle, it is relatively straight forward to measure a rotation curve using the so-called tangent-point method, which exploits the geometry of the system. Outside the Solar Circle, however, measuring the rotation curve is more challenging, as we shall discuss.

1.2.2 Inside the Solar Circle - the tangent-point method

The geometry inside the Solar Circle can be exploited in order to measure the rotation curve in this region (see Figure 1.6). Given a radial velocity profile along a line-of-sight, from e.g. HI or CO profiles, the extremum radial velocity will be measured at the point that is closest to the Galactic centre. This point is a tangent point, and the measured radial velocity here is infact equal to the circular velocity less the component of LSR velocity projected into the line of sight, if we assume circular orbits. The Galactocentric radius and circular velocity at the tangent point and in the plane ($b = 0^{\circ}$) is given by

$$R_G = R_0 \sin(\ell) \tag{1.2}$$

$$v(R_G) = v_0 \sin(\ell) + v_{T,los} \tag{1.3}$$

where v_0 is the circular velocity of the LSR, R_0 is the Galactocentric radius of the Sun, and $\mathrm{v}_{T,los}$ is the radial velocity with respect to the LSR at the tangent point. Hence with the observation of multiple sightlines, the circular velocity can be mapped as a function of Galactocentric radius, and the rotation curve of the inner Galaxy is determined.

For each Galactocentric radius, there are two sightlines that can be used in the tangent-point method: one in the first quadrant, and the other in the fourth quadrant. In the first quadrant the radial velocities are positive (object moving away), and so the tangent point velocity is given by the maximum value. In the fourth, the radial velocities are negative, and the tangent point velocity is given by the minimum value.

Use of the tangent-point method relies upon the assumption of an axisymmetric disk. How it has been used is discussed in Section 1.3. Regarding the extremum velocity as that due to

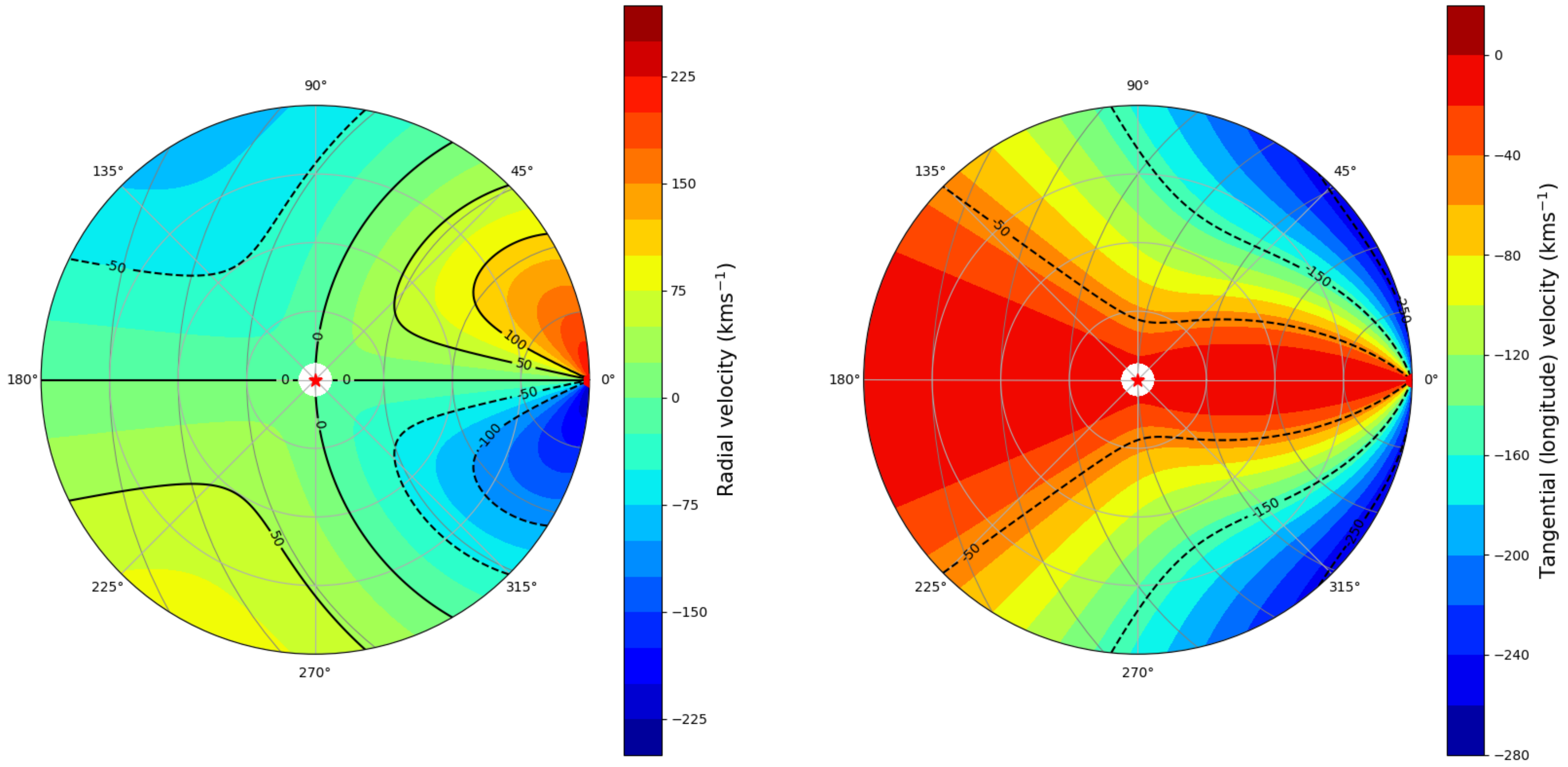

FIGURE 1.4: *Contour plots of the radial (left) and tangential (right) velocity components in the Galactic plane ($b = 0°$), with respect to the LSR, calculated using $R_0 = 8.0\,kpc$ and a flat rotation curve with circular velocity of $233\,km\,s^{-1}$. The latitudinal velocity component is not shown since it is zero everywhere in the Galactic plane. The plots are centered on the Sun (red star symbol), with the Galactic centre at $0°$ (red hexagon). The grey circles are at 2 kpc intervals.*

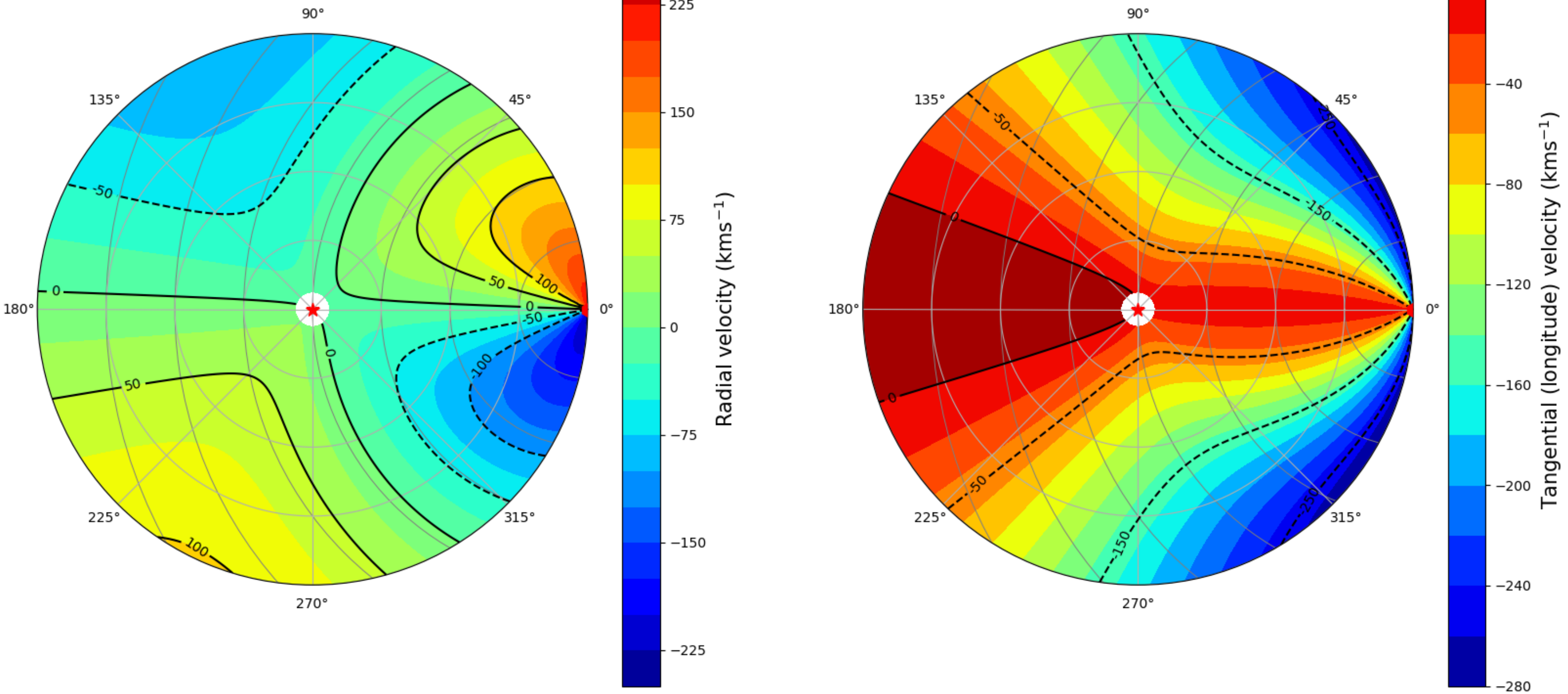

FIGURE 1.5: *Contour plots of the radial (left) and tangential (right) velocity components in the Galactic plane ($b = 0°$), with respect to the Sun, calculated using $R_0 = 8.0\,\mathrm{kpc}$, a flat rotation curve with circular velocity of $233\,\mathrm{km\,s^{-1}}$, and Solar motion of (8.6, 13.9, 7.1) $\mathrm{km\,s^{-1}}$ (McMillan, 2017). The latitudinal velocity component is not shown since it is zero everywhere in the Galactic plane. The plots are centered on the Sun (red star symbol), with the Galactic centre at 0° (red hexagon). The grey circles are at 2 kpc intervals.*

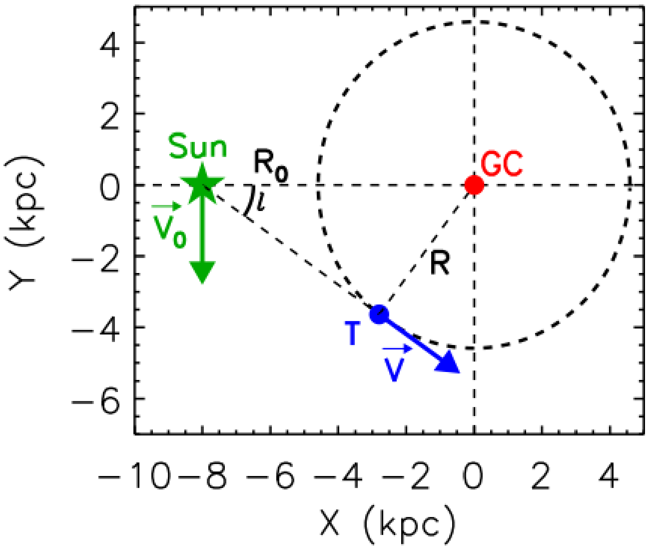

FIGURE 1.6: *Figure 1 of Chemin et al. (2015): the geometry of the system: Sun, tangent point (T), Galactic Center (GC) assumed by the tangent-point method. The Sun is at radius* R_0*, T at radius R. The circular velocities are* v_0 *at* R_0*, and v at R,* ℓ *being the Galactic longitude. The Northern and Southern Galactic Poles are respectively in front of and behind the reader.*

purely circular motion may be incorrect if we consider kinematic effects from non-axisymmetric components such as the bar or spiral arms. Chemin et al. (2015) simulated the impact of the bar and spiral arms on the inferred rotation curve, and found it had a significant effect such that the rotation curve was flawed at $R_G < 4 - 4.5\,\mathrm{kpc}$. In these innermost regions, the tangent-point rotation curve reflects local motions instead of the true rotation curve of the Galaxy. This region corresponds to sightlines within $\sim 30°$ of the Galactic centre. They concluded that using an incorrect rotation curve in this region has important concequences when determining the mass profile of the inner Galaxy, in particular that of the bulge.

1.2.3 Outside the Solar Circle

Measuring the rotation curve outside the Solar Circle is challenging. Both accurate distances to the tracers and their azimuthal velocities are required. In this Section we describe the different approaches in doing so. First, we detail the Galactocentric velocities in which we work. The equations that follow are also made use of in Chapter 6.

We define the Galactocentric velocities as follows, with v_r, v_l and v_b the velocities in the radial, longitudinal and latitudinal directions in the heliocentric frame and determined with proper motions.

$$\begin{aligned}
u &= (v_r + k_1)\cos b\cos(\phi+\ell) - (v_\ell + k_2)\sin(\phi+\ell) \\
&\quad - (v_b + k_3)\sin b\cos(\phi+\ell) \\
v &= (v_r + k_1)\cos b\sin(\phi+\ell) + (v_\ell + k_2)\cos(\phi+\ell) \\
&\quad - (v_b + k_3)\sin b\sin(\phi+\ell) \\
w &= (v_r + k_1)\sin b + (v_b + k_3)\cos b
\end{aligned} \tag{1.4}$$

The Solar motion is accounted for by k_1, k_2 and k_3,

$$\begin{aligned}
k_1 &= U_\odot\cos\ell\cos b + V_{g,\odot}\sin\ell\cos b + W_\odot\sin b \\
k_2 &= -U_\odot\sin\ell + V_{g,\odot}\cos\ell \\
k_3 &= -U_\odot\cos\ell\sin b - V_{g,\odot}\sin\ell\sin b + W_\odot\cos b
\end{aligned} \tag{1.5}$$

where ($U_\odot$, $V_\odot$, $W_\odot$) describe the Solar peculiar motion and $V_{g,\odot}$ is the azimuthal velocity of the Sun about the Galactic centre, given by $V_{g,\odot}$=$v_0 + V_\odot$ with v_0 the azimuthal velocity of the LSR.

In order to measure the rotation curve, the azimuthal velocity v of tracers must be sampled along the Galactocentric radius. To use the above equation for v, for a tracer at ℓ, b, we must know i) the radial velocity, ii) the proper motion components in ℓ and b directions, iii) the distance to the tracer. In reality, all three of these requirements are not always met, and studies use assumptions in order to approximate a rotation curve given a lack of information.

A commonly used assumption is that the orbits are perfectly circular and parallel to the plane, i.e $u = 0$ and $w = 0$. This is reasonable in the mean if we are considering tracers close to the midplane in an axisymmetric disk. This allows for the azimuthal velocity equation to be written in terms of either radial velocity, longitudinal velocity, or latitudinal velocity, alone. The appropriate equation can then be used for the data at hand.

If only radial velocity data are available, and assuming $u = 0$ and $w = 0$, we can write the equation for v in terms of heliocentric radial velocity,

$$v = \frac{R_G(v_r + k_1)}{R_0\sin\ell\cos b} \tag{1.6}$$

This is essentially what we use in Chapters 2-4. The $\sin\ell$ and $\cos b$ factors in the denominator mean that this method is only useful at longitudes away from the Galactic centre ($\ell = 0°$) and the anticentre ($\ell = 180°$), and at latitudes away from the Galactic poles ($b = \pm 90°$). This method requires a distance measurement which is usually acquired separately to the radial velocity measurement, or determined with additional information. For example, a spectro-photometric distance estimate can be obtained using the stellar parameters determined from spectroscopy (along with the radial velocity measurement), in combination with photometry of the object.

We can also write an equation for v in terms of the longitudinal velocity, v_ℓ, for instances when only the proper motion is available,

$$v = \frac{R_G(v_\ell + k_2)}{R_0 \cos\ell - d\cos b} \tag{1.7}$$

This method is particularly useful in instances where the distance (via parallax) and proper motion are measured together. For example, the Outer Galactic Rotation Curve project with VERA (VLBI[4] Exploration of RadioAstrometry, Honma et al., 2000) has succeeded in using simulataneously determined parallaxes and proper motions of masers to measure the rotation speed at points in the outer disk (Sakai et al., 2013; Nakanishi et al., 2015). However, since masers are sparse in the outer disk, the sampling of Galactocentric radius is meagre. Kawata et al. (2018) use Gaia DR2 parallaxes and proper motions to measure the rotation curve in the anticentre out to $R_G \sim 12\,\mathrm{kpc}$. But, while Gaia DR2 provides both proper motions and parallaxes, in the more distant outer disk ($R_G > 12\,\mathrm{kpc}$) the error in the parallaxes quickly become significant, and the conversion to a reliable distance is generally not possible (see Section 6.1).

An equation for v can also be written in terms of v_b,

$$v = -\frac{R_G(v_b + k_3)}{R_0 \sin\ell \sin b} \tag{1.8}$$

This last equation is only suitable if the objects are away from the plane, i.e $b \neq 0$, but since we made the assumption of zero mean vertical motion, $w = 0$, suitable for objects near the midplane, this equation is not so useful. Additionally, v_b of objects in or near the plane will be very small, and so it is not a practically attractive option.

In the ideal scenario of radial velocity, proper motion, and accurate distance data being available, the rotation curve (and other Galactocentric velocities) can be determined via equation 1.4 without any prior assumption of the Galactic velocity field. This is what we do in Chapter 6. This method has no restrictions on the ℓ, b coordinates of the tracers – it can be used throughout

---

[4] Very Long Baseline Interferometry

the disk. Kawata et al. (2018) used this method on a sample in the anticentre that have Gaia DR2 proper motions and radial velocity measurements.

1.3 Tracers of disk kinematics

1.3.1 Gas tracers

A variety of tracers have been used in studies of the kinematics of the Galactic disk. For example, the IAU recommended standard of the circular velocity at the Sun is 220 $\mathrm{km\,s^{-1}}$ (Kerr and Lynden-Bell, 1986), which is a result based mainly on the analysis of tracers of the gaseous ISM, including CO, H I 21 cm and H II radio recombination line observations. In recent decades the work of Brand and Blitz (1993) has been particularly influential, which presented the velocity field of the outer disk using H II regions located over the longitude range $90° < \ell < 270°$ and out to a Galactocentric radius of 17 kpc. How the rotation varies outward from the Solar Circle is more challenging to measure than within because of the greater reliance on the uncertain distances to, in these cases, the ISM tracers.

It has been common practice to associate H II radio recombination and CO lines with star forming regions whose distances are specified by spectroscopic parallax. More recent studies have made use of masers in star forming regions with much better geometrically-defined distances, and these have begun to favour a higher rotation speed. Honma et al. (2012) used a sample of 52 masers associated with pre-main sequence stars to find the rotational velocity of the LSR to be between 223 $\mathrm{km\,s^{-1}}$ and 248 $\mathrm{km\,s^{-1}}$, with a flat rotation curve. Reid et al. (2014) took a similar approach, using an expanded sample of over 100 masers to refine the circular rotation speed at the Sun to $240 \pm 8\,\mathrm{km\,s^{-1}}$. Bobylev et al. (2016) support a raised circular speed ($236 \pm 6\,\mathrm{km\,s^{-1}}$) and a nearly flat rotation curve, based on a large sample of open clusters. These results are each rendered systematically uncertain by both R_0 and $V_\odot$.

A feature of the studies to date is a drop in sensitivity with increasing Galactocentric radius as the number or quality of available measurements declines. In the case of maser measurements, just a handful are available beyond $\mathrm{R}_G \sim 12$ kpc. Similarly, the number of star clusters catalogued at $\mathrm{R}_G \geq 10$ kpc is limited to a few tens. This is an unavoidable consequence of the inherent low spatial frequency of these object classes outside the Solar Circle. Hence, Galactic rotation of the outer disk remains highly uncertain.

1.3.2 Stellar tracers

The frequency of stars at large Galactocentric radii is much higher than either masers or H II regions and work has been undertaken exploiting helium-burning clump giants that can serve as a form of standard candle (Castellani et al., 1992). Examples of this, emphasising measurement of the outer disk, are the works by López-Corredoira (2014), using proper motions from PPMXL[5] and by Huang et al. (2016) using LSS-GAC[6] and APOGEE [7] radial velocities. As older objects with ages typically exceeding 1 Gyr, clump giants will be subject to significant kinematic scatter, including asymmetric drift. This is a drawback that gas tracers are free from.

The mean circular speed of a stellar population tends to drift behind that of a similar group moving on perfectly circular orbits. This is known as asymmetric drift, given by (e.g. Binney and Tremaine, 2008)

$$v_a(R_G) = \frac{\sigma_u^2(R_G)}{2v(R_G)}\left[\frac{\sigma_v^2(R_G)}{\sigma_u^2(R_G)} - 1 + R_G\left(\frac{1}{R_d} + \frac{2}{R_\sigma}\right) - \frac{R_G}{\sigma_u^2(R_G)}\frac{\partial \overline{uw}}{\partial w}\right] \tag{1.9}$$

where σ_u, σ_v, σ_w are the velocity dispersions in the Galactocentric radial velocity u, azimuthal velocity v, and vertical velocity w, and assuming that both the density of tracers and their radial velocity dispersion exponentially decline with scalelengths R_d and R_σ respectively. Asymmetric drift arises due to the epicyclic motion of stars, combined with the exponentially declining stellar density profile with Galactocentric radius. Consequently, the true circular velocity of a population can only be obtained after correction for asymmetric drift. The magnitude of asymmetric drift is proportional to the radial velocity dispersion of the chosen tracer, and this is dependent on its age – σ_u is largest for older populations, as the stars have had longer to become kinematically heated. Asymmetric drift is therefore largest for older stars, and the correction required to obtain the rotation curve is significant. Robin et al. (2017) modelled the asymmetric drift as a function of R_G, and found that in the outer disk, the asymmetric drift varies between approximately $4 - 17\,\mathrm{km\,s^{-1}}$ for disk stars aged between $1 - 10\,\mathrm{Gyr}$. Quantifying asymmetric drift is challenging since it relies on assumptions such as R_d and R_σ which are not well tied down.

---

[5] PPMXL (Roeser et al., 2010) is a catalog of positions and proper motions referred to the ICRS (International Celestial Reference System)

[6] LAMOST Spectroscopic Survey of the Galactic Anticentre (Xiang et al., 2017). LAMOST is the Large Sky Area Multi-Object Fibre Spectroscopic Telescope.

[7] The Apache Point Observatory Galactic Evolution Experiment (DR12 release, see Alam et al., 2015)

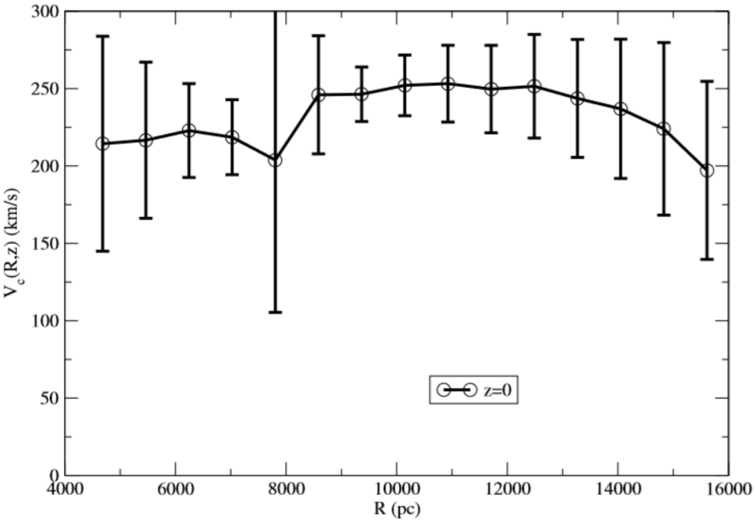

FIGURE 1.7: *Part of Figure 6 from López-Corredoira (2014): The rotation speed as a function of Galactocentric radius, adopting* $R_0 = 8\,kpc$*,* $v_{g,\odot} = 250\,km\,s^{-1}$ *and a LSR azimuthal speed of* $v_0 = 238\,km\,s^{-1}$.

It is then desirable, when measuring the rotation curve, to use a kinematic tracer that has negligible asymmetric drift. However, the very youngest stars (OB stars), which will have not had time to build up asymmetric drift, will not be well-mixed in the disk and will not have travelled far from their birthplace. In addition to this, OB stars are the least abundant spectral type, and so would not provide the dense sampling required. It is clear these stars are not suitable to probe the global disk kinematics. A-type stars are relatively older than these, with ages typically ranging between $0.1 - 1$ Gyr. These stars are old enough that they have had time to depart from their birthplace, but young enough that they have not yet built up significant asymmetric drift. It is these stars that we turn our focus to in the following Sections, along with slightly older (< 5 Gyr) F-type stars.

Recent measurements of the rotation curve using stellar tracers have either taken a longitude-averaged approach or focused on the anticentre direction. Figure 1.7 presents the rotation curve in the Galactic plane found by López-Corredoira (2014), who use red clump giants spanning a wide range of longitudes. In the outer disk, they find the rotation curve to be fairly flat until ~ 13 kpc, after which it gradually declines out to their maximum reach of 16 kpc. Huang et al. (2016) also use red clump giants over a wide range of longitudes in the outer disk, measuring a rotation curve that is sharply rising from $\sim 225\,\mathrm{km\,s^{-1}}$ to $260\,\mathrm{km\,s^{-1}}$ between $R_G = 11 - 15$ kpc – quite different to that of López-Corredoira (2014). Tian et al. (2017) use a sample of clump giants that are mostly located towards the anticentre, but do cover a wide range of longitudes. They separate their sample into younger (< 2 Gyr) and older (> 2 Gyr) clump giants,

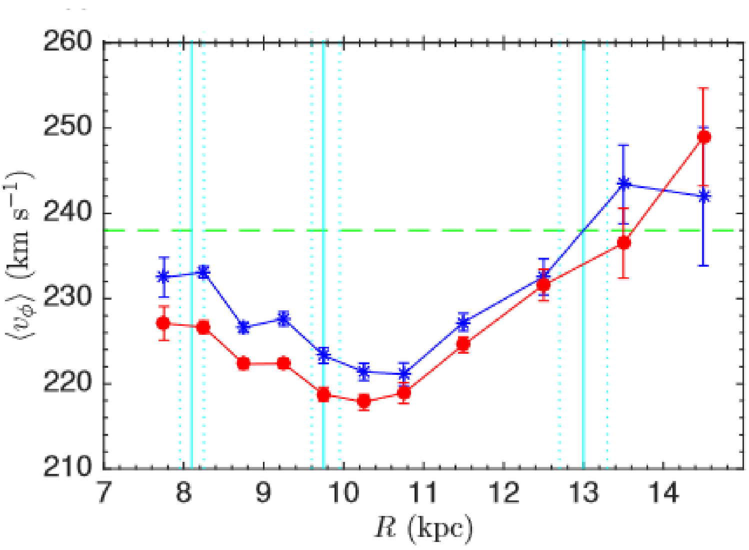

FIGURE 1.8: *Part of Figure 7 from Tian et al. (2017): The variation of average azimuthal velocity with Galactocentric radius of young red clump giants (<2 Gyr, blue line) and old red clump giants (>2 Gyr, red line). The green dashed line indicates $238\,\mathrm{km\,s^{-1}}$ as a reference, which is their adopted circular speed at the solar neighbourhood.*

determining the trend of azimuthal velocity for each. Figure 1.8 presents their findings of rising trends, qualitatively similar to the result of Huang et al. (2016). The azimuthal velocity trend for the older stars (red line) is generally offset from that of the younger stars (blue line) in the sense that the older stars lag behind by $\sim 5\,\mathrm{km\,s^{-1}}$ – likely a result of asymmetric drift. Most recently, Kawata et al. (2018) used Gaia DR2 parallaxes and proper motions of a sample of $> 10^6$ stars located in the anticentre to determine the rotation curve out to $R_G < 12\,\mathrm{kpc}$. They measured it to be approximately flat in the outer disk, with stars orbiting the Galactic centre slower than the LSR by $\sim 20\,\mathrm{km\,s^{-1}}$.

Despite the uncertainty of rotation curve in the outer disk, there is a history of reported velocity anomalies near the Perseus region. For instance, the map of observed HII region radial velocities projected onto the Galactic plane, as presented by Brand and Blitz (1993), revealed surprisingly little variation of radial velocity over the range $110° < \ell < 140°$. Russeil (2003) used star forming regions to report a departure of $-21 \pm 10\,\mathrm{km\,s^{-1}}$ from mean circular speed related to the Perseus Arm over $90° < \ell < 150°$. CO and HI data, as presented in Reid et al. (2016), favour differing velocities in this longitude range, with HI preferring typically more negative radial velocities than the CO to the tune of $\sim 10-20\,\mathrm{km\,s^{-1}}$. Further kinematical studies are required in order to begin to fill out the picture of how exactly such anomalies arise and set constraints on their origin.

With the Perseus region aside, data limitations have meant few constraints exist on non-axisymmetric perturbations. Recently efforts have been made to probe non-axisymmetric motions in the disk using young objects such as Cepheids and OB stars (Bobylev and Bajkova, 2017; Bobylev, 2017; Kawata et al., 2019). These young stars will not have travelled far from their birthplace and likely trace the kinematics of spiral structure. However, studies of non-axisymmetric motions such as these rely heavily on our understanding of the global kinematics.

1.3.3 A-type stars

In this work I examine the kinematics of the outer Galactic disk using A and F-type stars. Main sequence (MS) A-type stars of Solar metallicity have effective temperatures ranging from $\sim 10000\,\mathrm{K}$ for A0 stars, down to $\sim 7500\,\mathrm{K}$ for A9 stars, with surface gravities around ~ 4.3 dex. Their masses range between $1.6-3\,\mathrm{M}_{\odot}$. Early-A stars remain on the main sequence for $\sim$ 200 Myr, and late-A stars for up to 1 Gyr. A-type stars are good candidates for stellar tracers of Galactic disk kinematics. We summarise their advantages below, and explore the points in the text that follows.

- They are intrinsically relatively luminous, with absolute magnitudes in the i band of $\sim$0.5 to 2.
- As younger objects, they have experienced significantly less scattering within the Galactic disk compared to older stars (Dehnen and Binney, 1998), and consequently the resulting asymmetric drift is expected to be small.
- Their frequency in the outer disk allows for a much denser sampling than is available from ISM tracers.
- They are very efficiently selected from photometric Hα surveys.

Hα absorption is strongest in A0-A5 dwarf stars. Drew et al. (2008) showed that the combination of IPHAS photometry of the Hα narrow-band with r and i broad-band measurements can be exploited in order to effectively select samples of early-A stars. In order to demonstrate this, we make use of two plots from Drew et al. (2005), shown in Figure 1.9. The top panel shows the unreddened tracks of main sequence stars (black line), giant stars (red line), and supergiant stars (green line). The expected positions of particular spectral types are shown for the main sequence track, with A0 stars at the origin. The bottom panel shows how these tracks are affected by increasing reddening; the tracks for $E(B-V) = 0$, 2, and 4 are shown. The dashed line is the reddening locus for A0 V stars, forming the early-A reddening line. There is a significant angle between particularly the main sequence track and the reddening line. Hence, in principle, samples of a particular spectral type of main sequence stars can be selected from a strip parallel to its reddening locus in the $r-i$, $r-H\alpha$ plane. Additionally, it is therefore straightforward to measure extinctions from the disparity between the observed (reddened) colours, with intrinsic (unreddened) colours. By assigning absolute magnitudes appropriate to the selected spectral type, extinction-corrected photometric distances can be estimated well enough for sample selection purposes.

Photometric errors will of course result in some level of contamination when selecting a sample of a particular spectral type. The selection of early-A stars is arguably the most simple selection due to their location at the bottom of the tracks, reducing the potential for contamination by other spectral types. Drew et al. (2008) showed this method can be used effectively by selecting samples of A stars using $\Delta(r-H\alpha) = 0.03$, relative to the early-A reddening line, and recovering the known reddenings and distances to the open clusters NGC 7510 and NGC 7790. They also applied this method to the massive northern OB association Cyg OB2, finding a sample of over 1000 A-type stars with $13.5 < r < 20$. Sale et al. (2010) used this selection method, again with $\Delta(r-H\alpha) = 0.03$, to pick out a sample of over 40000 A stars, in order to set constraints on the anticentre stellar density profile. This method for the effective selection of large samples of A stars, and consequently the determination of their extinction, can be exploited for the purpose of kinematic studies.

Dehnen and Binney (1998) used Hipparcos data to measure the velocity dispersion of Solar neighbourhood stars as a function of colour (see their Figure 5). For early-A stars, they return velocity dispersions of approximately $(\sigma_u, \sigma_v, \sigma_w) = (14, 11, 6)\ \mathrm{km\,s^{-1}}$, and for late-A stars these values are slightly greater at approximately (19, 12, 8) $\mathrm{km\,s^{-1}}$. The asymmetric drift of these young stars is likely to be minimal. To demonstrate, we consider Equation 1.9 and adopt $R_d = 3\,\mathrm{kpc}$ (Jurić et al., 2008), $v(R_G) = 233\,\mathrm{km\,s^{-1}}$ (McMillan, 2017), and crudely $R_\sigma = 16.4\,\mathrm{kpc}$ (Huang et al., 2016), which is not well known. The last term of Equation 1.9 can be ignored if we consider stars confined to the midplane. We recover an asymmetric drift in the Solar neighbourhood of $\sim 1\,\mathrm{km\,s^{-1}}$ for early-A stars, and $\sim 2\,\mathrm{km\,s^{-1}}$ for late-A stars. This suggests these stars will make good kinematic tracers, especially in studies of the rotation curve.

A-type stars have absolute magnitudes in the i band of ~0.5 to 2. This relative brightness is valueable when sampling distant regions, especially in the presence of large amounts of extinction

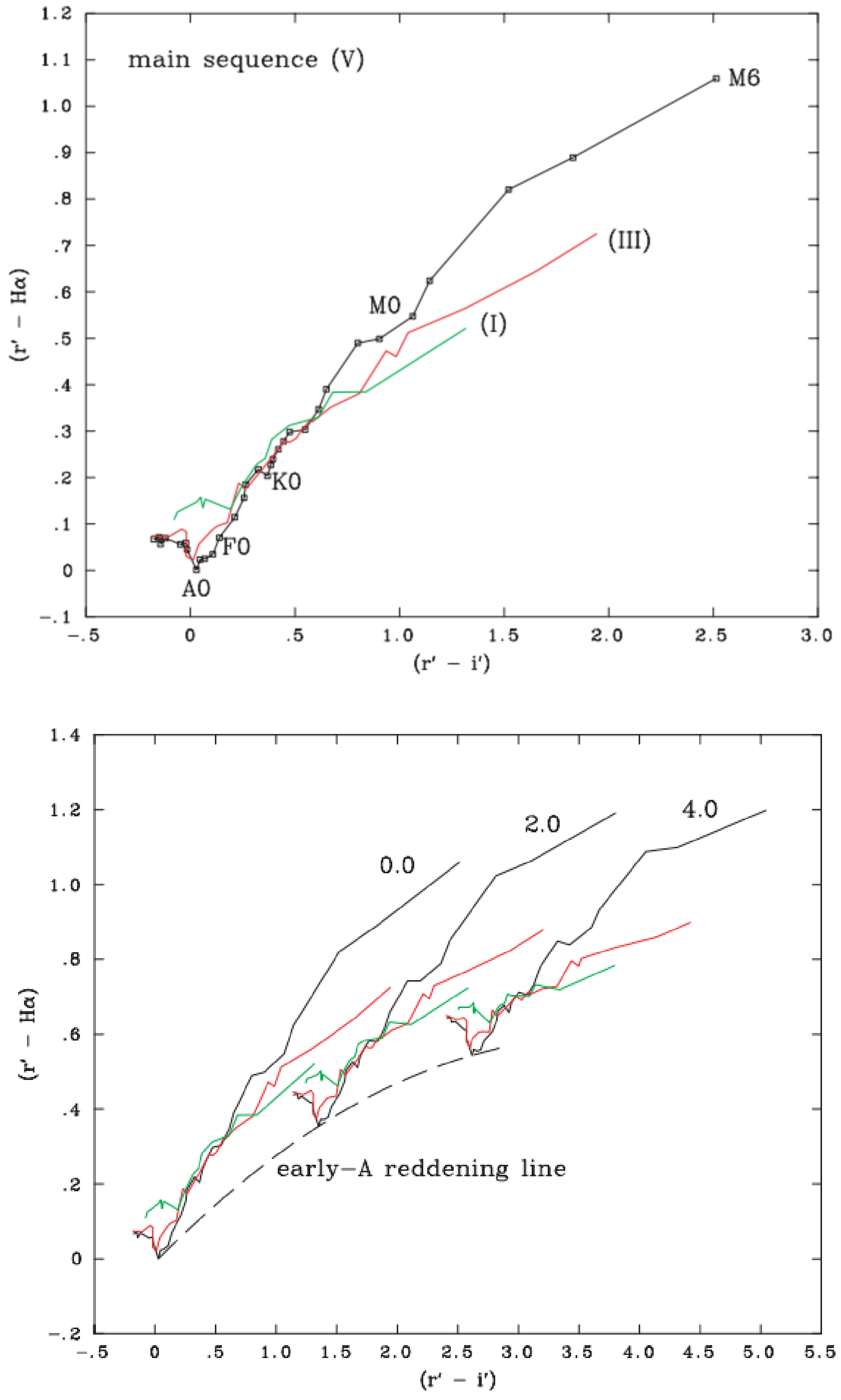

FIGURE 1.9: *Top: Figure 4 from Drew et al. (2005) – the expected positions of unreddened main sequence stars (black line), with the giant and supergiant tracks superimposed (red and green respectively). Bottom: Figure 5 from Drew et al. (2005) – the effect of interstellar extinction, calculated according to an* $R = 3.1$ *Galactic law, on synthetic stellar tracks. The colours are the same as in the top panel. The three sets shown apply to* $E(B-V) = 0, 2, 4$, *as labelled. The dashed line is the reddening locus for A0 V stars – the 'early-A reddening line'.*

Class	**Percentage (%)**
V	63
IV, III	17
II, I	3
Ap	5
Am	12

TABLE 1.3: *The distribution of A-type stars (Jaschek and Jaschek, 1990).*

from dust in the disk. For example, an A star with apparent magnitude of $i = 18$, as has been observed by e.g. IPHAS, with absolute magnitude of $M_i = 1.5$, and suffering from $A_i = 2$ mags of extinction as appropriate for some locations in the Galactic plane, will be at a distance of 8 kpc from the Sun. Hence, these bright, numerous A stars can provide dense sampling deep into the outer disk.

The above arguments can also be made for the relatively older (< 5 Gyr) F type stars, albeit the arguments are marginally less strong. Main sequence F-type stars of Solar metallicities have effective temperatures ranging between $6000-7500$ K, with masses of $1-1.6\,\mathrm{M}\odot$. Early-F stars have absolute magnitudes in the i band of $\sim 2-3$. As we did for the A stars, an F star with apparent magnitude $i = 18$ mag suffering from $A_i = 2$ mag of extinction, and $M_i = 2.5$ mag, would be located 5 kpc away from the Sun. In a magnitude limited sample, F stars on average will probe closer to the Sun than the A stars. Early-F stars have velocity dispersions of $(\sigma_u, \sigma_v, \sigma_w) = (23, 15, 9)\,\mathrm{km\,s^{-1}}$ in the Solar neighbourhood (Dehnen and Binney, 1998), equating to an asymmetric drift of $< 4\,\mathrm{km\,s^{-1}}$ if we adopt the same values as described for the A stars. F star samples can be selected from the $r-i$, $r-H\alpha$ diagram in the same way as A stars, but the raised selection strip may result in increased contamination. In this work, we use a sample that consists of $\sim 60\%$ A stars and 40% F stars, and show that both can be used to probe Galactic disk kinematics, although A stars are especially effective.

A proportion of A stars show chemical peculiarities (see Table 1.3). The most frequent are Am stars, or ‘metallic-line’ stars. These are A-type or early-F type stars of which nearly all heavy elements are enhanced. This results in a spectral classification that varies depending on the lines used in order to determine it. For example, a spectral type determined using the Ca II K line is found to be earlier by a few spectral subclasses than that determined using the hydrogen lines or lines from other metals. Ap stars, or ‘peculiar A-type’ stars, are stars in which only some elements are enhanced and are usually of spectral class A or B. In particular, the silicon or manganese absorption lines are often greatly enhanced. Both Am and Ap stars are slow rotators ($v \sin i < 100\,\mathrm{km\,s^{-1}}$) compared to normal A stars ($v \sin i > 100\,\mathrm{km\,s^{-1}}$). The slow rotation allows for chemical separation in the stellar atmosphere, resulting in chemically peculiar spectra. In normal A stars, chemical separation is completely dominated by the mixing effects from fast rotation. The Ap stars also have strong magnetic fields which work to interfere with the chemical separation of ionised elements, hence enhancing only certain elements. Chemically peculiar stars present a challenge for the spectral classification of stars needed, for example, in the determination of spectro-photometric distances. Whilst the blue region of chemically peculiar stars includes absorption lines due to manganese and other heavy elements, there is little impact on the redder calcium triplet (CaT) region, and we can avoid complication by determining spectral classes with this region.

1.4 The sightlines

In this work, we examine the kinematics of a sample of A and F stars, with a particular focus on measuring the rotation curve. The A and F stars that we use are located in two pencil-beam sightlines in the Galactic plane of the outer disk. The sightlines have a 1° diameter, centered at $\ell = 178^\circ$, $b = 1^\circ$ and $\ell = 118^\circ$, $b = 2^\circ$. Figure 1.3 shows the location of the sightlines in the Milky Way. In both sightlines, our sampling begins just before the Perseus Arm and reaches out to beyond the Outer Arm. We also show the approximate alignment of the central bar at 30° relative to the Galactic centre-Sun line, which crosses paths with our $\ell = 118^\circ$ sightline at the far end of our sampled region. We detail the reasoning behind the chosen sightlines below. At the time of choosing (pre-2011), Gaia DR2 with its proper motion data was a distant prospect, and so the focus was on choosing sightlines that could provide useful sampling of radial velocity changes.

The $\ell = 118^\circ$ sightline was chosen since, in principle, radial velocities measured there should sample the strong shear in Galactic rotation and hence provide insight into how the rotation changes with Galactocentric radius outside the Solar Circle. This particular sightline is also one that presents relatively low total extinction (Sale et al., 2014) and limited CO emission (Dame et al., 2001), thereby promising access to greater distances. It is consistent with these properties that there is a raised stellar density visible at this location of up to twice the average for the region (see Farnhill et al., 2016). It is worth noting that there is a history of reported velocity anomalies of ISM tracers in a longitude range that includes this sightline (mentioned in Section 1.3). Our analysis should reveal whether these anomalies also exist in the velocities of A/F stars.

Sightlines near the Galactic anticentre intersect the direction of dominant circular motion essentially at right angles, leading to the expectation of measured radial velocities close to 0 (in the LSR frame) and exhibiting negligible change with increasing distance. We chose to observe a near-anticentre sightline ($\ell = 178^\circ$) so that it serves as a control, directly revealing e.g. radial velocity measurement bias and the magnitude of kinematic scatter. Again, the particular choice made is of a pencil-beam that is subject to relatively light extinction. At $\ell = 178^\circ$, higher extinction is found a degree away, on and below the Galactic equator.

A gradual decline in metallicity may be expected along our outer disk sightlines, since the average metallicity of stars in the Milky Way decreases with Galactocentric radius. Previous studies estimate this gradient to be around $d[\mathrm{Fe/H}]/dR_G = -0.06$ to $-0.08\,\mathrm{dex\,kpc^{-1}}$ (Friel et al., 2002; Sale et al., 2010; Cheng et al., 2012), but some find the gradient flattens off in the outer disk (Lemasle et al., 2008; Huang et al., 2015). Our sampling reaches out to $R_G \sim 14\,\mathrm{kpc}$ in the $\ell = 118^\circ$ sightline, and $R_G \sim 15\,\mathrm{kpc}$ in the $\ell = 178^\circ$ sightline. For a gradient of $d[\mathrm{Fe/H}]/dR_G = -0.07\,\mathrm{dex\,kpc^{-1}}$, this corresponds to metallicities getting down to $[\mathrm{Fe/H}] = -0.4$ to -0.5. Although these values may be reduced if the gradient does indeed flatten in the outer disk, we bear the potential impact from a metallicity gradient in mind throughout this work.

1.5 Outline of thesis

The kinematics of stars in the outer Galactic disk is poorly known. In addition to setting a constraint on the Galactic potential, secure knowledge of the motions of stars at all radii and longitudes in the Galactic disk facilitates studies of non-axisymmetric motion, such as streaming motions due to spiral density waves or transient winding arms. Understanding the kinematics of the disk in full, including the rotation law, will help to map out its structure, and set constraints on its formation and evolution. In this work, we explore the kinematics of near-main sequence A/F stars as kinematic tracers in two outer disk pencil-beams, with a view to future fuller exploitation via spectroscopy on forthcoming massively multiplexed wide-field spectrographs (e.g. WEAVE, in construction for the William Herschel Telescope).

- In Chapter 2 the target selection process and observations are described. The dataset comprises spectroscopy of 2070 mostly A and F type stars, selected using IPHAS $r-i$, $r-H\alpha$ colours, and observed using HectoSpec. The selection of data for further analysis is detailed; after a count-cut, 887 spectra at $\ell = 118^{\circ}$ and 434 at $\ell = 178^{\circ}$ remain.

- The method of analysis is described in Chapter 3. Markov Chain Monte Carlo (MCMC) simulations are used to measure stellar parameters and radial velocities for our spectroscopic sample, by comparison with a set of template spectra. Extinction-corrected spectro-photometric distances are then determined.

- Chapter 4 presents the outer disk kinematics as determined from the radial velocity data and spectro-photometric distances of our A and F star sample. The observed trends of RV with distance are compared with those expected from often-used flat and slowly rising rotation curves. The impact of unresolved binaries and distance error is considered, and a comparison of our results with other tracers and earlier works is made. The potential of signatures from spiral arm perturbations is explored.

- Our results are validated in Chapter 5 by means of comparison with higher-resolution long-slit spectra, HectoSpec spectra with more tailored sky-subtraction, and expectations from a Galactic model.

- In Chapter 6 Gaia DR2 proper motion information is incorporated into our analysis. The outer disk kinematics is presented, as revealed by the full space motions of our A and F star sample. The Galactocentric velocity trends, including the rotation curve, are discussed in terms of potential kinematic perturbers.

- Chapter 7 looks ahead, preparing the methods employed in this work for future use with large scale spectroscopic surveys such as WEAVE. Our Parallel Tempering MCMC method is introduced, and its capability is demonstrated with use of simulated spectra.

- A summary is presented in Chapter 8.

Chapter 2

Dataset

2.1 Target selection

The original data selection for this project came from an observing programme proposed by Farnhill et al. in 2011. The data were obtained by H. Farnhill and N. Wright. The experiment proposed was to measure the trend in radial velocity with distance of 1500 mainly A-type stars in two outer disk pencil-beams that could then be compared to customized models of disk kinematics. One of the sightlines observed was at $\ell = 118^\circ$, $b = +2^\circ$. This was chosen because it lies in the longitude range of maximal radial velocity shear ($\ell \sim 110^\circ - 120^\circ$). Its positive latitude is appropriate to match the mean larger scale Galactic mid-plane which is modified in this range by the warp (Kalberla and Kerp, 2009; Goodman et al., 2014). It also presents relatively low total extinction (Sale et al., 2014) and limited CO emission (Dame et al., 2001), thereby promising access to greater distances. The other was a control sightline, chosen to be near the anticentre at $\ell = 178^\circ$, $b = +1^\circ$, since this longitude is at right-angles with Galactic rotation and hence no significant radial velocity shear would be present. Radial velocities in this sightline can provide insights into intrinsic scatter and facilitate fine-tuning of the Galactic disk models.

The sample was selected using the IPHAS $r - i$, $r - H\alpha$ colour-colour diagram, as shown in Figure 2.1. As discussed in Section 1.3.3, it has been shown that the properties of the $r - i$, $r - H\alpha$ colour-colour diagram can be exploited easily and efficiently in order to select samples of main sequence A0-A5 stars. The significant angle between the main sequence track and the reddening line allows the disentanglement of intrinsic colour and interstellar extinction. In the selection of the HectoSpec sample, this method was extended to extract samples of both

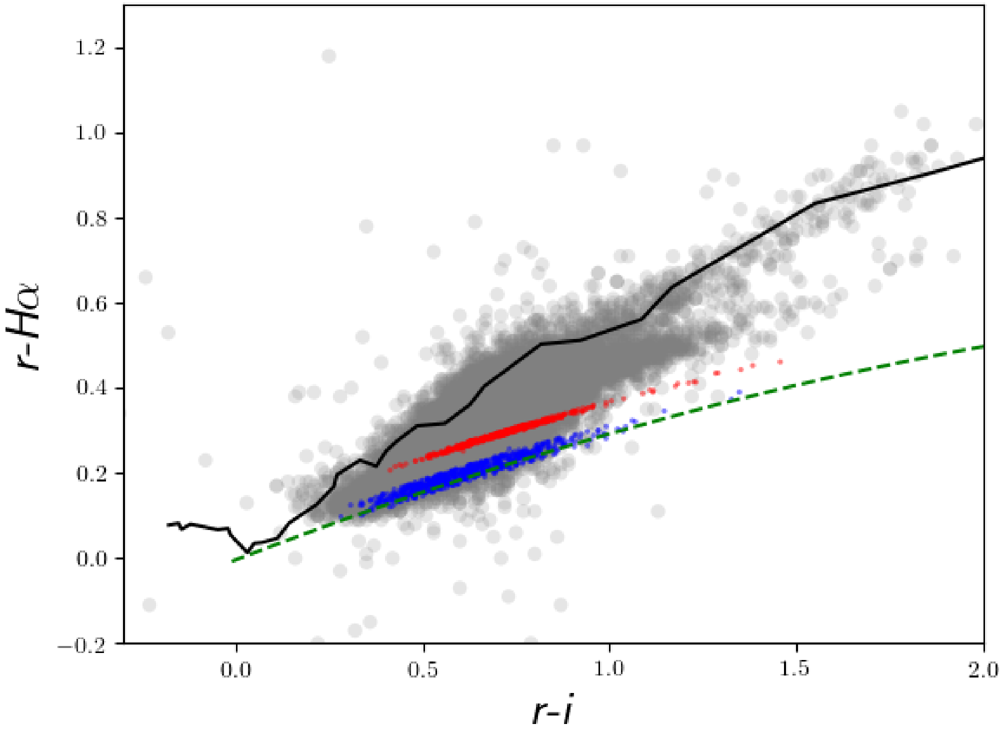

FIGURE 2.1: *IPHAS colour-colour diagram with HectoSpec targets overlaid. The grey points are IPHAS sources with $r < 19$. The HectoSpec stars fall in two distinct selection strips: the top strip selecting F-type stars (red points) and the bottom strip selecting A-type stars (blue points). The black line is an empirical unreddened main sequence track, and the green dashed line is the early-A reddening line.*

A and F stars. A-type stars were chosen since they are young and have low kinematic scatter, making good candidates as tracers of Galactic kinematics. The F-type stars were included, in part because of a collaborative agreement, and because they would sample a closer distance range than the A stars, probing the kinematics of the Perseus Arm at $d \sim 2-3$ kpc. The candidate A stars were selected from a strip in the $r-i$, $r-H\alpha$ diagram of 0.04 mag wide, just above the early-A reddening line, and the candidate F stars were selected from a strip 0.08 - 0.09 mag above the line. The gap between the two bands contains a mixture of the two stellar types. Due to the shape of the main sequence track, contamination by some reddened B stars was possible, although the scale of this is mitigated by their relative rarity.

2.2 Observations

The spectra were gathered using the MMT's multi-object spectrograph, HectoSpec (Fabricant et al., 2005). HectoSpec benefits from a 6.5 m primary mirror and boasts 300 fibres covering a 1° diameter field of view, with each fibre subtending 1.5" on the sky. A total of 8 fibre configurations were observed: 6 for the $\ell = 118^\circ$ sightline and 2 for the control. Of the 300 fibres, 30 were used for obtaining sky spectra. The high-dispersion 600 lines mm^{-1} grating was used with the aim to provide more accurate radial velocities, providing $\sim 2.4\,Å$ resolution as measured from narrow sky lines. This equates to a resolving power of $R \sim 3600$ in our analysed wavelength range. The observations were performed over 6 nights in Sep-Nov 2011 and cover a total wavelength range of $6532 - 9045\,Å$ with a sampling of $0.56\,Å$. Table 2.1 details the observations on each date, giving the i magnitude range observed, exposure time, achieved count range, and number of targets. Figure 2.2 shows the object positions on the sky.

The observed objects have magnitudes spanning the range $14.2 \leq i \leq 18.5$, which are expected to populate a heliocentric distance range of approximately 2 to 10 kpc (or 11.5 – 15 in distance modulus). To demonstrate a typical case, an A star with absolute magnitude of 2.4 and apparent magnitude of 14.2 would be at a distance of ~ 2 kpc if its visual extinction was 1 mag. Similarly, if the A star has apparent magnitude of 18.5, it would be at a distance of 10 kpc for an extinction of 1.5 mag. The use of both F and A stars ensure the heliocentric distance distribution is well sampled, as the selected F stars will lie closer on average than the intrinsically brighter A stars. An F star with apparent magnitude at our faint limit of 18.5, absolute magnitude of 3.2 and visual extinction of 1.5, would be at a distance of ~ 6 kpc compared to an equivalent A star at 10 kpc. Rough estimates of the distance moduli distributions of the A and F star sample, as determined by H. Farnhill, are presented in Figure 2.3.

2.3 Selection of data for analysis

The HectoSpec data were reduced using the HSRED[1] pipeline, and a mean sky spectrum was determined using the dedicated sky fibres. This was subtracted off all target fibres in the same configuration. We applied a quality cut to the data, accepting spectra with an average count level between 8475 – 8675 Å of more than 2000, to ensure a large enough signal-to-noise ratio (S/N) for reliable RV and stellar parameter measurements. This cut off level was determined

---

[1] Information on the latest version of HSRED can be found at `https://www.mmto.org/node/536`

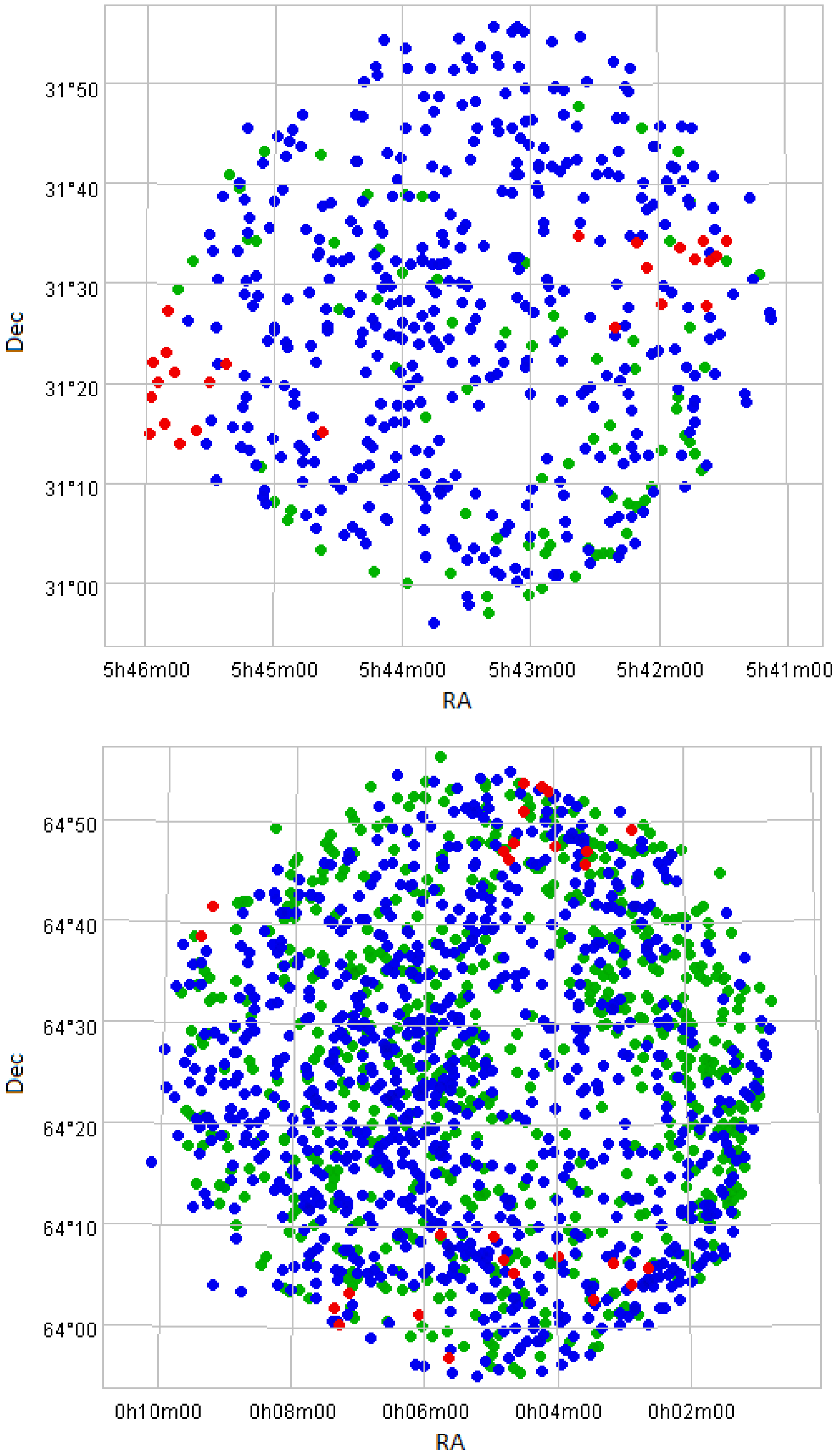

FIGURE 2.2: *Object positions on the sky for the* $\ell = 178°$ *sightline (top) and* $\ell = 118°$ *sightline (bottom). The green points show objects removed from the sample due to the counts cut (*$<$ 2000*), and the red points show objects removed due to signs of red leak. The blue points are the remaining sample.*

Date of observation	***i* magnitude**	**Exposure (min)**	**Count range**	**Number of spectra**	ℓ (°)
17-09-2011	16.5-17.5	140	390-5163	266	118°
18-09-2011	16.5-17.5	135	1000-4012	259	
19-09-2011 (a)	14.7-16.5	75	204-2983	258	
19-09-2011 (b)	17.5-18.5	265	143-2843	264	
21-10-2011	15.3-17.5	135	869-13003	256	
18-11-2011 (a)	14.8-16.5	75	1452-12352	253	
17-11-2011	17.0-18.0	165	1192-4607	252	178°
18-11-2011 (b)	14.2-17.5	120	662-41194	262	

TABLE 2.1: *The details of the observations: date of observation, i magnitude range observed, exposure time, achieved count range, number of targets observed, Galactic longitude of sightline.*

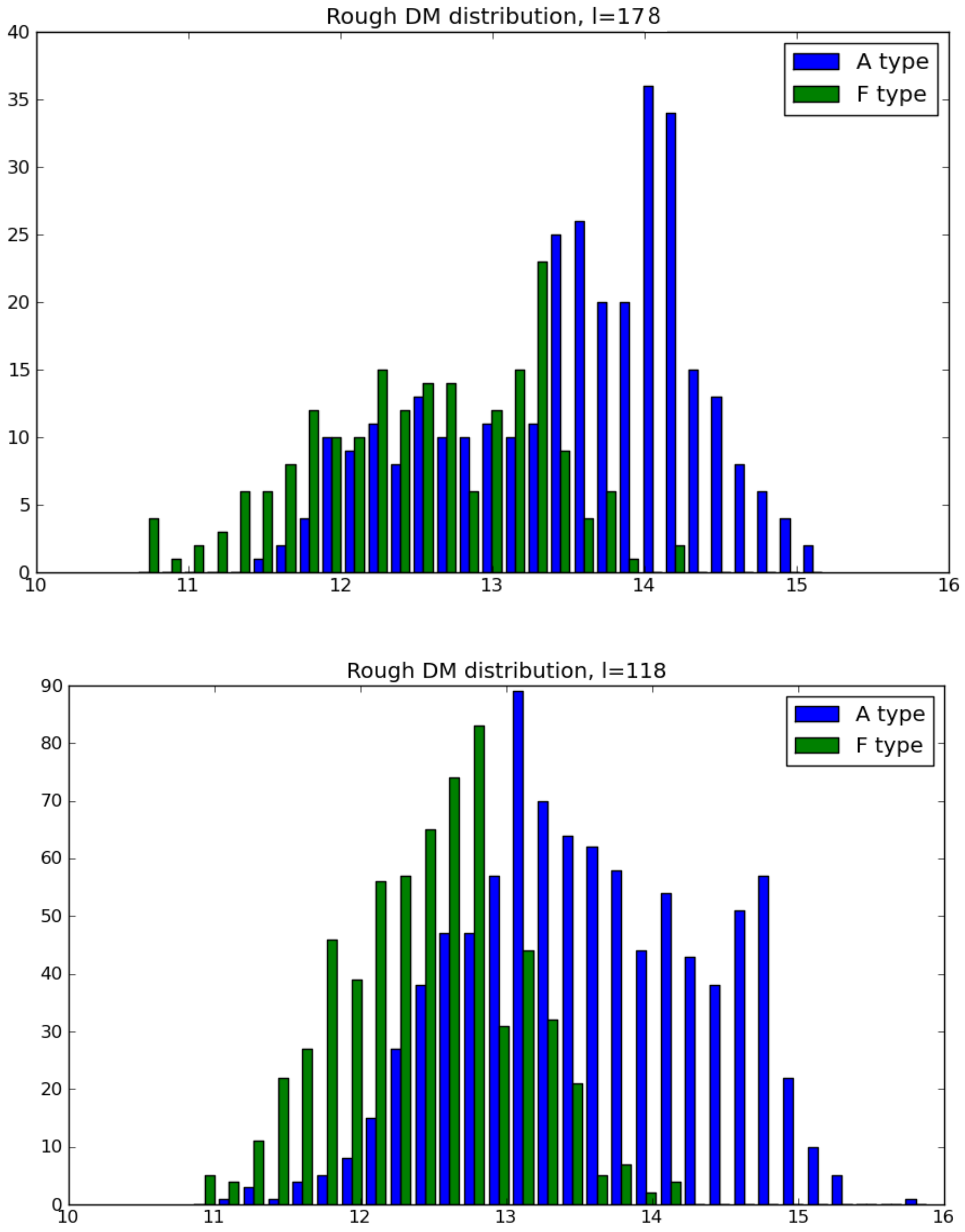

FIGURE 2.3: *Estimates of the distance moduli distributions, as determined by H. Farnhill, for the $\ell = 178^\circ$ sightline (top panel) and $\ell = 118^\circ$ sightline (bottom panel). The distributions of the A and F stars are separated by blue and green colours respectively.*

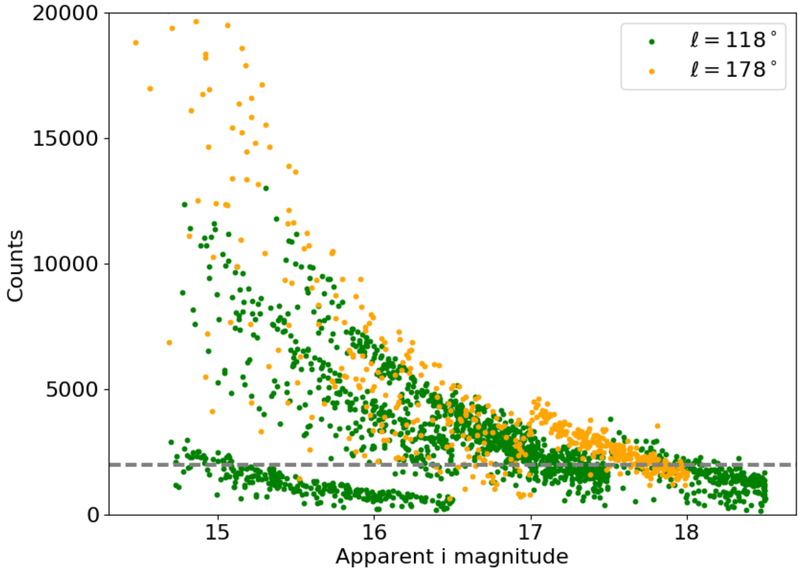

FIGURE 2.4: *Count level (average between* $8475 - 8675Å$*) vs. apparent i magnitude for* $\ell = 118^\circ$ *(green) and* $\ell = 178^\circ$ *(orange). The grey dashed line represents the minimum accepted count level of 2000. There are 749 stars with counts* < 2000*, and 1321 with counts* ≥ 2000.

empirically by eyeballing both the spectra and their best-match template fits which are used for RV and stellar parameter measurements. The minimum S/N corresponding to this count cut is 23, which is a wavelength-averaged measure over the CaT region. There are 887 spectra at $\ell = 118^\circ$ and 434 spectra at $\ell = 178^\circ$ that survive this cut. Consequently there are 669 spectra at $\ell = 118^\circ$ and 80 spectra at $\ell = 178^\circ$ that are not used due to their counts being below 2000. These removed objects are shown in Figure 2.2 in green.

Figure 2.4 shows the count levels vs apparent *i* magnitude, with the horizontal line representing the minimum accepted count level. The distinct trends are due to weather, varying levels of moonlight, and exposure time changes (see Table 2.1). The configurations exposed on 19-09-2011 and 18-11-2011, both for targets with $i \leq 16.5$, present contrasting count levels due to a significant transparency change. The effective magnitude faint limit overall is $i \sim 17.5 - 18$.

Figure 2.5 shows three A-type stellar spectra (blue lines) with varying count levels, and each with apparent magnitude $i \sim 16$. From top to bottom the counts are ~ 8000, representing the maximum observed count level for this magnitude, ~ 4000, a typical count level, and ~ 2000, the minimum count cut. The mean sky spectrum is also shown (orange line), reduced to 10% of its original count level. The total wavelength range shown ($8470 - 8940Å$) is the region we use for measuring RVs and stellar parameters. Whilst much smaller than the total range covered by the data, it is chosen as it includes the CaT lines and some prominent Paschen lines. The CaT lines and Paschen lines are well defined in F and A stars respectively, making them informative spectral lines for making stellar parameter and radial velocity measurements. The selected wavelength range is also relatively unaffected by telluric absorption lines. The only other strong photospheric absorption line potentially available to us is Hα, which is very far away in wavelength at $6563\AA$, and close to the blue limit of the MMT spectra at $6532\AA$.

We excluded the region between the red dashed lines $(8610-8700\AA)$ in Figure 2.5 from our analysis, since it is a region affected by sky lines that frequently do not subtract well. It also covers the diffuse interstellar band at $8620\AA$. The narrow emission-like features, particularly at the redder end, are incompletely subtracted sky lines. The CaT lines are indicated by crosses, located at $8498.0\AA$, $8542.1\AA$ and $8662.1\AA$, although in A stars they are blended with Paschen lines, which are indicated by circles at $8502.5\AA$, $8545.4\AA$, $8598.4\AA$, $8665.0\AA$, $8750.5\AA$ and $8860.4\AA$.

Longward of $8500\AA$, HectoSpec is affected by second order light contamination known as red-leak. The HSRED pipeline attempts a correction of this, although it is not always successful. Red-leak is problematic when determining stellar parameters since it alters both the continuum level and the relative depth of the absorption lines, rendering accurate template-matching impossible. Contaminated spectra are betrayed by an upturn in the continuum at the red end, reversing the decline shortward of 8500 Å. An example of a contaminated F star is shown in Figure 2.6. We identify these spectra in our sample as those which possess a mapping function (of best-fit template onto the observed spectrum) with a positive gradient (see Section 3.1.4 for details). These spectra are removed from the sample, leaving 855 target spectra in the $\ell = 118^\circ$ sightline and 409 in the $\ell = 178^\circ$ sightline. These removed objects are shown in Figure 2.2 in red.

With a large set of observed spectra of A and F stars and corresponding IPHAS photometry, we could begin to measure stellar parameters and radial velocities, and hence calculate extinctions and spectro-photometric distances for the stars.

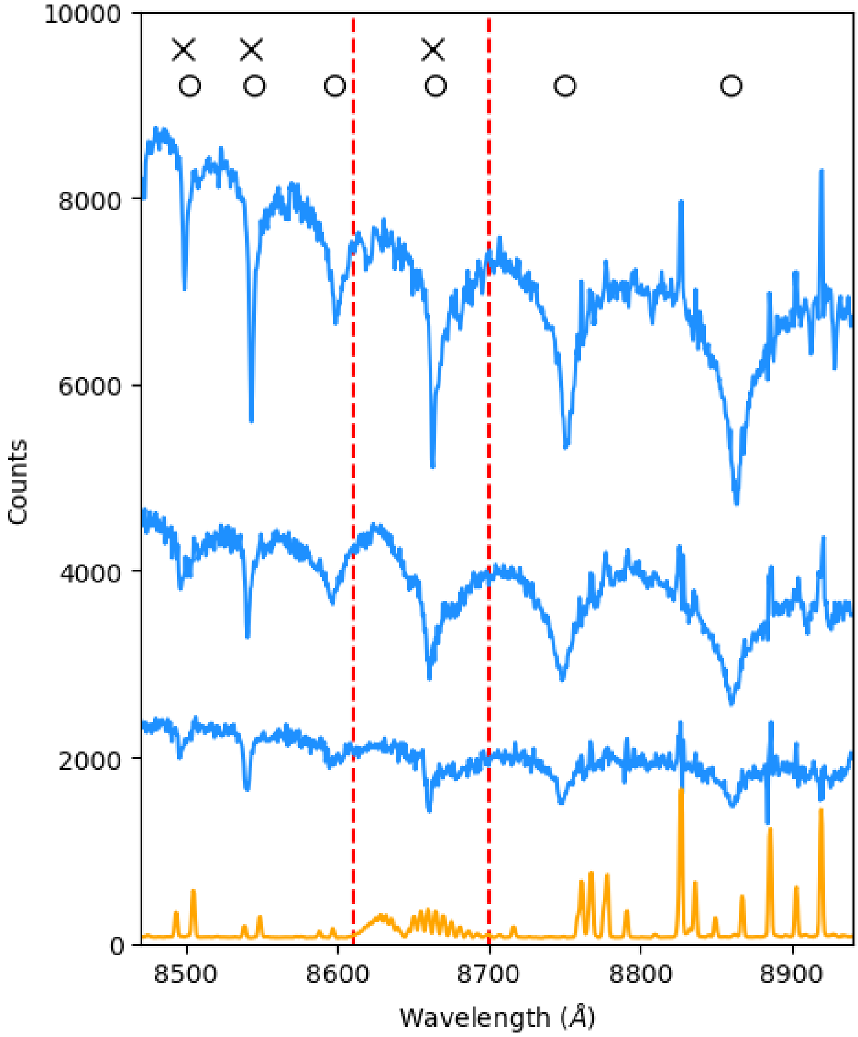

FIGURE 2.5: *Close up of the CaT region of three A-type stellar spectra (blue lines) with varying count levels and apparent magnitudes* $i \sim 16$. *The mean sky spectrum is also shown (orange line), which has been scaled down to 10% of its original counts. We exclude the region between the red dashed lines from our analysis since this region is affected by sky lines which frequently do not subtract well. The narrow emission-like features in the stellar spectrum are incompletely-subtracted sky lines. The prominent ∼triangular absorption lines are Paschen lines, indicated by a circle. In later-type stars the CaT lines, indicated by a cross, become obvious and strengthen as the Paschen lines fade.*

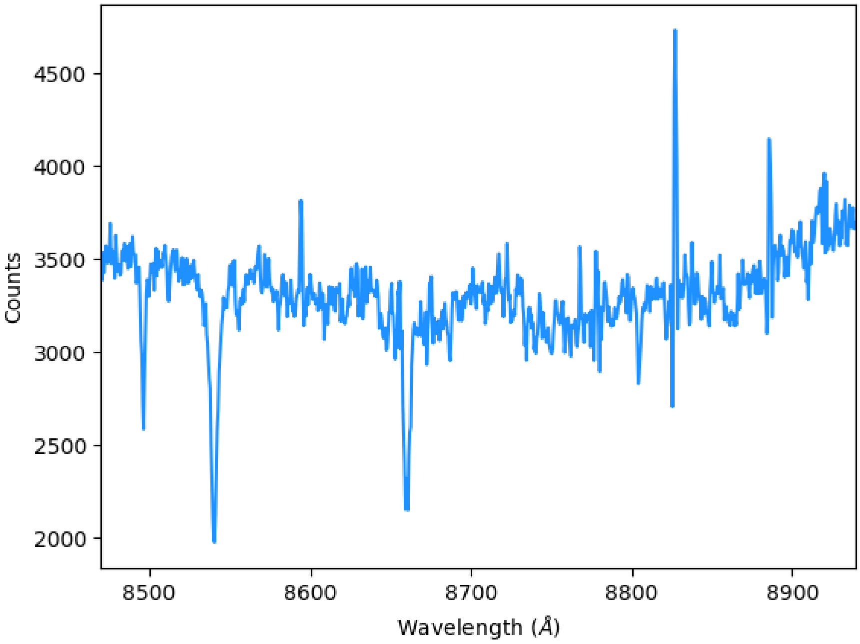

FIGURE 2.6: *The spectrum of an F star contaminated by red leak.*

Chapter 3

Method of analysis

3.1 Determination of astrophysical parameters

3.1.1 Overview

Two methods of analysis to measure the astrophysical parameters of interest (RV, $T_{\rm eff}$, $\log g$ and $v \sin i$) in the CaT range have been explored. Both methods are underpinned by comparison of each target spectrum with a set of templates.

The first technique considered was cross-correlation, where each target spectrum was cross-correlated with every template, and the stellar parameters were adopted from the template which produced the tallest cross-correlation function peak. However, a significant weakness of this method is that it does not lend itself easily to error propagation, and it does not readily support a continuous parameter space.

Consequently, we explored using a Markov Chain Monte Carlo (MCMC) method, which provides full-parameter fits. The target spectra are compared with the template set, interpolated as needed, by mapping the templates directly on to the observations and hence eliminating the need for separate continuum fitting to both the template spectrum and target spectrum. The interpolation of the template set is linear and allows for intermediate parameter values. For these reasons, and that parameter estimates come with an uncertainty, we ultimately favoured the MCMC method over cross-correlation.

Both of the methods and the template set used are described in more detail below. The RV measurements for both methods are in agreement within the uncertainties, with a slight bias to more negative values in the case of cross-correlation. The median offset between MCMC and cross-correlation RV measurements is $2.0\,\mathrm{km\,s^{-1}}$ – an amount that falls inside our median RV error estimate of $\sim 4.4/6.8\,\mathrm{km\,s^{-1}}$ for F stars/A stars.

3.1.2 Template spectra

In order to determine the needed quantities from the target spectra obtained, comparisons must to be made with a set of synthetic spectra. We initially set out using those from Coelho (2014), however we soon encountered problems because of an issue to do with the treatment of the Paschen line profiles. Essentially, the Paschen line profiles of the templates were too deep for a specific T_{eff}, $\log g$ combination, resulting in erroneous stellar parameter determination. This was most apparent for the $\log g$ measurements which were unrealistically high.

Consequently, we moved to another set of templates. These synthetic spectra were calculated using the approach of Gebran et al. (2016) and Palacios et al. (2010). These authors used SYNSPEC48 (Hubeny and Lanz, 1992) to calculate the spectra based on ATLAS9 model atmospheres (Kurucz, 1992), which assume local thermodynamic equilibrium, plane parallel geometry and radiative and hydrostatic equilibrium. Since our method of selection favours main sequence to giant A/F stars, the assumption of LTE is not an issue. We collected 1470 template spectra that sample the parameter domain as follows:

- $[\mathrm{Fe/H}] = 0, -0.5$
- $[\alpha/\mathrm{Fe}] = 0$
- $5000 \leq T_{\mathrm{eff}}$ (K) ≤ 15000, in steps of 500 K
- $3.0 \leq \log g \leq 5.0$, in steps of 0.5
- $0 \leq v \sin i$ ($\mathrm{km\,s^{-1}}$) $\leq 300\,\mathrm{km\,s^{-1}}$, in steps of $50\,\mathrm{km\,s^{-1}}$

The metallicity is not treated as a free parameter in the same way as the others are: instead we use two distinct template sets, one with $[\mathrm{Fe/H}] = 0$ and the other $[\mathrm{Fe/H}] = -0.5$, and compare the results (see Section 3.4). We do this because of the limited spectral coverage and resolution of our data. Our numerical trials of metallicity as a free parameter showed it to be underconstrained and prone to interfere with the descent onto the best-fitting values of other parameters. Nevertheless, there is an expectation that with increasing heliocentric distance along both pencil-beams,

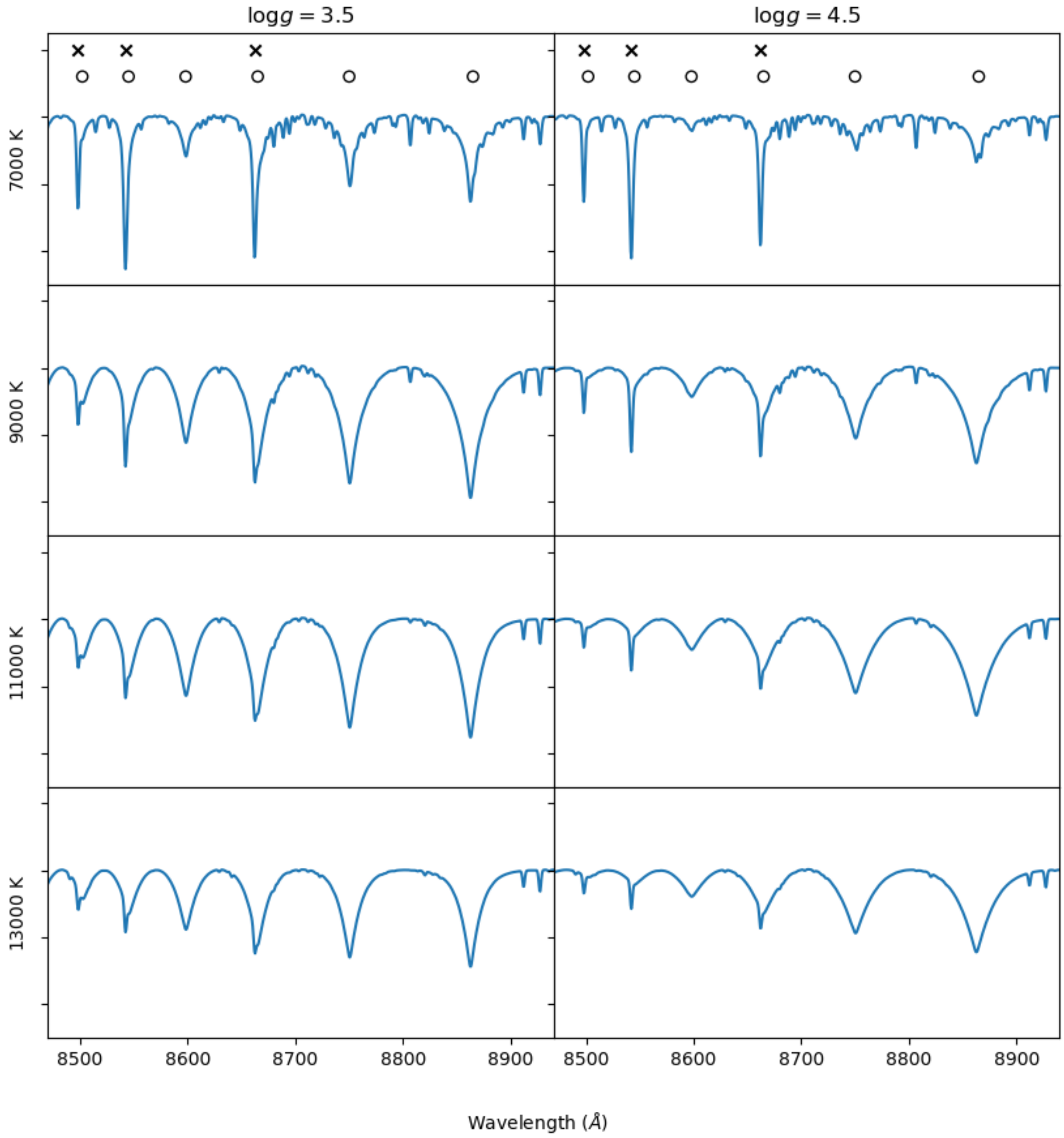

FIGURE 3.1: *Examples of template spectra, normalised for comparison. From top to bottom: templates with* $T_{\rm eff} = 7000, 9000, 11000, 13000$ *K. Left: templates with* $\log g = 3.5$*, and right: templates with* $\log g = 4.5$*. Those shown here have no rotational broadening. The Paschen lines are indicated with a circle, and CaT lines with a cross.*

there is likely to be a gradual decline in metallicity (see Section 1.4). At the median Galactocentric radius for the targets in each sightline, $R_G \sim 11$ kpc for $\ell = 118^\circ$ and $R_G \sim 13$ kpc for $\ell = 178^\circ$, a gradient of -0.07 dex kpc^{-1} (Sale et al., 2010) corresponds to [Fe/H] ~ -0.21 and [Fe/H] ~ -0.35 respectively. Hence it is appropriate to gauge the effect of modest changes in adopted metallicity.

The model spectra have a resolution of $R = 10000$, cover $3600 - 9650$ Å and have a constant wavelength sampling of 0.05 Å. However for this work, the templates have been broadened with a gaussian filter to match the resolution of the HectoSpec spectra and rebinned to a sampling of 0.56 Å (also to match the data). Figure 3.1 shows some examples of these smoothed templates, which have been roughly normalised for comparison. The left side are templates with $\log g = 3.5$, and the right $\log g = 4.5$. From top to bottom the templates have $T_{\text{eff}} = 7000, 9000, 11000, 13000$ K. The Paschen lines are indicated with a circle, and CaT lines with a cross.

3.1.3 Cross-correlation

The method of cross-correlation was popularised in astronomy by the works of Simkin (1974) and Tonry and Davis (1979). Since then it has been common practice when measuring radial velocities from observed spectra, being utilised across a vast range of astronomical ventures: from the first detection of an exoplanet around a Sun-like star (Mayor and Queloz, 1995), to the redshifts of galaxies (e.g. Drinkwater et al., 2000). Cross-correlation is a method that essentially slides every template spectrum over the target spectrum. At each point along the ‘slide’, i.e. at each trial RV, the value of the cross-correlation function (CCF) is calculated. When the two overlapped spectra become aligned, the CCF rises to form a peak. The location of the peak tells us the best match radial velocity difference between the template and the spectrum. The taller the peak, the stronger the similarity of the template and the spectrum, and hence the template producing the highest CCF peak is chosen as the best-fit template. For each spectrum, we adopt the stellar parameters of its best-fit template.

In order to cross-correlate target spectra with templates they must first be normalised. A continuum was chosen for each target spectrum and template spectrum via a linear fit passing through 3 sections of the spectrum, $8300 - 8325Å$, $8810 - 8813Å$, and $8925 - 8940Å$. These sections were chosen as they contain no noticable spectral features and reside outside of regions of strong sky lines, to minimise the potential impact of bad sky-subtraction. Each target and template spectrum was normalised using its continuum fit.

The cross-correlation function, $c(n)$, is given by

$$c(n) \equiv g \times t(n) = \frac{1}{N\sigma_g \sigma_t} \sum_m g(m)t(m-n) \tag{3.1}$$

where $g(n)$ is the target spectrum, $t(n)$ is the template spectrum, N is the number of bins, with bin number n, and σ_g and σ_t are the root mean square (RMS) of the spectra given by

$$\sigma_g^2 = \frac{1}{N}\sum_n g(n)^2 \tag{3.2}$$

$$\sigma_t^2 = \frac{1}{N}\sum_n t(n)^2 \tag{3.3}$$

This formalism is taken from Tonry and Davis (1979).

Each normalised target spectrum was cross-correlated with every normalised template spectrum. The cross-correlation was performed over the range $8470 - 8940\AA$. For each velocity shift to be cross-correlated, the wavelength axis of the template was shifted using the Doppler formula. The shifted template was then linearly interpolated to line up with the wavelength binning of the target spectrum. The value of the cross-correlation function was then computed. The velocity range considered was $< |500\,\mathrm{km\,s^{-1}}|$.

A gaussian was fit to the tip of the peak of each cross-correlation function. The peak height was taken as the value of the CCF at the centre of the gaussian fit. In general, this value is a little different to the peak of the CCF itself. The best template for each star was chosen to be the one yielding the cross-correlation function with the tallest peak. The centre of the gaussian defines the radial velocity of the star, with respect to the frame of the telescope. The choice of fitting a gaussian to the peak was arrived at after experimentation of different options, and is a consistent method of measuring the parameters of the CCF peak.

Numerical experiments, cross-correlating noisy versions of the templates with the template set, have shown that a gaussian fit to the top $\sim 5 - 15\%$ of the peak provides the most unbiased radial velocities. These experiments are described in greater detail below. The more localised gaussian fit avoids errors that could arise if a fit is made to the entire peak, as the latter is often skewed most likely by imprecision in the continuum fitting. For the HectoSpec data, we made a fit to the top 10% of the peak.

Figure 3.2 shows an example of the cross-correlation of a HectoSpec spectrum. The top panel shows the normalised HectoSpec spectrum with its best-fit template overlayed. The corresponding CCF is shown in the bottom panel, along with the gaussian fit to the tip of the peak.

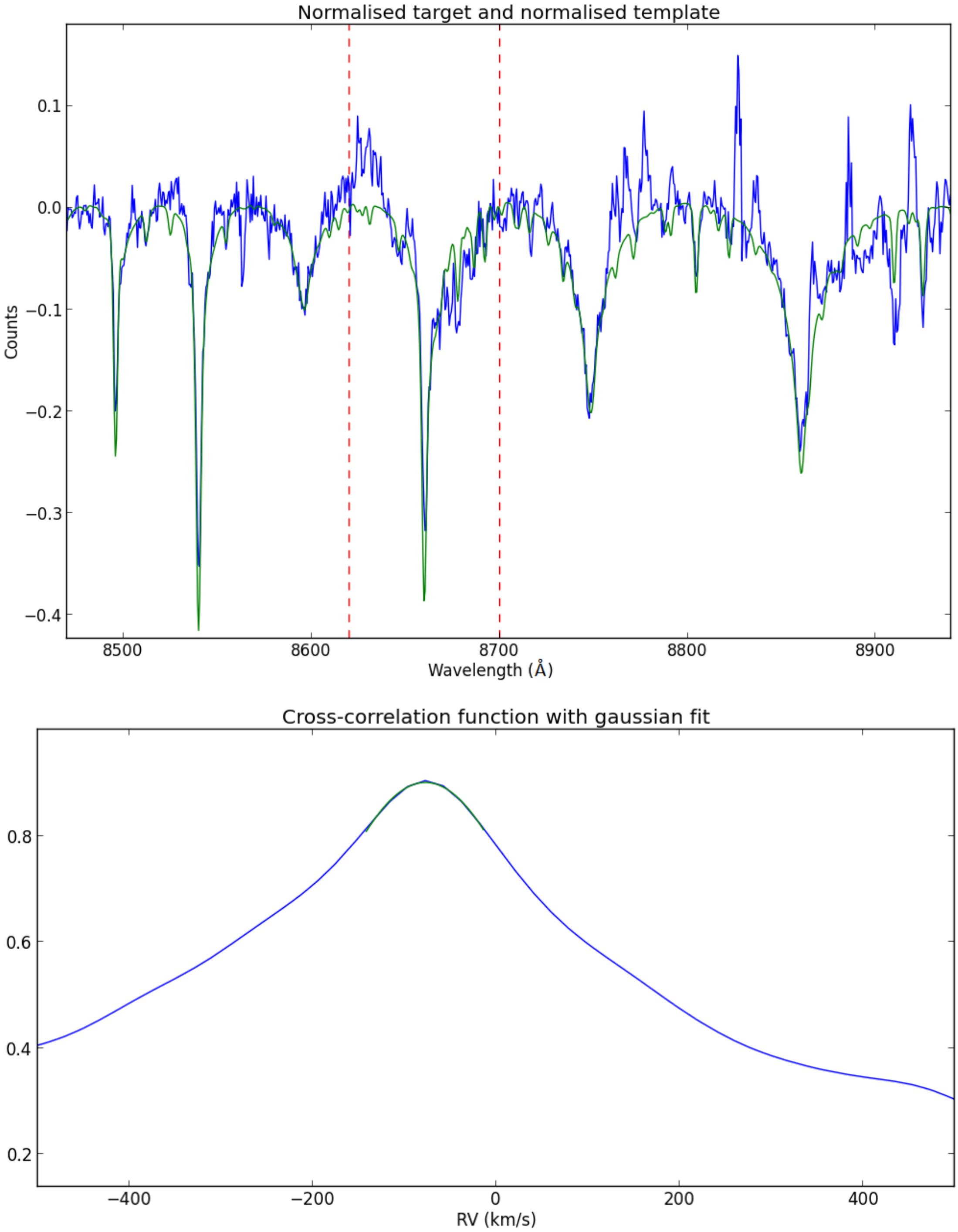

FIGURE 3.2: *An example of the cross-correlation of a HectoSpec spectrum with its best-fit template. The top panel shows the normalised HectoSpec spectrum (blue) with its normalised best-fit template overlayed (green). The bottom panel shows the corresponding CCF (blue), with a gaussian fit to the tip of the peak (green).*

3.1.3.1 Investigating systematic errors through the cross-correlation of noisy shifted templates with templates

To improve the algorithm and to understand the systematic errors, noisy versions of the template spectra, shifted by 50 km s^{-1}, were cross-correlated with the templates. Varying levels of noise were added to the templates to replicate spectra with S/N ranging from 20 to 100. Since the radial velocity, effective temperature, $\log g$, and $v \sin i$ of the 'target' (noisy template) were all known, the reliability of the algorithm could be evaluated and improved upon.

The accuracy of the measured RV and best-template match was greatly improved when the target spectrum and template spectrum had the same bin sampling, and the template spectrum was broadened to match the (synthetic) instrumental broadening of the target spectrum.

Various methods of continuum fitting were tested, such as a linear fit, a third-order polynomial fit, and fits with a range of fixed slopes. The fixed slope fits produced bad results. There was little difference between the results for the linear or third order fits, and hence for simplicity the linear fit was chosen as the best option.

Gaussians were fit to varying percentages of the tip of the tallest peak. We found the more localised fits of $\sim 5-15\%$ provided the most accurate results in terms of best-template choice, and returned RVs closest to the true value. Consequently we chose to fit the gaussian to the top 10% of the peak in the HectoSpec data analysis.

The parameter to compute as a means to choose the best-fit template was investigated. There were 3 initial options which were thought to be potentially suitable choices. These were the tallest peak height, the contrast between the peak height and the RMS of the cross-correlation function outside of this peak, and the Tonry and Davis (1979) R-value. The R-value is given by $R = h/\sqrt{2}\sigma_a$, where h is the height of the peak, and σ_a^2 is the RMS of the antisymmetric component of the CCF. For each parameter, the template with the largest value was chosen to be the best fit. Our investigations found:

- The R-value depends on the symmetry of the cross-correlation function. It is often thought of as a measure of the similarity of two cross-correlated subjects. However, in our experiments, the accuracy of template match and RV results were not satisfactory, probably due to some skew of the peak from imprecision in the continuum fitting.

- We took the contrast to be the ratio of the height of the tallest peak to the RMS of the cross-correlation function outside of $\pm 3\sigma$ of the peak. The height of the tallest peak was measured by taking the maximum value in the cross-correlation function. For this parameter, the accuracy of template match and RV results were not satisfactory.

- The height of the tallest peak was measured to be the value of the cross-correlation function at the centre of the gaussian. The results of the experiments show this parameter was best for choosing the best-fit template and measuring the RVs.

As we became more familiar with the cross-correlation technique, its flaws became more apparent. The most damning is that it does not easily lend itself to error propagation. There are obvious systematic errors that, while we could work to minimize them, are unavoidable, particularly in the complicated business of continuum fitting. Lastly, it does not support a continuous parameter space. For these reasons, we explored an alternative method: MCMC.

3.1.4 MCMC assisted full-parameter fitting

A Markov Chain is a mathematical process that transitions from one state to another, with the probability of transitioning to a particular state depending only on the previous state. Regardless of how the process got to its present state, the possible future states are fixed. After a while (and subject to certain conditions) the probability distribution of possible states converges to the 'stationary distribution'. Markov Chain Monte Carlo simulation is a Bayesian method that exploits this feature by using a Markov Chain whose stationary distribution is the posterior probability distribution of the model in question. By randomly sampling from the converged Markov Chain, we are essentially sampling from the posterior probability distribution.

In practice a set of 'walkers' form the Markov Chain, and are set to explore the parameter space along paths that are responsive to a likelihood function. Eventually the walkers converge to the place of highest likelihood - revealing the posterior probability distribution which can be marginalised over the parameters.

The first step in this process is a mapping of template spectra on to each observed spectrum. This is a novel feature that allows us to avoid the tricky business of normalisation of both the target spectrum and templates, and it is then possible to monitor how the mapping numerically influences the outcome. The mapping function we have adopted is linear which we find to be an adequate approximation over the short wavelength range considered (8470-8940 Å) in the case of the HectoSpec CaT data. This process introduces two extra free parameters to be fit: the gradient and the intercept of the mapping function. These are nuisance parameters.

The posterior probability distributions of the 6 free parameters ($T_{\rm eff}$, $\log g$, $v \sin i$, RV, mapping gradient and intercept) are obtained assuming a likelihood function of the form:

$$\mathscr{L}(y, \sigma^2; x_1, ..., x_n) \propto e^{-\frac{1}{\alpha}\sum_i \frac{(x_i - y_i)^2}{2\sigma_i^2}} \tag{3.4}$$

where x refers to the target star spectrum sampled at pixels $i = 1...n$ and y refers to the template spectrum. Our choice of a Gaussian likelihood function assumes the difference between observed spectrum and template at each pixel follows a gaussian distribution. Since the pixels in a resolution element are not independent, we compensate by dividing the summation by the number of pixels per resolution element, α. This is 4.3 in our case. σ_i is the noise level of the target star at pixel i, assumed to be gaussian, given by

$$\sigma_i = \sqrt{\sigma^2_{sky+star,i} + \sigma^2_{sky,i}} \tag{3.5}$$

where $\sigma^2_{sky+star,i}$ is the count level of the raw spectrum (before sky subtraction), and $\sigma^2_{sky,i}$ is the count level of the sky spectrum.

By linearly interpolating the template grid, templates with intermediate parameter values are produced and hence the model parameter space can be rendered continuous. The RV range is sampled by shifting the wavelength axis of the template according to the Doppler formula.

The ‘EMCEE’ PYTHON package (Foreman-Mackey et al., 2013) is used to execute the MCMC parameter space exploration. It implements the affine-invariant MCMC ensemble sampler described in Goodman and Weare (2010). Our procedure is set up for 200 walkers, with their initial parameters chosen by randomly selecting from a grid covering the total parameter space. The walkers quickly depart from these gridded values. The priors used are flat for all parameters, with the range available to each parameter matching the range in the template set. The range of the RV prior covers all realistic values (±500 km s^{-1}), and the ranges of the slope and intercept of the mapping function were determined by experimentation with the dataset ($\pm 1.0 \times 10^{-5}$ for the slope and ± 0.1 for the intercept).

After many steps, the walkers converge (we use 2000 steps with a 700 step burn-in to start with). The distribution of parameter values returned by them define the posterior probability

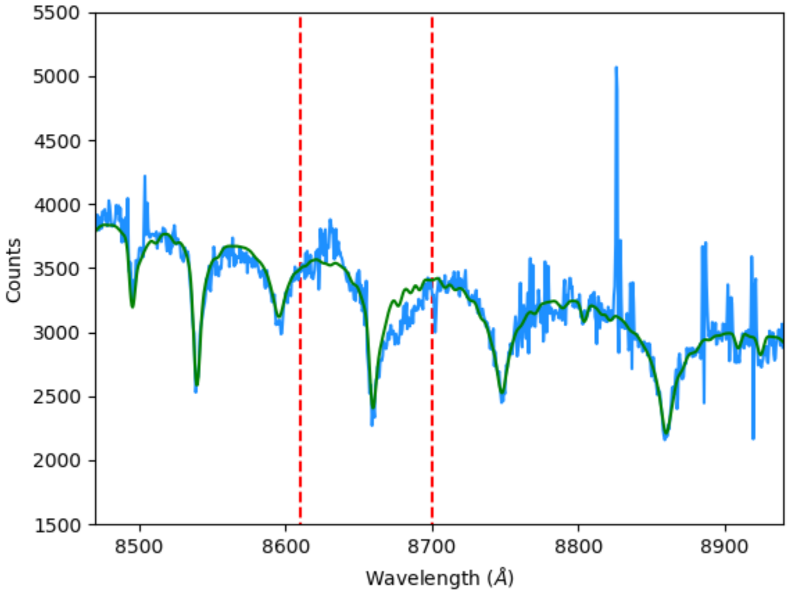

FIGURE 3.3: *An A star spectrum (blue) with best-fitting template match (green).*

distribution of the parameters. These are typically of the form of a gaussian. The medians of the marginalized distributions are adopted as the best estimates of parameter values and the uncertainties are based on the 16th and 84th percentiles, roughly corresponding to 1 standard deviation from the mean/median. Figure 3.3 shows an example of an observed A star spectrum (blue line), with best-fitting template (green line). The posterior probability distributions for this object is shown in Figure 3.4. Figure 3.5 shows the fitting function used (blue line), compared to the stellar spectrum divided by the template (orange line) - it is typical in its demonstration that a linear function is a good approximation. The path of the walkers, after the burn-in, is shown in Figure 3.6. For the particular set up described here, and on a mid-range machine (Intel i3-5005U CPU, 8 GB RAM at 1600 MHz), the compute time per target spectrum was $\sim$ 20 minutes.

3.2 Derived stellar parameters

The stellar parameters for the HectoSpec sample of A/F stars presented here are determined with the favoured MCMC method and the Solar metallicity template grid. The impact of reduced metallicity is considered in Section 3.4.

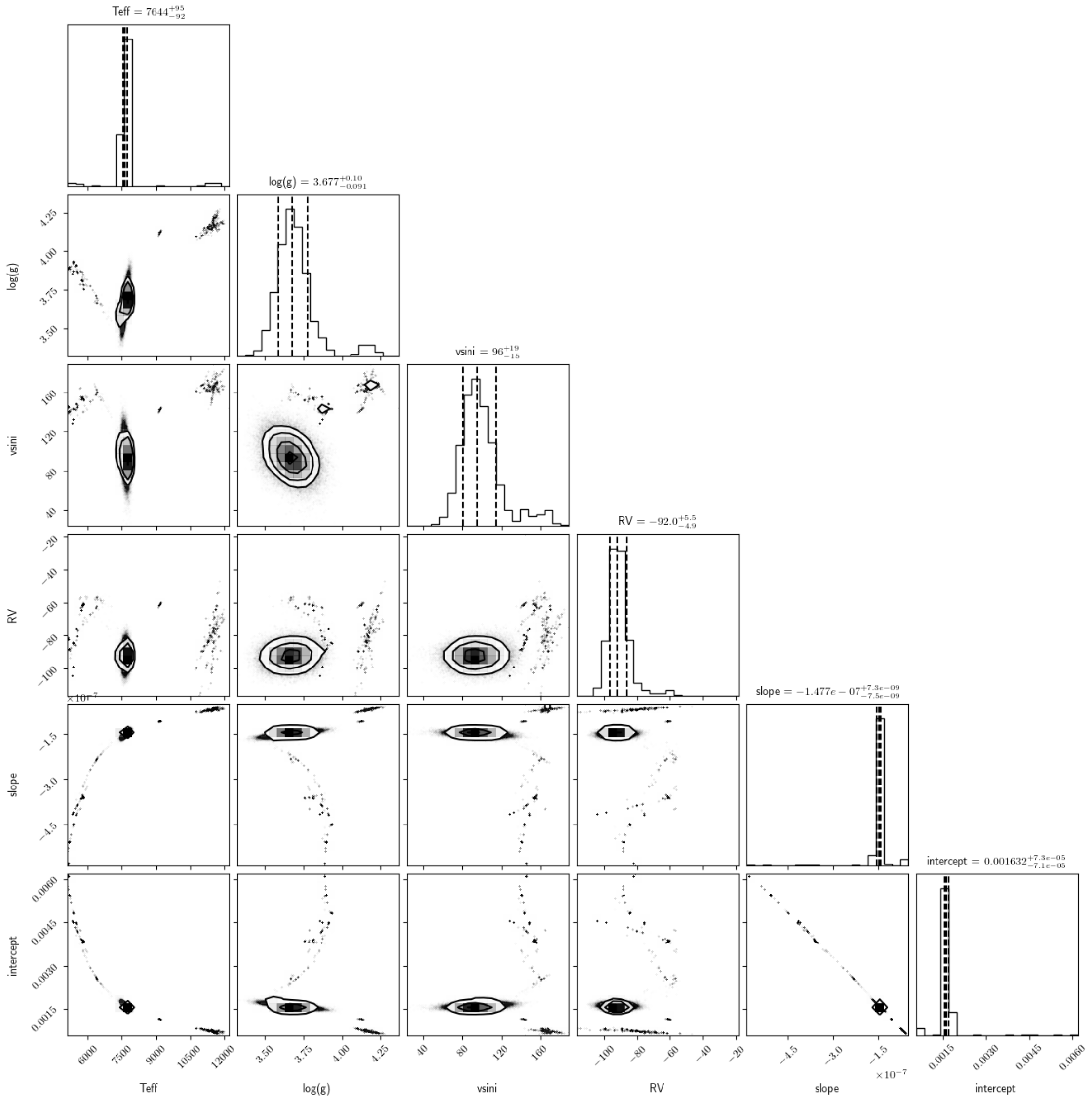

FIGURE 3.4: *A corner plot showing the posterior probability distributions of the parameters for the spectrum shown in Figure 3.3. The histograms are the marginalised distributions, with dashed lines indicating the median and 16th and 84th percentiles.*

3.2.1 T_{eff}

The measured T_{eff} distribution for both sightlines combined can be seen in Figure 3.7. The red bars represent the stars originally selected from the IPHAS $r-i$, $r-H\alpha$ colour-colour diagram as F stars, and the blue bars represent the A stars. 78% of the stars selected as candidate F stars have measured T_{eff} values of $6000-7500$ K (typical of F stars), and 81% of the candidate A stars have T_{eff} values of $7500-10000$ K (typical of A stars). It is necessary to point out that the template set spans temperatures inclusive of G stars ($T_{\mathrm{eff}} \leq 6000$ K) and B stars ($T_{\mathrm{eff}} > 10000$ K). Stars measured as G stars make up only 2% of the total sample and B stars just 4%. These are mainly stars that have contaminated the IPHAS $r-i$, $r-H\alpha$ selection strips (see Figure 2.1).

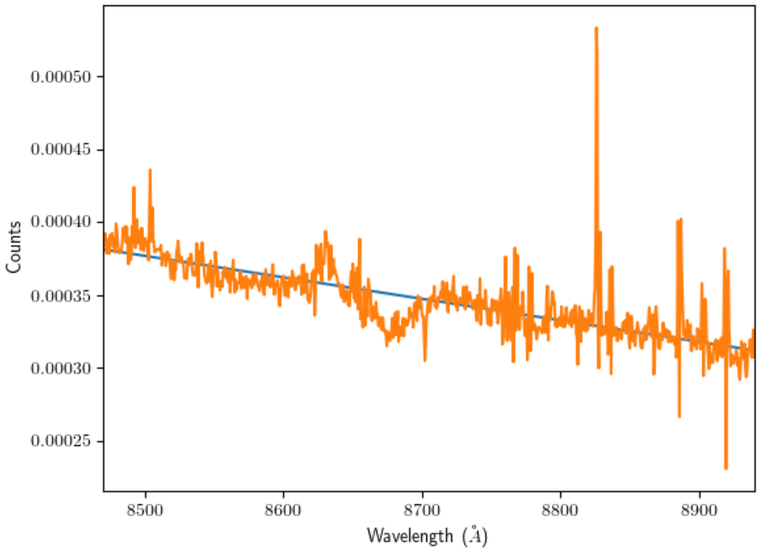

FIGURE 3.5: *The fitting function (blue line) corresponding to the object of Figure 3.3. The orange line shows the stellar spectrum divided by the template, showing the linear fitting function is a good approximation. The prominent narrow spikes at* > 8800Å *and wiggle between* $8600-8700$Å *are due to incompletely subtracted sky lines in the observed spectrum (see Section 2.2).*

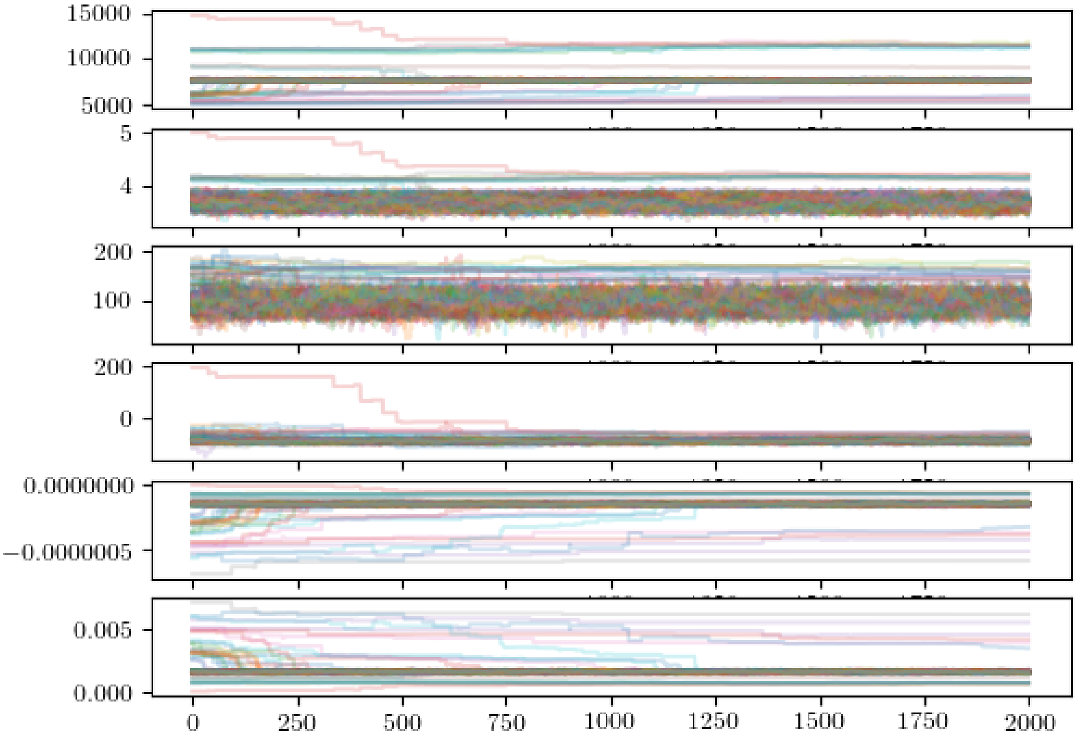

FIGURE 3.6: *The path of the walkers, after the burn-in, for the object in Figure 3.3. Top to bottom:* $T_{\rm eff}$, $\log g$, $v \sin i$, *RV, slope, intercept.*

Given the modest levels of contamination (e.g. only 12% of the inital A star selection turned out to be cooler than 7500 K), the method of selection is shown to be very effective and practically viable. For simplicity in the remainder of the document, we label stars as either F or A-type, with best-fit $T_{\rm eff} = 7500\,\mathrm{K}$ as the boundary dividing them.

The positive and negative errors in $T_{\rm eff}$ as a function of $T_{\rm eff}$ are shown in the top panel of Figure 3.8. The median of the positive and absolute values of the negative errors combined is $\sim 150\,\mathrm{K}$. However the average error increases with temperature and there are a number of targets that have large asymmetric errors, betraying an unresolved fit dilemma.

The expected spectral behaviour is that, as temperature increases, the Paschen line depths increase until $T_{\rm eff} \sim 9000\,\mathrm{K}$, and become shallower again as temperature continues to rise (see Figure 3.1). This means there can be a degeneracy where the Paschen line profiles of a lower temperature template are similar to that of a higher temperature template, with the addition of line broadening effects associated with surface gravity and rotation. Stars suffering from this degeneracy present an issue for the MCMC method as their posterior is multi-modal, with maxima at both the 'correct' parameter solution (global maximum), and at the 'incorrect' solution with similar Paschen line profile (local maximum). In theory, it should be possible to distinguish between these two solutions since the CaT lines are more obvious as temperature declines below 9000 K. However, a multi-modal posterior is a challenge for the MCMC walkers since they can become stuck at a local maximum, unable to escape and find the global maxima. A solution to this, known as Parallel Tempering MCMC (PTMCMC), is explored in Section 7.1.

The set of stars with large $T_{\rm eff}$ errors ($> 1000\,\mathrm{K}$) comprises only 85 of the 1261 targets, and are henceforth removed from the sample. These are represented by empty circles in Figure 3.8. This leaves a total sample made up of 711 A stars ($T_{\rm eff} > 7500\,\mathrm{K}$) and 472 F stars ($T_{\rm eff} \leq 7500\,\mathrm{K}$): broken down into the sightlines, there are 479 A stars and 311 F stars in the $\ell = 118^\circ$ sample, and 232 A stars and 161 F stars in the $\ell = 178^\circ$ sample.

3.2.2 $\log g$

The middle panel of Figure 3.8 shows the positive and negative errors in $\log g$ from the posterior distributions as a function of $T_{\rm eff}$, for the A and F stars at Solar metallicity. It is clear from the figure that the formal $\log g$ error rises steadily with decreasing effective temperature. The median error at $T_{\rm eff} > 7500\,\mathrm{K}$ is 0.09, while below this it increases to 0.14. This trend most likely

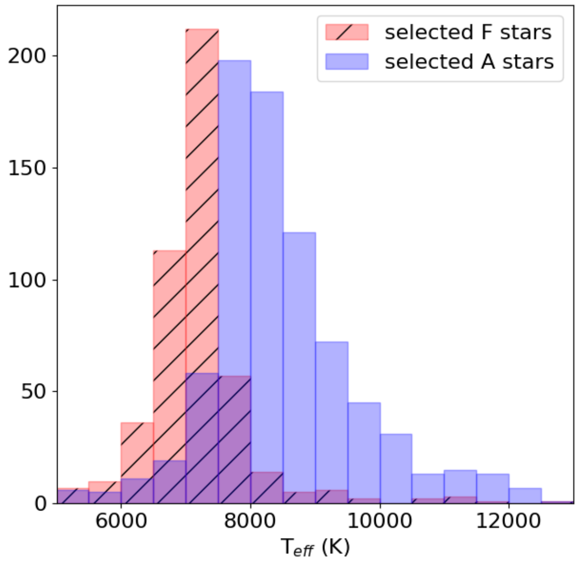

FIGURE 3.7: *Superposed distributions of measured T_{eff} values (for both sight lines combined) of stars selected as probably F-type (red histogram) and A-type (blue histogram). Of the stars initially selected as A-type, only 12% are cooler F/G stars.*

tracks the growing importance of H^- continuum opacity with decreasing effective temperature (masking off the lower photosphere), causing the wings of the lines to become less sensitive to surface gravity. Gray and Corbally (2009) have noted a 'dead zone' among mid-late F stars in which dwarf and giant spectra are nearly indistinguishable at these wavelengths.

In F stars with appreciably reduced Paschen line profiles, in particular, this underlying astrophysical trend is compounded to an extent by the moderate spectral resolution of the data. We find for these cooler stars that the fits begin to exhibit a 3-way degeneracy for combinations of temperature, gravity and metallicity. An example of this degeneracy at work in the CaT in cooler F stars was presented by Smith and Drake (1987). However, with metallicity fixed, it is possible to identify temperature and gravity albeit with greater error on the latter. The returned F star $\log g$ distribution, shown in Figure 3.9, is skewed strongly in favour of near-MS objects, with a median value of 4.5 and interquartile range 4.1-4.8, tapering off into a tail reaching down to one object with $\log g \simeq 3.0$ (the lower bound on the template set). This skewed distribution is somewhat in contrast to what we would expect, for example the $\log g$ distribution of F stars from a Besançon model (Robin et al., 2003) returns a median of 4.2, with interquartile range 4.0-4.4. While the model distribution agrees with our measurements in terms of tailing off at low $\log g$ values (~ 3), disagreement arises at large $\log g$ where very few model F stars have $\log g > 4.7$.

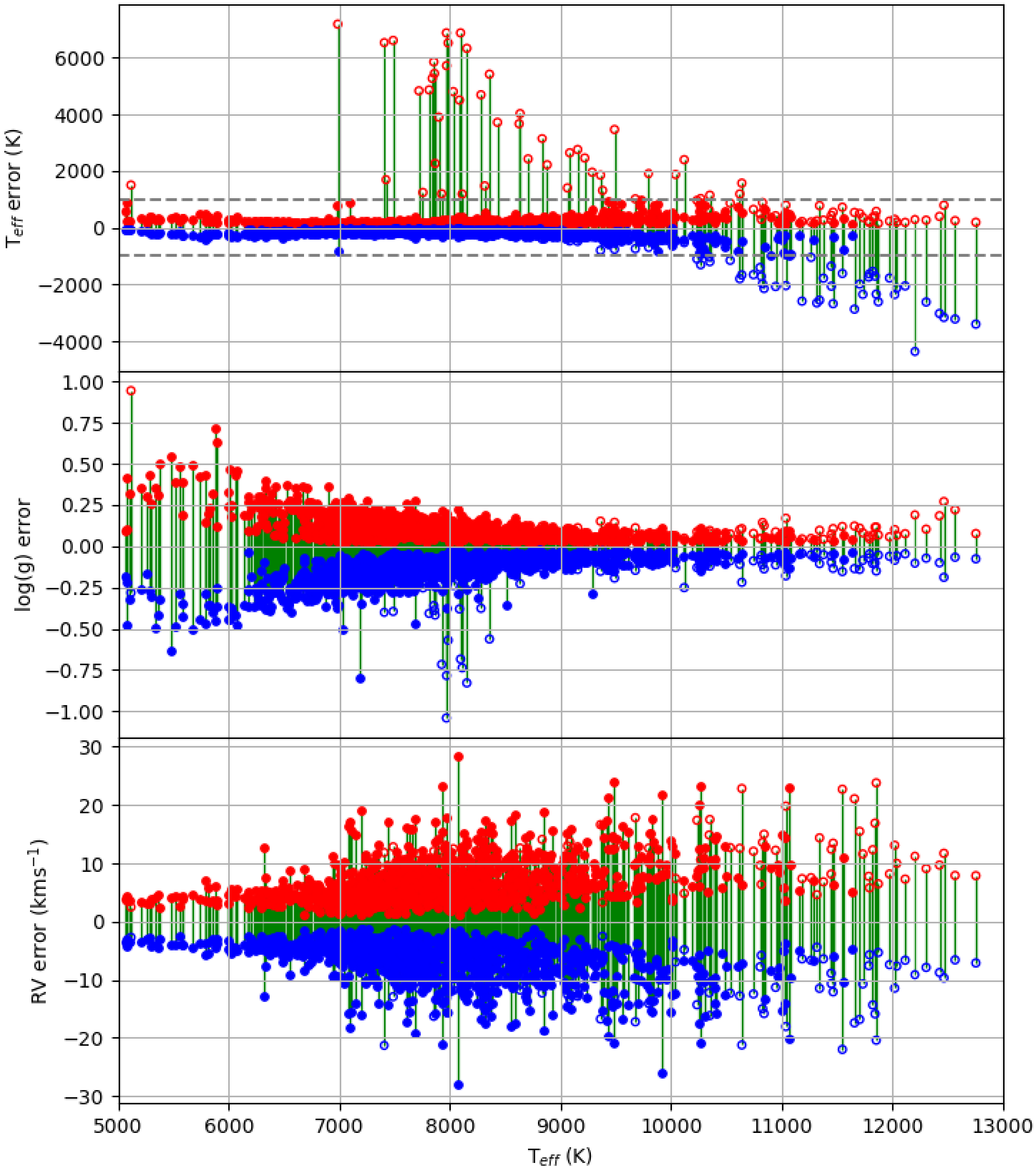

FIGURE 3.8: *Positive (red) and negative (blue) errors in T_{eff} (top panel), $\log g$ (middle panel) and RV (bottom panel) as a function of T_{eff}. The grey dashed lines in the top panel represent the T_{eff} error cut: points with $|error| >$1000 K that are removed from the sample are shown in this Figure, represented by empty circles. The green bars connect the positive and negative errors for each individual target.*

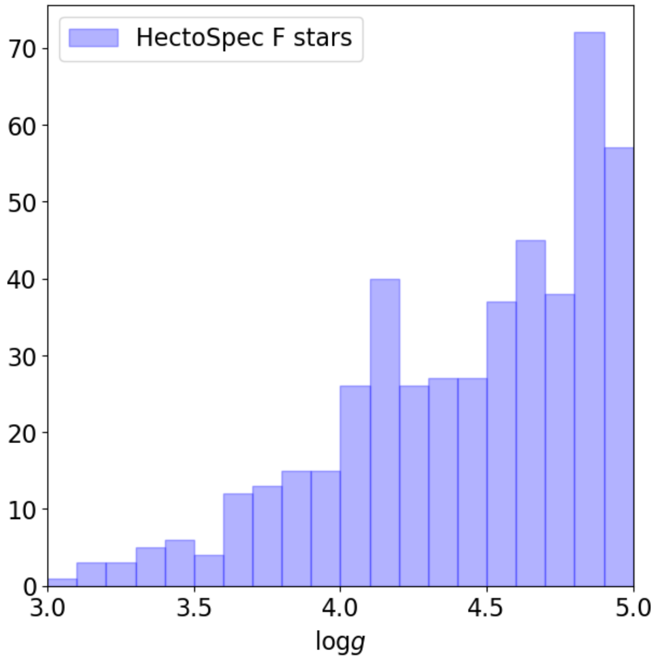

FIGURE 3.9: *Distribution of measured* $\log g$ *values of F stars for both sight lines combined.*

The distribution of measured $\log g$ values for the A stars can be seen in Figure 3.10. Also shown is the distribution of $\log g$ for A stars from a Besançon model (Robin et al., 2003) for $\ell = 118^{\circ}$, after convolving with a gaussian of $\sigma = 0.09$ to emulate the HectoSpec measurement error, for a more useful comparison. The two distributions are similar, although the measured HectoSpec distribution has a tail at large values of $\log g$ that is not seen in the Besançon model, and its peak is not perfectly matched. A shift of the Besançon distribution of $+0.15$ brings the two distributions into rough alignment. This could be evidence of a bias in our measurements. We appraise the impact of this in Section 4.5. The stars occupying the high-end tail, which appears more extended than in the Besançon model distribution, are mainly cooler objects carrying larger-than-median errors (see Figure 3.8).

3.2.3 $v \sin i$

Figure 3.11 shows the measured $v \sin i$ distribution for both sightlines combined, separated into F stars (red bars) and A stars (blue bars). The distribution is as expected, with generally low values for F stars and a spread from low to high values for A stars (Royer, 2014). The median error on $v \sin i$ for stars with $T_{\rm eff} < 10000$ K is $\sim 20\,{\rm km\,s^{-1}}$, increasing to $\sim$40 $\rm km\,s^{-1}$ for stars with $T_{\rm eff} > 10000$ K that are more commonly fast rotators. There is evidence of a slight negative correlation between individual $\log g$ and $v \sin i$ parameter fits. This is because, as $\log g$ increases,

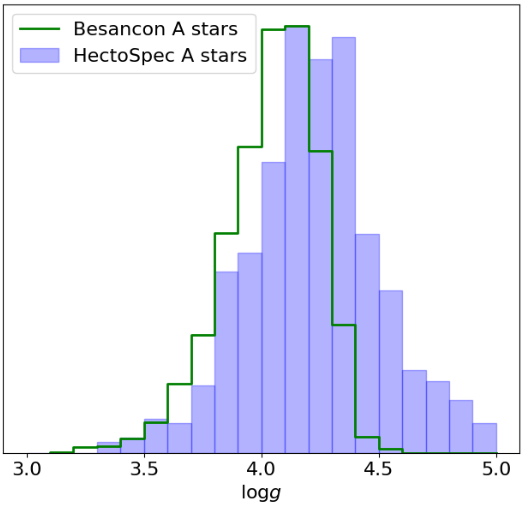

FIGURE 3.10: *Distribution of measured* $\log g$ *values of A stars for both sight lines combined (blue histogram). The distribution of* $\log g$ *values of A stars from a Besançon model for* $\ell = 118°$ *is also shown (green histogram). This has been convolved with a gaussian of* $\sigma = 0.09$ *to emulate the HectoSpec measurement error.*

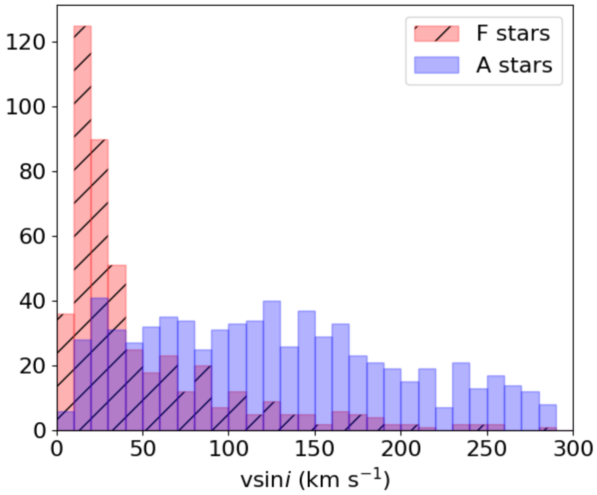

FIGURE 3.11: *The distributions of measured* $v \sin i$ *values, separated into F stars (red) and A stars (blue), and shown overplotted. The two lines of sight are merged within each distribution.*

the absorption line profiles become shallower and more wing-dominated. The effect is qualitatively similar as $v \sin i$ increases, resulting in a negative correlation as the parameters essentially compensate for each other.

3.2.4 RV

The bottom panel in Figure 3.8 shows the errors on measured RV as a function of T_{eff}. The median error is $\sim 4.4\,\mathrm{km\,s^{-1}}$ for F stars and $\sim 6.8\,\mathrm{km\,s^{-1}}$ for A stars. This difference is attributable to the growing contrast of the CaT lines with decreasing effective temperature. These sharp, narrow CaT lines are excellent RV estimators since they allow for precise alignment of the templates. In the cooler F stars, the CaT lines are at their most prominent, providing our most confident RV measures. For hotter A stars the CaT lines gradually diminish, resulting in increased RV uncertainty.

3.3 Extinctions, absolute magnitudes and distances

Since our goal was to study the kinematics of the stars along the sightlines, it was essential to also determine distances to the stars. By combining the IPHAS photometry data with our measured stellar parameters, we could use isochrones to obtain an absolute magnitude and hence the spectro-photometric distance to the star. As the observed sightlines lie in the Galactic plane, it is also paramount to correct for the impact of extinction from the interstellar medium.

The heliocentric distance, d, of each star was calculated via the following equation

$$d = 10^{(\mu+5)/5} \tag{3.6}$$

with μ being the distance modulus with extinction, given by

$$\mu = (m_i - M_i) - A_i \tag{3.7}$$

in which m_i is the apparent magnitude in the i band, M_i is the absolute magnitude, and A_i is the extinction.

We obtained absolute magnitudes from Padova isochrones[1] by interpolating on the T_{eff} and $\log g$ scales (Bressan et al., 2012; Chen et al., 2015). Figure 3.12 illustrates the process. The Padova $\log g$ and T_{eff} scales for MS object are shown, coloured by the absolute i magnitude. The black point at $T_{\mathrm{eff}} = 9000\,\mathrm{K}$, $\log g = 4.2$ represents an example HectoSpec object with typical error bars. For all HectoSpec objects, we interpolated a value for M_i on the basis of its median $\log g$

---

[1] `http://stev.oapd.inaf.it/cgi-bin/cmd`

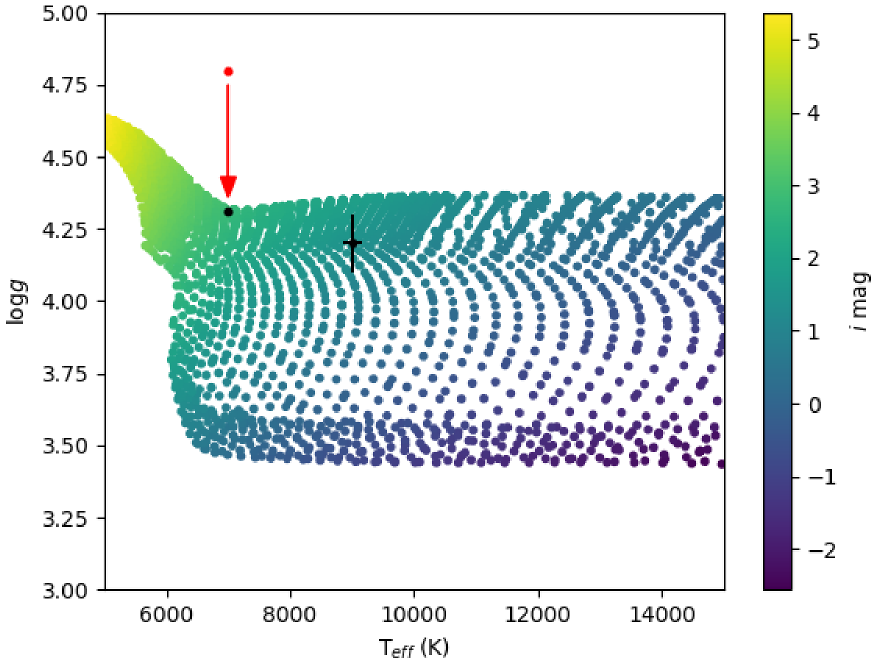

FIGURE 3.12: *An illustration of the process of obtaining absolute magnitudes. The Padova absolute i magnitude, represented by the colour scale, is shown as a function of* $T_{\rm eff}$ *and* $\log g$. *The black dot at* $T_{\rm eff} = 9000\,K$, $\log g = 4.2$ *represents an example of a HectoSpec object with typical error bars. The corresponding i value is obtained by interpolation on the Padova* $T_{\rm eff}$, $\log g$ *grid, and its uncertainty is obtained by interpolating on the* $1-\sigma$ *parameter errors. The red point represents an object with unrealistically large* $\log g$, *which is reset to the MS to adopt an i magnitude.*

and $T_{\rm eff}$ returned by the MCMC fits, and calculated an error on M_i using its $\log g$ and $T_{\rm eff}$ 1σ values. Where $\log g$ exceeds the maximum present in the Padova isochrones for the specified $T_{\rm eff}$ (represented by the red point), we reset $\log g$ to the maximum. The effect of this is to place such objects, plausibly, on the main sequence. The median error on the absolute magnitudes (due to stellar parameter uncertainties) is ~0.3. This is the dominant error source in our measured kinematics.

The extinction of each target was calculated using

$$A_i = 2.5[(r-i)_{\rm obs} - (r-i)_{\rm int}] \tag{3.8}$$

where $(r-i)_{\rm obs}$ is the observed colour of the star taken from IPHAS photometry. The coefficient of 2.5 is the ratio of A_i to $A_r - A_i$ for main sequence A/F stars with reddening levels similar to the HectoSpec data, using the Fitzpatrick law with $R_V = 3.1$ (Fitzpatrick, 1999). The intrinsic colour of the star, $(r-i)_{\rm int}$, is calculated for the template grid via synthetic photometry and following Drew et al. (2014),

$$(r-i)_{\text{int}} = -2.5\log\left[\frac{\int T_r \lambda F_\lambda d\lambda}{\int T_r \lambda F_{\lambda,V} d\lambda}\right] + 2.5\log\left[\frac{\int T_i \lambda F_\lambda d\lambda}{\int T_i \lambda F_{\lambda,V} d\lambda}\right] \tag{3.9}$$

where T_r and T_i are the transmission profiles for the IPHAS r and i bands, λ is wavelength, F_λ is the flux distribution of the template, and $F_{\lambda,V}$ the flux distribution of Vega. The value for each target star was obtained by interpolating on this grid based on the measured T_{eff} and $\log g$.

The median error on intrinsic colour is ~0.01, corresponding to the range from interpolation with the 1σ T_{eff} and $\log g$ values, i.e. due to stellar parameter uncertainties. The median error on A_i, also due to stellar parameter and photometric uncertainties, is ~0.05. After dereddening the observed magnitudes, μ is obtained: across the entire sample the interquartile range for the error in μ is 0.2 to 0.4. The errors at the low end of this range are associated with early-A stars. Almost all stars have extinctions $A_i < 2$.

Figure 3.13 shows the A_i extinctions as a function of estimated distance modulus for both sight-lines. Also shown are the mean extinction trends from Sale et al. (2014) across the two pencil-beams, including the expected dispersion in extinction (grey shaded region). This comparison provides some insight into the plausibility of the distance modulus distribution of our sample. An important difference to be aware of is that the Sale et al. (2014) trends were computed from IPHAS photometry of all probable A-K stars, down to apparent magnitudes that are appreciably fainter (to $i \sim 20$) than those typical of our analysed spectra ($i < 18$). In both sight lines, there is evidence that the spectroscopic samples favour lower extinctions than the fainter-weighted photometrically-based trends. This is most likely a straight-forward observational selection effect.

To check this, we have examined the impact of the counts cut we placed on the spectra included in the analysis: specifically, we have compared median estimates of extinction, derived from their $r-i$ colour, of the stars analysed (counts > 2000), to the lower-count stars not analysed. Table 3.1 presents the median observed $r-i$ colours for stars with < 2000 counts and stars with > 2000 counts. Assuming an A star has a typical intrinsic colour of $r-i = 0.07$, and an F star has intrinsic colour of $r-i = 0.20$, we used equation 3.8 to calculate the a median estimate of A_i of the two stellar types, in the two count groups. We found that for both directions the cut biases the typical extinction of the A stars to lower values: the strength of effect is that the unanalysed objects have a median A_i that is greater by ~ 0.4 magnitudes. This helps explain

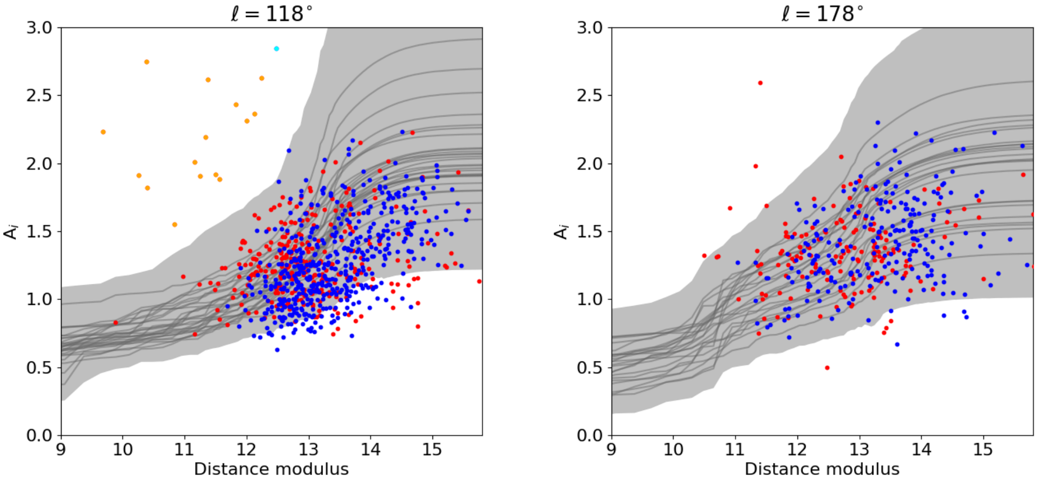

FIGURE 3.13: *The extinction, A_i, of F stars (red points) and A stars (blue points) as a function of distance modulus. Left: $\ell = 118°$, right: $\ell = 178°$. Also shown in each panel are the photometrically-predicted mean extinction trends (grey lines) across the pencil-beam (Sale et al., 2014). The grey shaded region defines the expected dispersion in extinction at every distance within the beam. Stars that lie far from the trend in the upper panel are highlighted by a change of colour – orange for the F stars and cyan for one A star.*

		$(r-i)_{obs}$		A_i		ΔA_i
		counts < 2000	**counts** > 2000	**counts** < 2000	**counts** > 2000	
$\ell = 118°$	**A**	0.76	0.58	1.73	1.28	-0.45
	F	0.71	0.72	1.28	1.30	+0.02
$\ell = 178°$	**A**	0.79	0.66	1.80	1.48	-0.32
	F	0.76	0.73	1.40	1.33	-0.07

TABLE 3.1: *The median observed $r-i$ colours and i band extinction for A and F stars in the two sightlines, with counts < 2000 and counts > 2000.*

the tendency for the blue A-star data points, particularly, to sit lower in Figure 3.13. Among the cooler, on-the-whole closer, F stars there is little difference.

The alternative explanation for the underestimated extinctions – overlarge distance moduli – runs into difficulty when it is recalled that there may be systematic overestimation of surface gravities (see Sections 3.2.2 and 5.1). We view this comparison as tensioning against accepting and correcting for such a bias in $\log g$, as this would drive up the distance moduli, creating a yet bigger offset in Figure 3.13.

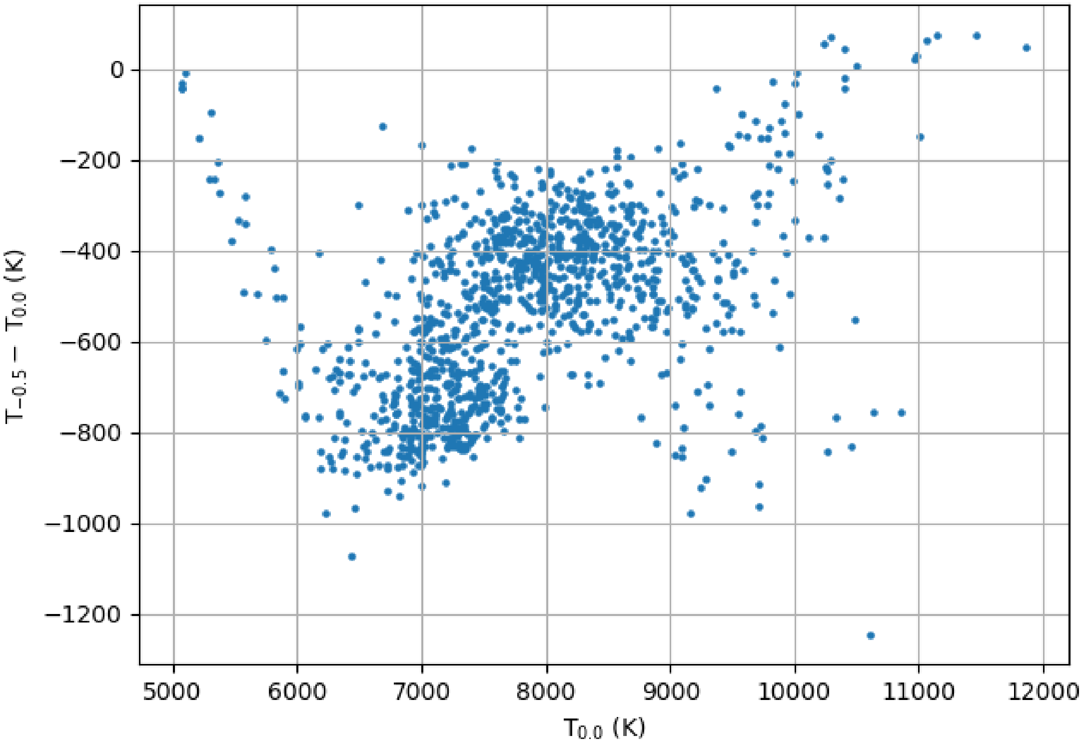

FIGURE 3.14: *Difference between measured* $T_{\rm eff}$ *values for* [Fe/H] $= -0.5$ and 0.0.

3.4 The effect of metallicity

So far all the parameters obtained and described have been computed for Solar metallicity. As noted in Section 3.1.2, we expect a gradual decline of metallicity with increasing heliocentric distance along our sightlines. In order to gauge the effect of this we have measured the stellar parameters and RVs again, as described in Section 3.1.4, but with [Fe/H] set to -0.5. The comparison is presented below. We remove any objects with large $T_{\rm eff}$ errors (> 1000 K) at [Fe/H] $= -0.5$, to match our treatment of the [Fe/H] $= 0$ objects.

Figure 3.14 shows the difference between the measured $T_{\rm eff}$ values for a reduced metallicity of [Fe/H] $= -0.5$ and Solar, as a function of $T_{\rm eff}$ measured using Solar metallicity templates. The reduced-metallicity fits typically return cooler temperatures, of order $\Delta T_{\rm eff} \sim -700$ K for F stars and $\Delta T_{\rm eff} \sim -400$ K for A stars. The slope at $T_{\rm eff} < 6000$ K is a response to the edge of the template grid.

Figure 3.15 shows that the $v \sin i$ values are weakly affected, with differences to the tune of $< 20\,{\rm km\,s^{-1}}$. This is of the order of uncertainty for this parameter. The reduced-metallicity fits tend to return larger values for F stars, and smaller values for A stars. The radial velocity values

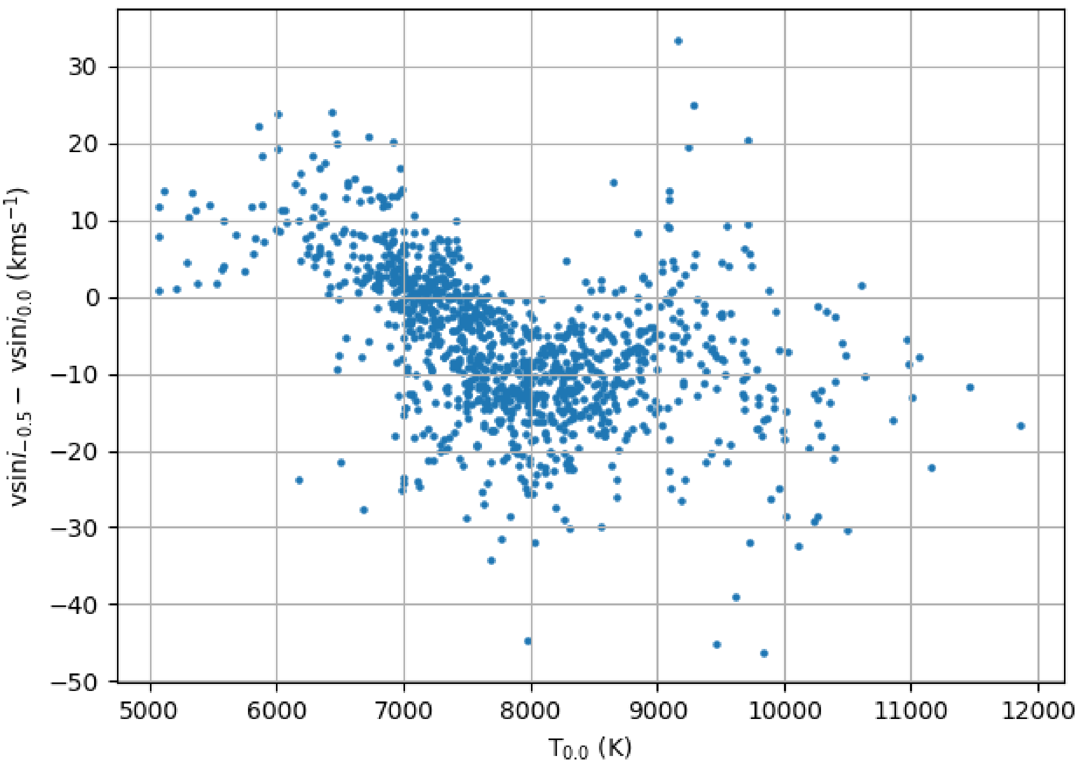

FIGURE 3.15: *Difference between measured* $v\sin i$ *values for* [Fe/H] $= -0.5$ and 0.0.

for the reduced-metallicity set are generally slightly larger for F stars (see Figure 3.16). For A stars they are smaller, with a median difference of $\sim -3.0\,\mathrm{km\,s^{-1}}$.

The reduced-metallicity $\log g$ values are lower, with the difference steadily growing larger for cooler temperatures (Figure 3.17). For the A stars, the median difference is $\Delta \log g \sim -0.17$. For the F stars the difference is much more marked and the $\log g$ values are unrealistically low for a population of objects that must be more localised than the A stars given the common faint magnitude limit. It is highly improbable that many among the F star sample would present [Fe/H] significantly less than 0, since the great majority of these fainter objects should lie within a distance of 5 kpc. We estimate this limiting radius for the case of a warmer main sequence F star with $T_{\mathrm{eff}} = 7000\,\mathrm{K}$, $i = 17.5$ (see Figure 2.4), $A_i \sim 1.3$ (typical HectoSpec value – see Figure 3.13) and $M_i = 2.6$. At $\ell = 118°$, a distance of 5 kpc corresponds to a Galactocentric radius of ~10.6 kpc, or a metallicity change, according to the global gradient, of ~ 0.2.

A new Padova absolute magnitude scale, suitable for the changed metallicity, was used for determining distance moduli for the A stars. The net effect on the distance modulus scale is a small increase compared with the Solar metallicity scale ($\Delta\mu \sim +0.12$).

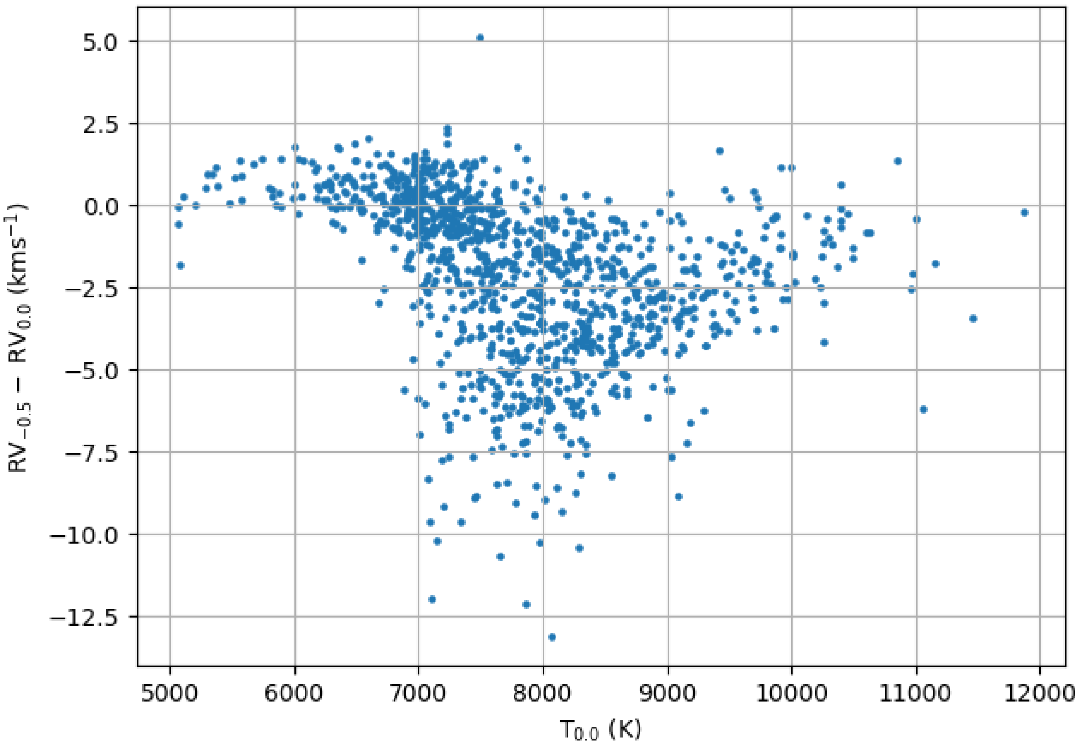

FIGURE 3.16: *Difference between measured RV values for* [Fe/H] $= -0.5$ and 0.0.

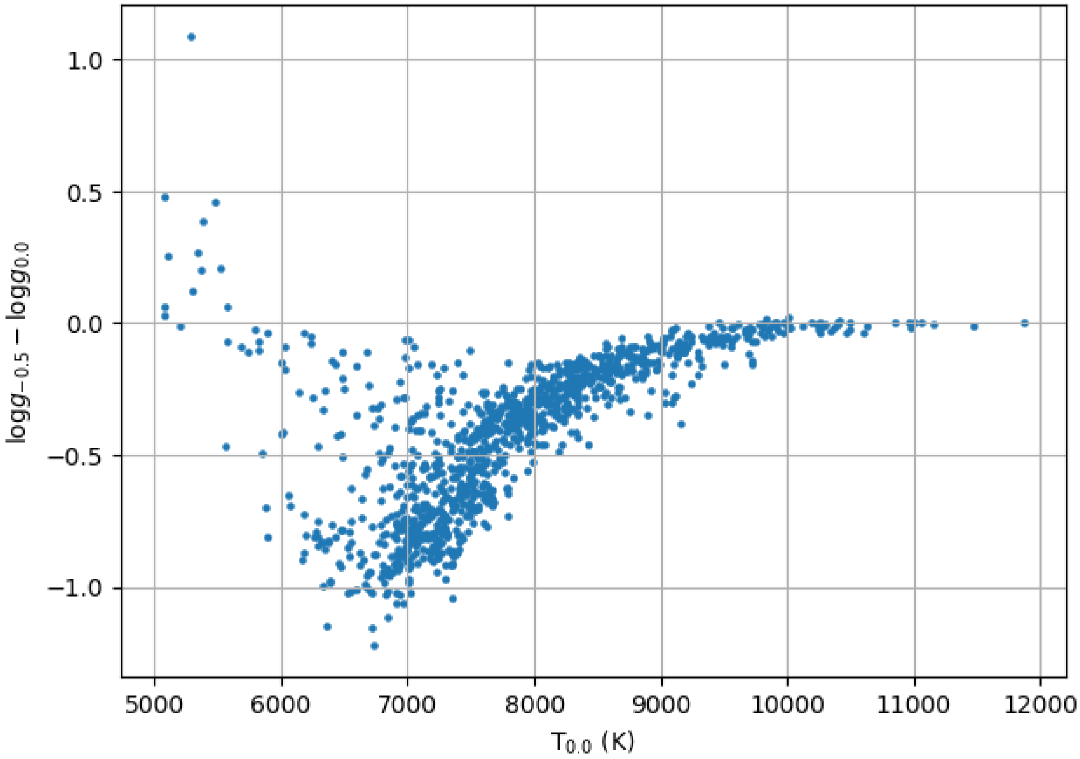

FIGURE 3.17: *Difference between measured* $\log g$ *values for* [Fe/H] $= -0.5$ and 0.0.

Consequently, for the reasons above, we fix the metallicity of the HectoSpec F stars at [Fe/H] = 0. Throughout the remainder of Part I we continue to take note of the impact of the A stars having a reduced metallicity, although it proves to be small.

Chapter 4

Outer disk kinematics from radial velocities

The trend of RV with distance modulus can be compared with what we would expect to see as an averaged trend if consensus views of the Galactic rotation law apply. If all the stars move on circular orbits about the Galactic centre, we would expect to observe a trend of RVs that are a spread (due to velocity dispersion) around a curve whose shape depends on the sightline observed, the assumed rotation curve and LSR parameters (circular velocity and Galactocentric distance of the LSR, v_0 and R_0). The comparisons made in this Section are with a flat rotation curve with LSR parameters $R_0 = 8.3\,\mathrm{kpc}$, $v_0 = 240\,\mathrm{km\,s^{-1}}$, similar to those often used in the literature, and with the slowly rising rotation curve derived in Brand and Blitz (1993) with their adopted parameters $R_0 = 8.5\,\mathrm{kpc}$, $v_0 = 220\,\mathrm{km\,s^{-1}}$. We have converted our observed radial velocities to the LSR frame adopting the Solar peculiar motion from Schönrich et al. (2010), ($U_\odot$, $V_\odot$, $W_\odot$) = (11, 12, 7) $\mathrm{km\,s^{-1}}$. Any mentions of radial velocity for the remainder of this Chapter are referring to those in the LSR frame. We begin by presenting the results for $\ell = 178^\circ$, the direction where the rotational component of motion of the stars is effectively nullified.

4.1 $\ell = 178^\circ$

The trend of RV with distance modulus, μ, for this pencil-beam is shown in Figure 4.1. The red dashed line shows the expected average trend based on a flat rotation curve assuming a circular speed of 240 km s^{-1} (although at this sightline the shape of the rotation curve makes little difference). The green line is the weighted mean of the RVs computed for the Solar metallicity stars, plotted as individual data points, at each step in μ. The yellow line is the weighted mean for A stars with [Fe/H] $= -0.5$ and F stars with Solar metallicity. The weighted RV is calculated via the following process:

- Every (μ, RV) data point is assumed to be associated with a gaussian error distribution with $\sigma = \sigma_\mu$ where σ_μ is the error on μ.
- At the ith step ($\mu = \mu_i$), the data points (μ_n, RV$_n$) with error distributions in μ overlapping μ_i are included in forming the running average, provided $|\mu_n - \mu_i| < \sigma_{\mu_n}$. The weighting per data point is in proportion to the value of its gaussian error function at μ_i – thereby taking into account the error in μ in all data points.
- In obtaining the mean RV at $\mu = \mu_i$, the contributing RV values are also weighted, with weight proportional to $1/\sigma_{RV}^2$, where σ_{RV} is the mean of each datapoint's positive and negative RV error.
- A final weighting is applied in computing the mean in order that the contribution from data points at $\mu < \mu_i$ balances the contribution from data points at $\mu > \mu_i$. This limits the influence of data from the most densely populated part of the μ distribution on the mean trend. This is achieved by weighting the data points on either side of μ_i, such that the total weight on each side is 1.
- We set the minimum number of points required for calculation of the mean to either side of $\mu = \mu_i$ to 50. If this value is lowered the weighted mean trend is extended to regions with low number statistics, resulting in greater uncertainty.

The shaded region around the mean trend line is the standard error of the weighted mean RV at each μ_i.

In Figure 4.1, the F stars dominate the lower end of the range in μ, while the A stars mostly occupy a spread from $\mu \sim 12$ to $\mu \sim 15$ (or a heliocentric distance range from $d \sim 2$ to 10 kpc). Of the F stars, 90% (145 of 165) lie within $\mu = 11.4 - 14.5$ ($d = 1.9 - 7.8$ kpc). 90% of the A stars with [Fe/H] $= 0$ (209 of 232) lie within $\mu = 11.8 - 14.8$ ($d = 2.3 - 9.0$ kpc). In the case of reduced metallicity, [Fe/H] $= -0.5$, the A star distance range is stretched a bit to lie within $\mu = 11.6 - 15.1$ ($d = 2.1 - 10.6$ kpc). Ruphy et al. (1996) found a radial cutoff of the stellar

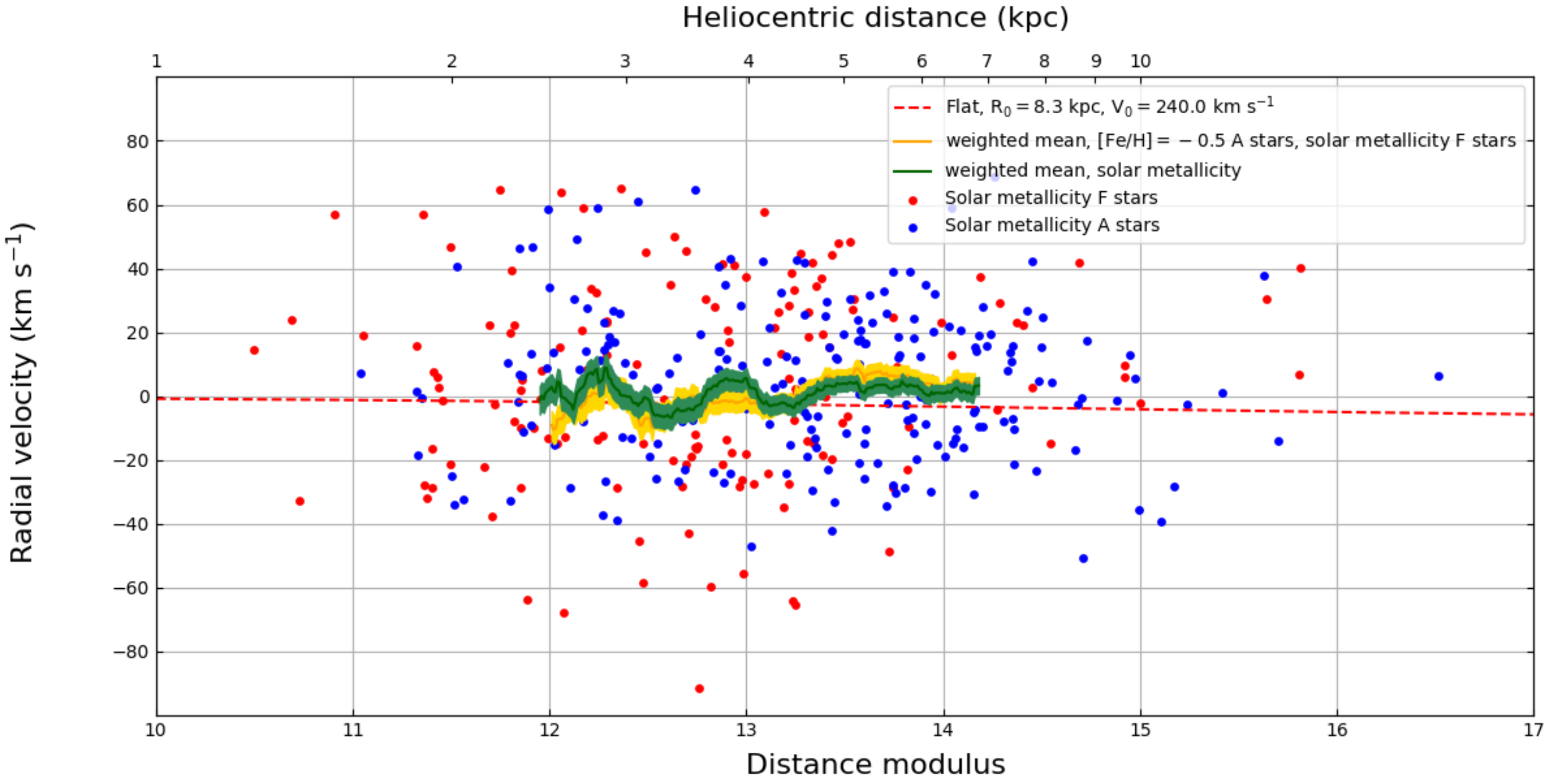

FIGURE 4.1: *The trend of RVs with distance modulus for $\ell = 178°$. The green line is the weighted mean of the RVs of the Solar metallicity stars, and the yellow line is obtained on combining $[Fe/H] = -0.5$ A stars with Solar metallicity F stars. The shaded regions represents the standard error of the mean in RV. The blue points are A stars and the red points F stars, both with metallicity assumed as Solar. The red dashed line shows the expected trend for a flat rotation law, which at this sightline will fall close to $\sim$zero regardless of the v_0, R_0 or shape of the rotation law adopted.*

disk at $R_G = 15 \pm 2\,\mathrm{kpc}$, and Sale et al. (2010) found the stellar density of young stars declines exponentially out to a truncation radius of $R_G = 13 \pm 0.5_{statistical} \pm 0.6_{systematic}$ kpc, after which the stellar density declines more sharply, as the exponential scale length shortens. The density of our sample in this sightline also drops off at these distances, but we cannot be sure whether this decline originates in the Galactic disk or is a selection effect.

We find the overall trend in RV follows the expected flat behaviour, although it is offset in velocity by a mean amount of $3.5\,\mathrm{km\,s^{-1}}$. The results adopting [Fe/H] $= -0.5$ for the A stars are very similar as expected, but with a slightly smaller mean offset of $3.0\ \mathrm{km\,s^{-1}}$. There is evidence of a possible small wavelength calibration offset arising from the comparison of the HectoSpec observations with independent higher-resolution spectra, effecting the RV scale by only a couple of $\mathrm{km\,s^{-1}}$, described later in Section 5.1. Taking these findings together we infer that the RV scale is reliable to within $\sim 5\ \mathrm{km\,s^{-1}}$ but cannot rule out the presence of a small positive bias in the measurements.

We have computed the RV dispersion of the sample stars, in broad spectral type groups, around the measured mean trend, in order to compare them with the expected dispersions from Dehnen and Binney (1998) (see Table 4.1). Clearly the measured dispersions, σ_{178°, are larger than the Dehnen and Binney (1998) results. Part of this discrepancy is attributable to our measurement errors, ε_{RV}, but the larger share of it may be a consequence of stellar multiplicity. At least a half of the sample objects are likely to be members of multiple systems, and of those around 15% may be in nearly equal mass ratio binaries (Duchêne and Kraus, 2013). Whilst the spectroscopic resolution of our data is insufficient to pick out spectroscopic binaries, there can nevertheless be observed binary orbital motions present up to a level of $\sim 40\ \mathrm{km\,s^{-1}}$ in typical cases. To demonstrate, for a binary system with total system mass of $m_1 + m_2 = 3\,M_\odot$, e.g. an A star with a lower mass companion, with a period P of ~ 40 days (typical of A stars, see top axis of Figure 4.2), we can use[1]

$$\frac{V^3_{1r,max}}{\sin^3 i} = \frac{m_2^3}{(m_1+m_2)^2}\frac{2\pi G}{P} \tag{4.1}$$

to obtain $V_{1r,max}/\sin i = 40\,\mathrm{km\,s^{-1}}$ for $m_2 = 1$, i.e. a mass ratio of $q = 0.5$. Here, $V_{1r,max}$ is the maximum observable radial velocity of the system due to binary motion, and i is the inclination of the orbital plane of the binary system relative to the plane of the sky. It is the closest binaries, who have the shortest period, that possess the fastest orbital motions. The true observed radial velocity due to binary motion is modulated by the phase of the system and its inclination. As

---

[1] assuming the orbits are nearly circular

Stellar Type	$T_{\rm eff}$ **range**	**No. stars**	σ_{DB}	ε_{RV}	$\sqrt{\sigma_{DB}^2+\varepsilon_{RV}^2}$	σ_{178°	**excess** σ
Early-A	]8500-10000]	67	14	7.2	15.7	20.7	13.5
Late-A	]7500-8500]	151	19	5.5	19.8	21.7	8.9
Early-F	]6500-7500]	139	23	4.2	23.4	27.8	15.0

TABLE 4.1: *Expected RV dispersion from Dehnen and Binney (1998) (σ_{DB}) compared to the measured RV dispersion (σ_{178°) for early-A - early-F stars (Solar metallicity set). Also given are the typical HectoSpec measurement errors (ε_{RV}) for the different subtype ranges, and the quadrature sum in combination with σ_{DB}. Finally, the excess σ required to reconcile σ_{DB} and σ_{178° are provided. These excesses are compatible with the extra dispersion likely to be introduced by the presence of spectroscopic binaries in the sample (on the order of* $10\,{\rm km\,s^{-1}}$*).*

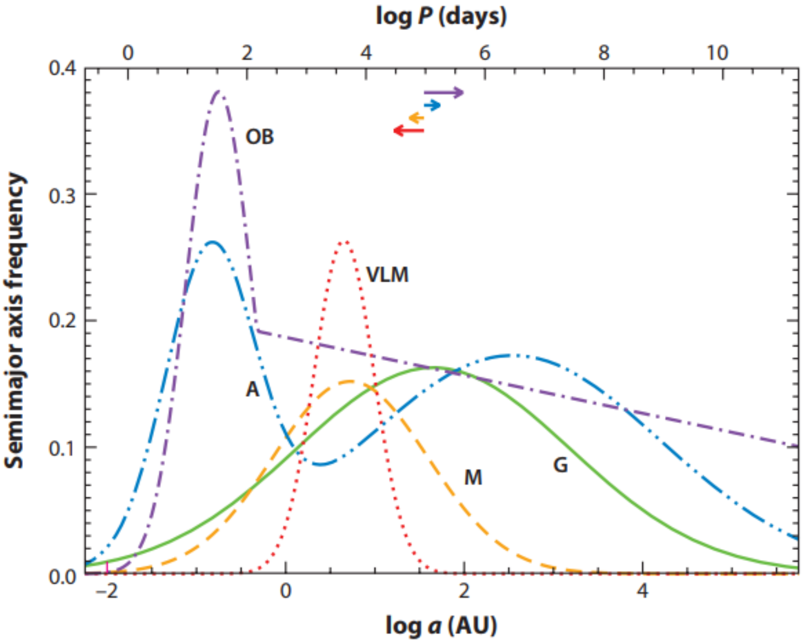

FIGURE 4.2: *Figure 2 of Duchêne and Kraus (2013): Schematic forms of the orbital period distribution (top horizontal axis) for field multiple systems among Solar-type stars (green curve), low-mass stars (orange curve), very low-mass (VLM) stars and brown dwarfs (red curve), intermediate-mass stars (blue curve), and high-mass stars (purple curve). The bottom horizontal axis represents the semimajor axis and is held fixed for all populations. The orbital period shown is for systems with a total mass of* $1.5\,M_\odot$*. The coloured arrows represent the offset of the curves from the logP axis for systems with total mass of* $30\,M_\odot$ *(purple),* $5\,M_\odot$ *(blue),* $0.5\,M_\odot$ *(orange) and* $0.15\,M_\odot$ *(red). For our purpose we focus on the blue curve, appropriate for A stars, which is shifted to the left by a small amount relative to the logP axis.*

the data in Table 4.1 indicate, the excess dispersion on top of measurement error is in the region of 10 $\rm km\,s^{-1}$ for all 3 spectral type groups. We look at this in more detail in Section 4.3.

4.2 $\ell = 118^\circ$

The results for this sightline are shown in Figure 4.3. Again, the green line is the mean trend for Solar metallicity stars and the yellow for [Fe/H] $= -0.5$ A stars and Solar metallicity F stars. The mean trends, calculated in the same way as for $\ell = 178^\circ$ described in Section 4.1, deviate more strongly from expectations based on a flat or slowly rising rotation curve (shown in the Figures by the red dashed/dotted lines). The measured trends are appreciably flatter. The $\ell = 118^\circ$ results are similar for both A star metallicities, indicating that metallicity is not having a strong effect on the interpretation of the results. The mean RV trend (for either A-star metallicity) spans the heliocentric distance range from $d \sim 2.5$ to 9 kpc ($R_G \simeq 9.7$ to 14.8 kpc), with the RV decreasing slowly from ~ -40 to $-70\,\mathrm{km\,s^{-1}}$.

For context, we note that the Perseus Arm is likely to pass closest to this line of sight at a distance of 2.5 to 3 kpc (Reid et al., 2014). This overlaps the bottom end of the distance range that we sample. The Outer Arm is expected to pass at a distance of approximately 6 kpc in this sightline, which is within our sampled range. In Figure 4.3 there is no clear sign of a distinct localised RV perturbation that might be attributed to either the Perseus or Outer Arm. Nevertheless, spiral arm perturbations are explored further in Section 4.6.

The velocity dispersions around the RV mean trend for the three spectral type groups specified in Table 4.1 at the $\ell = 118^\circ$ sightline are: $19.8\,\mathrm{km\,s^{-1}}$ for the early-A stars, $21.1\,\mathrm{km\,s^{-1}}$ for the late-A stars, and $24.3\,\mathrm{km\,s^{-1}}$ for the early-F stars. These values are similar to those measured for the anticentre sightline (shown in Table 4.1), which permits the same interpretation that binary orbital motions are a third factor contributing to the overall observed dispersion.

At this sightline, we can convert our measured radial velocities into circular speeds if we assume the stars are on circular orbits, i.e. the measured radial velocity entirely comprises the projected circular motion. We used the following equation

$$v = R_G \left(\frac{RV}{R_0 \sin\ell \cos b} + \frac{v_0}{R_0} \right) \tag{4.2}$$

with R_0 the Galactocentric radius, R_G, of the Sun, v_0 the circular velocity of the LSR, and ℓ, b, the Galactic longitude and latitude.

We converted the weighted mean RV trends in Figure 4.3 to circular speed, which are shown in Figure 4.4 as a function of Galactocentric radius. The green line is for an assumed Solar metallicity, and the orange is for a reduced metallicity of the A stars. The agreement between the two shows the adopted metallicity has little impact on the results. Our measured Galactic rotation law is strongly rising, from $v \sim 230\,\mathrm{km\,s^{-1}}$ at $R_G \sim 11\,\mathrm{kpc}$, $v \sim 260\,\mathrm{km\,s^{-1}}$ at $14\,\mathrm{kpc}$. We discuss this Figure further in Section 4.5.

In the following Sections, we consider whether the photometric consequences of binarity could distort the measured RV trend, discuss the observed departure from a flat or slowly rising rotation law, and consider the possibilities for detecting spiral arm perturbations.

4.3 Potential bias from binaries

The relatively flat distribution of RVs seen at $\ell = 118^\circ$ in place of the expected falling trend may possibly be a consequence of a combination of unrecognised binaries placed at inappropriately short distances, and significant smearing due to distance error. In this Section we discuss the potential effects of binarity, and describe the simulation we used to test these effects on the observed $\ell = 118^\circ$ trend.

If a target star is actually an unresolved binary system, the measured apparent magnitude will be brighter than if it were a single star. Considering Equation 3.6, an over-bright apparent magnitude, combined with an absolute magnitude corresponding to the primary star, results in an underestimated distance to the system. To put this another way, the absolute magnitude adopted in our analysis is too faint.

In fact, the maximum underestimation of an absolute magnitude due to multiplicity is 0.753 mag, corresponding to replacing a single star by two stars each of the same mass. To demonstrate, the absolute magnitude (in a certain photometric band) of a single star, M_s, with luminosity L_s, is given by

$$M_s = M_\odot - 2.5\log_{10}\left(\frac{L_s}{L_\odot}\right) \tag{4.3}$$

where $M_\odot$ and $L_\odot$ are the absolute magnitude and luminosity of the Sun respectively. Similarly, for a binary system comprising of two equal mass stars, each with luminosity L_s,

$$M_b = M_\odot - 2.5\log_{10}\left(\frac{L_b}{L_\odot}\right) = M_\odot - 2.5\log_{10}\left(\frac{2L_s}{L_\odot}\right) \tag{4.4}$$

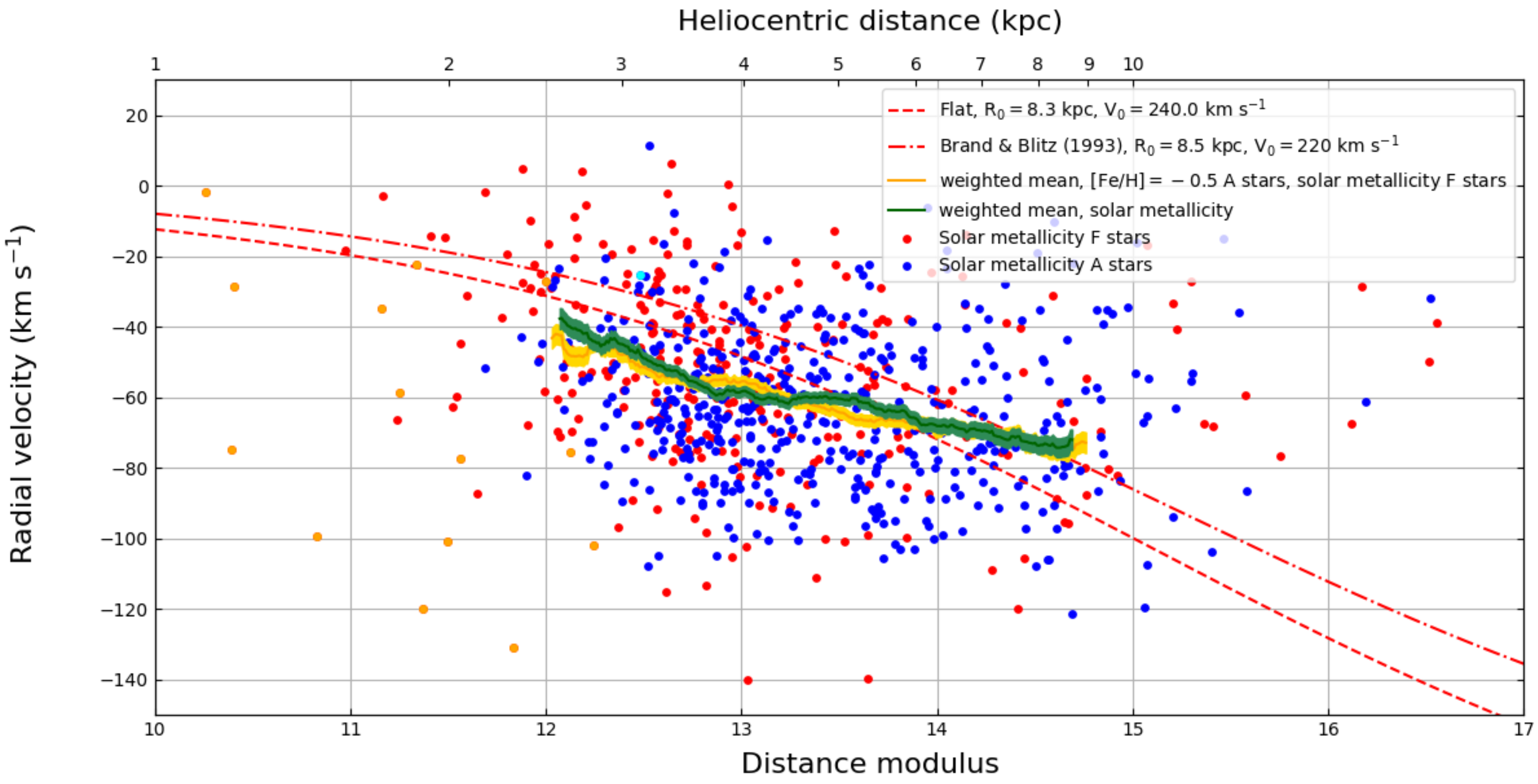

FIGURE 4.3: *The trend in RV with distance modulus at* $\ell = 118°$. *The red dashed/dotted lines show the expected trends for a flat rotation law and the Brand and Blitz (1993) slowly rising rotation law (see legend). The green line is the weighted mean of the RVs obtained using stellar parameters returned for Solar metallicities, and the yellow line is the alternative result obtained on swapping in A star data computed for* $[Fe/H] = -0.5$. *The shaded regions represent the standard error of the mean in RV. The individual data points in blue are obtained from A stars, while red is used for the F stars (computed for Solar metallicity). The cyan point is the A star identified as lying far from the IPHAS mean extinction trend, and the orange points the F stars (see Figure 3.13).*

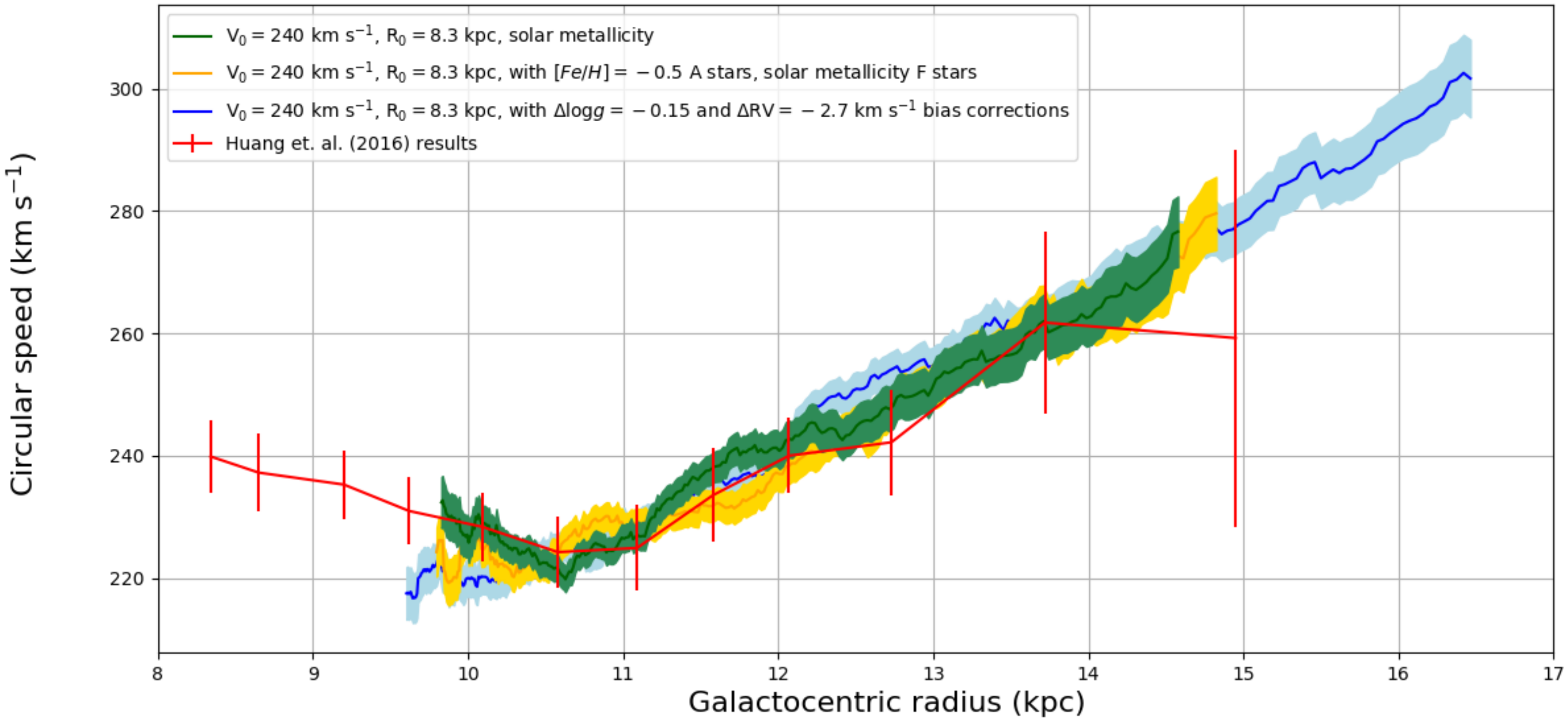

FIGURE 4.4: *Galactic disk circular speed results from Huang et al. (2016) are reproduced in red. The circular speeds derived from the mean RV trend for results at $\ell = 118°$, adopting Solar metallicity, are in green. Results obtained with $\Delta \log g = -0.15$ and $\Delta RV = -2.7\,\mathrm{km\,s^{-1}}$ potential bias corrections are shown in blue. Orange is used for the results obtained when the A star parameters for $[Fe/H] = -0.5$ are used in place of Solar metallicity parameters. The shaded region around each HectoSpec line represents its error – propagated from the error on the mean trend in Figure 4.3.*

The difference between these two absolute magnitudes is given by

$$M_s - M_b = 2.5\log_{10}(2) \simeq 0.753 \tag{4.5}$$

This offset between apparent magnitudes leads to a maximum underestimation of the distance to a system such that the measured distance = (true distance)/$\sqrt{2}$. In principle this might erroneously flatten the overall observed RV distribution by bringing in a group of objects at more negative RV and greater μ to mix with less negative values at smaller μ.

For systems with unequal mass components the offset in absolute magnitude is reduced. However, systems with unequal mass will have a combined intrinsic colour that is redder than that of the primary component (Hurley and Tout, 1998), leading to an overestimation of extinction and, again, an underestimation of distance. If the absolute magnitude of a single star in photometric band X is denoted

$$M_{X,1} = M_{X,\odot} - 2.5\log_{10}\left(\frac{L_{X,1}}{L_{X,\odot}}\right) \tag{4.6}$$

and similarly for a binary system comprised of components labelled 1 and 2,

$$M_{X,3} = M_{X,\odot} - 2.5\log_{10}\left(\frac{L_{X,1}+L_{X,2}}{L_{X,\odot}}\right) \tag{4.7}$$

then the difference between the colour of a binary system, (X-Y)$_3$, and a single star, (X-Y)$_1$, is given by

$$(X-Y)_3 - (X-Y)_1 = 2.5\log_{10}\left(\frac{(L_{Y,1}+L_{Y,2})}{(L_{X,1}+L_{X,2})}\frac{L_{X,1}}{L_{Y,1}}\right) \tag{4.8}$$

For equal mass systems this reduces to 0, however for unequal mass systems the value depends on the mass of the system and the component mass ratio, q. This is evident in Figure 4.5, which shows approximate absolute magnitudes M$_i$ and intrinsic $r-i$ colours of single stars of various masses (red points), and of binary stars with varying mass ratios, in steps of 0.1 (blue points). The red triangles indicate systems with primary mass of 1, 2 and 3 M$\odot$, from right to left. The analogous figure for $B-V$ was presented by Hurley and Tout (1998) as their Figure 1. The maximum colour difference in the range shown is 0.044, for a primary mass of 1.8 M$_\odot$, and a mass ratio of $q = 0.8$. The track for this particular system is coloured green in Figure 4.5. The M$_i$ value for this binary system is 0.36 mag brighter than its primary star. These offsets lead to an underestimation of distance such that the measured distance is 0.81× the true distance - not as strong effect as expected for $q = 1$ binaries.

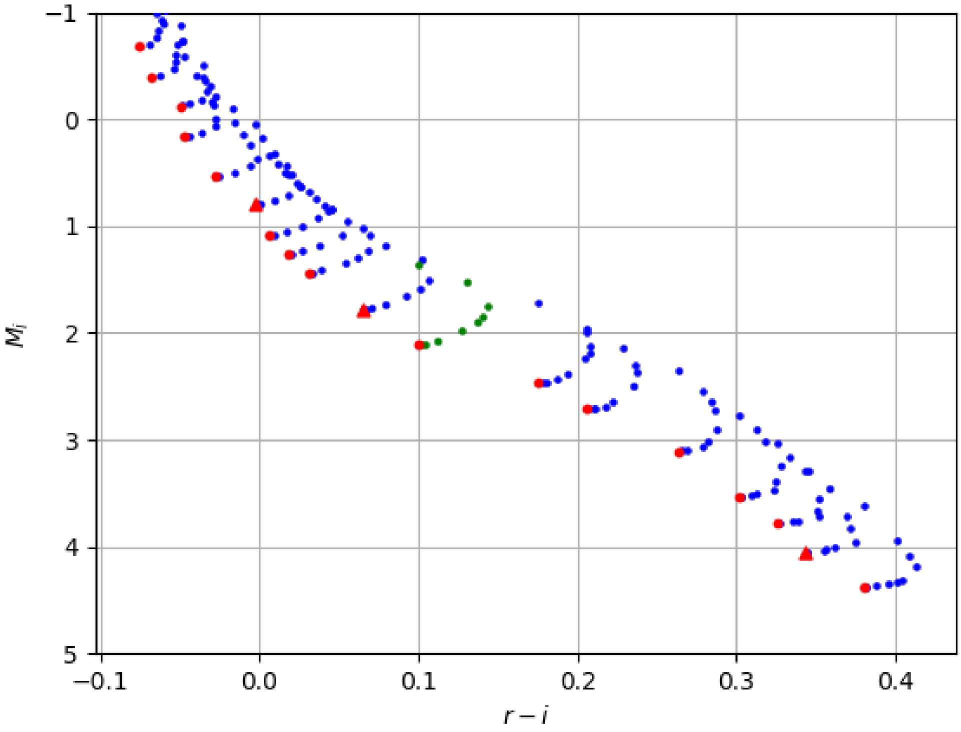

FIGURE 4.5: *Absolute magnitude M_i and intrinsic $r-i$ colour of single (or primary) stars of various masses (red points), and of binary stars with varying $q = m_2/m_1$ in steps of 0.1 (blue points). Red triangles indicate systems with primary mass of 1, 2 and 3 M⊙, from right to left. The green track is that with the largest colour difference.*

In order to test the effect of binarity on the calculated weighted average RV trend, we have performed an outline simulation that focuses on this factor. Our method is as follows. We select three sets of stars of different spectral type groups: early-A, late-A and early-F. The size of the sets are the same as the HectoSpec $\ell = 118°$ groups (early-A: 168 stars, late-A: 281 stars, early-F: 259 stars). We randomly select 70% of stars in each group to be binaries. Each binary is randomly assigned a primary mass, m_1, from a uniform distribution with bounds depending on the spectral type: $1.3-1.6\,\mathrm{M}_\odot$ for early-F, $1.6-2\,\mathrm{M}_\odot$ for late-A, and $2-3\,\mathrm{M}_\odot$ for early-A. The secondary mass, m_2, is assigned at random via a mass ratio, q, obeying the distribution $f(q) = q^{-0.5}$ (Duchêne and Kraus, 2013). The distance modulus assigned to each star is sampled from the HectoSpec μ distribution for its spectral type group. In order to compensate for the expected net decrease in μ associated with treating binary stars as single, these reference distributions are first modified by a uniform retrospectively determined shift of +0.16. The assigned RVs follow a flat rotation curve with $v_0 = 240\,\mathrm{km\,s^{-1}}$ at $\ell = 118°$, broadened by an amount consistent with the scatter defined by Dehnen and Binney (1998) and measurement error (see Table 4.1).

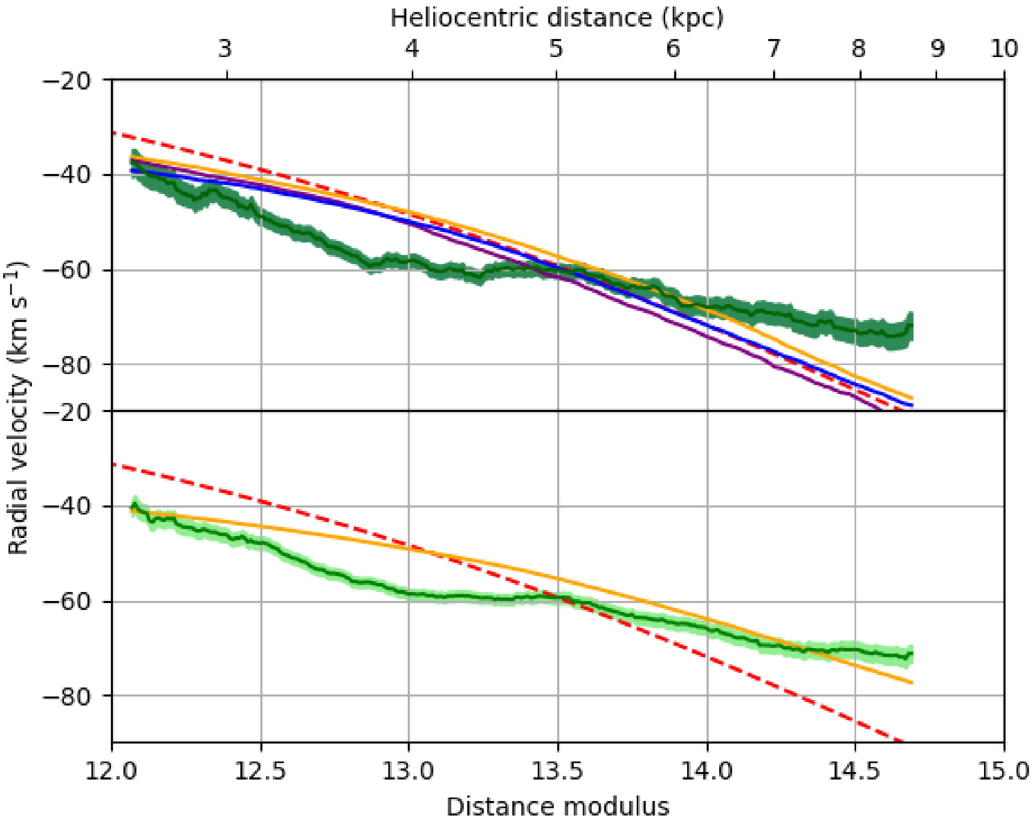

FIGURE 4.6: *The results of simulations to test the effects on the mean RV trend of undetected binaries and distance modulus errors. In the top panel, the purple line is the mean RV trend for the simulation incorporating unresolved binaries. The orange line is the result from the simulation testing the effect of distance modulus error only, while the blue line shows the simulated effect of both unresolved binaries and distance modulus errors. The observed RV trend is overlaid in green. In the bottom panel, we test the effect of doubling our distance modulus errors (orange line). The greater error induces more flattening. The light green line in this case is the mean RV trend of the HectoSpec data obtained on adopting doubled distance modulus errors.*

The final adjustment is to include a component of binary orbital motion. This additional velocity component from binary orbital motion, whilst adding to the overall scatter, would not produce a bias on the RV results since the space orientation of binary orbital axes across a large sample is random and must cancel out. Nevertheless, a period, P, inclination, i, and phase, ϕ, are randomly assigned for each binary star. The period is selected from the distribution of A star periods shown in Figure 4.2. The inclination is chosen from a uniform distribution in $\cos i$, and the phase from a uniform distribution between 0 and 2π. In the final reconstruction of the observed RV distribution, each simulated binary star has its distance modulus reduced to the equivalent single value according to the computed difference in intrinsic colour and absolute magnitude.

The simulation of 708 stars was performed 10000 times, and the mean RV trend was calculated each time. The mean of these 10000 trends is shown as the purple line in the top panel of Figure 4.6. The binary stars are pulled by varying amounts to shorter distances and bring with them their on-average more negative RV. A flattening of trend is seen, but our numerical experiment indicates it is modest. The deviation away from a flat rotation law that we find at $\ell = 118^\circ$, shown as the green line, is much more pronounced, leading us to conclude that an appeal to stellar multiplicity to explain it falls well short, quantitatively.

4.4 Potential bias from distance error due to photometric and stellar parameter uncertainties

Another factor that will cause some flattening of the $\ell = 118^\circ$ trend is distance error due to photometric and stellar parameters uncertainties. The derived distance distribution is essentially the true distance distribution broadened by its uncertainty. Consequently, the mean RV trend spans this slightly broader distribution, causing a flattening. To test the extent of this, we performed a simulation similar to the one described above used to test the effect of unresolved binaries. However this time we disregard binary stars, and after assigning a suitably scattered RV with measurement error to each notional star, we shifted the corresponding distance modulus by an amount within the typical level of error from the HectoSpec data. The result is shown as the orange line in the top panel of Figure 4.6. The resultant mean trend is somewhat flattened, but not by an amount that makes it parallel to the result from observation. To complete the picture, we performed this simulation again but now including unresolved binaries as described above. The blue line shows the result. The amount of flattening is similar to that due to the distance errors alone. At shorter distances it is slightly more pronounced, and at further distances it is less. This is expected since the binaries are pulled to shorter distances, bringing with them their on-average more negative RV.

In order to achieve a flattening of the simulated curve by an amount that begins to mimic the trend deduced from the A/F star data, we find we need to double the distance errors relative to those propagated from the data as described in Section 3.3. The bottom panel of Figure 4.6 illustrates this. Whilst it is certainly a possibility the estimation of distance errors in our sample, which arise from photometric and stellar parameter uncertainties, is optimistic at $\sim 15\%$ ($\Delta\mu = 0.3$), growing them all by as much as a factor of two is rather less credible. Our simulations lead us to believe that the deviation of the observed trend of RV from that of a flat rotation law can not be solely explained by binarity, distance error, or even a combination of the two.

4.5 Comparisons of results with other tracers and earlier work

In this Section we compare our results with those from previous studies, which make use of other types of tracers.

Using H II region data, Brand and Blitz (1993) presented sparse-sampled measurements that mainly captured heliocentric distances out to ∼4 kpc at the Galactic longitudes of interest here (see their Figure 1). The overlap with our results thus runs roughly from 2 to 4 kpc. Near the anticentre Brand and Blitz (1993) generally favoured slightly negative radial velocities, ranging from -18 to $+8$ km s^{-1} (9 datapoints, from their Table 1), to be compared with a small positive bias here (Figure 4.1). In the longitude range $110^\circ < \ell < 130^\circ$, the relevant measurements are spread between -30 and -56 km s^{-1} (13 datapoints). This is entirely compatible with our results.

A denser comparison between our results and other studies can be made using RV data of H I and CO clouds. Since both sightlines miss the latitude of peak gaseous emission for their longitudes, the total amount of both H I and CO is not particularly large. Nevertheless, the measured gaseous RV distributions are broadly consistent with our findings from HectoSpec, and the detail is informative. The top panel of Figure 4.7 shows that the H I 21 cm data from EBHIS (The Effelsberg-Bonn H I Survey, Winkel et al., 2016) in the $\ell = 178^\circ$ sightline scatter around RV $\simeq$ 0 at much reduced dispersion compared to the HectoSpec A/F stars. We find that the mean RV measures from our optical spectroscopy are shifted relative to the H I data by $\sim +8\,\mathrm{km\,s^{-1}}$. This is evidence of either (or a combination of) a small positive bias in our RV measurements, or that the H I column samples a greater column through the outer disk than our stellar sample. In this sightline, the expected radial velocities slowly become more negative with greater distance, to the tune of $-5\,\mathrm{km\,s^{-1}}$ at $d = 10\,\mathrm{kpc}$ (see the red dashed line in Figure 4.1). If the H I column probes futher than our HectoSpec sample, the average RV of the H I will be slightly more negative, resulting in a small offset like we observe.

The comparison with EBHIS data at $\ell = 118^\circ$ shown in the bottom panel of Figure 4.7 shows the A/F star data line up with the main $\sim -60\,\mathrm{km\,s^{-1}}$ H I emission peak, while the peak at $\sim 0\,\mathrm{km\,s^{-1}}$ (from the Local Arm, seen in H I) is clearly absent. This is to be expected given that none of the A/F stars selected and measured will be local. The H I data also present a peak at $\sim -90\,\mathrm{km\,s^{-1}}$ that is largely absent from the stellar data. This is unsurprising since our central result from the $\ell = 118^\circ$ sightline is the RV flattening that implies a relative absence of stars in this more negative velocity range (at distances where a flat or gently rising rotation law would predict they exist). We note that the CO data from the COMPLETE (Coordinated Molecular Probe Line Extinction and Thermal Emission, Ridge et al., 2006) survey exhibits the same RV behaviour as the H I data.

One possible inference from the absence of these negative RVs in our data is that the distance range occupied by our sample of stars does not, in reality, extend to the distances where existing rotation laws would predict a RV of $\sim -90\,\mathrm{km\,s^{-1}}$. This distance is $d \sim 8\,\mathrm{kpc}$ (see Figure 4.3). In other words, our longer distances would be significant over-estimates. However this directly contradicts the implication from a positive bias in our $\log g$ measurements, as discussed in Section 3.2.2, which suggests our distances are in fact underestimated. On the other hand, another reasonable inference is that the H I and CO gas at the most negative radial velocities lies mainly outside the range sampled by the A/F stars, beyond $d \sim 9\,\mathrm{kpc}$.

Huang et al. (2016) have used red clump giants drawn from a wide range of Galactic longitudes sampling the outer disk to find a broadly flat longitude-averaged rotation law within $R_G < 25\,\mathrm{kpc}$, with typical circular speed $v_0 = 240 \pm 6\,\mathrm{km\,s^{-1}}$. But over our sampled region, between $R_G \simeq 10-15\,\mathrm{kpc}$, their inferred rotation law is quite sharply rising out of a dip at $R_G \sim 11\,\mathrm{kpc}$. Figure 4.4 compares the Huang et al. (2016) results (red line) with the rotation curve derived from the mean RV trend we obtain at $\ell = 118^\circ$ adopting Solar metallicity (green line). In constructing this Figure, we choose the same LSR parameters as favoured by Huang et al. (2016), $R_0 = 8.3\,\mathrm{kpc}$ and $v_0 = 240\,\mathrm{km\,s^{-1}}$. The agreement is very good.

We commented before in Section 3.2.2 that there may be a positive bias in the derived stellar surface gravities. The amount of bias may very well be in the region of $\Delta \log g = +0.15$, as suggested by Figure 3.10. We have also considered whether there is a small positive bias in the measured RV. There are a few sources of this consideration, namely: (i) the offset seen in Figure 4.1, (ii) the offset compared to the EBHIS H I profile, (iii) the offset compared to 7 remeasurements in Section 5.1 at red and blue wavelengths. If all stellar surface gravities are adjusted down by 0.15 dex, and a potential RV bias of $2.7\,\mathrm{km\,s^{-1}}$ (a value representative of the offsets listed above) is also taken out uniformly, the trend in circular speed acquires the form of the blue line in Figure 4.4. The main impact of these changes is to stretch the results out to

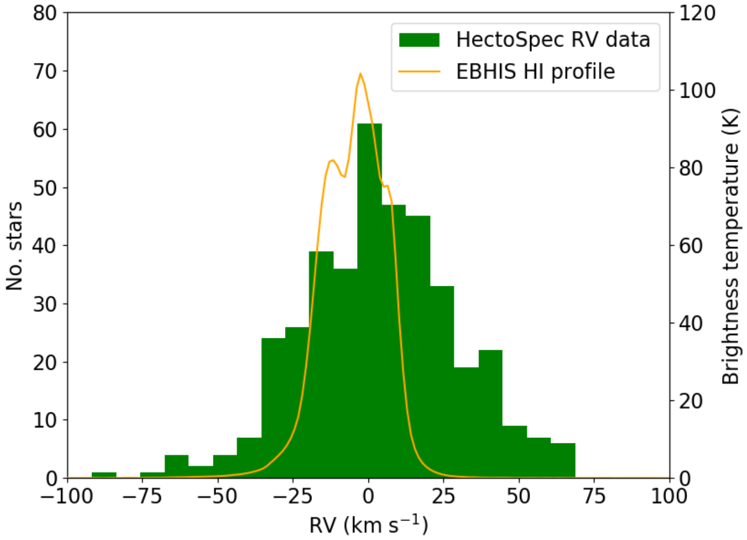

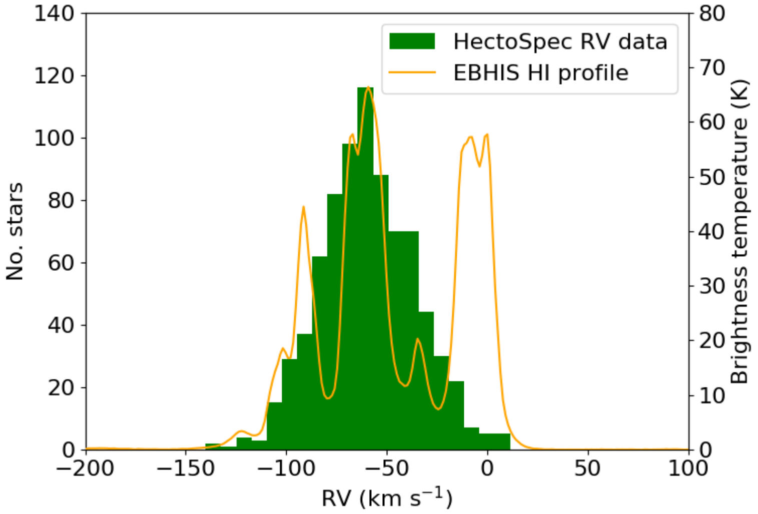

FIGURE 4.7: *The H I profile at $\ell = 178°$ (top) and $\ell = 118°$ (bottom) is shown by the orange line, overlayed on the HectoSpec RV data (green histogram).*

an increased Galactocentric radius, in response to the possible $\log g$ correction. The outcome remains consistent with the Huang et al. (2016) results.

So we have that both the clump giants and, now, our A/F star sample favour a rotation law that rises out to $R_G \sim 14$ kpc, after a minimum near ~ 11 kpc. But we have also demonstrated how distance error can modify the observed RV-distance trend. And indeed Binney and Dehnen (1997) presented a thought experiment that drew attention to how a linear increase in Galactic rotation into the outer disk would arise this way. The particular example they presented was of the inferred law from tracers confined within a ring – mimicking gas tracers associated with spiral arms – at 1.6 times the Sun's Galactocentric radius. These were subject to distance uncertainties similar to the larger errors considered in the lower panel of Figure 4.6. This extreme is avoided here. The spread in our stellar parameters ($\Delta M_i \sim 2$) and apparent magnitudes ($\Delta m_i \sim 1.5$, see Figure 2.4), combined with gently rising extinction (see Figure 3.13), yields an underlying stellar distribution that should span at least 5 kpc – nor is there an expectation these stars would be confined to e.g. just the Perseus Arm. This leaves us cautiously supporting the case for an increase in circular speed outside the Solar Circle and looking forward to the more extensive studies needed to clarify the situation.

4.6 Spiral arm perturbations

Spiral arms in galactic disks are widely viewed as linked with non-axisymmetric kinematic perturbations. To assess whether our data can expose such an effect, we examine the $\ell = 178^\circ$ sight line, since it is close to the radial direction that minimises shear due to Galactic rotation and more easily reveals low-amplitude perturbations that may be associated with spiral arm structure. Monguió et al. (2015) used B4-A1 stars to find a stellar overdensity due to the Perseus spiral arm at a heliocentric distance of $1.6 \pm 0.2\,\mathrm{kpc}$ in the anticentre direction, and Reid et al. (2014) used parallaxes of 24 star forming regions to find the arm to be located at 2 kpc. The Perseus Arm is therefore located just where our sampled region begins. Reid et al. (2014) also found evidence that an Outer Arm is located at a heliocentric distance of 6 kpc in the anticentre direction. This arm lies near the far end of our sampled region.

The scale of radial velocity perturbation depends on the model adopted for the origin of the perturbation. On the one hand, Monari et al. (2016) simulated the effect of a spiral potential on an axisymmetric equilibrium distribution function (emulating the Milky Way thin stellar disk) and found radial velocity perturbations of order $-5\,\mathrm{km\,s^{-1}}$ within the arms and $+5\,\mathrm{km\,s^{-1}}$ in between them. On the other, Grand et al. (2016) favour the transient winding arm view and find the perturbation of young stars ($< 3\,\mathrm{Gyr}$) to be considerably stronger at up to $\pm 20\,\mathrm{km\,s^{-1}}$, with the sense of perturbation changing across the arm.

We do not see any clear signs of perturbations, negative or positive, aligned with the Outer Arm in the HectoSpec $\ell = 178^\circ$ results. However since the HectoSpec RV error is comparable with predicted perturbations at the lower end of the expected range, and the stellar sample is subject to distance error, it is not obvious that we should expect to detect them in our data. In order to test this, we conducted another simulation. A sample of stars the same size as

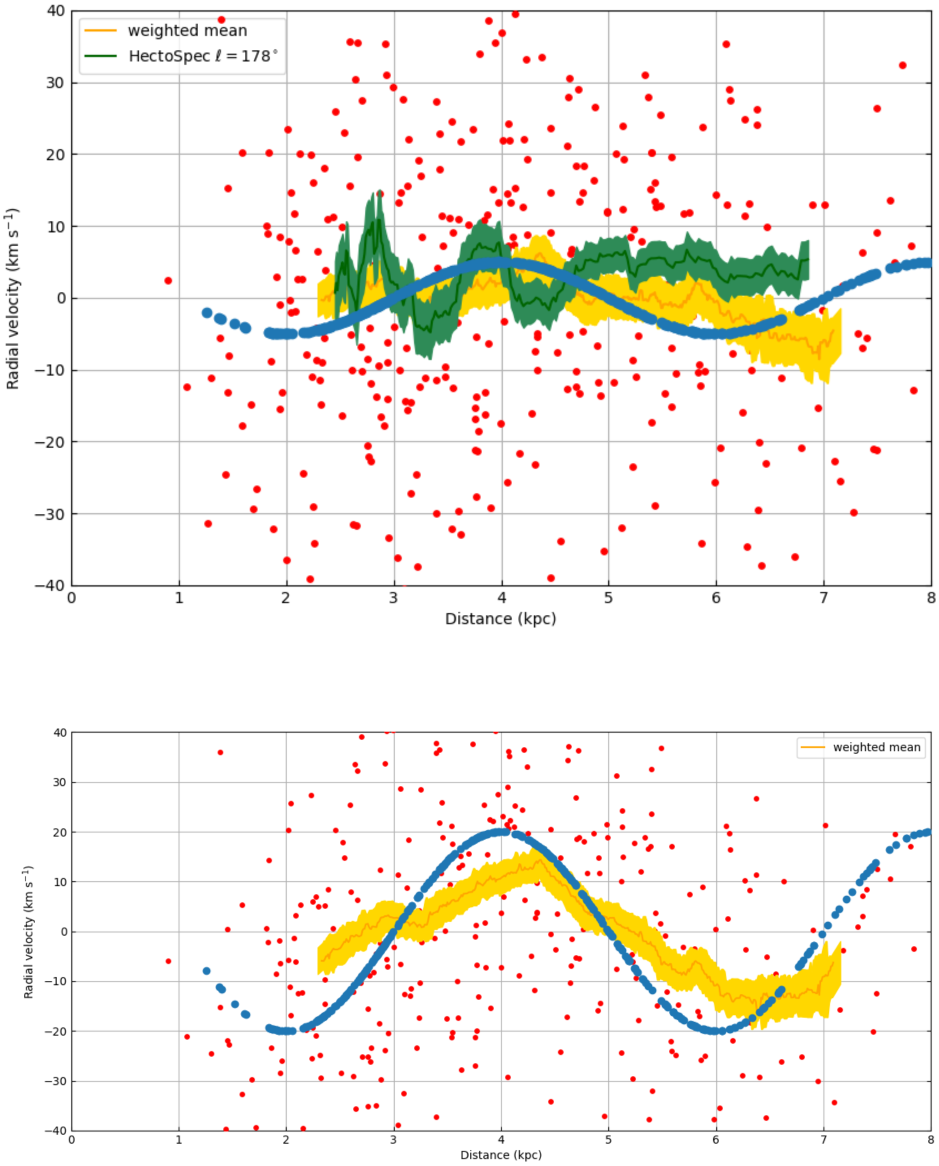

FIGURE 4.8: *The results of the spiral arm simulation for perturbations of amplitude 5 km s^{-1} (top) and 20 km s^{-1} (bottom) at $\ell = 178^\circ$. The input sinusoidal spiral arm perturbation is shown by the blue data points, and the resulting data with added errors and scatter are shown by the red points. The weighted mean trends are shown by the orange lines. The weighted mean RV trend observed at $\ell = 178^\circ$, shown by the green line, is overlayed in the top panel for comparison.*

the HectoSpec $\ell = 178^\circ$ sample and with the same distance distribution were assigned RVs according to a sinusoidal waveform – three separate tests were conducted with amplitudes of 5, 10 and 20 km s^{-1}. Two spiral arms were put at 2 kpc and 6 kpc, with the maximum perturbation amplitude aligned with the arms. Velocity scatter, RV error and distance error were then applied to the distribution, and a mean trend was computed as in Section 4.1.

Figure 4.8 show the measured weighted mean (orange line) corresponding to the $5\,\mathrm{km\,s^{-1}}$ perturbation (top) and $20\,\mathrm{km\,s^{-1}}$ perturbation (bottom). The input perturbation is shown by the blue dots, and the resulting data with errors and scatter applied is shown by the red dots. The results obtained for the small perturbations ($5\,\mathrm{km\,s^{-1}}$) exhibit no clear signs of the input sinusoid's phasing or wavelength, giving a mean trend compatible with zero for most of the sampled range. In contrast, the results for the larger amplitude perturbations do show signs of the input phasing, wavelength and amplitude. We conclude that spiral arm perturbations of small amplitude would be unlikely to appear with clear statistical significance in our results, but those of larger amplitude would.

Returning to the HectoSpec $\ell = 178^\circ$ results themselves (shown as the green line in the top panel of Figure 4.8), we do observe a wave-like structure in the mean RV trend with amplitude $\sim 5 - 10\,\mathrm{km\,s^{-1}}$, but not at an implied phase or long-enough wavelength that would make sense in comparison with the expected locations of the Perseus Arm and Outer arms (at $\sim 2\,\mathrm{kpc}$ and $\sim 6\,\mathrm{kpc}$ in this sightline, respectively). If the RV wobble is real, rather than a sample size effect, it is most likely a local effect unconnected with the larger scale structure of the Galactic disk. But we must discard the possibility of large amplitude (10-20 $\mathrm{km\,s^{-1}}$) perturbations in this direction. The results for this sightline are in keeping with the findings of Fernández et al. (2001), who used both OB stars and Cepheids to limit perturbations to under $3\,\mathrm{km\,s^{-1}}$.

Finally we comment on the form of the $\ell = 118^\circ$ results (Figure 4.3). Specifically, can a spiral arm perturbation explain the observed deviation from the trend predicted by a flat rotation law? To make this comparison, the same three simulations as described above for the $\ell = 178^\circ$ sightline were conducted for $\ell = 118^\circ$. In this case the spiral arms are located at 3 and 6.5 kpc (Reid et al., 2014) and account is taken of the expected combination of Galactic azimuthal and radial perturbations along the line of sight. Figure 4.9 show the results of these simulations, with the input perturbation of amplitude $5\,\mathrm{km\,s^{-1}}$ in the top panel and $20\,\mathrm{km\,s^{-1}}$ in the bottom panel.

In this sightline the observed RV trend, when compared with the simulation alternatives, shows a deviation from the flat rotation law of a scale similar to that of the largest ($20\,\mathrm{km\,s^{-1}}$) perturbation investigated, particularly at distances $< 4\,\mathrm{kpc}$. This stands in clear contrast to the low-amplitude perturbation compatible with the $\ell = 178^\circ$ sightline. Beyond 4 kpc there is no obvious sinusoidal structure in the RV trend. Notably, the RV trend is roughly flat in the vicinity of the Outer Arm, which is expected to cross this sightline at $\sim 6.5\,\mathrm{kpc}$. The larger amplitude perturbation seen shortwards of 4 kpc combined with a lack of sinusoidal form beyond this leads

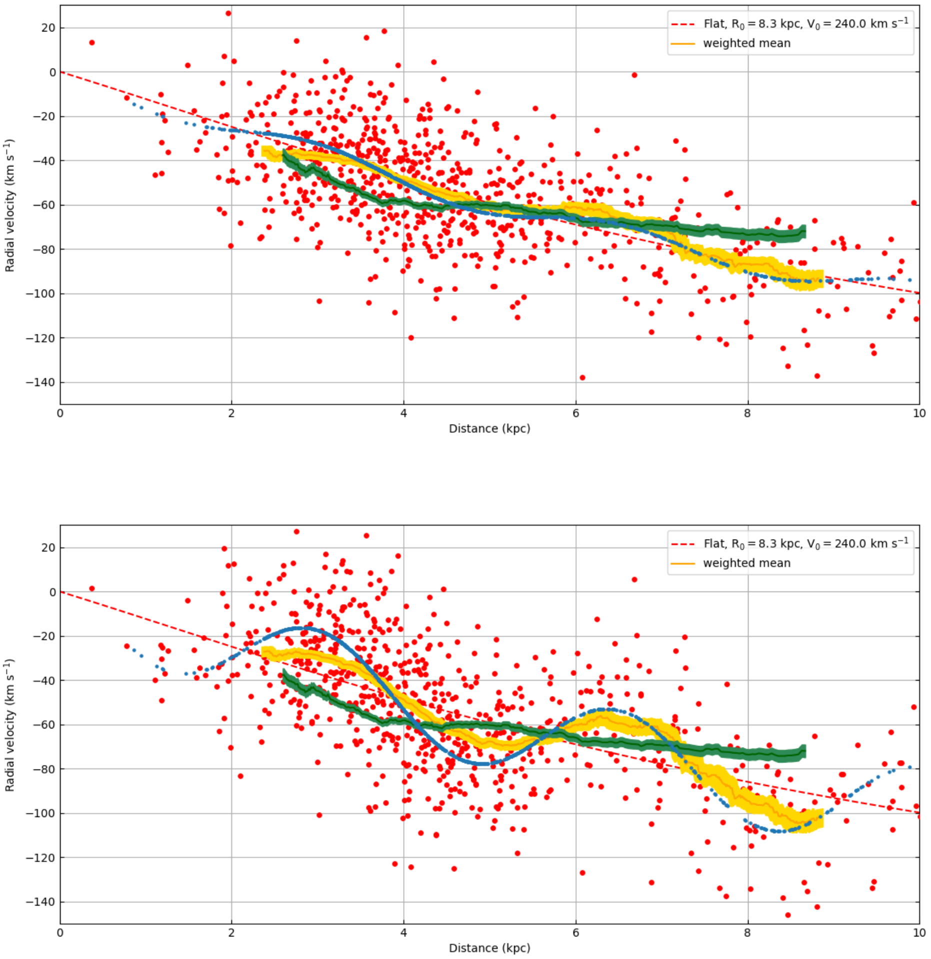

FIGURE 4.9: *The results of the spiral arm simulation for perturbations of amplitude 5* $\mathrm{km\,s^{-1}}$ *(top) and 20* $\mathrm{km\,s^{-1}}$ *(bottom) at* $\ell = 118°$. *The input sinusoidal spiral arm perturbation is shown by the blue data points, and the resulting data with added errors and scatter are shown by the red points. The weighted mean trends are shown by the orange lines. The weighted mean RV trend observed at* $\ell = 118°$, *shown by the green line, is overlayed in the top panel for comparison.*

us to conclude there is no simple coherent way of interpreting our radial velocity trends in terms of one class of spiral arm perturbation model.

Chapter 5

Validation of derived stellar parameters

5.1 Stellar parameters - A comparison with higher-resolution long-slit spectra

As a check on the reliability of the derived parameters and their errors, we obtained additional higher-resolution long-slit red and blue spectra for 7 stars for which we have HectoSpec data. These were accompanied by 5 RV standard stars (with 3 observed more than once), which we used to test the reliability of the ISIS wavelength scale. Of particular interest in this comparison were the measured surface gravities and RVs, since it is these parameters that have shown signs of potential bias. The 7 objects reobserved were chosen to cover a spread in $\log g$ from 3.5 to 4.5, as determined from the HectoSpec data, lying across the peak of the distribution in Figure 3.10. The T_{eff} range, again determined from the HectoSpec data, spans $\sim 7900-9500$ K, with one object outside this range with $\sim 11900\pm^{150}_{2600}$ K – the large error indicating the unresolved fit dilemma described in Section 3.2.1.

The spectra were gathered as service observations using the Intermediate-dispersion Spectrograph and Imaging System (ISIS) of the 4.2 m William Herschel Telescope during 3 nights in Oct-Dec 2016. ISIS is a high-efficiency, double-armed, medium-resolution ($R\sim 500-12000$) long-slit spectrograph. The R1200B grating was used on the blue arm, and the R1200R grating on the red arm, providing resolution elements for a 1” slit of 0.85 Åand 0.75 Årespectively, or resolving powers of $R\sim 4700$ and $R\sim 11500$ for our analysed wavelength range. The resolving power in the red region is significantly greater than that of the HectoSpec data ($R \sim 3600$), providing potentially superior RV precision. Additionally, the long-slit capability should allow for better sky subtraction than can be achieved with a fibre spectrograph, due to fibre spectrographs being effected by variations in the sky continuum (spatially), and in the fibre-to-fibre response.

The total wavelength coverage of the blue spectra is 3800 – 4740 Å and for the red spectra it is 8110 – 9120 Å. The blue and red spectra have a constant wavelength sampling of 0.22 Å and 0.24 Å respectively. The positions, apparent *i* magnitudes and ISIS exposure times of the reobserved objects are shown in Table 5.1, and the observed RV standard stars and their positions are shown in Table 5.2.

The raw images were processed and sky-subtracted and the resultant spectra were wavelength calibrated, all with use of the Image Reduction and Analysis Facility (IRAF). Figure 5.1 shows the ISIS spectrum of one of the re-observed objects (target 1), along with its HectoSpec spectrum. All have been roughly normalised for comparison, and the wavelength ranges shown are those used in our analysis. The incompletely-subtracted sky lines in the HectoSpec spectrum between 8600 – 8700 Åare obvious, whereas the sky-subtraction from the long-slit spectrograph ISIS is better behaved. The S/N of the ISIS spectrum (S/N$\sim$ 26) is lower than that of HectoSpec (S/N$\sim$ 86) due to the ISIS observation exposure times being much shorter, and the mirror size being smaller. For the particular object shown, the total ISIS exposure time was 30 min (see object 1 in Table 5.1), compared to 75 min for the HectoSpec observation (see the 18-11-2011 (a) observation in Table 2.1). The mirror diameter used by ISIS is 4.2 m, and by HectoSpec is 6.5 m, resulting in the light-gathering area of ISIS being 42% of that of HectoSpec.

The spectra were then passed through the MCMC full-parameter fitting method, as described in Section 3.1.4. For the red spectra the same wavelength limits were adopted as for HectoSpec (8470 – 8940 Å), and the blue wavelength range used was 4000 – 4600 Å, covering some of the Balmer series whilst excluding the Ca II K and H lines since they suffer from interstellar absorption. The measured parameters and RV were then compared to those measured from the HectoSpec spectra (see Table 5.3), or to values from the literature in the case of the RV standards (see Table 5.2), to reveal any systematic differences. The weighted mean difference between measured RV for the ISIS RV standard stars and RV from the literature is $-0.7\,\mathrm{km\,s^{-1}}$ for the blue spectra, with a dispersion of $3.4\,\mathrm{km\,s^{-1}}$, and $+0.1\,\mathrm{km\,s^{-1}}$ for the red spectra, with a dispersion of $1.7\,\mathrm{km\,s^{-1}}$. Hence we are confident the ISIS wavelength scale is reliable to at least within a few $\mathrm{km\,s^{-1}}$.

Target	**RA**	**DEC**	***i* mag**	**Exposure (s)**
1	00:03:41	+64:29:43	14.94	3×600
2	00:06:36	+64:22:38	14.89	3×1200
3	00:03:47	+64:17:12	14.77	3×600
4	00:07:37	+64:07:51	14.78	3×600
5	00:05:36	+63:57:55	14.84	3×800
6	00:04:02	+64:29:49	14.91	2×1200
7	00:07:13	+64:46:18	14.82	2×1200

TABLE 5.1: *Positions, apparent i magnitudes, and exposure times of the reobserved objects used for the HectoSpec-ISIS comparison.*

Standard	**RA**	**DEC**	**Obs. date**	**Bary. RV (km s^{-1})**		**Lit. RV (km s^{-1})**
				Blue	**Red**	
HD42807	06:13:13	+10:37:38	18-10-16	$13.7\pm^{0.1}_{0.1}$	$4.3\pm^{0.2}_{0.1}$	6.1
HD50692	06:55:19	+25:22:33	18-10-16	$-14.0\pm^{1.9}_{0.1}$	$-15.6\pm^{0.1}_{1.0}$	-15.0
HD219172	23:13:49	+15:21:58	20-10-16	$0.5\pm^{0.2}_{0.2}$	$-2.9\pm^{0.2}_{0.2}$	-2.8
			15-12-16	$-4.5\pm^{0.2}_{0.2}$	$-1.1\pm^{0.2}_{0.2}$	
HD221584	23:32:45	+63:17:17	18-10-16	$-27.8\pm^{0.8}_{0.2}$	$-23.9\pm^{0.2}_{0.2}$	-25.0
			20-10-16	$-24.4\pm^{0.2}_{0.3}$	$-28.7\pm^{0.2}_{0.2}$	
			15-12-16	$-24.4\pm^{0.2}_{0.3}$	$-24.0\pm^{0.2}_{0.2}$	
HD10780	01:47:45	+63:51:05	20-10-16	$2.9\pm^{0.1}_{0.2}$	$3.4\pm^{0.1}_{2.1}$	2.6
			15-12-16	$-2.4\pm^{0.1}_{0.1}$	$4.4\pm^{0.1}_{0.2}$	

TABLE 5.2: *The observed radial velocity standards, their positions, measured RV from blue and red spectra, and literature RV (in the Barycentric frame).*

Figure 5.2 shows the difference between the ISIS measurements (blue points for blue spectra and red points for red spectra) and the HectoSpec measurements. The error bars represent both the ISIS and HectoSpec uncertainties. The targets are in ascending order of $T_{\rm eff}$, as determined from the ISIS red spectra. In general the differences in outcome are reassuringly modest and show the method is working satisfactorily. The dashed lines represent the weighted mean difference between the ISIS red and HectoSpec measurements (red line) and ISIS blue and HectoSpec measurements (blue line).

The weighted mean difference between the red ISIS and HectoSpec measurements, and the standard deviation of the spread, are: $\Delta T_{\rm eff} = -216 \pm 1335$ K, $\Delta \log g = -0.36 \pm 0.18$, $\Delta v \sin i =$

Object	**HectoSpec red**	**ISIS blue**	**ISIS red**	**ISIS blue**	**ISIS red**	**HectoSpec red**	**ISIS blue**	**ISIS red**	**ISIS blue**	**ISIS red**
	$T_{\rm eff}$ **(K)**			$\Delta T_{\rm eff}$ **(K)**		$\log g$			$\Delta \log g$	
1	$8022\pm^{70}_{95}$	$7729\pm^{63}_{64}$	$7665\pm^{115}_{101}$	-293	-357	$4.25\pm^{0.05}_{0.07}$	$4.26\pm^{0.33}_{0.30}$	$3.99\pm^{0.11}_{0.10}$	+0.01	-0.26
2	$7935\pm^{69}_{58}$	$7656\pm^{62}_{66}$	$7703\pm^{76}_{73}$	-279	-232	$3.50\pm^{0.06}_{0.06}$	$3.42\pm^{0.25}_{0.16}$	$3.21\pm^{0.09}_{0.08}$	-0.08	-0.29
3	$7963\pm^{69}_{84}$	$7590\pm^{54}_{62}$	$7796\pm^{89}_{95}$	-373	-167	$4.11\pm^{0.06}_{0.07}$	$3.76\pm^{0.23}_{0.34}$	$3.66\pm^{0.08}_{0.08}$	-0.35	-0.45
4	$9507\pm^{167}_{161}$	$8818\pm^{286}_{326}$	$8331\pm^{2957}_{219}$	-689	-1176	$4.28\pm^{0.03}_{0.04}$	$3.71\pm^{0.14}_{0.15}$	$3.51\pm^{0.15}_{0.13}$	-0.57	-0.77
5	$8792\pm^{139}_{157}$	$8887\pm^{143}_{143}$	$11043\pm^{344}_{1332}$	+95	+2251	$4.55\pm^{0.06}_{0.08}$	$3.86\pm^{0.06}_{0.08}$	$3.99\pm^{0.06}_{0.07}$	-0.69	-0.56
6	$8782\pm^{78}_{86}$	$8676\pm^{171}_{229}$	$11299\pm^{158}_{1710}$	-106	+2517	$3.94\pm^{0.03}_{0.04}$	$3.82\pm^{0.08}_{0.09}$	$3.65\pm^{0.05}_{0.05}$	-0.12	-0.29
7	$11872\pm^{149}_{2605}$	$8761\pm^{366}_{964}$	$11370\pm^{202}_{378}$	-3111	-502	$4.08\pm^{0.07}_{0.05}$	$3.16\pm^{0.21}_{0.12}$	$3.84\pm^{0.06}_{0.07}$	-0.92	-0.24
	$v \sin i$ **(km s^{-1})**			$\Delta v \sin i$ **(km s^{-1})**		**LSR RV (km s^{-1})**			**ΔLSR RV (km s^{-1})**	
1	$46\pm^{14}_{13}$	$41\pm^{8}_{7}$	$50\pm^{8}_{6}$	-5	+4	$-23.5\pm^{2.3}_{3.0}$	$-28.4\pm^{2.8}_{2.5}$	$-22.2\pm^{3.0}_{2.8}$	-4.9	+1.2
2	$197\pm^{10}_{12}$	$191\pm^{14}_{12}$	$211\pm^{13}_{14}$	-6	+14	$-99.0\pm^{3.7}_{4.1}$	$-94.3\pm^{8.3}_{7.5}$	$-106.2\pm^{5.8}_{5.5}$	+4.7	-7.2
3	$76\pm^{10}_{8}$	$28\pm^{10}_{7}$	$25\pm^{7}_{6}$	-48	-51	$-40.2\pm^{3.3}_{2.8}$	$-49.2\pm^{2.1}_{1.7}$	$-44.0\pm^{1.7}_{1.7}$	-9.0	-3.8
4	$194\pm^{14}_{16}$	$221\pm^{24}_{25}$	$248\pm^{34}_{49}$	+27	+54	$-67.9\pm^{6.0}_{4.9}$	$-71.1\pm^{10.9}_{9.9}$	$-73.7\pm^{11.4}_{9.8}$	-3.2	-5.8
5	$113\pm^{19}_{20}$	$50\pm^{9}_{7}$	$51\pm^{10}_{6}$	-63	-62	$-54.1\pm^{5.6}_{5.3}$	$-65.9\pm^{3.0}_{2.8}$	$-54.6\pm^{4.8}_{4.5}$	-11.8	-0.5
6	$153\pm^{13}_{10}$	$167\pm^{19}_{21}$	$123\pm^{25}_{20}$	+14	-30	$-37.0\pm^{4.4}_{3.8}$	$-62.2\pm^{9.2}_{9.5}$	$-38.5\pm^{4.9}_{4.8}$	-25.2	-1.5
7	$140\pm^{51}_{25}$	$287\pm^{10}_{20}$	$238\pm^{39}_{37}$	+147	+98	$-67.9\pm^{6.5}_{5.3}$	$-82.6\pm^{17.0}_{16.1}$	$-64.6\pm^{9.1}_{8.3}$	-14.7	+3.3

TABLE 5.3: *The measured stellar parameters of the HectoSpec red spectra, and the ISIS blue spectra and ISIS red spectra. Also shown are the differences between the ISIS and HectoSpec measurements (ISIS - HectoSpec).*

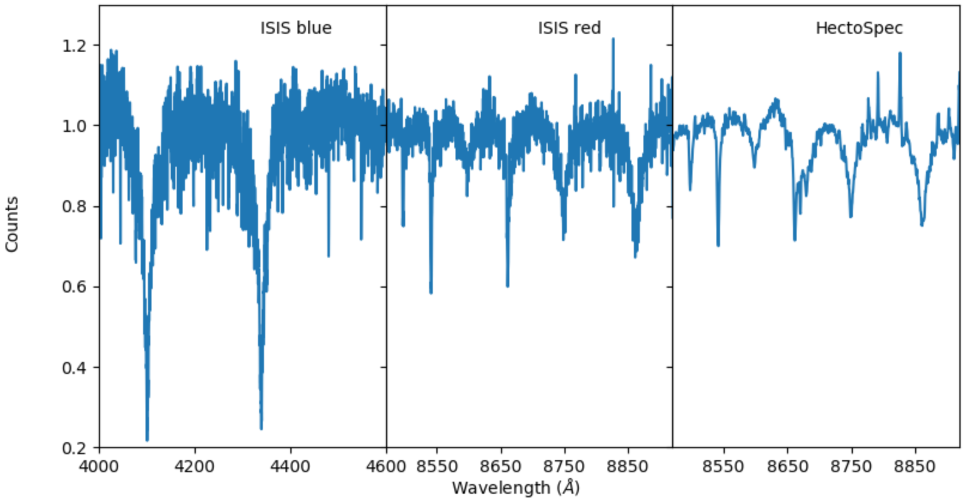

FIGURE 5.1: *The ISIS blue spectrum, ISIS red spectrum, and HectoSpec spectrum of a target 1 in Table 5.1. All have been roughly normalised for comparison.*

$-24 \pm 53\,\mathrm{km\,s^{-1}}$, $\Delta\mathrm{RV} = -1.9 \pm 3.5\,\mathrm{km\,s^{-1}}$. The small mean difference in measured RV indicates the HectoSpec wavelength calibration may be systematically and positively offset by an amount well below measured random errors. The larger difference in $\log g$ suggests there may be a bias towards over-large values in the HectoSpec data. This potential bias is not the first evidence: the comparison between our A star $\log g$ distribution and that from a Besançon model is shown in Figure 3.10 and we see the HectoSpec distribution peaks at a slightly larger value. We examined the impact of this possible bias in Section 4.5. However, the measured $\log g$ values of the ISIS data are generally lower than those expected from a near-MS sample, and lie in the lower tail of the Besançon mode – yet again indicating that $\log g$ is a tricky parameter to measure in these circumstances.

The blue data points in Figure 5.2 provide the comparison between the ISIS blue and HectoSpec data. The weighted mean offsets and standard deviations obtained are: $\Delta T_{\mathrm{eff}} = -289 \pm 1017\,\mathrm{K}$, $\Delta\log g = -0.43 \pm 0.32$, $\Delta v\sin i = -18 \pm 63\,\mathrm{km\,s^{-1}}$, $\Delta\mathrm{RV} = -7.7 \pm 8.8\,\mathrm{km\,s^{-1}}$. As with the red, there is a sizable offset in $\log g$. The RV difference is larger than that measured for the red spectra, potentially as a result of the fewer absorption lines fitted in the blue region and the lower accuracy achieved.

A method check was performed by comparing the measured parameters from the red and blue ISIS spectra, eliminating the potential for differences due to a change of instrument. Hales et al. (2009) performed a similar comparison between the red and blue ranges as observed with

ISIS, and found a tendency for the red determined spectral type to be earlier by 0.9 subtypes. They attributed this to strengthening of the Ca II H and K absorption lines by an interstellar component. Although we exclude these lines in the fitting procedure, we find a modest offset in effective temperature, with the red range suggesting a slightly hotter star with very little change in surface gravity. The weighted mean difference between the red and blue ISIS measurements, and the standard deviation of the spread, are: $\Delta T_{\text{eff}} = 112 \pm 1279\,\text{K}$, $\Delta \log g = 0.02 \pm 0.31$, $\Delta v \sin i = -2 \pm 28\,\text{km}\,\text{s}^{-1}$, $\Delta\text{RV} = 6.1 \pm 11.1\,\text{km}\,\text{s}^{-1}$.

The comparison with higher-resolution spectra has provided useful insights – the offsets between the ISIS and Hectospec measurements are reassuringly modest and are similar to those expected due to random errors. Our employed method works well. The larger offset in the derived surface gravities is further evidence of a potential bias, although the surprisingly low $\log g$ measurements for the ISIS spectra persuade us that $\log g$ is a particularly tricky parameter to measure reliably.

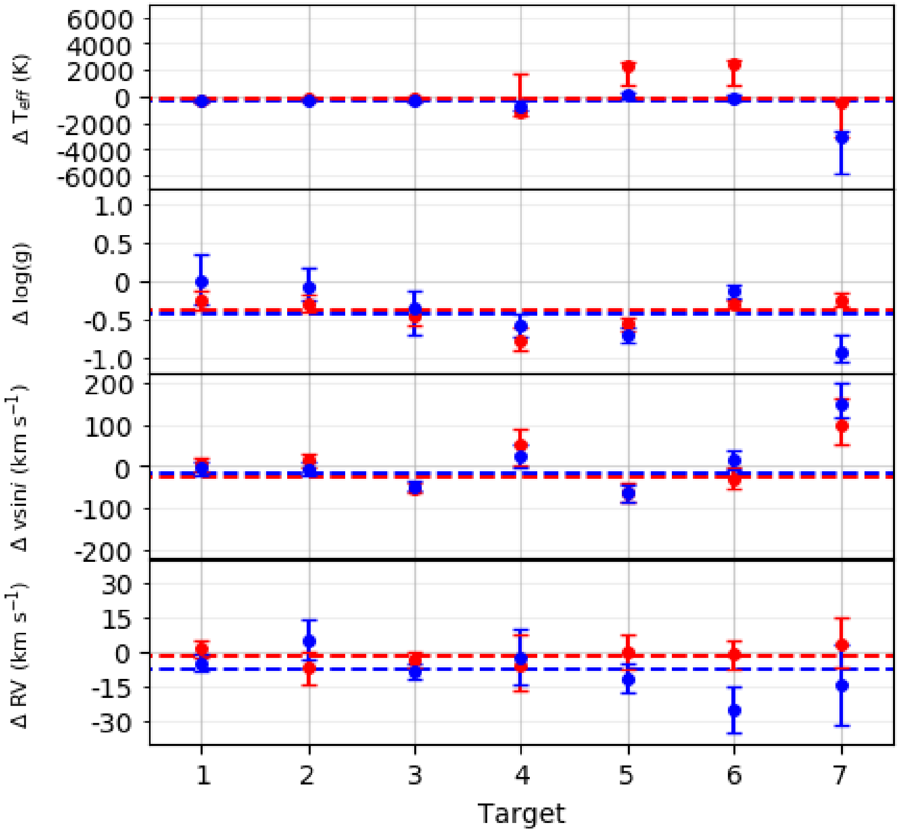

FIGURE 5.2: *Differences between ISIS and HectoSpec measured stellar parameters. The blue points represent the differences between measurements from the blue ISIS and HectoSpec spectra, and the red points specify differences between the red ISIS and HectoSpec spectra. The targets are in ascending order of $T_{\rm eff}$, as determined from the ISIS red spectra. The error shown on each datapoint is the quadratic sum of the HectoSpec error and ISIS error. The dashed lines represent the weighted mean difference between the ISIS red and HectoSpec measurements (red line) and ISIS blue and HectoSpec measurements (blue line).*

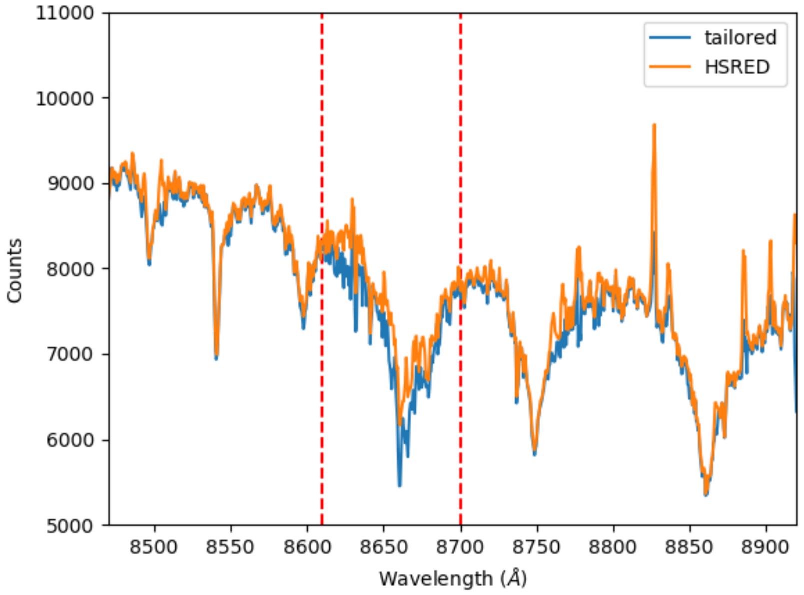

FIGURE 5.3: *An example of a HectoSpec spectrum, reduced using the default HSRED pipeline using a mean sky spectrum (orange line), and using a more tailored sky-subtraction treatment (blue line). We exclude the region between the red dashed lines due to it typically being a region of incomplete sky-subtraction.*

5.2 Comparison with HectoSpec spectra with tailored sky-subtraction

The HectoSpec spectra were reduced using their default pipeline, HSRED. For each configuration, a mean sky spectrum from 30 dedicated fibres was subtracted from each HectoSpec target spectrum. H. Farnhill, who made the original data selection, performed a more tailored sky-subtraction on a subset of 194 HectoSpec targets by making use of the individual sky spectra. The subset objects are all from the same observation configuration. Figure 5.3 shows an example of a HectoSpec spectrum which was been reduced using the default HSRED pipeline using a mean sky spectrum (orange line), along with the same spectrum which has had the more tailored sky-subtraction treatment (blue line). The region between the red lines is a region that typically suffers from incomplete sky-subtraction, and it is evident the more tailored sky-subtraction also struggles in this range. In order to gauge the impact of using a mean sky spectrum, as is the case for our HectoSpec sample, we compare our measured stellar parameters with those obtained by running the more tailored sky-subtraction spectra through our MCMC routine (see Section 3.1.4 for method details). We exclude the region between the red dashed lines ($8610-8700\AA$) in our analysis.

The top panel of Figure 5.4 shows the difference between the measured T_{eff} from the tailored

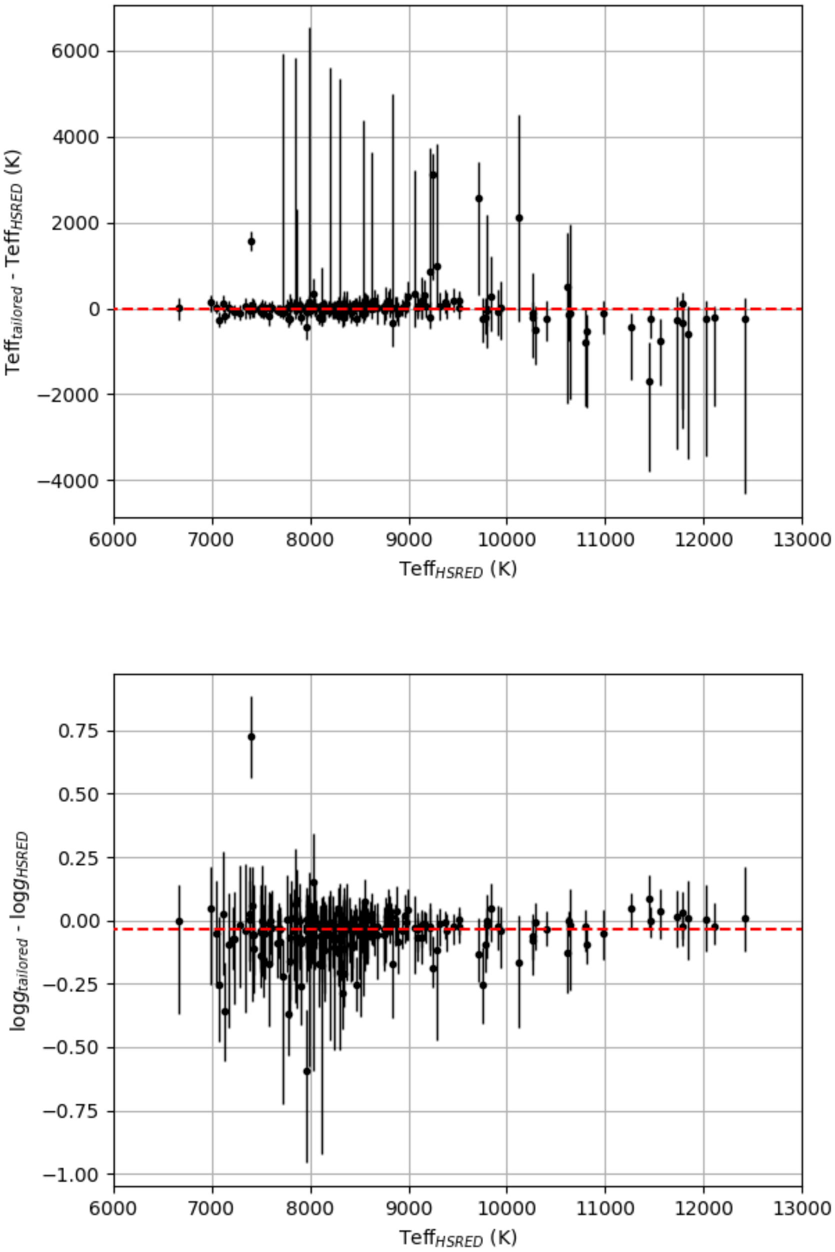

FIGURE 5.4: *A comparison of measured* T_{eff} *(top) and* $\log g$ *(bottom) of spectra reduced using the default HSRED pipeline, and spectra with a more tailored sky-subtraction. The error bars represent the uncertainties from both the HSRED and tailored measurements. The red line is the mean of the difference between the two measurements, weighted by the errors.*

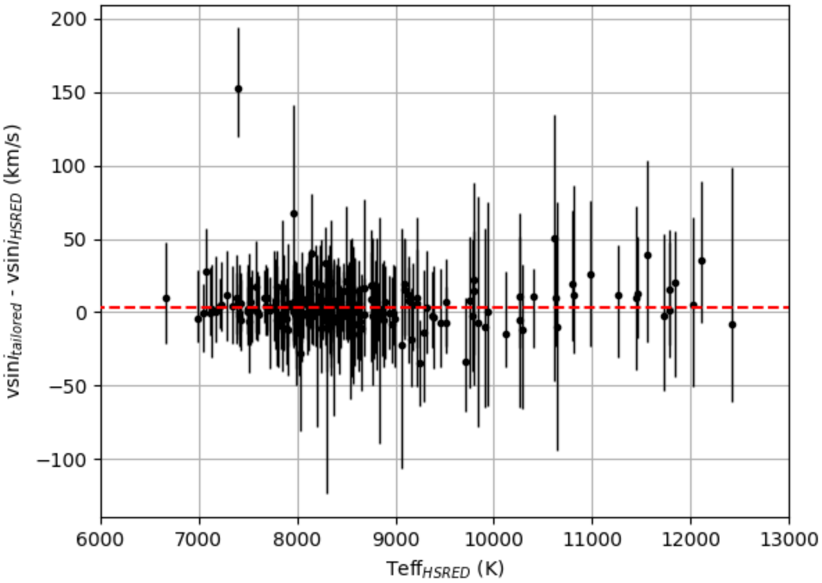

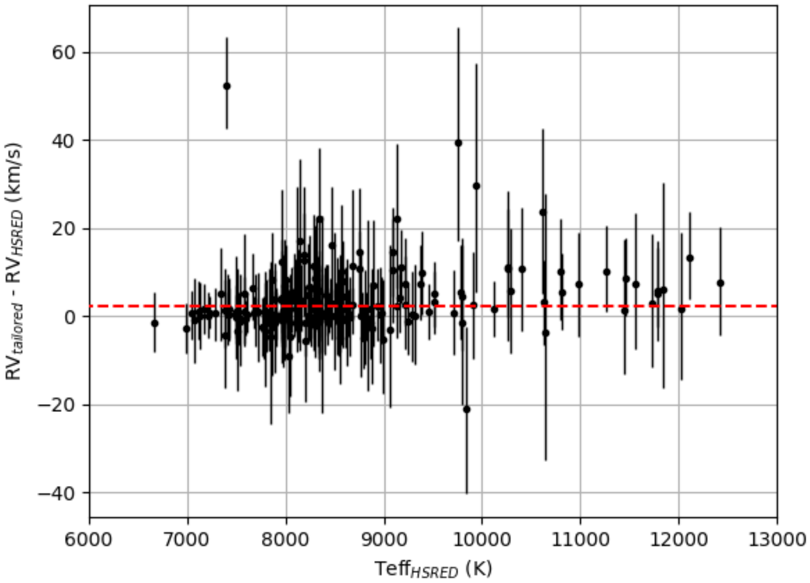

FIGURE 5.5: *A comparison of measured* $v\sin i$ *(top) and RV (bottom) of spectra reduced using the default HSRED pipeline, and spectra with a more tailored sky-subtraction. The error bars represent the uncertainties from both the HSRED and tailored measurements. The red line is the mean of the difference between the two measurements, weighted by the errors.*

spectra and the measured T_{eff} from the HSRED spectra, as a function of the HSRED T_{eff}. The error bars represent the uncertainties from both the tailored and HSRED pipelines. Similarly, the bottom panel shows the difference between the $\log g$ measurements. The red line is the weighted mean of the differences. Figure 5.5 shows the differences for the $v\sin i$ measurements (top panel) and RVs (bottom panel). The weighted mean and spread of the differences are:

- $T_{\mathrm{eff}}: -3 \pm 413\,\mathrm{K}$
- $\log g: -0.03 \pm 0.10$
- $v\sin i: 4 \pm 16\,\mathrm{km\,s^{-1}}$
- RV: $2.5 \pm 7.2\,\mathrm{km\,s^{-1}}$

The subset with more tailored sky-subtraction typically returns slightly more positive RVs. We have already reported evidence of a small positive bias in our RV measurements (see Section 4.5), and this test suggests a more tailored sky-subtraction process would make this bias slightly stronger. However, in general the differences are very small and the two measurements are consistent within their uncertainties. We conclude that a more tailored sky-subtraction of all objects would not significantly effect our results, and using the default HSRED reduced HectoSpec spectra is justified.

5.3 Comparison of results with expectations from a Galactic model

In this Section, we compare our results with expectations from a Galactic model. Our specific aims include the analysis of the target selection process - are the strips in the $r-i$, $r-H\alpha$ diagram contaminated by other stellar types, and if so by how much? We also aim to analyse the method employed and results obtained. In particular, we examine the impact of our treatment of binaries as single stars. Also considered are the extinctions, specifically keeping in mind the apparent bias in our measurements to lower values, as discussed in Section 3.3. We examine the resulting distance distribution in context of these potential biases. We do not examine the full kinematics here since it has been considered throughout.

5.3.1 The Galactic disk model

The simulation described here was run for 1,000,000 disk stars located in a specific direction - we analysed both of our chosen sightlines at $\ell = 118^\circ$, $b = 2^\circ$, and $\ell = 178^\circ$, $b = 1^\circ$. We adopted $R_0 = 8.3\,\mathrm{kpc}$ throughout (Reid et al., 2014).

5.3.1.1 Initial mass

Initial masses were randomly selected from the range $1 - 20\mathrm{M}_\odot$, with the probability of each mass proportional to the single star initial mass function (IMF) of Maschberger (2013), described by the probability density function (pdf)

$$pdf(m_*) = A\left(\frac{m_*}{\mu_*}\right)^{-\alpha}\left(1+\left(\frac{m_*}{\mu_*}\right)^{1-\alpha}\right)^{-\beta} \tag{5.1}$$

where m_* is mass in units of Solar mass, $\alpha = 2.3$ is the high-mass exponent, $\beta = 1.4$ is the low-mass exponent, $\mu_* = 0.2$ is a scale parameter, and A is a normalising constant, given by

$$A = \frac{(1-\alpha)(1-\beta)}{\mu_*}\frac{1}{G(m_{u*}) - G(m_{l*})} \tag{5.2}$$

with m_{u*} and m_{l*} the upper and lower mass limits, and

$$G = \left(1+\left(\frac{m_*}{\mu_*}\right)^{1-\alpha}\right)^{1-\beta} \tag{5.3}$$

Figure 5.6 shows the IMF. In the range considered this is basically a power law with slope -2.3. For lower masses, the slope drops off slightly. The Maschberger (2013) IMF is essentially indistinguishable from those of Kroupa (2001) and Chabrier (2003). Although we do incorporate binary systems (see Section 5.3.1.6), for simplicity we use the single star IMF for the single and primary star masses. The secondary star masses are assigned via the mass ratio distribution. Hence, our total stellar population does not strictly follow the IMF, although the effect is negligible in our region of interest at $> 1\mathrm{M}_\odot$. Figure 5.7 shows the initial masses of single and primary stars (blue line), and of all stars i.e. single, primary and secondary (orange line), showing the difference is negligible in this mass range.

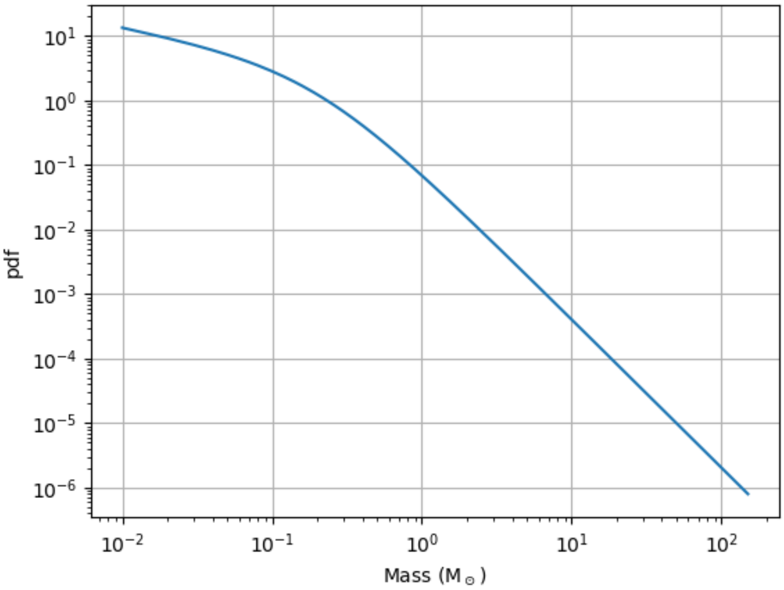

FIGURE 5.6: *Single star IMF from Maschberger (2013)*

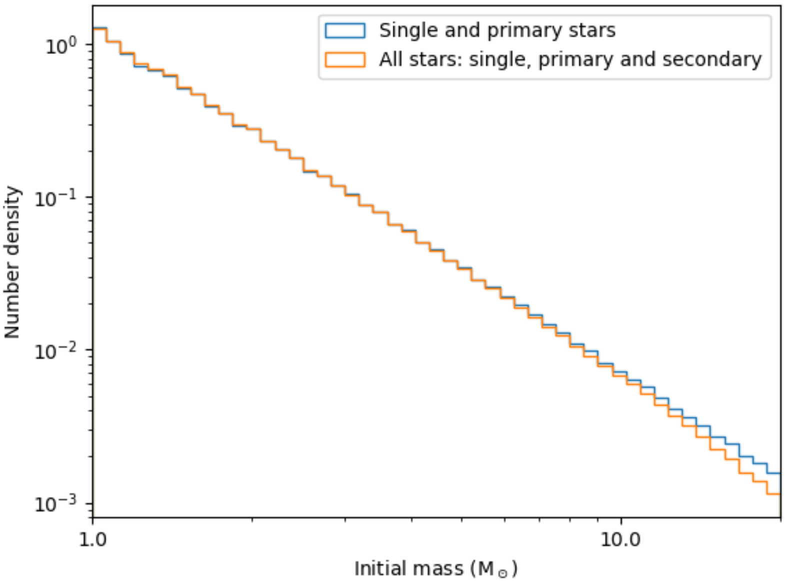

FIGURE 5.7: *Initial masses of single and primary stars compared to initial masses of all stars (single, primary and secondary). Plot is for stars at* $\ell = 118°$ *but it is the same at* $\ell = 178°$.

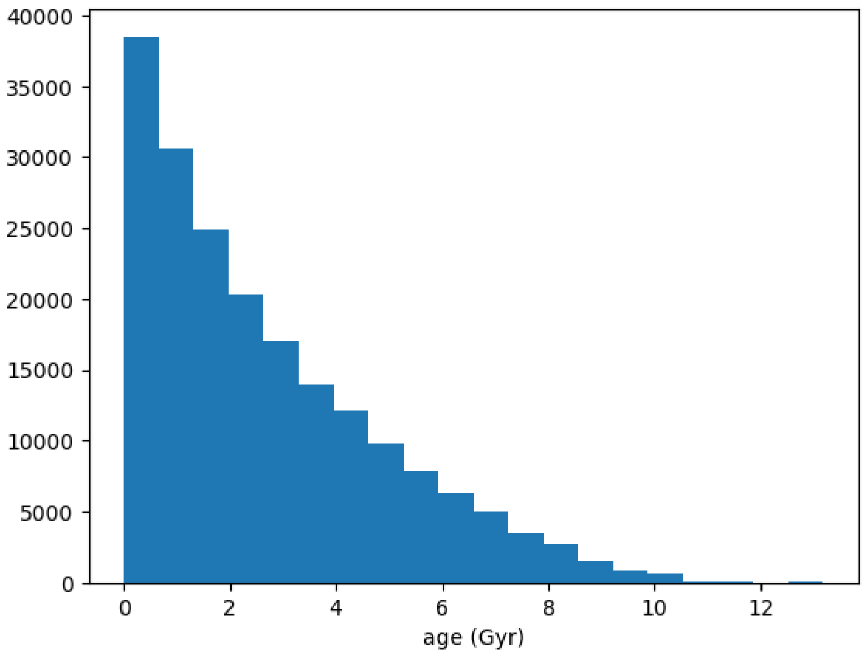

FIGURE 5.8: *Simulated distribution of ages of alive stars.*

5.3.1.2 Age

The stellar ages were selected from a uniform distribution from 0-13.6 Gyr, emulating a flat star formation history. We do this since it is simple, and is not far from expectations of a roughly constant or slowly declining star formation history (Snaith et al., 2014, 2015; Zonoozi et al., 2019), particularly since the objects of interest to us are relatively young. The maximum mass for a certain age was taken from Padova isochrones with appropriate metallicity (see Section 5.3.1.7), and if the mass of a certain object exceeded this it was considered dead and was thrown away into a remnant bin. Of our 1,000,000 simulated stars in each sightline, 80% became remnants, although this percentage depends on the minimum mass considered. Hence, there were $\sim 200,000$ stars available to analyse in each sightline, and it is only these that we consider in the remainder of this Section. Figure 5.8 shows the distribution of ages of the alive stars at $\ell = 118°$ (the Figure is the same for $\ell = 178°$). For reference, the maximum age of an F star ($\sim 1.3\,\mathrm{M}_\odot$) is ~ 5 Gyr, and for an A star ($\sim 2.3\,\mathrm{M}_\odot$) is ~ 1 Gyr. The oldest stars in the simulation with age > 10 Gyr are G stars of $1\,\mathrm{M}_\odot$.

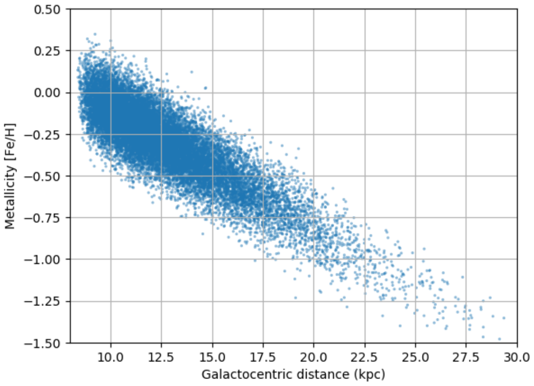

FIGURE 5.9: *Simulated metallicity vs. Galactocentric radius for* $\ell = 118°$ *(left) and* $\ell = 178°$ *(right).*

5.3.1.3 Metallicity

The initial metallicity was randomly selected from a Gaussian distribution with mean [Fe/H] $= 0$ and a dispersion of 0.12, which are values suitable for the Solar neighbourhood (Robin et al., 2003). The metallicity gradient of $d[\text{Fe/H}]/dR_G = -0.07\,\text{dex kpc}^{-1}$ from e.g. Sale et al. (2010) was then applied, with use of the individual distances (see Section 5.3.1.4). Figure 5.9 shows metallicity as a function of Galactocentric radius at $\ell = 118°$ (left) and $\ell = 178°$ (right). The stars pack to lower R_G at $\ell = 118°$, resulting in metallicities closer to the Solar value on average compared to at $\ell = 178°$.

5.3.1.4 Distance

Following Jurić et al. (2008), the stellar density profile within the disk was given by,

$$\rho_D(R_G, z; L, H) = \rho_D(R_0, 0)e^{R_0/L}\exp\left(-\frac{R_G}{L} - \frac{z+z_\odot}{H}\right) \tag{5.4}$$

where R_G is the Galactocentric radius, z is the height above the Galactic plane, $L = 2600\,\text{pc}$ is the scale length, $H = 300\,\text{pc}$ is the thin disk scale height, and $z_\odot = 25\,\text{pc}$ is the height of the Sun above the Galactic plane. We set $\rho_D(R_0, 0)e^{R_0/L} = 1$ since this is just a scale factor and doesn't affect the overall distribution of distances. The thick disk could be modelled using the same density profile multiplied by a normalisation and with different scale lengths, but we do not do this here since the contribution from the thick disk stars will be small.

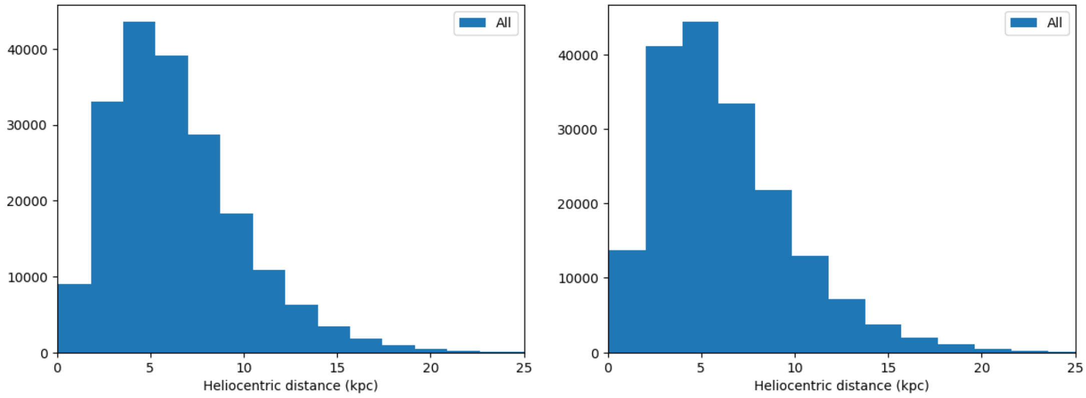

FIGURE 5.10: *Distribution of heliocentric distances of all simulated stars at* $\ell = 118^\circ$ *(left) and* $\ell = 178^\circ$ *(right).*

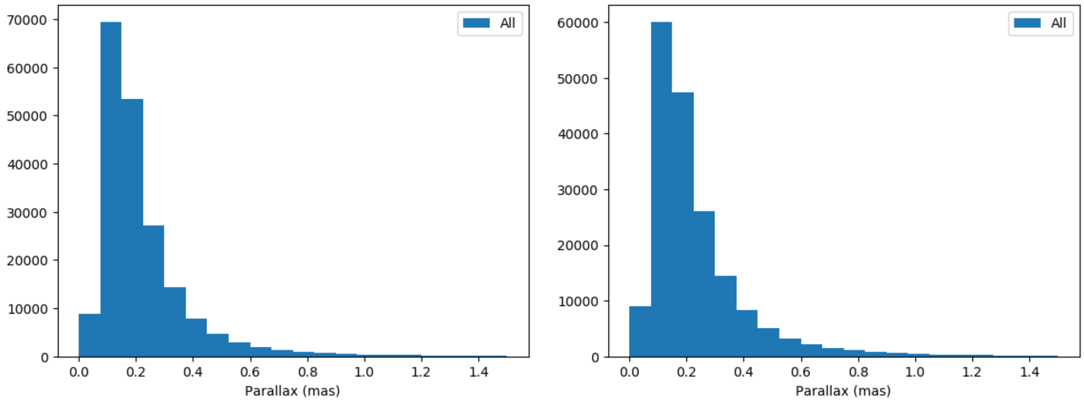

FIGURE 5.11: *Distribution of parallaxes of all simulated stars (i.e. directly inverted distances) at* $\ell = 118^\circ$ *(left) and* $\ell = 178^\circ$ *(right).*

A volume element along the sightline is given by

$$dV = \pi \tan^2(0.5\alpha_d)d^2dr \tag{5.5}$$

where d is the heliocentric distance and α_d is the angular diameter of the sightline (1° in our case), however we again set the coefficient to 1 since it is a scale factor.

The heliocentric distances are randomly selected from a range $0-50$ kpc (arbitrarily large) with the probability of each distance proportional to the density profile multiplied by the volume element at that distance. Figure 5.10 shows the distribution of distances for all stars at $\ell = 118^\circ$ (left) and $\ell = 178^\circ$ (right). Similarly, Figure 5.11 shows the parallaxes, i.e. the directly inverted distances (without errors).

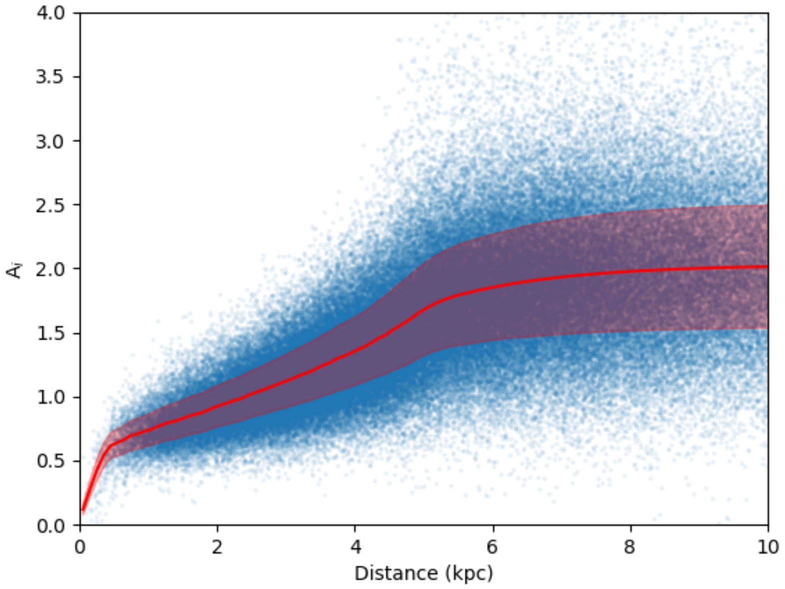

FIGURE 5.12: *Simulated extinction A_i as a function of heliocentric distance at $\ell = 118°$, along with the mean extinction trend and its dispersion. The corresponding figure for $\ell = 178°$ is very similar.*

5.3.1.5 Extinction

To get extinctions for the stars we used Sale et al. (2014) mean extinction trends. There is a grid of 28 extinction trends available within the $\ell = 118°$ sightline, and 26 in the $\ell = 178°$. Each object was randomly assigned an extinction trend, and the extinction was interpolated from this trend given the distance to the object. We chose to use a grid of extinction trends rather than an average trend since the finer resolution better emulates reality, in the case that the stars are evenly distributed across the sightline.

The extinction trends were given as a function of A_{5495}, which is close enough to A_V for purpose here. To obtain the extinction in different bands, we converted the interpolated A_{5495} (or A_V) to r, i, H_α using $A_r \sim 0.83A_V$, $A_i \sim 0.59A_V$ and $A_{H_\alpha} \sim 0.76A_V$ (Sale and Magorrian, 2015). These are values calculated for early-A stars assuming moderate extinction ($A_i \sim 1$) and Fitzpatrick law with $R_v = 3.1$, although the ratios do not vary greatly for other stellar types and are sufficient for purpose.

Figure 5.12 shows the simulated A$_i$ extinction as a function of distance at $\ell = 118°$, along with the mean of the extinction trends and its dispersion. The corresponding figure for $\ell = 178°$ is very similar.

5.3.1.6 Binaries

To consider stellar multiplicity, we randomly assigned some stars a secondary component. To do so, all stars were assigned a random number between $0-1$, and if the number was less than the binary fraction appropriate for that star, it was made the primary component of a binary system and a secondary component was created. The binary fractions and corresponding mass ranges used are:

- 0.5 for F/G stars ($< 1.6\,\mathrm{M}_\odot$)
- 0.7 for A stars ($1.6-3\,\mathrm{M}_\odot$)
- 0.8 for B stars ($3-14\,\mathrm{M}_\odot$)
- 0.9 for O stars ($> 14\,\mathrm{M}_\odot$)

The stated binary fractions approximately follow those in Duchêne and Kraus (2013), and the mass ranges roughly correspond to the Padova MS track with an appropriate temperature. Overall, $\sim 54\%$ of initially simulated stars are chosen to be primary components of a binary system - resulting in $\sim 70\%$ of total simulated stars in binary systems (primary and secondary).

If a star was selected as a primary component in a binary system, the mass ratio of the system, q, was selected from the binary mass ratio distribution, $f(q) = q^{-0.3}$. We used -0.3 as this is a mid-range value of the stars we are interested in (Duchêne and Kraus, 2013). The secondary star was then created with mass $m_2 = q \times m_1$ where m_1 is the mass of the primary star. The age, metallicity, distance and extinction of the secondary star was taken to be the same as that of the primary.

5.3.1.7 Padova isochrones: magnitudes, T_{eff} and $\log g$

To obtain absolute magnitudes we used a set of Padova isochrones with different metallicities. In order to aquire a Padova isochrone with a certain metallicity, the heavy mass fraction Z must be specified. Our set of isochrones span $0.0005 \leq Z \leq 0.0264$, with $Z_\odot = 0.0152$ (Bressan et al., 2012, as used in the Padova models). This corresponds to $-1.5 \leq$ [Fe/H] $\leq +0.2$ in steps of 0.1. The Z matching a given [Fe/H] was obtained using an online X,Y,Z calculator[1], selecting

---

[1] http://astro.wsu.edu/cgi-bin/XYZ.pl

the Grevesse and Sauval (1998) abundances since their $Z_\odot$ was the closest to the Bressan et al. (2012) value.

For each object (single, primary and secondary), we select the isochrone with closest metallicity to the object, and then interpolate on this isochrone using the mass and age of the star to get corresponding absolute r, i and $H\alpha$ magnitudes, and $T_{\rm eff}$ and $\log g$ values. The interpolation is 'nearest', to ensure a realistic (physical) combination of parameters is selected. The Padova isochrones also provide a 'stage' flag, catagorising each star into one of the following stages[2]:

- stage 0 = PMS, pre main sequence
- stage 1 = MS, main sequence
- stage 2 = SGB, subgiant branch, or Hertzsprung gap for more intermediate+massive stars
- stage 3 = RGB, red giant branch, or the quick stage of red giant for intermediate+massive stars
- stage 4 = CHEB, core He-burning for low mass stars, or the very initial stage of CHeB for intermediate+massive stars
- stage 5 = still CHEB, the bluward part of the Cepheid loop of intermediate+massive stars
- stage 6 = still CHEB, the redward part of the Cepheid loop of intermediate+massive stars
- stage 7 = EAGB, the early asymptotic giant branch, or a quick stage of red giant for massive stars
- stage 8 = TPAGB, the thermally pulsing asymptotic giant branch

For simplicity, we group the stages into pre-MS (stage 0), MS (stage 1), and post-MS (stages 2-8). Figure 5.13 shows the amount of pre-MS stars, MS stars, and post-MS stars for all simulated stars (top) and the A and F samples overlayed (bottom). Of all simulated stars, 80% are MS, 19% are post-MS and just 1% are pre-MS. Of the selected A stars, 99% are MS, and of the F selected stars, 94% are MS. The vast majority being MS is of course expected, but the overall percentage is dependent on the mass-limits - a reduced lower-mass limit would introduce more long-lived low mass stars, thereby increasing the fraction of MS stars.

---

[2] list from `http://stev.oapd.inaf.it/cmd_3.1/faq.html`

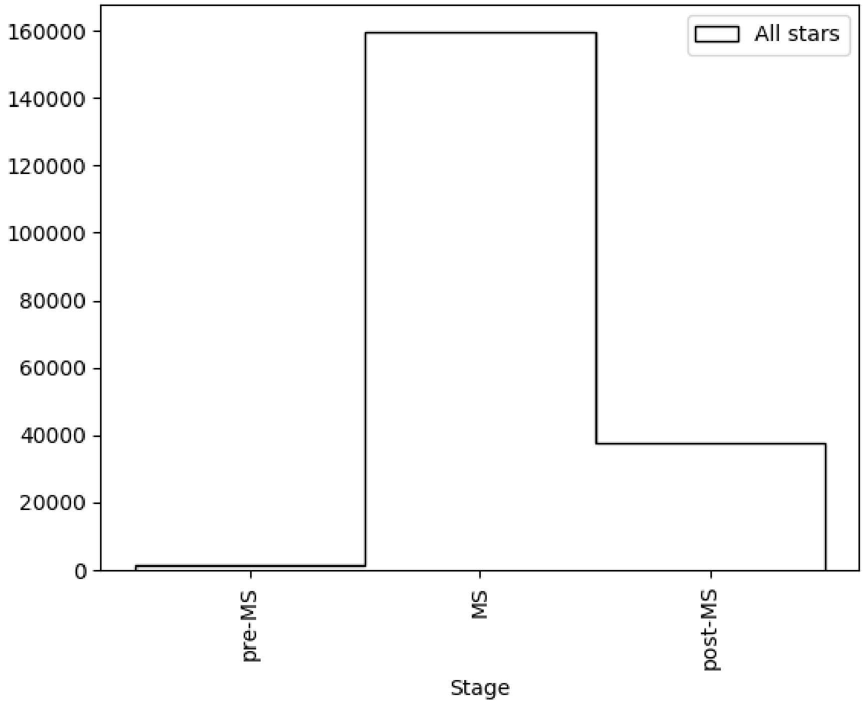

FIGURE 5.13: *The distribution of simulated stars that are pre-MS, MS and post-MS.*

Absolute magnitudes, M, were computed for single stars and for the binaries, as if unresolved. For binary systems the total absolute magnitude of the system, M_{tot}, was computed for each photometric band using the following equations:

$$\frac{L_{tot}}{L_{\odot}} = \frac{L_1}{L_{\odot}} + \frac{L_2}{L_{\odot}} = 10^{\frac{M_{\odot}-M_1}{2.5}} + 10^{\frac{M_{\odot}-M_2}{2.5}} \tag{5.6}$$

$$M_{tot} = M_{\odot} - 2.5\log_{10}\left(\frac{L_{tot}}{L_{\odot}}\right) \tag{5.7}$$

where $\mathrm{M}_{\odot}$ is the absolute magnitude of the Sun, which is $\simeq 4.4$ in r, 4.1 in i, and 4.2 in H_{α}. For single stars, we simply set $L_2 = 0$ to get its absolute magnitude. We then compute the total apparent magnitudes, m_{app}, using

$$m_{app} = M_{tot} + 5\log_{10}(d) - 5 \tag{5.8}$$

where d is the heliocentric distance in parsecs.

Errors on the apparent magnitudes were computed using an exponential function fit to IPHAS data following the formality of Robin et al. (2003):

$$\sigma(m_{app}) = A + \exp(Cm_{app} - B) \tag{5.9}$$

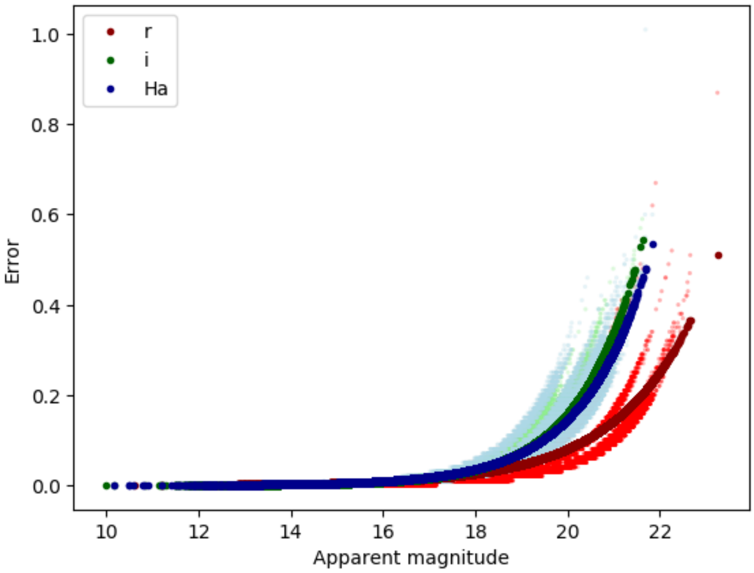

FIGURE 5.14: *Photometric error function in different bands (darker curves), fit to IPHAS data (lighter data points) at $\ell = 118^\circ$. The corresponding figure for $\ell = 178^\circ$ is very similar.*

The function is fit on IPHAS data seperately for each band r, i, $H\alpha$ (see Figure 5.14). Robin et al. (2003) state this form is typical of CCD photometric errors. The 'measured' apparent magnitude is then randomly selected from a normal distribution with mean m_{app} and standard deviation taken from the fit above. We noted that the Padova $r - H\alpha$ colour, which should be 0 for A0 stars, is systematically too low by ~ 0.02, so this is corrected for using a simple shift.

Since our metallicity grid is discrete, we briefly quantify the impact of this on the resulting parameters. For example if a 1 Gyr old star of 1.6 $M_\odot$ (i.e. a late-A star) had [Fe/H] $= -0.15$, the interpolated values using the isochrones with [Fe/H] $= -0.1$, compared to those with [Fe/H] $= -0.2$, are shown in Table 5.4. The difference between the two interpolated magnitudes is < 0.1 mag in all three bands, while the difference in resulting $r - i$ and $r - H\alpha$ colours is only 0.02 and 0.03. The interpolated $\log T_{\rm eff}$ values are different by 0.02, corresponding to a $T_{\rm eff}$ difference of 358 K, and the $\log g$ values differ by just 0.01. Hence the interpolated values for a star with [Fe/H] $= -0.15$ are satisfactorily close to what would be the true value that lies somewhere between the neighbouring grid points.

	[Fe/H]	
	−0.1	−0.2
r	2.19	2.10
i	2.05	1.99
$H\alpha$	2.13	2.06
$\log T_{\text{eff}}$	3.88	3.90
$\log g$	4.17	4.18

TABLE 5.4: *The r, i, $H\alpha$, $\log T_{\text{eff}}$, and $\log g$ values for a 1 Gyr old A star of 1.6 $M_{\odot}$, interpolated on Padova isochrones with* [Fe/H] of −0.1 and −0.2.

5.3.2 Simulation results

5.3.2.1 Selection process

With apparent magnitudes determined for each star/system, the $r-i$, $r-H\alpha$ diagram could be constructed and the HectoSpec target selection process emulated. Firstly, for stars with $13 < r < 19$ we compare the simulated colour-colour diagram with that of IPHAS data. Figure 5.15 shows these diagrams for $\ell = 118°$ (top) and $\ell = 178°$ (bottom). The simulated data are shown by the purple contours. The IPHAS data, which in a recent version have been calibrated relative to Pan-STARRS (Magnier et al., 2016), are traced by the red contours. The mismatch at the top ridge of the contours is caused by the lower mass limit of the simulation; this fills out if the limit is lowered. Overall, the contours line up nicely for both sightlines, showing the simulation is working well.

We emulate the HectoSpec A and F star selection by selecting stars in their corresponding strips in the $r-i$, $r-H\alpha$ diagram. The A stars were selected from a strip of 0.04 mag wide, located just above the early-A reddening line, and the F stars were selected from a strip 0.08 - 0.09 mag above the line. We applied a magnitude cut to select stars of similar magnitude to the HectoSpec objects. The magnitude cut was $15 < r < 19$ for $\ell = 118°$ and $14.5 < r < 19$ for $\ell = 178°$. Figure 5.16 shows the colour-colour diagrams of the simulated stars at $\ell = 118°$ and $\ell = 178°$. The blue points are simulated stars with $13 < r < 19$. The green points are the selected A stars, and the red points the F stars.

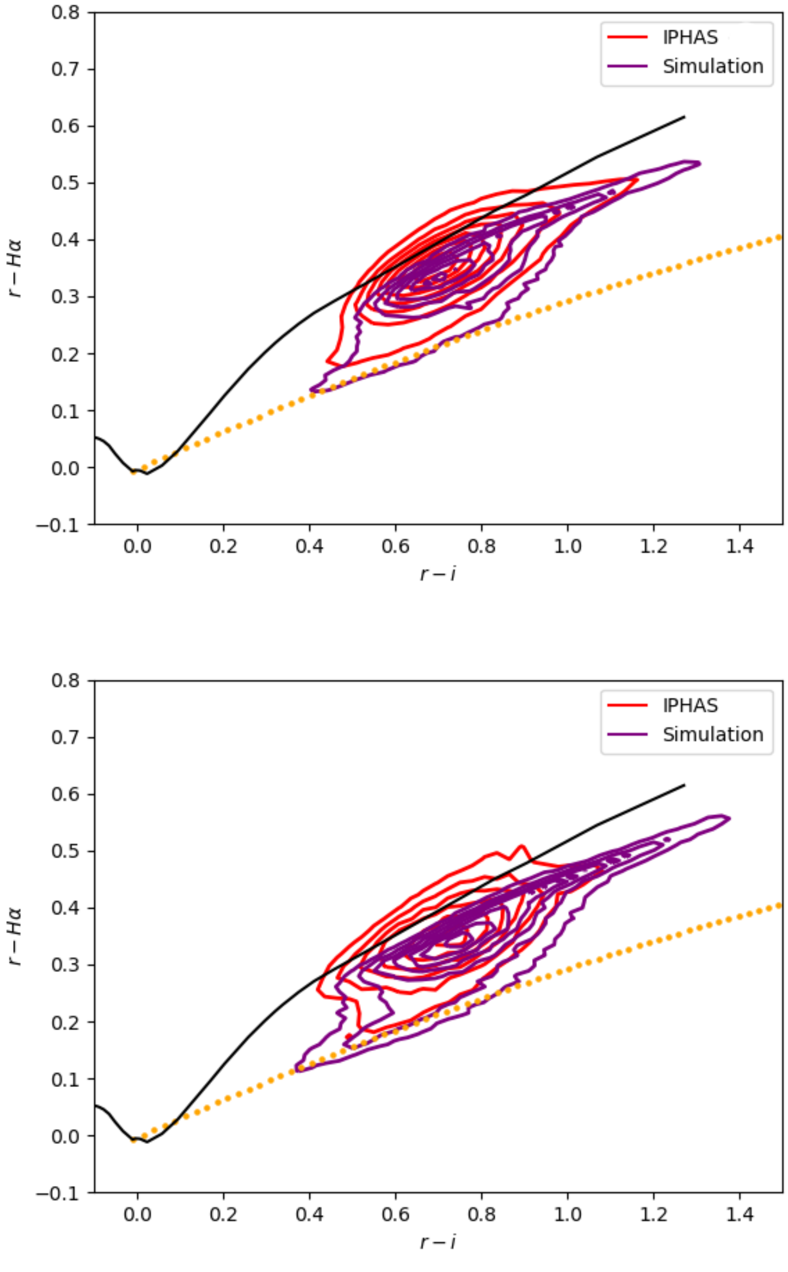

FIGURE 5.15: *$r-i$, $r-H\alpha$ colour-colour diagram for stars at $\ell = 118^\circ$ (top) and $\ell = 178^\circ$ (bottom) with $13 < r < 19$ from the simulation (purple) and IPHAS (red). The black line is the unreddened main sequence track, and the orange dotted line is the A0 reddening line.*

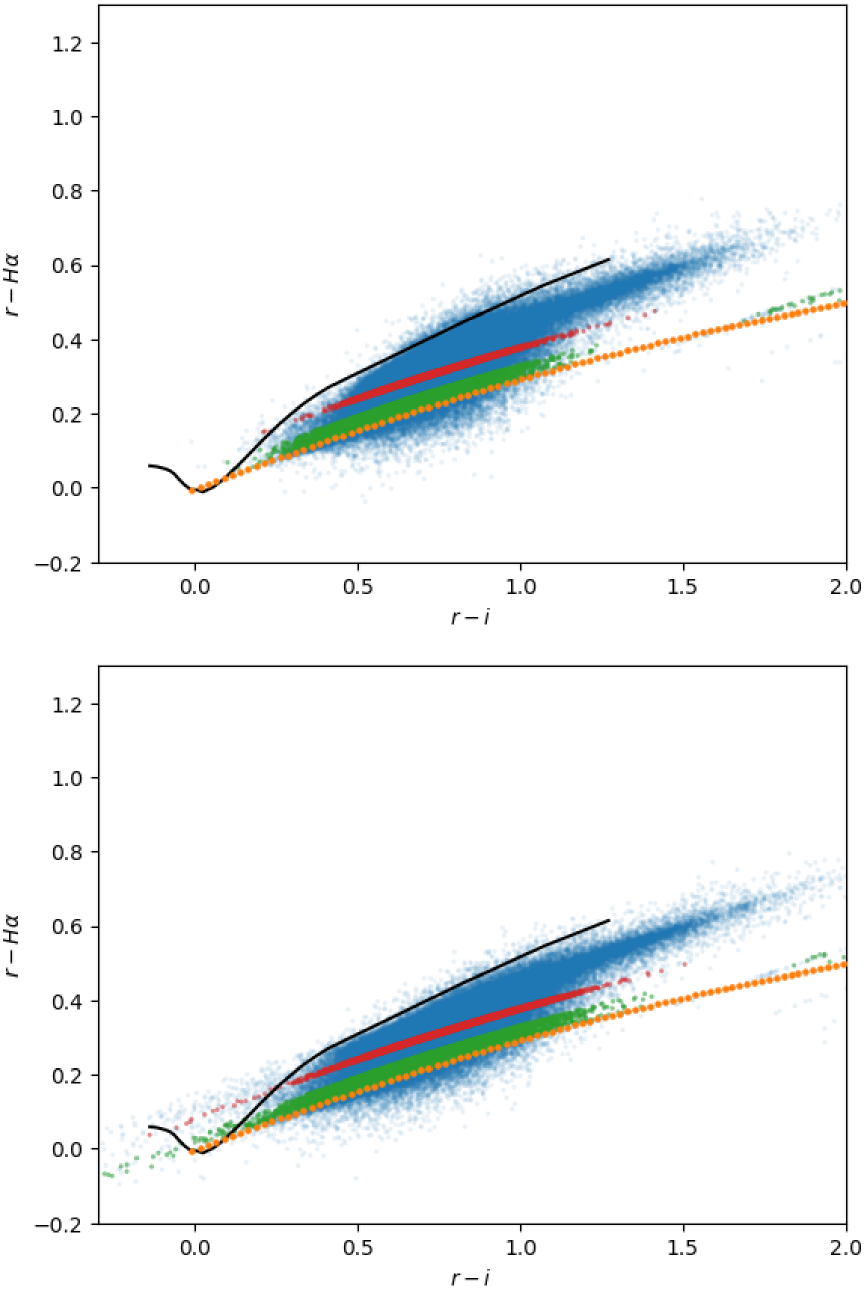

FIGURE 5.16: *$r-i$, $r-H\alpha$ colour-colour diagram for simulated stars at $\ell = 118^\circ$ (top) and $\ell = 178^\circ$ (bottom) with $13 < r < 19$ (blue points). The black line is the unreddened main sequence track, and the orange dotted line is the A0 reddening line. A stars (green points) are selected from a strip 0.04 wide above the A0 reddening line. F stars (red points) are selected from a narrower strip between 0.08 and 0.09 mag above the A0 redenning line. The selected A and F samples have a magnitude cut applied to emulate the HectoSpec samples, see text for details.*

5.3.2.2 Stellar parameters

5.3.2.3 Comparison with HectoSpec results

In order to directly compare the results of our Galactic simulation to those of the HectoSpec data, we first incorporated measurement error in the simulated physical parameters. The level of measurement error in each parameter of interest was taken as a typical value from the HectoSpec results. These were:

- $T_{\rm eff}$: $\sigma = 150\,\rm K$
- $\log g$: $\sigma = 0.14$ for $T_{\rm eff} \leq 7500\,\rm K$, $\sigma = 0.09$ for $T_{\rm eff} > 7500\,\rm K$
- absolute magnitudes: $\sigma = 0.3$
- Extinction, A_i: $\sigma = 0.05$

The 'measured' values of the parameters were randomly selected from a normal distribution with mean the 'true' simulated value and dispersion given by the σ listed above.

We took 1000 random samples of the simulated A and F stars which were selected from the strips in the $r-i$, $r-H\alpha$ diagram. The sample size was the same as the HectoSpec sample size in the specific sightline in question, with the same relative percentage of A ($\sim$ 60%) and F ($\sim$ 40%) stars. To emulate the HectoSpec apparent magnitude distribution, we binned the HectoSpec r magnitude distribution and selected the simulated stars with probability proportional to these bins. Figure 5.17 shows the r distributions at $\ell = 118^\circ$ (top) and $\ell = 178^\circ$ (bottom). The blue histogram is the mean distribution of the 1000 samples of simulated data, with black error bars representing the spread of the samples. The red histogram shows the distribution of the final HectoSpec sample. We see that the r distribution of our samples of simulated data exactly emulates that of the HectoSpec data.

We compare the $T_{\rm eff}$ distributions of selected A stars at $\ell = 118^\circ$ and $\ell = 178^\circ$ in Figure 5.18. For both sightlines, the peaks of the distributions are roughly aligned at $\sim 8000\,\rm K$, although the simulated data indicates a slightly larger spread in $T_{\rm eff}$ is expected from the selection process. A potential explanation for the discrepancy is we have overestimated our apparent magnitude errors or $T_{\rm eff}$ measurement errors in the simulation. If we consider stars with $T_{\rm eff} > 10000\,\rm K$ as B-type stars, the simulated data implies we expect the selected A star sample to consist of

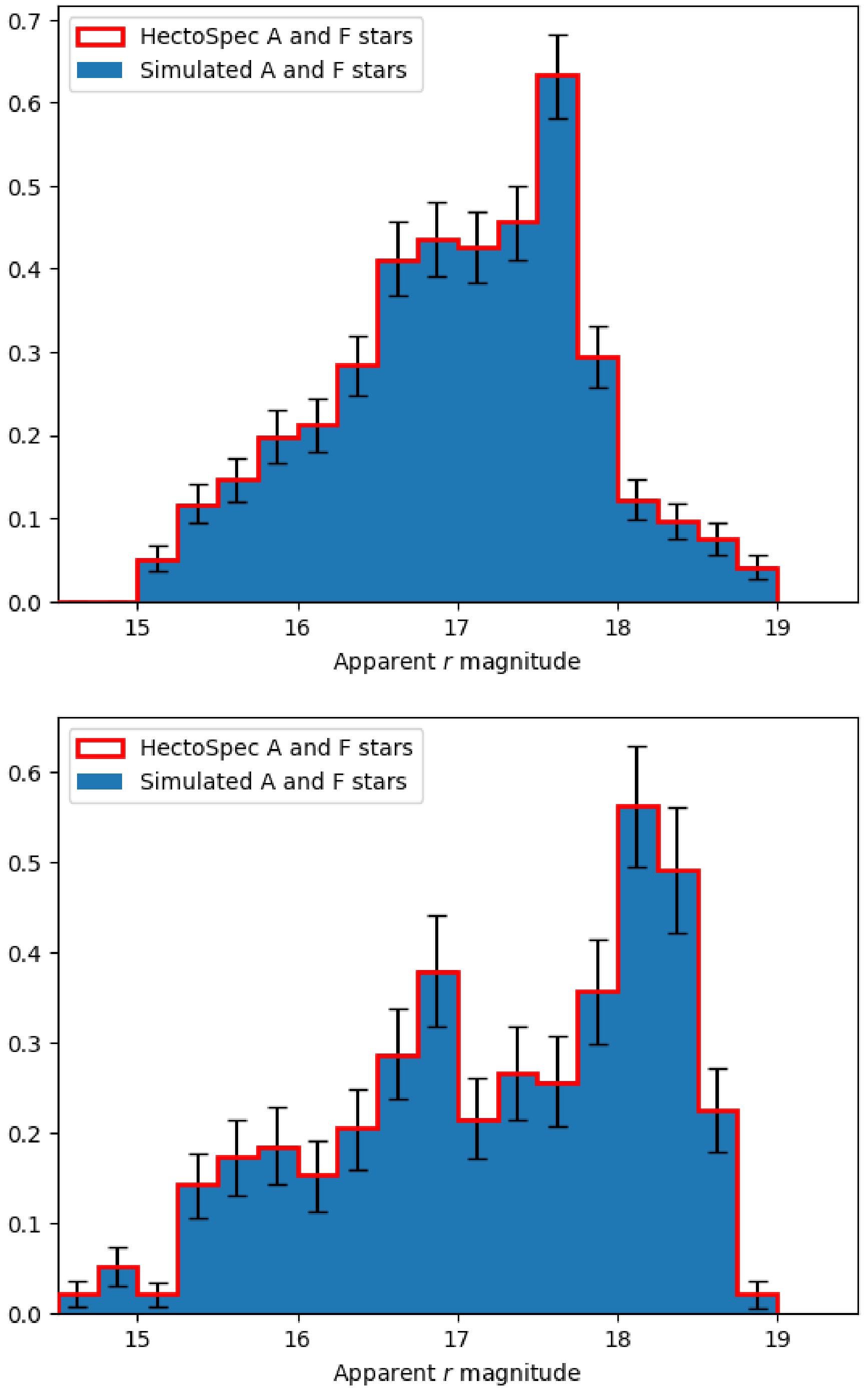

FIGURE 5.17: *The distribution of apparent r magnitudes at $\ell = 118^\circ$ (top) and $\ell = 178^\circ$ (bottom). The blue histogram is the mean distribution of the samples of simulated data, with black error bars representing the spread of the samples. The red histogram is that of the final HectoSpec sample.*

$\sim 19\%$ B stars. Similarly, $\sim 13\%$ of the selected A star sample have $T_{\rm eff} < 7500\,$K, i.e. F stars or later. Of the HectoSpec selected A star sample, only 6% are hotter than 10000 K, and 13% cooler than 7500 K. Since our imposed count cut preferentially selects objects with lower extinction, some of the more distant B stars with larger extinction may have been removed, potentially reducing the measured contamination of B stars in our HectoSpec sample compared to the simulation. The measured amount of contamination of F stars in the selected A stars matches the simulation.

The $T_{\rm eff}$ distributions of the selected F star samples are shown in Figure 5.19. In both sightlines, there is clearly an offset between the peaks of the simulated and HectoSpec data. The simulation suggests the measured $T_{\rm eff}$ distribution should be systematically cooler than the HectoSpec measurements by $\sim 1000\,$K. Since we used the same $r-i$, $r-H\alpha$ strips in both the simulation and HectoSpec data, it is possible the offset is caused by a photometric issue with the original IPHAS data that was available at the time of the HectoSpec selection. On the other hand, there could be an offset in the Padova magnitudes which are used in the simulated data. We have already mentioned the Padova $r-H\alpha$ colour is systematically too low by $\sim 0.02\,$mags, and so a small misalignment in the $r-i$, $r-H\alpha$ diagram would not be a surprise. Such a clear shift in HectoSpec vs simulated $T_{\rm eff}$ distribution is not observed for the A stars. This is perhaps due to the A star selection strip being located at the bottom of the $r-i$, $r-H\alpha$ diagram. The stars below this line are most likely early-A stars with larger photometric uncertainty. The amount of stars below the line quickly diminishes, potentially offering an explanation for the smaller spread of the HectoSpec A star $T_{\rm eff}$ distribution compared to the simulated distribution.

Of the simulated F star selection, $\sim 4\%$ are objects with $T_{\rm eff} < 6000\,$K, i.e. G-type stars, and $\sim 10\%$ are A-type with $T_{\rm eff} > 7500\,$K. The contamination levels of our HectoSpec F sample is 4% G stars and 18% A stars. The larger percentage of A star contamination may be again due to a small photometric issue with the IPHAS data or the simulated data.

Figures 5.20 and 5.21 show the distributions of extinction in the i band of the A and F stars respectively. In the A star distributions, we see evidence of our HectoSpec extinction distribution being lower than random sampling delivers. We have seen evidence of a bias to lower extinctions previously in Section 3.3, when comparing the HectoSpec A_i trends with mean extinction trends from Sale et al. (2014). This bias is due to our imposed > 2000 count cut preferentially selecting lower typical values for the A stars. The F stars were relatively unaffected, which is

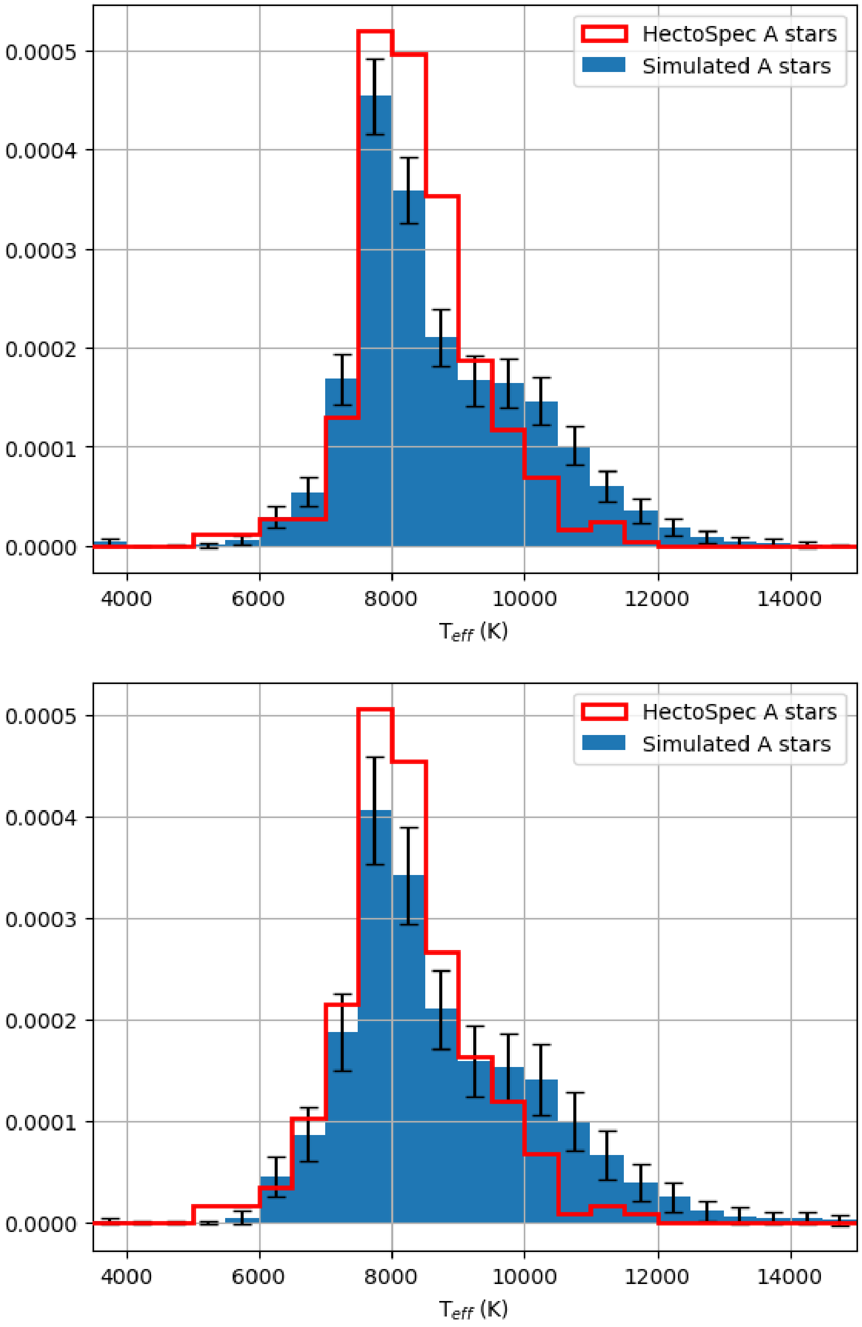

FIGURE 5.18: *The $T_{\rm eff}$ distributions of selected A stars at $\ell = 118°$ (top) and $\ell = 178°$ (bottom). The blue histogram is the mean distribution of the samples of simulated data, with black error bars representing the spread of the samples. The red histogram is that of the final HectoSpec sample.*

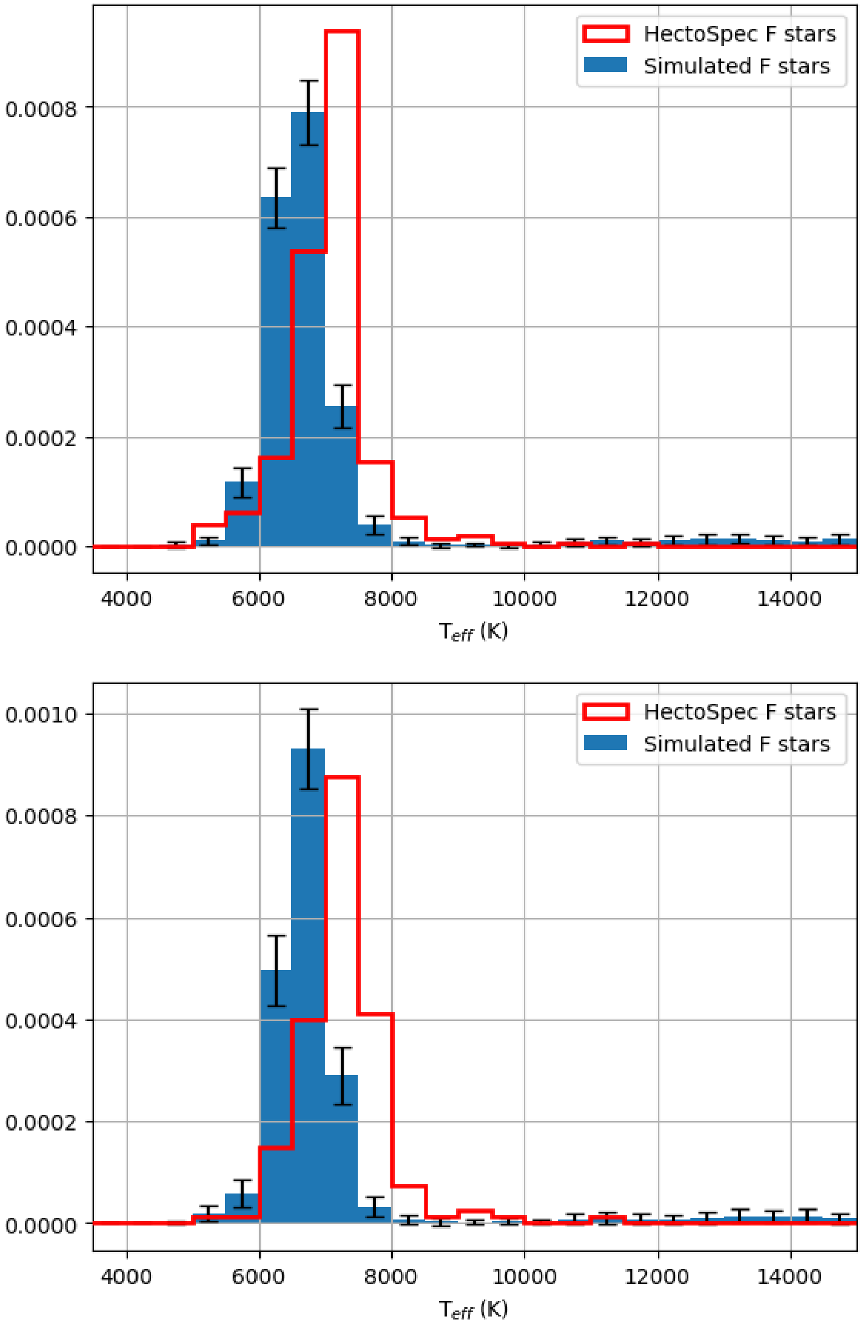

FIGURE 5.19: *The T_{eff} distributions of selected F stars at $\ell = 118^\circ$ (top) and $\ell = 178^\circ$ (bottom). The blue histogram is the mean distribution of the samples of simulated data, with black error bars representing the spread of the samples. The red histogram is that of the final HectoSpec sample.*

again supported by our comparison with the simulation, where the peaks of the distributions are roughly aligned.

The distributions of heliocentric distance of the A and F star samples combined are shown in Figure 5.22. The simulated distributions shown assume binary systems are indeed unresolved binaries, i.e. the absolute magnitude used is appropriate. In both sightlines the HectoSpec spectro-photometric distance distribution matches well with the expectation from the simulation. In fact, a K-S test determined the distance distribution of the HectoSpec sample and the simulated distance distribution may have been drawn from the same underlying distribution at a 95% confidence limit in $\sim 75\%$ of the randomised samples at $\ell = 118^\circ$, and $\sim 86\%$ at $\ell = 178^\circ$.

Next, we compare the distributions of heliocentric distance of the A and F star samples, where the simulated distance assumes the object is a single star, even if it is actually a binary. See Figure 5.23. This treatment is the same as we use for the HectoSpec sample. Again, in both sightlines the HectoSpec spectro-photometric distance distribution matches well with the expectation from the simulation. In this case, a K-S test determined the HectoSpec and simulated distance distributions may have been drawn from the same underlying distribution at a 95% confidence limit in $\sim 97\%$ of the randomised samples at $\ell = 178^\circ$. At $\ell = 118^\circ$, the two distance distributions were deemed to be drawn from different underlying distributions. Considering the differences between the HectoSpec measurements and the simulation, for example the skewed HectoSpec $\log g$ distribution, the bias to low extinctions due to the count cut, and potentially a small photometric offset, the measured spread of distances are satisfactorily similar to those simulated.

We quantify the impact of the treatment of binaries on the measured distance scale by comparing the simulated distance distribution that treats binaries as single stars to the distance distribution that treats them as unresolved binaries. The median difference between the two distance measurements of the objects is just 0.01 kpc for the A stars, and less than that for the F stars. The mean difference is 0.26 kpc for the A stars and 0.16 kpc for the F stars. These stated values are specifically for the binary fraction and mass ratio distribution used in our Galaxy model, which in general are not well known. Nonetheless, this implies our treatment of all stars in the HectoSpec sample as single stars does not have a strong impact on our results.

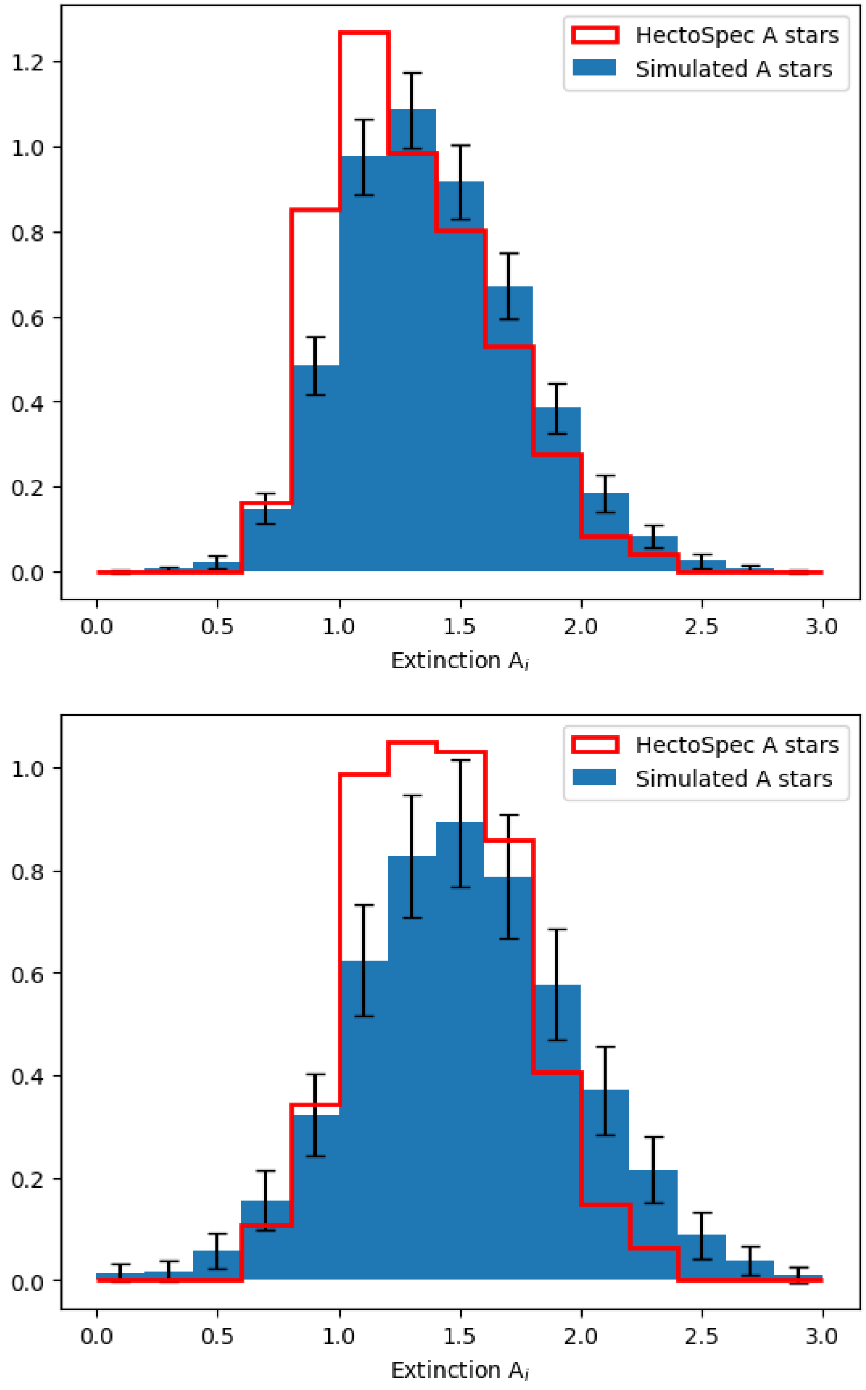

FIGURE 5.20: *The A_i distributions of selected A stars at $\ell = 118°$ (top) and $\ell = 178°$ (bottom). The blue histogram is the mean distribution of the samples of simulated data, with black error bars representing the spread of the samples. The red histogram is that of the final HectoSpec sample.*

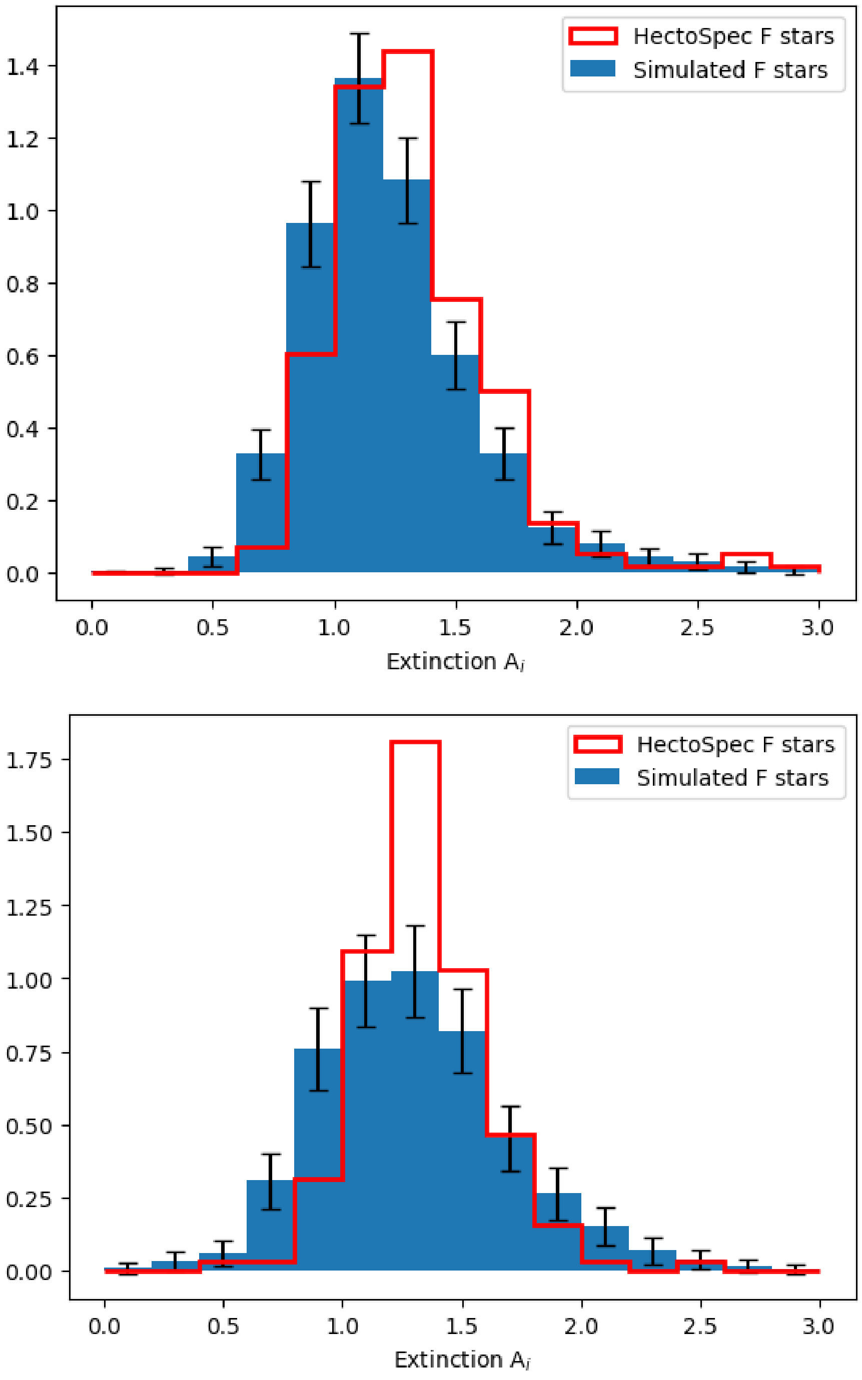

FIGURE 5.21: *The A_i distributions of selected F stars at $\ell = 118^\circ$ (top) and $\ell = 178^\circ$ (bottom). The blue histogram is the mean distribution of the samples of simulated data, with black error bars representing the spread of the samples. The red histogram is that of the final HectoSpec sample.*

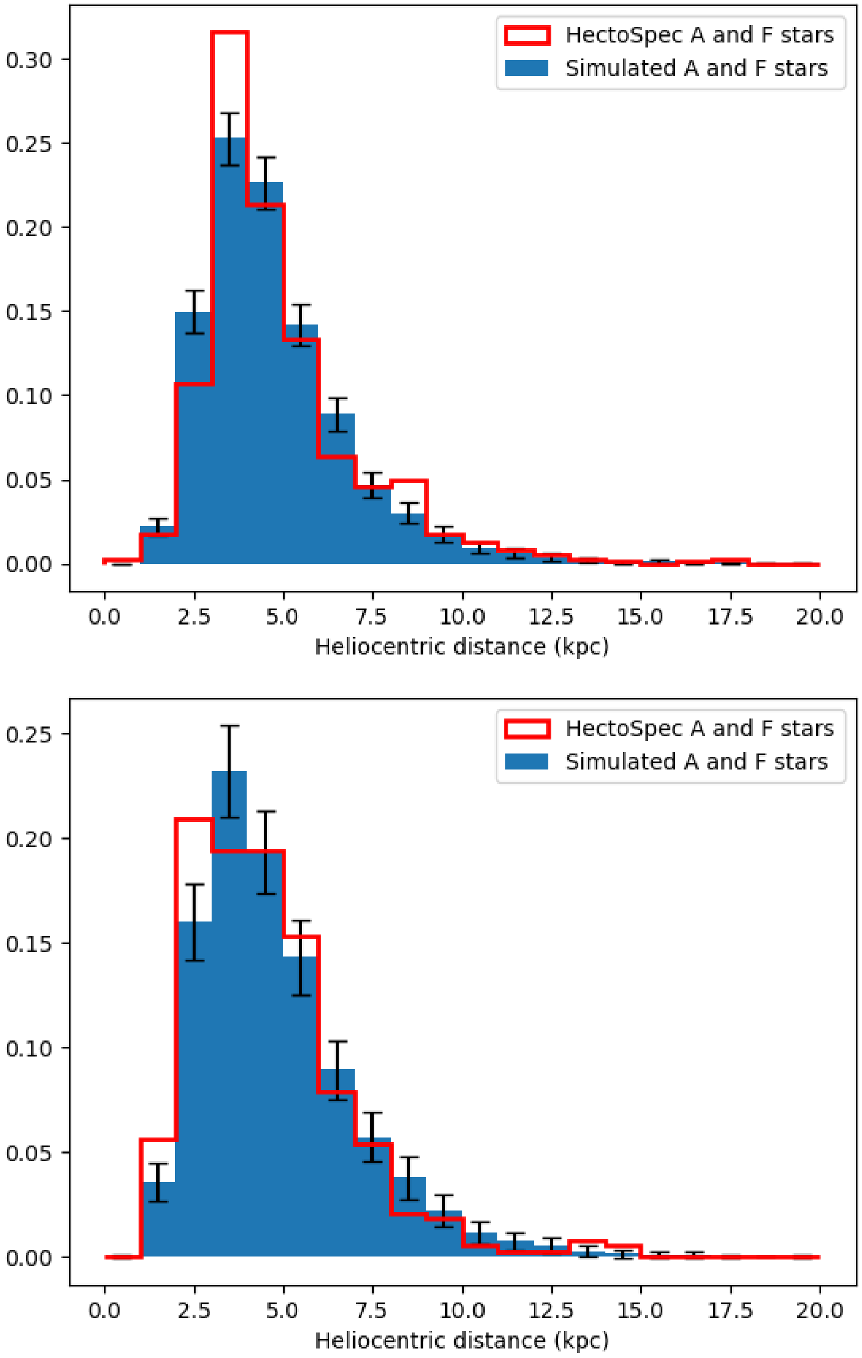

FIGURE 5.22: *The heliocentric distance distributions of selected A and F stars at* $\ell = 118°$ *(top) and* $\ell = 178°$ *(bottom). The simulated distribution assumes the binary systems are indeed unresolved binaries. The blue histogram is the mean distribution of the samples of simulated data, with black error bars representing the spread of the samples. The red histogram is that of the final HectoSpec sample.*

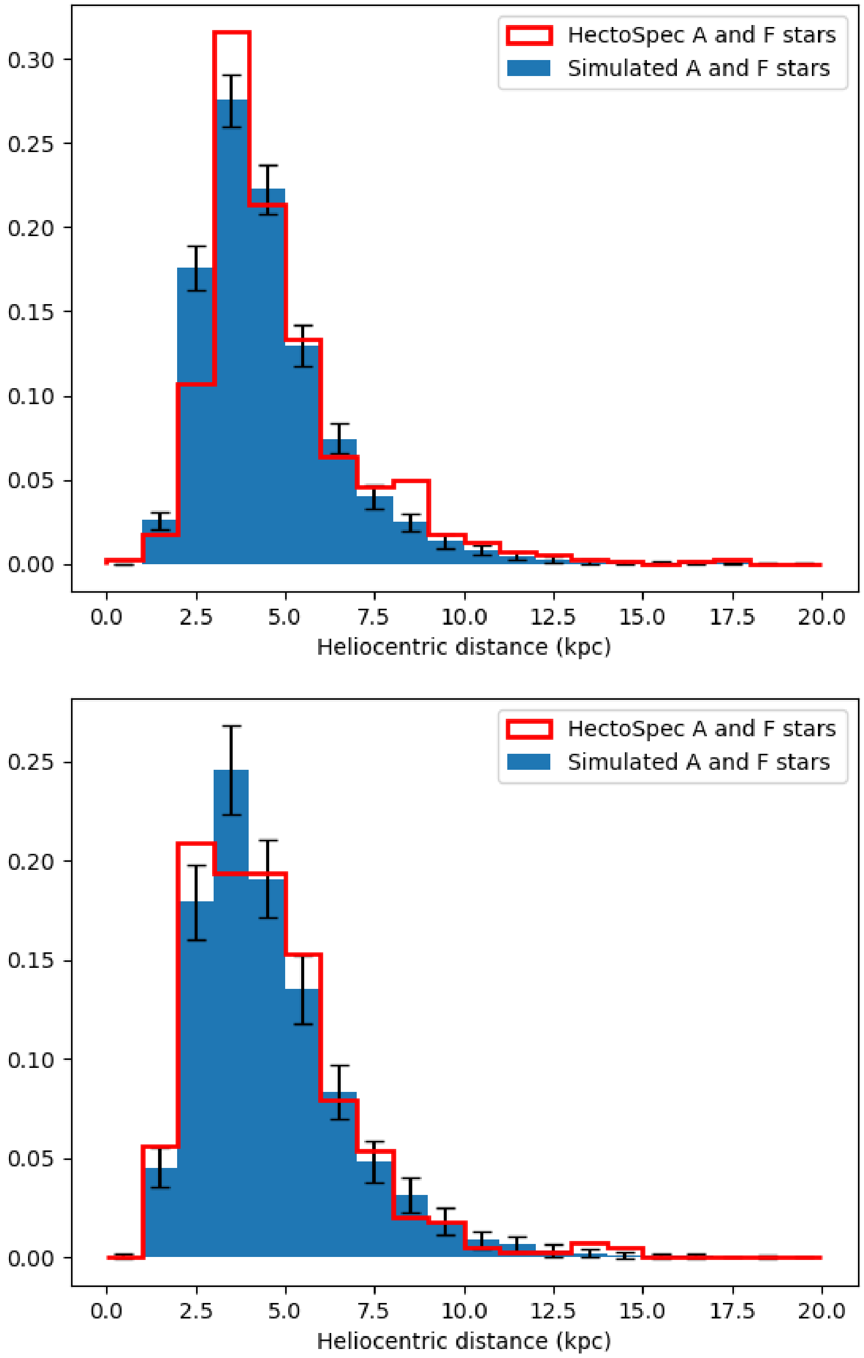

FIGURE 5.23: *The heliocentric distance distributions of selected A and F stars at* $\ell = 118^\circ$ *(top) and* $\ell = 178^\circ$ *(bottom). The simulated distribution treats binary systems as single stars – the same treatment as used for the HectoSpec sample. The blue histogram is the mean distribution of the samples of simulated data, with black error bars representing the spread of the samples. The red histogram is that of the final HectoSpec sample.*

5.3.2.4 Conclusions on simulations

The comparison of our measured stellar parameters, extinctions, and distances with those expected from a Galactic model has provided us with no unpleasant surprises. The levels of contamination that we simulate are generally in line with those that we measure. We see further evidence of our imposed count cut impacting the A star extinctions, causing a slight bias of our HectoSpec extinctions to lower values compared to the simulation. Despite this, the simulated distance distributions closely match our observed distributions, and our treatment of the HectoSpec sample as single stars is confirmed as not modifying the inferred kinematics (Chapter 4) in a significant way.

Chapter 6

Outer disk kinematics incorporating Gaia proper motions

6.1 Gaia DR2: parallaxes and proper motions

Gaia is a European Space Agency (ESA) space observatory that scans the sky to reveal the 3D distribution and measure space motions of stars down to 20th magnitude. Launched in 2013, Gaia has observed over 1 billion stars located in the Milky Way and beyond. Along with astrometry, Gaia also provides photometry in three passbands (G, G_{BP} and G_{RP}), and spectroscopy in order to obtain radial velocities and astrophysical parameters of objects down to 17th magnitude. The end-of-mission measurement precision for a G2V star with $G = 15$ is $\sim 26\,\mu$as for parallaxes and $\sim 14\,\mu\mathrm{as\,yr^{-1}}$ for proper motions.

The second data release, DR2, was made available on the 25th April 2018 (Gaia Collaboration et al., 2018a, 2016). This release provides the five-parameter astrometric solution (positions, parallaxes and proper motions) and photometry for more than 1.3 billion sources, along with radial velocities for over 7.2 million stars with $4 < G < 13$. However, for the faint distant stars that populate the outer disk, the radial velocity and parallax data are not good enough for use in kinematic studies. For example, Kawata et al. (2018) used $> 10^6$ stars from Gaia DR2 to study the azimuthal and vertical velocity field out to Galactocentric radius $R_G < 12\,\mathrm{kpc}$ in the anticentre direction, but the lack of radial velocity information and large parallax uncertainties for the fainter more distant stars prevented them from delving further into the outer disk (see also Gaia Collaboration et al., 2018b). This lack of adequate DR2 parallax and radial velocity data also rings true for our HectoSpec sample, which we go on to show below.

We have crossmatched our HectoSpec sample of A and F stars with the Gaia DR2 database, finding matches for all 780[1] stars in the $\ell = 118^\circ$ sightline, and all 393 in the $\ell = 178^\circ$ sightline. We applied two quality cuts according to the suggestions of Lindegren et al. (2018). These are:

- A quality cut depending on the unit weight error, u_L, of the Gaia data, which is a goodness-of-fit statistic on the model used to determine the astrometric parameters, given by

  $$u_L = \sqrt{\frac{astrometric\_chi2\_al}{astrometric\_n\_good\_obs\_al - N}} \tag{6.1}$$

  where $astrometric\_chi2\_al$ is the astrometric goodness-of-fit in the along-scan (AL) direction, $astrometric\_n\_good\_obs\_al$ is the number of good AL observations of the source used in the astrometric solution, and $N = 5$ is the number of astrometric parameters. We remove objects from the sample that have $u_L > 1.2 \times \max(1, \exp(-0.2(G - 19.5)))$, where G is the magnitude in the Gaia G band. This quality cut results in 23 objects being removed from the $\ell = 118^\circ$ sample, and 6 from the $\ell = 178^\circ$ sample.
- A cut based on the number of 'visibility periods used' of the Gaia data, indicating an astronometrically well-observed source. We remove objects with < 8 visibility periods. This affects no objects at $\ell = 118^\circ$. A further 2 objects are removed from the $\ell = 178^\circ$ sample.

Additionally, we limit our analysis to objects with spectro-photometric distance no larger than 10 kpc. There are few objects with distances beyond this, reaching out to ~ 20 kpc. These very large distances are unrealistic for our sample, and we deem them unreliable measurements. This results in the removal of just 27 more objects from the $\ell = 118^\circ$ sample, and 10 from the $\ell = 178^\circ$ sample. The final sample size is then 730 stars at $\ell = 118^\circ$ and 375 at $\ell = 178^\circ$, for which we have Gaia DR2 parallaxes and proper motions. Since our HectoSpec objects have $14 \lesssim i \lesssim 18$, corresponding to $15 \lesssim G \lesssim 19$, Gaia DR2 radial velocity data is not available for our sample.

The measurement uncertainty on Gaia DR2 parallaxes for our sample ranges from ~ 0.04 mas for the brightest objects to ~ 0.3 mas for the faintest. The majority have an uncertainty around

---

[1] In the previous Chapters, we stated there are 790 stars in the $\ell = 118^\circ$ sightline, however it since became apparent that 10 of these were infact duplicate observations, and we henceforth remove these from the analysis.

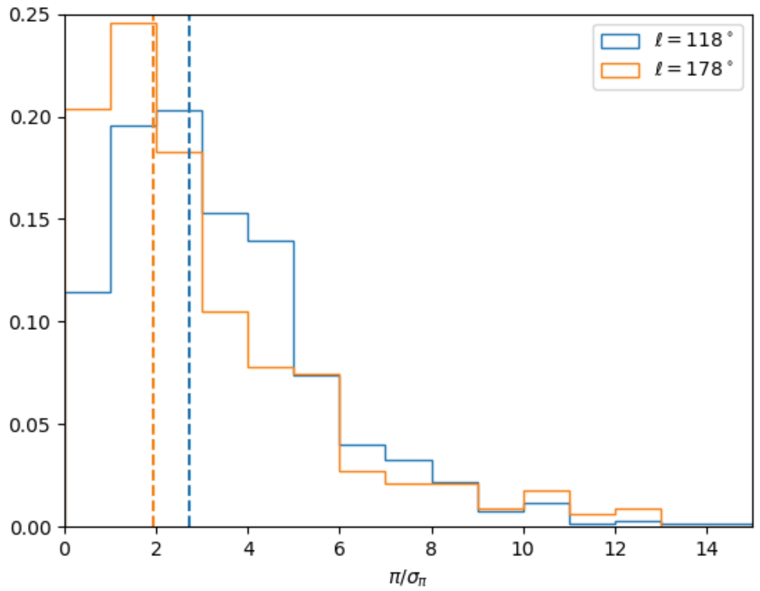

FIGURE 6.1: *Distribution of the Gaia DR2 parallax divided by parallax error for our HectoSpec sample. The dashed vertical lines represent the median detection level for the corresponding sightline:* 2.7σ *for* $\ell = 118^\circ$ *and* 1.9σ *for* $\ell = 178^\circ$.

0.1 mas. Over the distance range sampled (2-10 kpc, or a parallax range of 0.5-0.1 mas) these uncertainties are significant, amounting to percentage uncertainties of $\sim 20-100\%$, or equivalently, detections of $< 5\sigma$ (see Figure 6.1). The conversion of a parallax measurement with uncertainty to a distance measurement with uncertainty is not straight forward. It is an inference problem that can result in large asymmetric distance uncertainties, especially if the parallax detection is less than 5σ, as we indeed have here (Bailer-Jones, 2015). This is not true of our spectro-photometric distance errors, which are relatively small (median of 13%) and symmetric. Additionally, Gaia DR2 parallaxes carry systematic errors of up to 0.1 mas on global scales, with actual magnitude and distribution of the errors unknown (Lindegren et al., 2018).

For the aforementioned reasons, it is not obvious that Gaia DR2 parallax information would provide any improvement to our spectro-photometric distance scale. To check this, we have made comparisons with an alternative distance scale based on the Gaia DR2 parallaxes. Bailer-Jones et al. (2018) (hereafter BJ18) infer a distance scale using an exponentially decreasing space density prior. Their length scale varies with (ℓ, b) according to a model that reflects the expected distribution of stellar distances in the Galaxy as observed by Gaia. The median length scale used for the $\ell = 118^\circ$ objects is 1280 pc, and for the $\ell = 178^\circ$ objects is 1257 kpc.

Figure 6.2 compares the HectoSpec spectro-photometric distance scale with that from BJ18. We

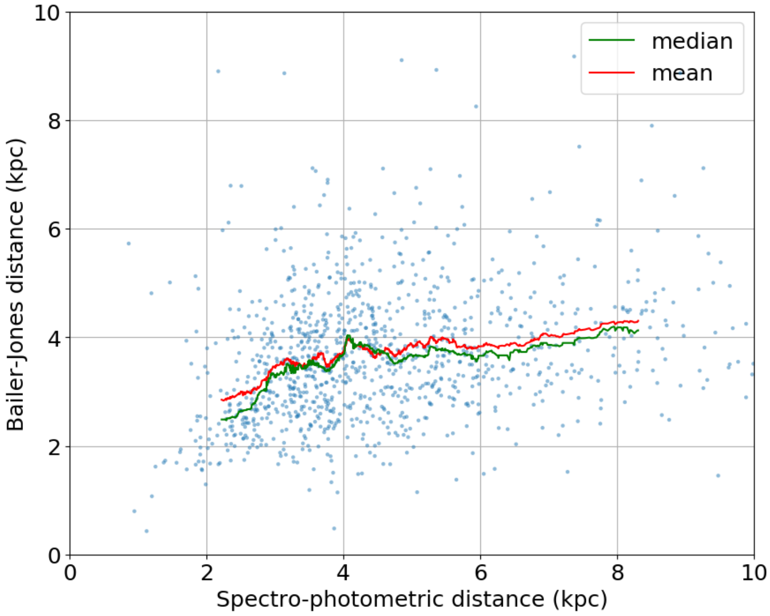

FIGURE 6.2: *A comparison of the HectoSpec spectro-photometric distances with the Bailer-Jones et al. (2018) distances. The green line is the running median and red line the running mean.*

see that at ≥ 4 kpc the BJ18 distances become significantly smaller than our spectro-photometric distances. This is signalling that at distances of $3-4$ kpc the parallax measurements are becoming sufficiently imprecise that the prior in the parallax inversion takes over. In fact, BJ18 state that for parallax precisions of better than 20% the prior has little impact on the resulting distance, giving rise to the data-dominated regime. For parallax precisions worse than this, we venture into the prior-dominated regime, which is where the majority of our HectoSpec sample reside. We conclude it is not appropriate to rely on Gaia DR2 parallax-based distance scales to probe further out than a few kpc from the Solar neighbourhood. Hogg et al. (2018) support this view, instead making use of the APOGEE–Gaia–2MASS–WISE overlap to train a model to predict parallaxes from spectro-photometric data of red giant-branch stars out to heliocentric distances of 20 kpc, without the use of a prior.

Our spectro-photometric scale does not depend on a distance-related prior, and hence does not carry an associated bias. This is particularly important, for example, in kinematic studies that depend so heavily on a reliable systematic-free distance scale. Hence continued use of our spectro-photometric distance scale is warranted as it is free of the aforementioned systematic errors, benefits from relatively small, symmetric uncertainties, and most importantly can be trusted out to distances beyond those that can be inferred from Gaia DR2 parallaxes.

Where Gaia DR2 does benefit us, though, is in its proper motions. Figures 6.3 and 6.4 show

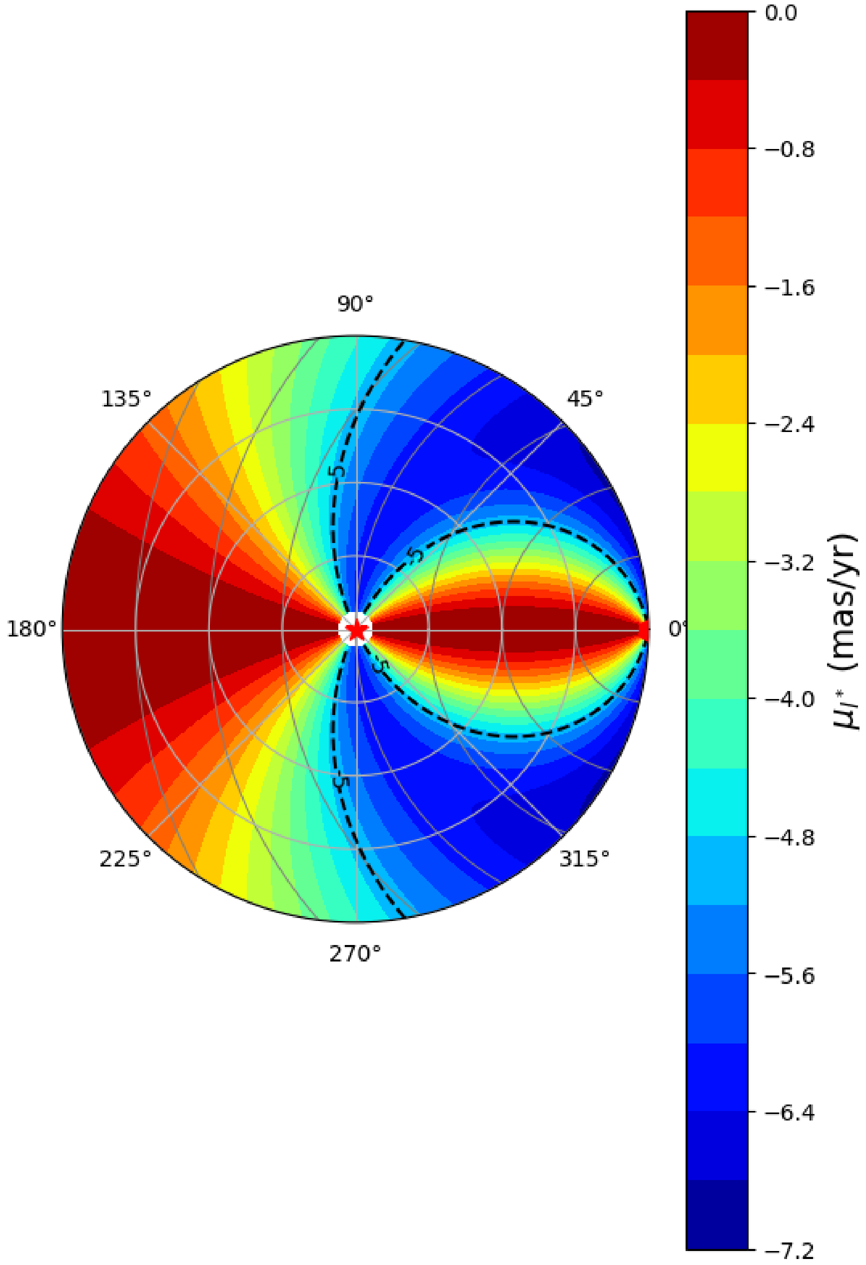

FIGURE 6.3: *Proper motion μ_ℓ^* contour plot in the Galactic plane ($b = 0°$), with respect to the LSR, calculated using $R_0 = 8.0$ kpc and a flat rotation curve with circular velocity of 233 km s^{-1}. The plot is centered on the Sun (red star symbol), with the Galactic centre at 0° (red hexagon). The grey circles are at 2 kpc intervals. The μ_b component (not shown) is flat and 0 since the orbits are in the Galactic plane, and hence the total proper motion μ (also not shown) is simply the modulus of μ_ℓ^*.*

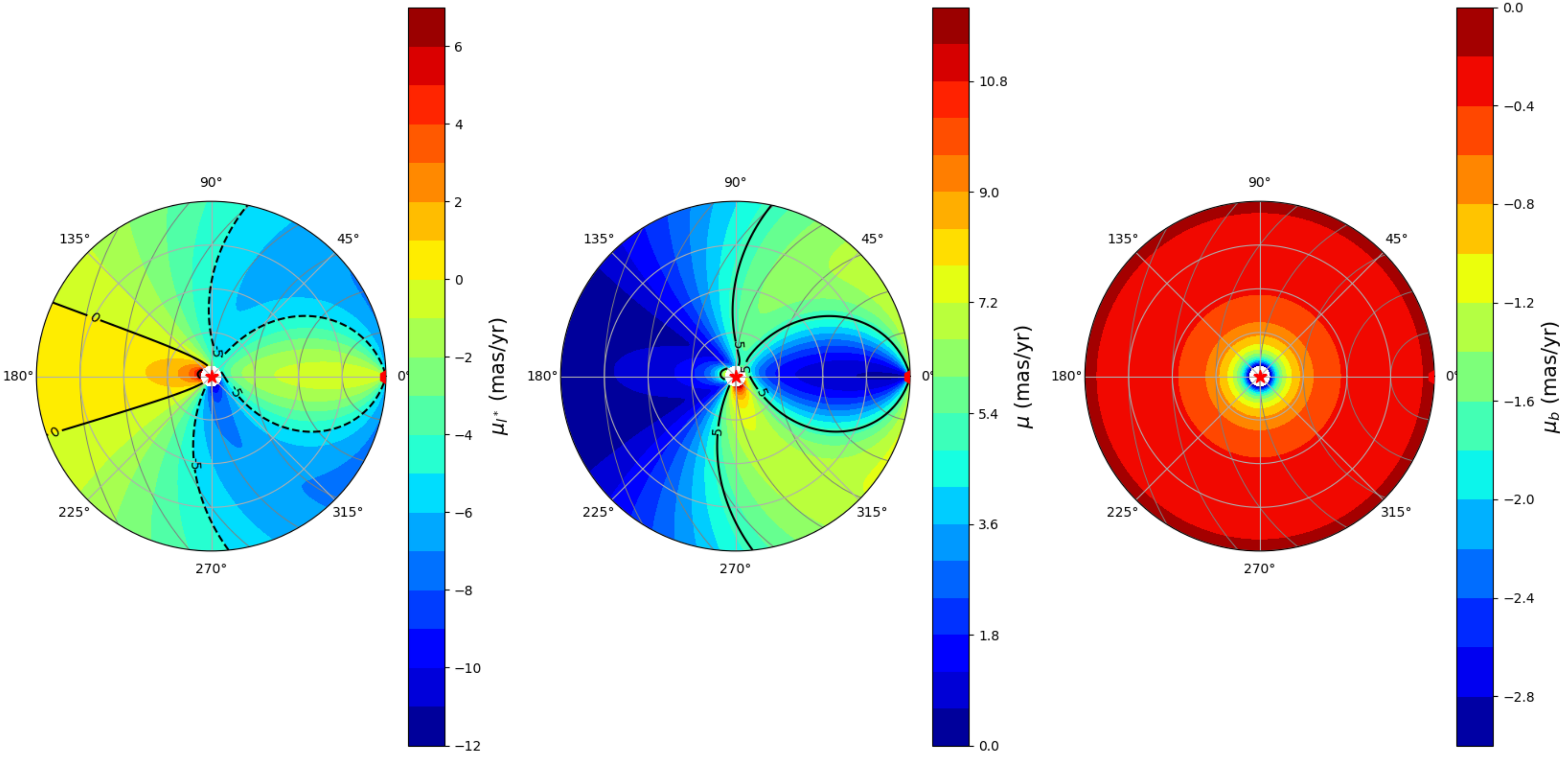

FIGURE 6.4: *Proper motion contour plots in the Galactic plane ($b = 0°$), with respect to the Sun, calculated using $R_0 = 8.0$ kpc, a flat rotation curve with circular velocity of 233 km s^{-1}, and Solar motion of (8.6, 13.9, 7.1) km s^{-1} (McMillan, 2017). The plots are centered on the Sun (red star symbol), with the Galactic centre at 0° (red hexagon). The grey circles are at 2 kpc intervals. The left panel shows $\mu_{\ell *}$, the middle shows μ, and the right shows μ_b. If the assumed Solar motion and rotation law are correct, these diagrams show how the proper motions would appear to Gaia (after conversion to Galactic coordinates) in the absense of any other random or scattered motion.*

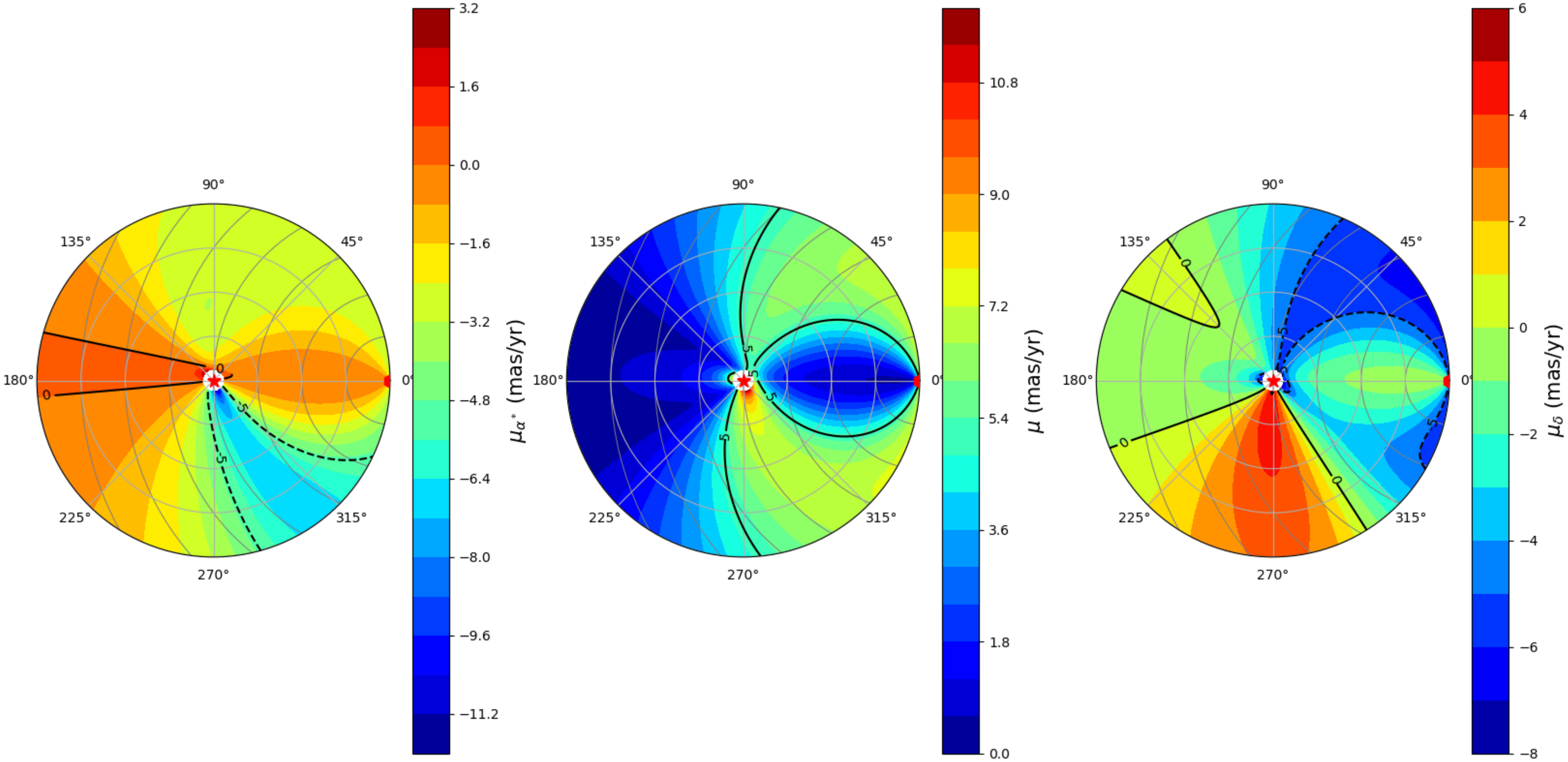

FIGURE 6.5: *Equatorial proper motion contour plots in the Galactic plane ($b = 0°$), with respect to the Sun, calculated using $R_0 = 8.0$ kpc, a flat rotation curve with circular velocity of 233 km s^{-1}, and Solar motion of (8.6, 13.9, 7.1) km s^{-1} (McMillan, 2017). The plots are centered on the Sun (red star symbol), with the Galactic centre at 0° (red hexagon). The grey circles are at 2 kpc intervals. The left panel shows μ_{α^*}, the middle shows μ, and the right shows μ_δ. If the assumed Solar motion and rotation law are correct, these diagrams show how the proper motions would appear to Gaia in the absense of any other random or scattered motion.*

expected Galactic proper motions (μ_l^*, μ_b) in the Galactic plane, in the reference frame of the LSR and in the reference frame of the Sun, respectively. Figure 6.5 shows the equatorial proper motions (μ_α^*, μ_δ) expected in the Galactic plane, with respect to the Sun. The expected proper motions are computed assuming a flat rotation curve using the values from McMillan (2017) (see the captions). We see that the scale of the equatorial proper motions expected in our outer disk sightlines, with respect to the Sun, are of the order ∼a few $\mathrm{mas\,yr^{-1}}$. Gaia DR2 provides typical random errors in μ_α^* and μ_δ of just $0.2\,\mathrm{mas\,yr^{-1}}$ for a $G = 17$ star, and hence the relative precisions are generally very good.

Figure 6.6 shows the distribution of proper motions divided by their errors. The μ_{α^*} component is shown in the top panel. The median detection levels are 16σ at $\ell = 118°$ and 3σ at $\ell = 178°$. The proper motion error is generally larger at $\ell = 178°$ because of how Gaia scans the sky – this sightline has been observed less times than the $\ell = 118°$ sightline, resulting in larger uncertainties. Additionally, μ_{α^*} component is close to zero in this sightline, making $\mu_{\alpha^*}/\sigma_{\mu_\alpha^*}$ small. The bottom panel shows the μ_δ component, with median detection levels of 6σ at $\ell = 118°$ and 7σ at $\ell = 178°$.

The proper motion components, μ_α^* and μ_δ, and their errors are shown as a function of our spectro-photometric distance in Figure 6.7. Also shown are the expected trends from Figure 6.5 in each sightline, i.e. using $R_0 = 8.0\,\mathrm{kpc}$, a flat rotation curve with circular velocity of $233\,\mathrm{km\,s^{-1}}$, and Solar motion of (8.6, 13.9, 7.1) $\mathrm{km\,s^{-1}}$ (McMillan, 2017). The $\ell = 118°$ data appears to agree well with the expected trends. This is perhaps surprising since our result in Section 4 found a rotation curve in this sightline that was sharply rising – quite different to the flat rotation law assumed here. However, the proper motion trends do not vary drastically with assumed rotation law, making it difficult to compare by eye. For example, if we adopt a rotation law similar to our sharply rising one, the main effect is that the μ_α^* trend drops to negative values more slowly, resulting in less negative values ($\sim -1\,\mathrm{mas\,yr^{-1}}$) at $< 4\,\mathrm{kpc}$.

The proper motions at $\ell = 178°$ are particularly interesting, since there appears to be an offset in both components between the measurements and expected values. The μ_{α^*} values are more positive than expected from a flat rotation law, and the μ_δ values are more negative than expected. In order to fully analyse the proper motions trends, and gauge the impact of these offsets, we combine the Gaia DR2 proper motions with our already-measured radial velocities and spectro-photometric distances to obtain full space motions. With these, we can examine the resultant Galactocentric radial, azimuthal and vertical velocity fields in our two pencil-beam

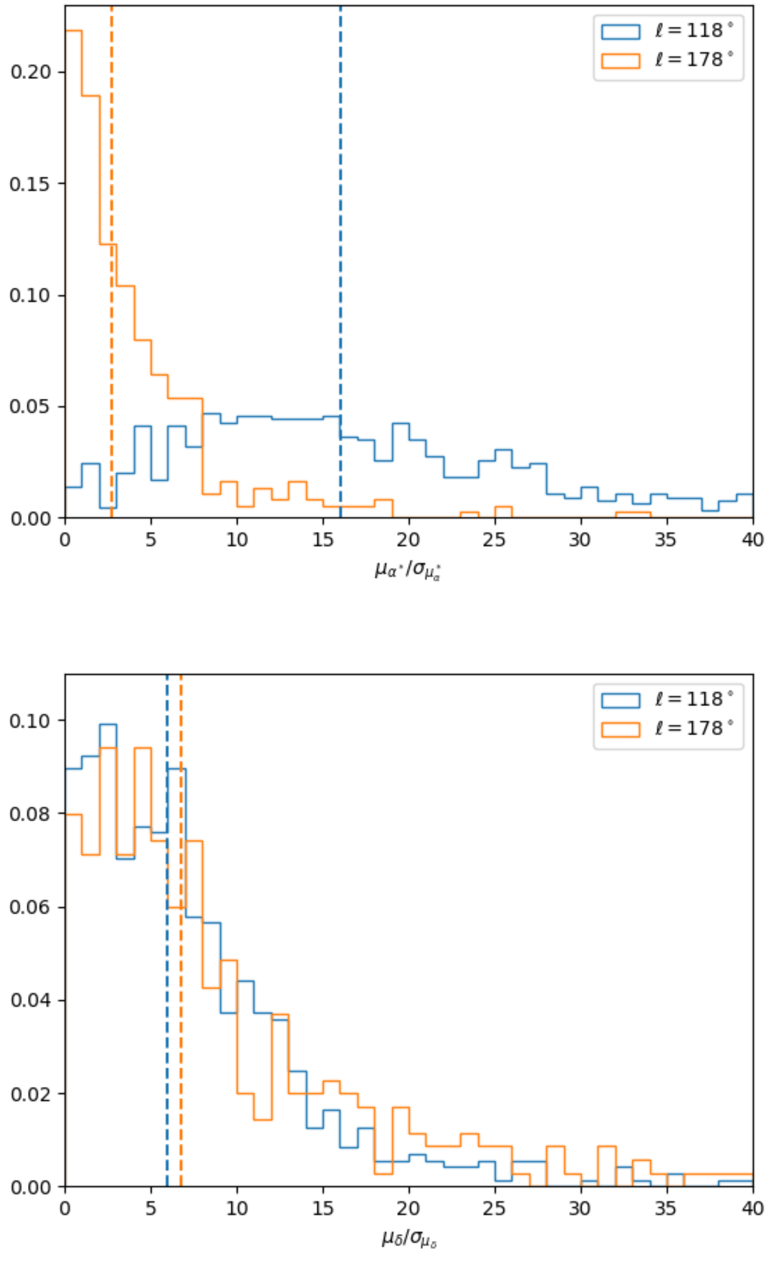

FIGURE 6.6: *Gaia DR2 proper motion divided by proper motion error for our HectoSpec sample, with the* μ_α^* *component in the top panel and* μ_δ *component in the bottom panel. The dashed vertical lines represent the median detection level for the corresponding sightline: for* μ_{α^*} *it is* 16σ *for* $\ell = 118^\circ$ *and* 3σ *for* $\ell = 178^\circ$*, and for* μ_δ *it is* 6σ *for* $\ell = 118^\circ$ *and* 7σ *for* $\ell = 178^\circ$.

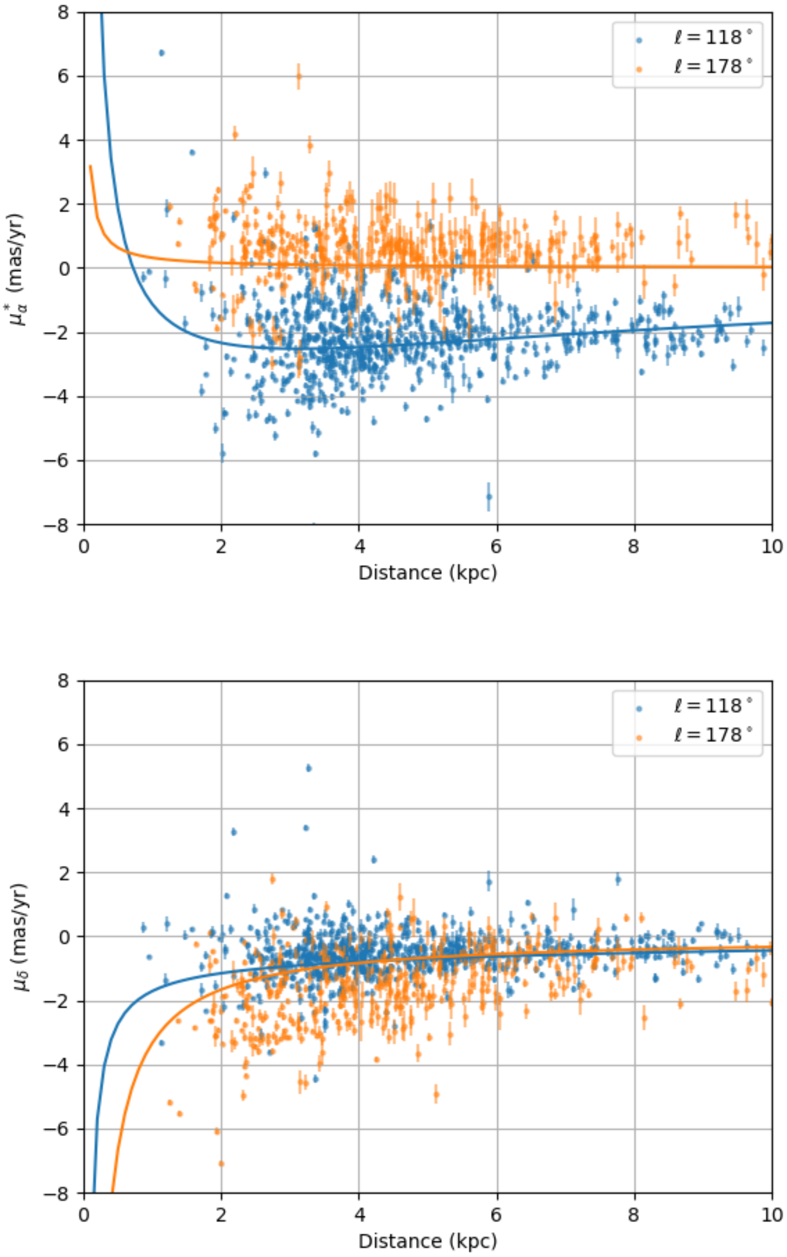

FIGURE 6.7: *Gaia DR2 proper motion components μ_α^* (top) and μ_δ (bottom) as a function of our spectro-photometric distance scale. The lines represent the expected trend in the particular sightline from Figure 6.5, i.e. using $R_0 = 8.0$ kpc, a flat rotation curve with circular velocity of 233 $\mathrm{km\,s^{-1}}$, and Solar motion of (8.6, 13.9, 7.1) $\mathrm{km\,s^{-1}}$ (McMillan, 2017).*

sightlines in the outer disk at longitudes $\ell = 118°$ and $\ell = 178°$. In particular, we can analyse the trends of the three velocity components with kinematic perturbers in mind, such as spiral arms or the central bar, to determine if we detect any signal from these and if so whether it agrees with existing expectations. We do this in Section 6.5.

6.2 Method of analysis

Having full space motions for our HectoSpec sample allows us to reframe them as Galactocentric velocities with no prior assumptions about the velocity field. In this section, we describe the method to do so, along with the coordinate systems used. See Figure 1.3 for a sketch of the Milky Way, showing the locations of our sightlines and demonstrating the angles used in the coordinate systems.

We mainly use the Galactic coordinate system defined by longitude ℓ and latitude b, with heliocentric radial velocity v_r, defined as positive if the object is moving away from the Sun, and tangential velocities v_ℓ, v_b, regarded as positive in the direction of increasing ℓ and b. The tangential velocities are derived from Gaia DR2 proper motions using,

$$v_\ell = 4.74 d \mu_{\ell^*} \tag{6.2}$$

$$v_b = 4.74 d \mu_b \tag{6.3}$$

where d is the heliocentric distance. We convert the proper motion components from equatorial α, δ to Galactic ℓ, b following Poleski (2018), using

$$\begin{bmatrix} \mu_{\ell^*} \\ \mu_b \end{bmatrix} = \begin{bmatrix} C_1 & C_2 \\ -C_2 & C_1 \end{bmatrix} \begin{bmatrix} \mu_{\alpha^*} \\ \mu_\delta \end{bmatrix} \tag{6.4}$$

where C_1 and C_2 are given by

$$C_1 = \frac{1}{\cos b}[\sin\delta_G \cos\delta - \cos\delta_G \sin\delta \cos(\alpha - \alpha_G)] \tag{6.5}$$

$$C_2 = \frac{1}{\cos b}[\cos\delta_G \sin(\alpha - \alpha_G)] \tag{6.6}$$

and $\alpha_G = 192.85948°$ and $\delta_G = 27.12825°$ are the equatorial coordinates of the North Galactic Pole (ESA, 1997). In order to transform the proper motion errors to Galactic coordinates we follow Luri et al. (2018). The variance-covariance matrix is given by

$$\mathbf{C}_{\ell^*\mathbf{b}} = \begin{bmatrix} \sigma^2_{\mu_{\ell^*}} & \rho^{\mu_b}_{\mu_{\ell^*}} \sigma_{\mu_{\ell^*}} \sigma_{\mu_b} \\ \rho^{\mu_b}_{\mu_{\ell^*}} \sigma_{\mu_{\ell^*}} \sigma_{\mu_b} & \sigma^2_{\mu_b} \end{bmatrix} = \begin{bmatrix} C_1 & C_2 \\ -C_2 & C_1 \end{bmatrix} \begin{bmatrix} \sigma^2_{\mu_{\alpha^*}} & \rho^{\mu_\delta}_{\mu_{\alpha^*}} \sigma_{\mu_{\alpha^*}} \sigma_{\mu_\delta} \\ \rho^{\mu_\delta}_{\mu_{\alpha^*}} \sigma_{\mu_{\alpha^*}} \sigma_{\mu_\delta} & \sigma^2_{\mu_\delta} \end{bmatrix} \begin{bmatrix} C_1 & -C_2 \\ C_2 & C_1 \end{bmatrix} \tag{6.7}$$

where $\rho^{\mu_\delta}_{\mu_{\alpha^*}}$ is the correlation coefficient between the equatorial proper motion measurements, and $\sigma_{\mu_{\alpha^*}}$ and σ_{μ_b} are the uncertainties in the proper motion components.

Figure 6.8 is analogous to Figure 6.7, but this time showing the Galactic proper motion components, μ^*_ℓ and μ_b, as a function of our spectro-photometric distances. The expected trends from Figure 6.4 are also shown. In the case of μ_b, the expected trends are the same for both sightlines since the orbits are confined to the Galactic plane and so they are simply representative of the Solar motion $W_\odot$. The μ_b measurements in both sightlines seem to agree with the expected trends, although there is more dispersion in the $\ell = 178^\circ$ measurements, probably due to the larger random errors. The μ^*_ℓ component at $\ell = 118^\circ$ roughly agrees with the expected trend, but as mentioned in the discussion of Figure 6.7, the expected trends do not vastly differ for alternative rotation laws, making by-eye judgement difficult. At $\ell = 178^\circ$, the μ^*_ℓ component is positively offset from the expected trend. We analyse these proper motions fully, in terms of Galactocentric velocities, in Section 6.3.

The cylindrical Galactocentric coordinate frame that we use is defined in Section 1.2. Equation 1.4 details the Galactocentric velocities (u, v, w). We calculate uncertainties on the (u, v, w) values by propagating the uncertainties on the variables (proper motion, R_G, d, Solar motion). For the Solar motion, we adopt the values of McMillan (2017): $U_\odot = 8.6 \pm 0.9\,\mathrm{km\,s^{-1}}$, $V_\odot = 13.9 \pm 1\,\mathrm{km\,s^{-1}}$, $W_\odot = 7.1 \pm 1.0\,\mathrm{km\,s^{-1}}$, $V_{g,\odot} = 247 \pm 3\,\mathrm{km\,s^{-1}}$, and distance of the Sun to the Galactic centre $R_0 = 8.20 \pm 0.09$. These values are slightly different to those we adopted in the previous Chapters: our main reason for this change is our need for a $V_{g,\odot}$ value, for which the McMillan (2017) value is recent and often used, and hence for consistency we also adopt their values for the Solar motion and distance. The analysis that follows considers the impact of a change in adopted parameters.

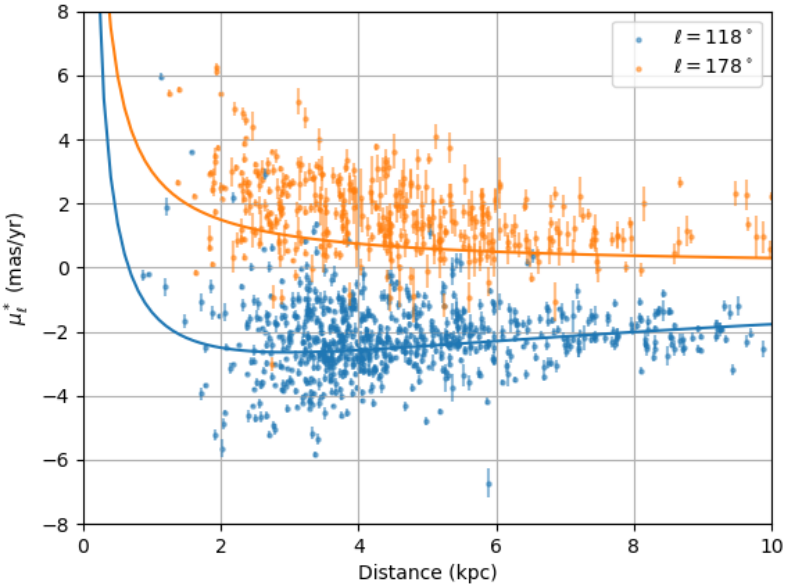

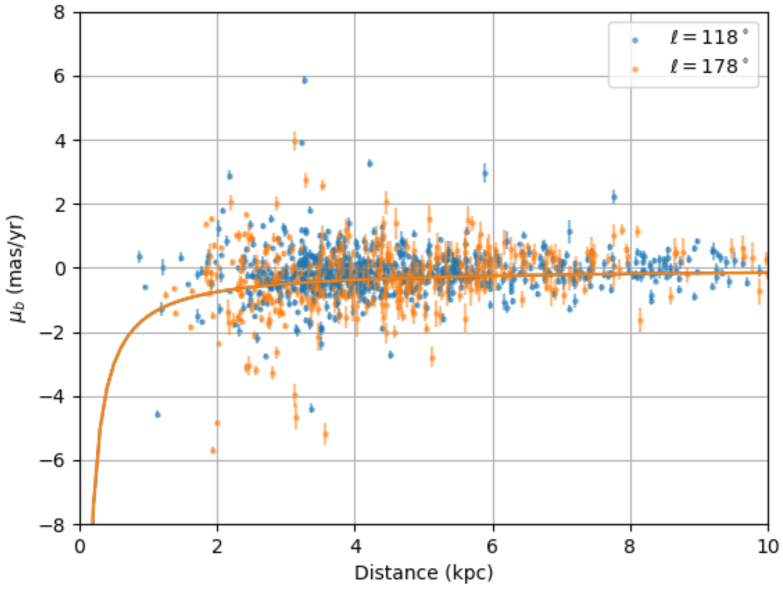

FIGURE 6.8: *Gaia DR2 proper motion components* μ_ℓ^* *(top) and* μ_b *(bottom) as a function of our spectro-photometric distance scale. The lines represent the expected trend in the particular sightline from Figure 6.4, i.e. using* $R_0 = 8.0\,\mathrm{kpc}$*, a flat rotation curve with circular velocity of* $233\,\mathrm{km\,s^{-1}}$*, and Solar motion of (8.6, 13.9, 7.1)* $\mathrm{km\,s^{-1}}$ *(McMillan, 2017).*

6.3 The Galactocentric velocity trends

In this Section and those that follow, we present the Galactocentric velocities as a function of distance, analysing the resulting trends with potential kinematic perturbers in mind. We also compare the $u-v$ diagrams of the A and F stars in order to determine if there are any intrinsic differences between the kinematics of the two stellar groups. The data used here to compute the full space motions is available through CDS[2], including positions, distances, velocities etc. of the final sample. We shall discuss each velocity component in turn, beginning with u, the radial component.

6.3.1 Radial motion

The trend of u with Galactocentric distance, $u(R_G)$, is shown in Figure 6.9 for $\ell = 178^\circ$ and Figure 6.10 for $\ell = 118^\circ$. Both sightlines show an overall negative gradient in u, determined from the weighted linear regression line (dashed line) fit to the data points, along with some wiggles in the weighted mean trend (green line, shaded to represent standard error of the mean). This negative gradient has been measured previously for the anticentre. For example, López-Corredoira and González-Fernández (2016) and Tian et al. (2017) both used clump giants located near the anticentre direction to achieve this (note that their definitions of u are opposite in sign to ours). The López-Corredoira and González-Fernández (2016) result is plotted in Figures 6.9 and 6.10 as a black dotted line, and is very similar to our result in the anticentre direction. From the line fitted to our data at $\ell = 178^\circ$, we find a gradient in Galactocentric radial velocity of $du/dR_G = -1.67 \pm 0.14\,\mathrm{km\,s^{-1}\,kpc^{-1}}$, with a zero point at $R_G(u=0) = 7.46 \pm 1.13\,\mathrm{kpc}$, to be compared with the López-Corredoira and González-Fernández (2016) result of $du/dR_G = -1.48 \pm 0.27\,\mathrm{km\,s^{-1}\,kpc^{-1}}$ and $R_G(u=0) = 8.84 \pm 0.45\,\mathrm{kpc}$. Tian et al. (2017) do not fit a linear trend but find the radial profile crosses $u = 0$ at $R_G \sim 9\,\mathrm{kpc}$ which is slightly further out than our measurement. Since the stated values depend on the adopted Solar motion which varies between studies, we have recomputed our results switching to the adopted Solar motions of these earlier works. Our results remain compatible with López-Corredoira and González-Fernández (2016), and still fall short of the $R_G \sim 9\,\mathrm{kpc}$ cross-point obtained by Tian et al. (2017).

The linear fit to the radial velocity profile at $\ell = 118^\circ$ is notably different. The measured gradient is much steeper than in the anticentre, and the $u = 0$ crosspoint is further out: we measure

---

[2] Available at `http://vizier.u-strasbg.fr/viz-bin/VizieR?-source=J/MNRAS/485/2312`

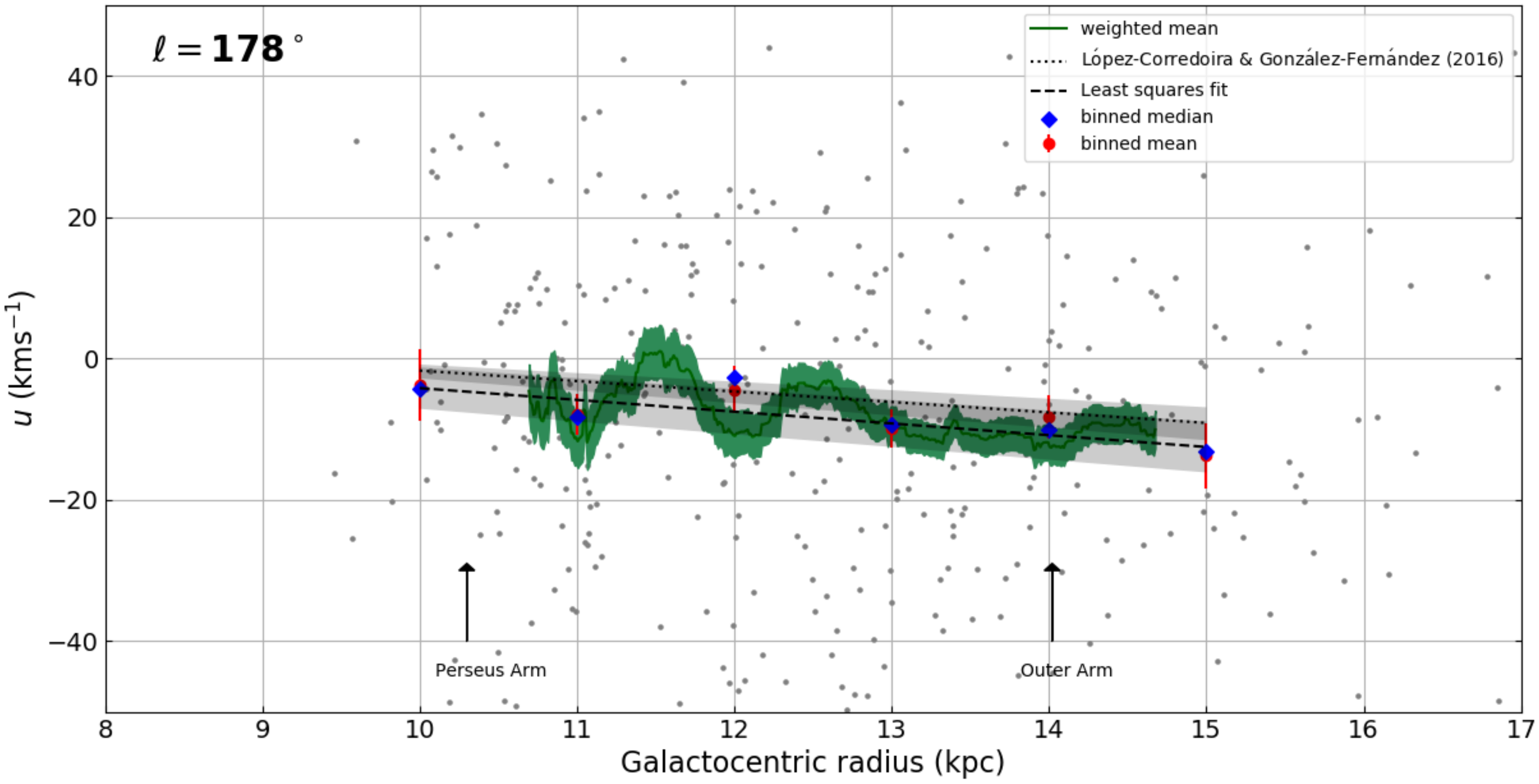

FIGURE 6.9: *The trend of u with R_G for $\ell = 178^\circ$. The green line is the weighted mean of the grey data points, and the shaded region represents the standard error of the mean. The red points are the mean u of 1 kpc bins, and the error bars are the standard error of the binned mean. The blue diamonds are the median u of 1 kpc bins. The black dashed line is a weighted linear regression line fit to the grey data points. The black dotted line is the López-Corredoira and González-Fernández (2016) result. Arrows indicate the approximate location of the Perseus and Outer Arms (Reid et al., 2014).*

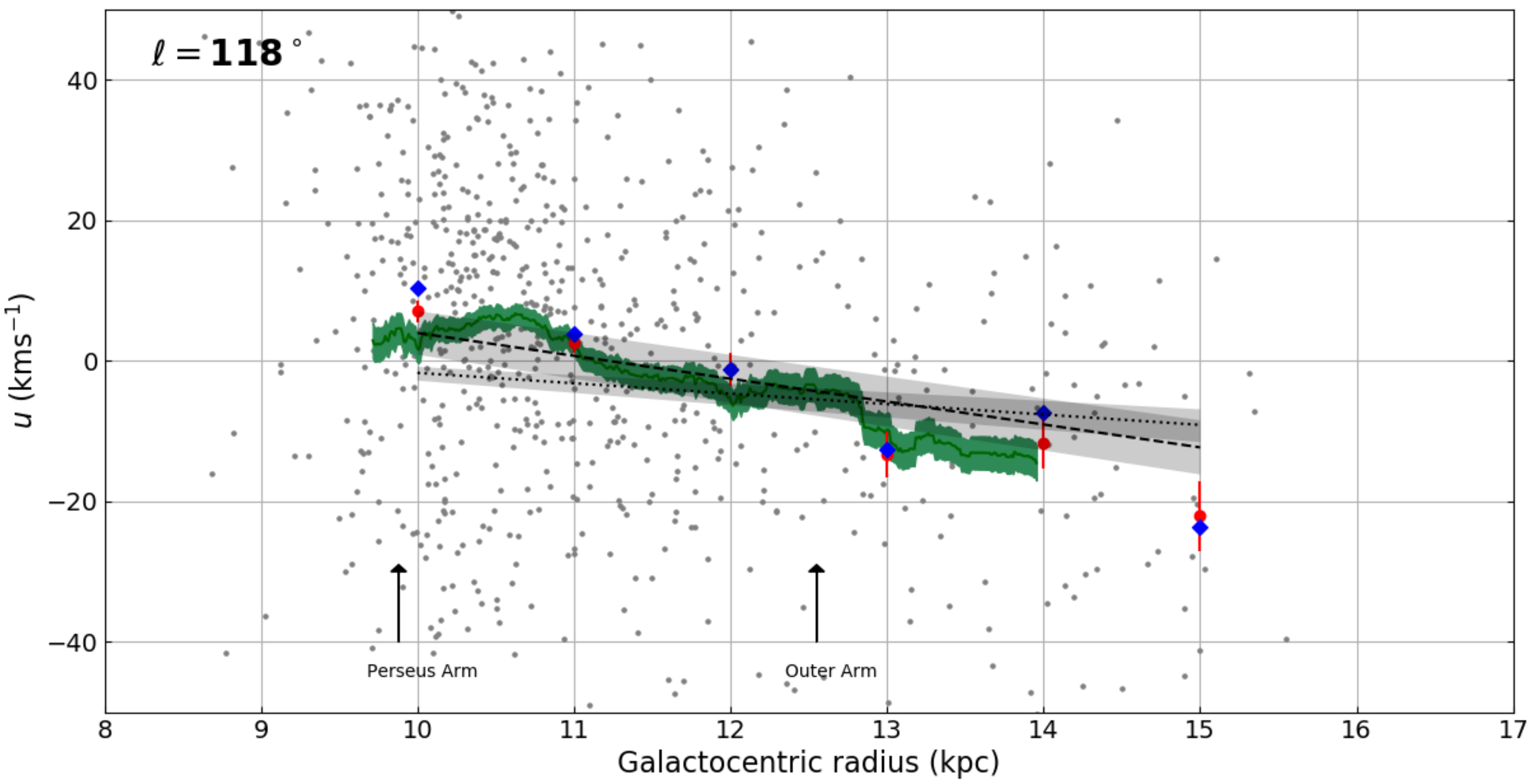

FIGURE 6.10: *The trend of u with R_G for $\ell = 118°$. The green line is the weighted mean of the grey data points, and the shaded region represents the standard error of the mean. The red points are the mean u of 1 kpc bins, and the error bars are the standard error of the binned mean. The blue diamonds are the median u of 1 kpc bins. The black dashed line is a weighted linear regression line fit to the grey data points. The black dotted line is the López-Corredoira and González-Fernández (2016) result. Arrows indicate the approximate location of the Perseus and Outer Arms (Reid et al., 2014).*

$du/dR_G = -3.25 \pm 0.15\,\mathrm{km\,s^{-1}\,kpc^{-1}}$ and $R_G(u=0) = 11.23 \pm 0.71$ kpc for the range covered. However if we move away from the idea of a linear trend and examine the mean trend directly, we notice at $\ell = 118^\circ$ the profile is almost step-like with a section of $u \sim 10\,\mathrm{km\,s^{-1}}$ for $R_G < 11$, a section of $u \sim 0$ from $11 < R_G$ (kpc) 13, and a section of $u \sim -10\,\mathrm{km\,s^{-1}}$ for $R_G > 13$ kpc.

The wiggles in the running means are likely to be due to the noise level of the data - hence why it is more noticeable in the less well-sampled $\ell = 178^\circ$ sightline. However, kinematic perturbations in the radial direction, for example linked to spiral arms and/or the bar, could be present. We explore possible explanations for the observed behaviour in the discussion (Section 6.5).

6.3.2 Azimuthal motion - the rotation curve

The rotation curve, $v(R_G)$, measured at $\ell = 178^\circ$ is shown in Figure 6.11 (green line). It is roughly flat. For our adopted Solar total azimuthal velocity $V_{g,\odot} = 247\,\mathrm{km\,s^{-1}}$, we measure a mean rotation speed over $R_G \sim 11 - 15$ kpc of $\sim 215\,\mathrm{km\,s^{-1}}$. The absolute value at which the trend lies scales directly with the assumed Solar motion, $(U_\odot,\ V_{g,\odot},\ W_\odot)^3$. For example, if we added $5\,\mathrm{km\,s^{-1}}$ to each component of our adopted Solar motion, the mean trend shifts to $\sim 222\,\mathrm{km\,s^{-1}}$. With our adopted Solar motion the trend is, more generally, $\sim 32\,\mathrm{km\,s^{-1}}$ slower than the adopted rotation speed of the Sun ($v - V_{g,\odot} = 215 - 247 = -32\,\mathrm{km\,s^{-1}}$). This is consistent with the findings of Kawata et al. (2018), who use Gaia DR2 proper motions for a very large sample ($> 10^6$) of stars located along the Galactic centre-anticentre line to determine the rotation speed. At $R_G = 10 - 12$ kpc, they measure the rotation speed to be $\sim 31\,\mathrm{km\,s^{-1}}$ slower than their assumed $V_{g,\odot}$. Our work confirms this result and almost doubles the radial range measured in the outer disk, extending to $R_G = 15$ kpc thanks to the greater reach of our spectro-photometric distance scale.

The rotation curve measured at $\ell = 118^\circ$, shown in Figure 6.12, is not the flat profile observed in the anticentre. Instead we observe a gradual increase from $\sim 222\,\mathrm{km\,s^{-1}}$ at 10.5 kpc to $242\,\mathrm{km\,s^{-1}}$ near 14 kpc - that is an increase of $\sim 20\,\mathrm{km\,s^{-1}}$ over $R_G = 10.5 - 14$ kpc.

A rising rotation law has been measured before, for example by Tian et al. (2017) who find a very similar result to our $\ell = 118^\circ$ result, except theirs is measured in the Anticentre. This is in contrast to our flat $v(R_G)$ trend measured in the anticentre. In Chapter 4 we measured

---

[3] It also scales with the assumed R_0, but this is much less significant than the effect from assumed Solar motion.

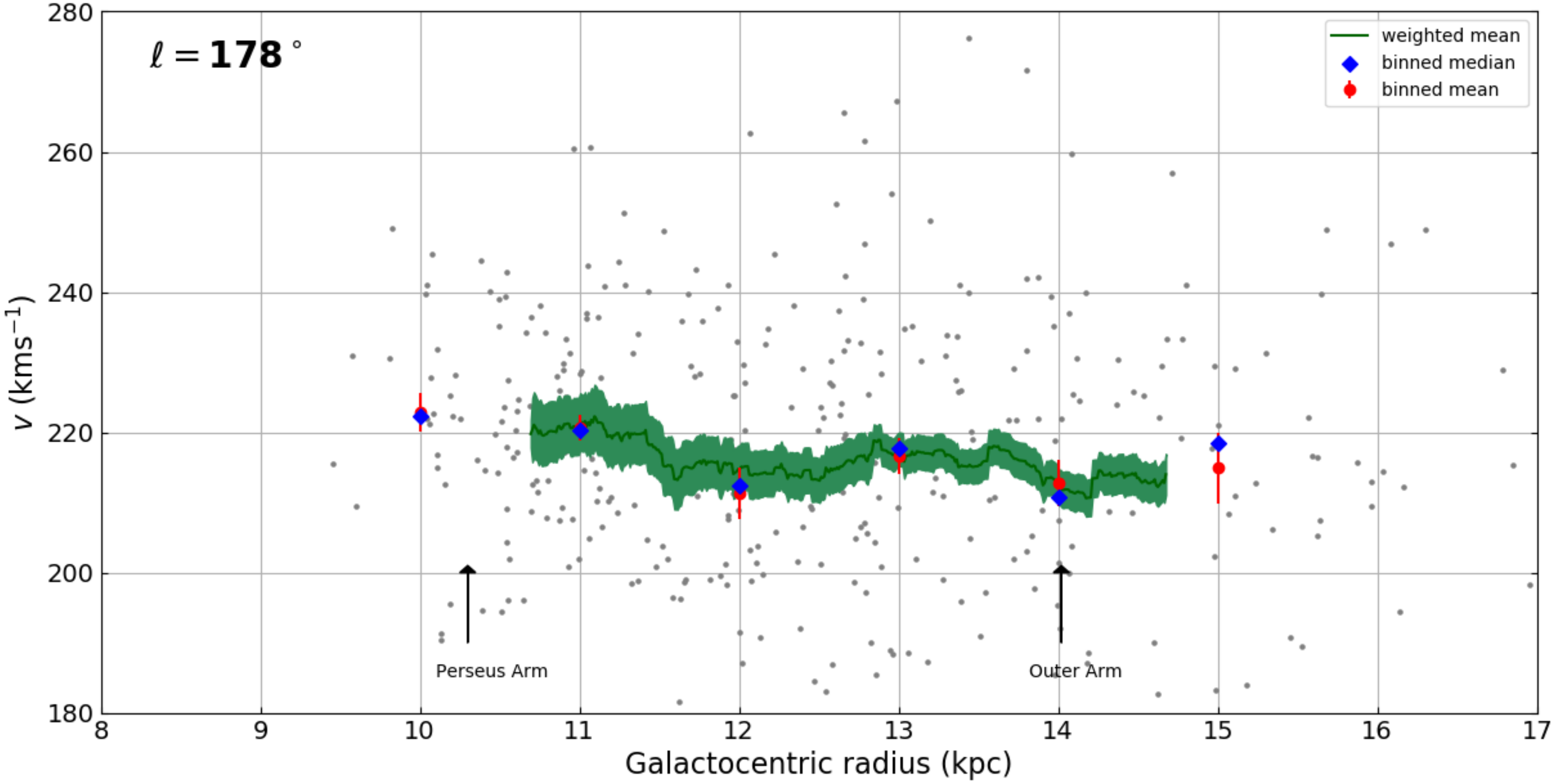

FIGURE 6.11: *The rotation curve for $\ell = 178^\circ$. The green line is the weighted mean of the grey data points, and the shaded region represents the standard error of the mean. The red points are the mean v of 1 kpc bins, and the error bars are the standard error of the binned mean. The blue diamonds are the median v of 1 kpc bins. Arrows indicate the approximate location of the Perseus and Outer Arms (Reid et al., 2014).*

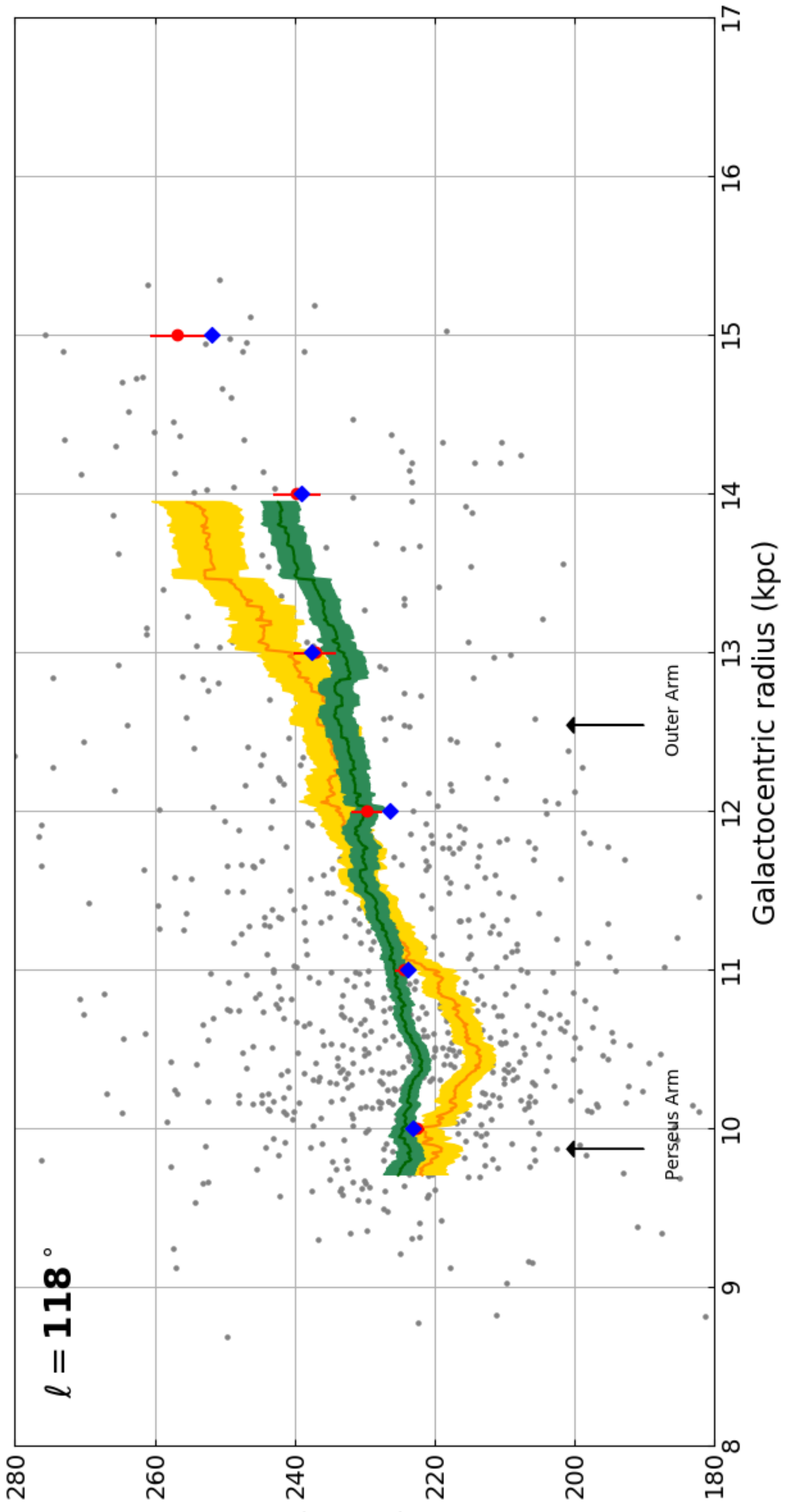

FIGURE 6.12: *The rotation curve for $\ell = 118°$. The green line is the weighted mean of the grey data points, and the shaded region represents the standard error of the mean. The red points are the mean v of 1 kpc bins, and the error bars are the standard error of the binned mean. The blue diamonds are the median v of 1 kpc bins. The yellow line shows the result from Chapter 4, i.e. using only the radial velocity data, for comparison. Arrows indicate the approximate location of the Perseus and Outer Arms (Reid et al., 2014).*

a rising rotation law at $\ell = 118^\circ$ using only radial velocity data. Without the proper motion information, it was necessary to make an assumption about the behaviour of $u(R_G)$ in order to calculate circular velocities from radial velocities. We chose to treat $u(R_G)$ as averaging to zero at all distances along the pencil-beam, i.e. that the orbits are on average circular. We show this rotation curve, derived using only radial velocities, on Figure 6.12 for comparison (yellow line). It has been recalculated using the Solar motion adopted here (see Section 6.2). We see that the rotation curve that takes into account the proper motion data (green line) is slightly flatter than our previous result - it does not dip as low at $R_G \sim 10.5\,\mathrm{kpc}$ or reach as high at $R_G > 13\,\mathrm{kpc}$. Clearly, the presence of a significant Galactocentric radial velocity term, u, that does not average to zero, has an impact on the rotation curve deduced from observed stellar motions.

Huang et al. (2016) measured a sharply rising rotation curve between $R_G = 11 - 15\,\mathrm{kpc}$ that is very similar to ours from Chapter 4 (see Figure 4.3) by using clump giants sampled over a broad fan of outer disk longitudes. However, unlike us, they did not make the assumption of zero radial motion, and instead treated a longitude-averaged $u(R_G)$ as a free parameter in their kinematic model of the Galaxy. The trend they find in $u(R_G)$ is much weaker than the trend we find here at $\ell = 118^\circ$. Our results are so markedly different in the two sightlines that it is apparent longitude-averaging the kinematic trends, such as (Huang et al., 2016) do, does not appropriately reflect reality. It is also becoming an unnecessary simplification thanks to the vast amounts of data from recent massively-multiplexed surveys, such as Gaia.

6.3.3 Vertical motion

Figure 6.13 shows the vertical velocities as a function of Galactocentric distance, $w(R_G)$, at $\ell = 178^\circ$, and Figure 6.14 shows the same for $\ell = 118^\circ$.

In the case of $\ell = 118^\circ$, the trend is roughly flat. The weighted linear regression line (black dashed) has a slope of $0.06 \pm 0.09\,\mathrm{km\,s^{-1}\,kpc^{-1}}$ - consistent with zero gradient. On average the vertical velocity is slightly positive at $\sim 2\,\mathrm{km\,s^{-1}}$, although this scales with the assumed $W_\odot$. If we reduce the adopted $\mathrm{W}_\odot$ by $2\,\mathrm{km\,s^{-1}}$, the trend lies at $\sim$zero. However it is not obvious that we should expect zero vertical motion, which would indicate an absence (or at least a non-detection) of kinematic perturbations associated with the warp of the plane or those induced by external satellites.

At $\ell = 178^{\circ}$ we observe something different. Firstly, the weighted linear regression (black dashed line) returns a steeper slope of $dw/dR_G = 1.03 \pm 0.13\,\mathrm{km\,s^{-1}\,kpc^{-1}}$. Secondly, the weighted mean (green line) indicates the trend is also oscillating. Whilst this wiggling may be in-part due to low number statistics, a similar effect has been noted in previous studies: most recently, Kawata et al. (2018) use Gaia DR2 proper motions of stars along the Galactic centre-anticentre line out to $R_G = 12\,\mathrm{kpc}$ to find a positive gradient of vertical velocity with Galactocentric radius and they also observe oscillations around this gradient. The results of Schönrich and Dehnen (2018), based on the Gaia-TGAS data set, exhibited this behaviour also. We discuss possible explanations of these perturbations in Section 6.5.

6.4 A and F star comparison - radial motion, asymmetric drift and vertex deviation

In order to determine if there are any intrinsic differences in the kinematics of the A and F stars measured, we examine the $u-v$ plane. Figure 6.15 shows the $\ell = 178^{\circ}$ objects in the $u-v$ plane, split into two distance bins: an inner region $10 < R_G$ (kpc) ≤ 13, and an outer region $13 < R_G$ (kpc) ≤ 16. There are a total of 235 stars (113 A and 122 F) in the inner region, and 117 stars (93 A and 24 F) in the outer region. Similarly, Figure 6.16 shows the $\ell = 118^{\circ}$ objects in the $u-v$ plane, in distance bins of $9 < R_G$ (kpc) ≤ 11, and $11 < R_G$ (kpc) ≤ 14. The $\ell = 118^{\circ}$ distance bins are better sampled than at $\ell = 178^{\circ}$, with 420 stars (225 A and 195 F) in the inner region and 257 stars (185 A and 72 F) in the outer region. We compare the kinematics of the two spectral-type groups in each distance bin, keeping in mind that the inner bin of each sightline has the largest sample size and most comparable number of A and F stars, and the $\ell = 118^{\circ}$ sightline in general has the larger number of stars, providing the more robust statistics.

6.4.1 Radial motion

The median u values (vertical dashed lines) are consistent within 1σ for the different spectral-type groups in both distance bins at $\ell = 178^{\circ}$. However in the better sampled $\ell = 118^{\circ}$ distance bins, the u value for A stars is positively offset from the F stars by $\sim 10\,\mathrm{km\,s^{-1}}$. In the inner distance bin, the median u values are positive and so the magnitude of u is larger for the A stars than the F stars. This is what we would expect if the u behaviour is a response to a kinematic perturbation. For example, if a sample of A and F stars are located at a similar R_G, the magnitude

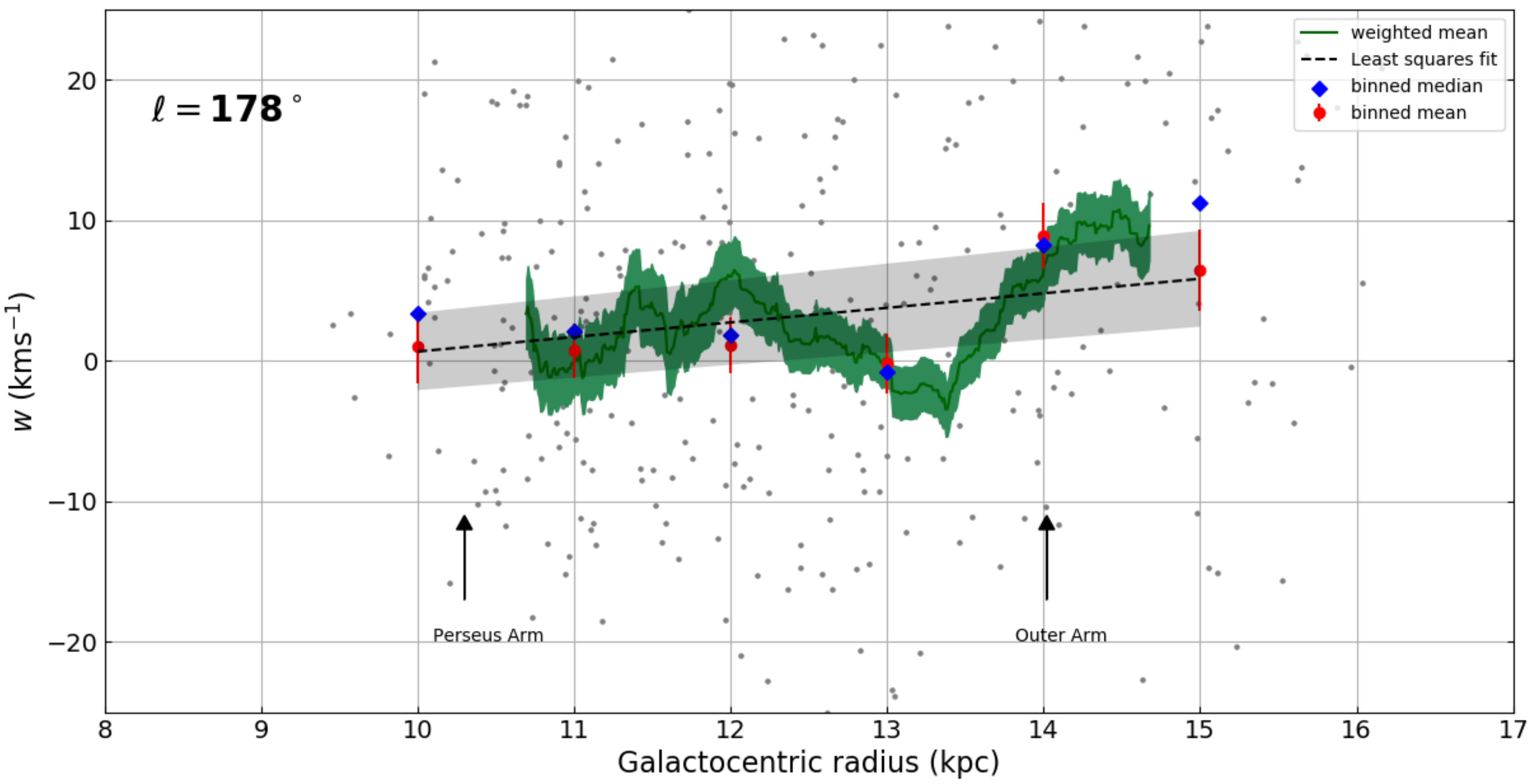

FIGURE 6.13: *The trend of w with R_G for $\ell = 178°$. The green line is the weighted mean of the grey data points, and the shaded region represents the standard error of the mean. The red points are the mean w of 1 kpc bins, and the error bars are the standard error of the binned mean. The blue diamonds are the median w of 1 kpc bins. The black dashed line is a weighted linear regression line fit to the grey data points. Arrows indicate the approximate location of the Perseus and Outer Arms (Reid et al., 2014). Note the vertical scale is 2× more sensitive than in the equivalent u and v plots, Figures 6.9 - 6.12.*

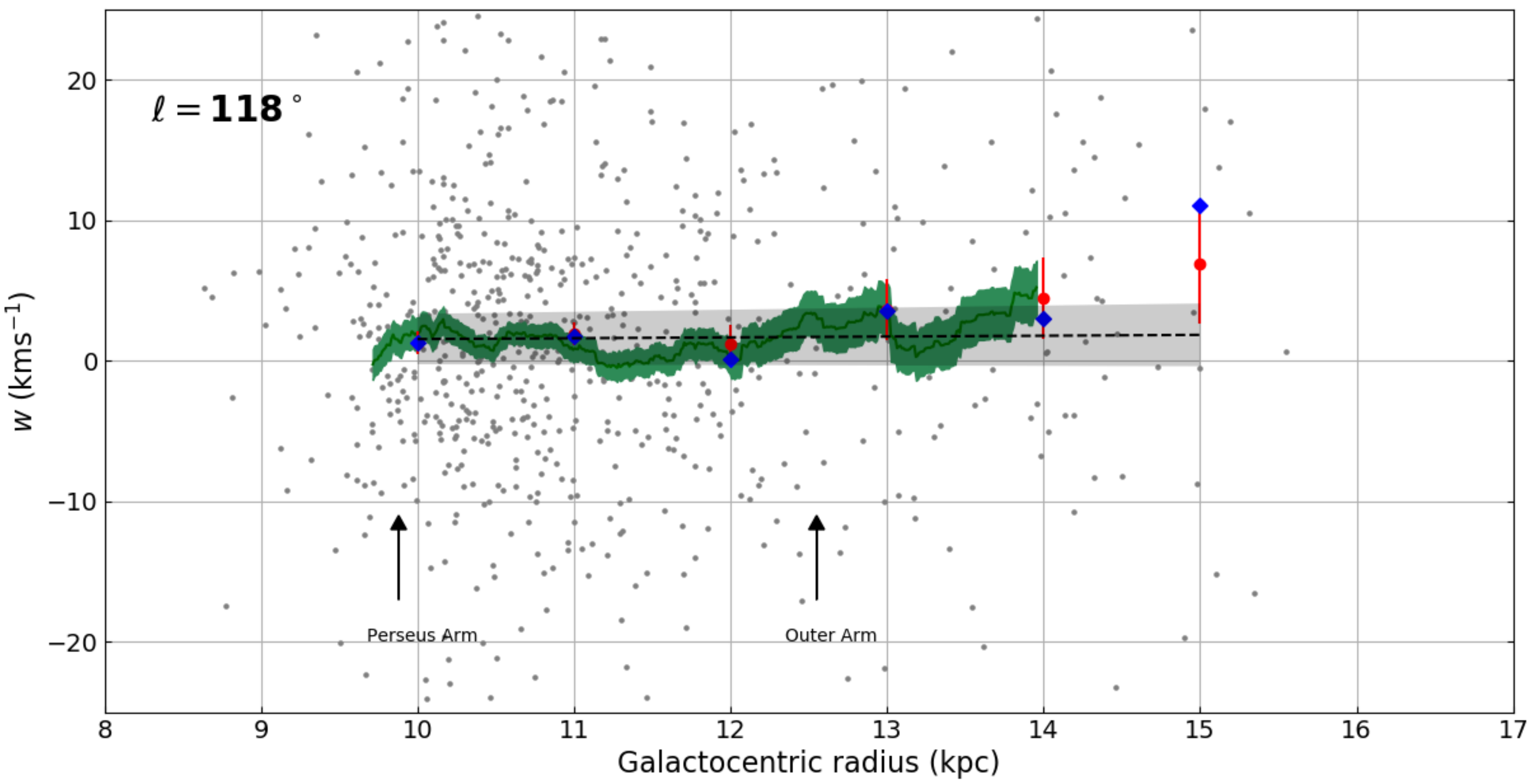

FIGURE 6.14: *The trend of w with R_G for $\ell = 118^\circ$. The green line is the weighted mean of the grey data points, and the shaded region represents the standard error of the mean. The red points are the mean w of 1 kpc bins, and the error bars are the standard error of the binned mean. The blue diamonds are the median w of 1 kpc bins. The black dashed line is a weighted linear regression line fit to the grey data points. Arrows indicate the approximate location of the Perseus and Outer Arms (Reid et al., 2014). Again the vertical scale is 2× more sensitive than in the equivalent u and v plots, Figures 6.9 - 6.12.*

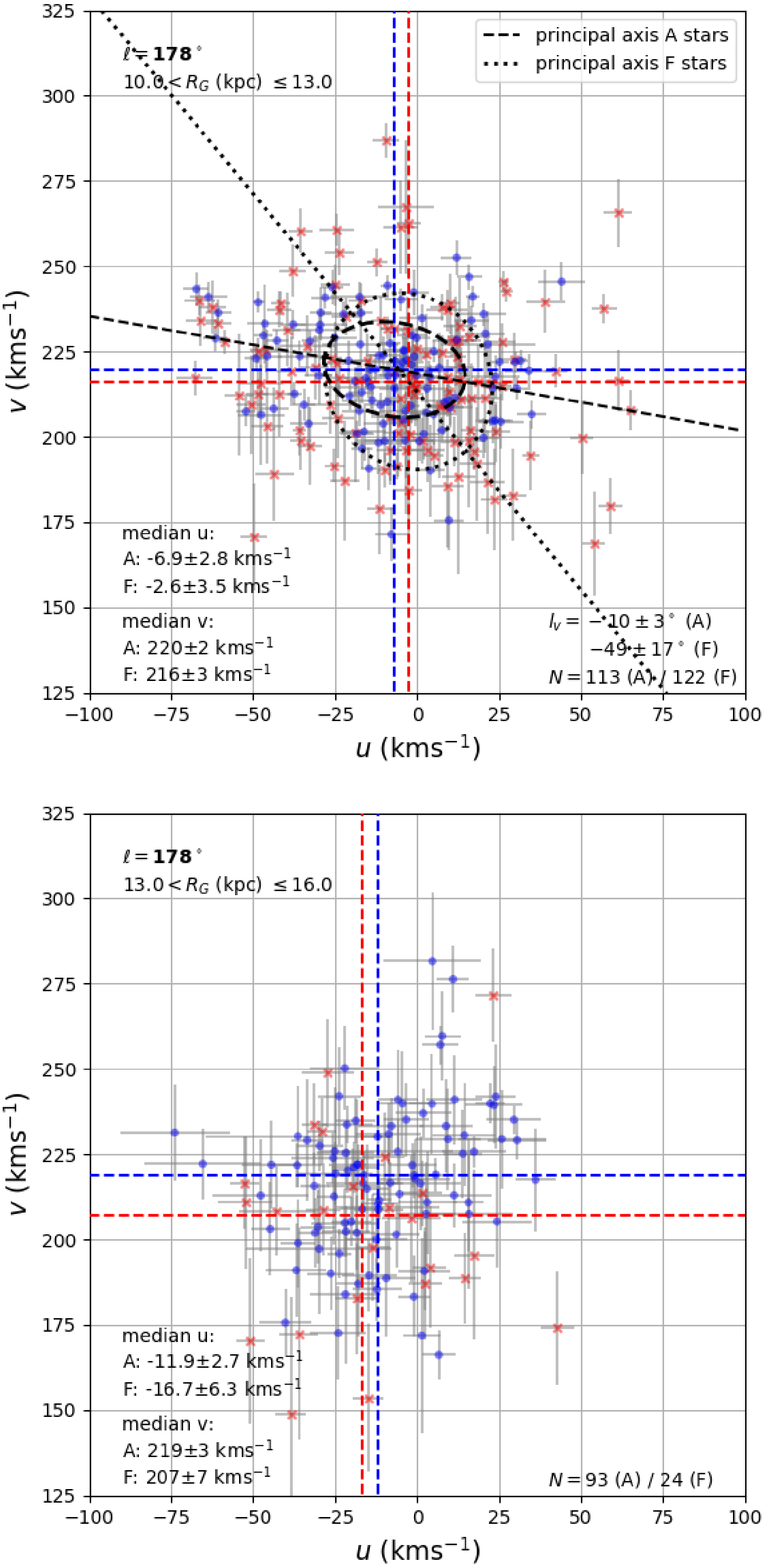

FIGURE 6.15: *The $\ell = 178^\circ$ objects in the u-v plane split into two distance ranges: an inner region $10 < R_G$ (kpc) ≤ 13 (top), and an outer region $13 < R_G$ (kpc) ≤ 16 (bottom). Blue circles represent A stars and red crosses represent F stars. The blue (red) dashed lines show the median u and v values for A (F) stars. The black dashed (dotted) lines show the velocity ellipsoid and its major axis, defining the vertex deviation, for the A (F) stars.*

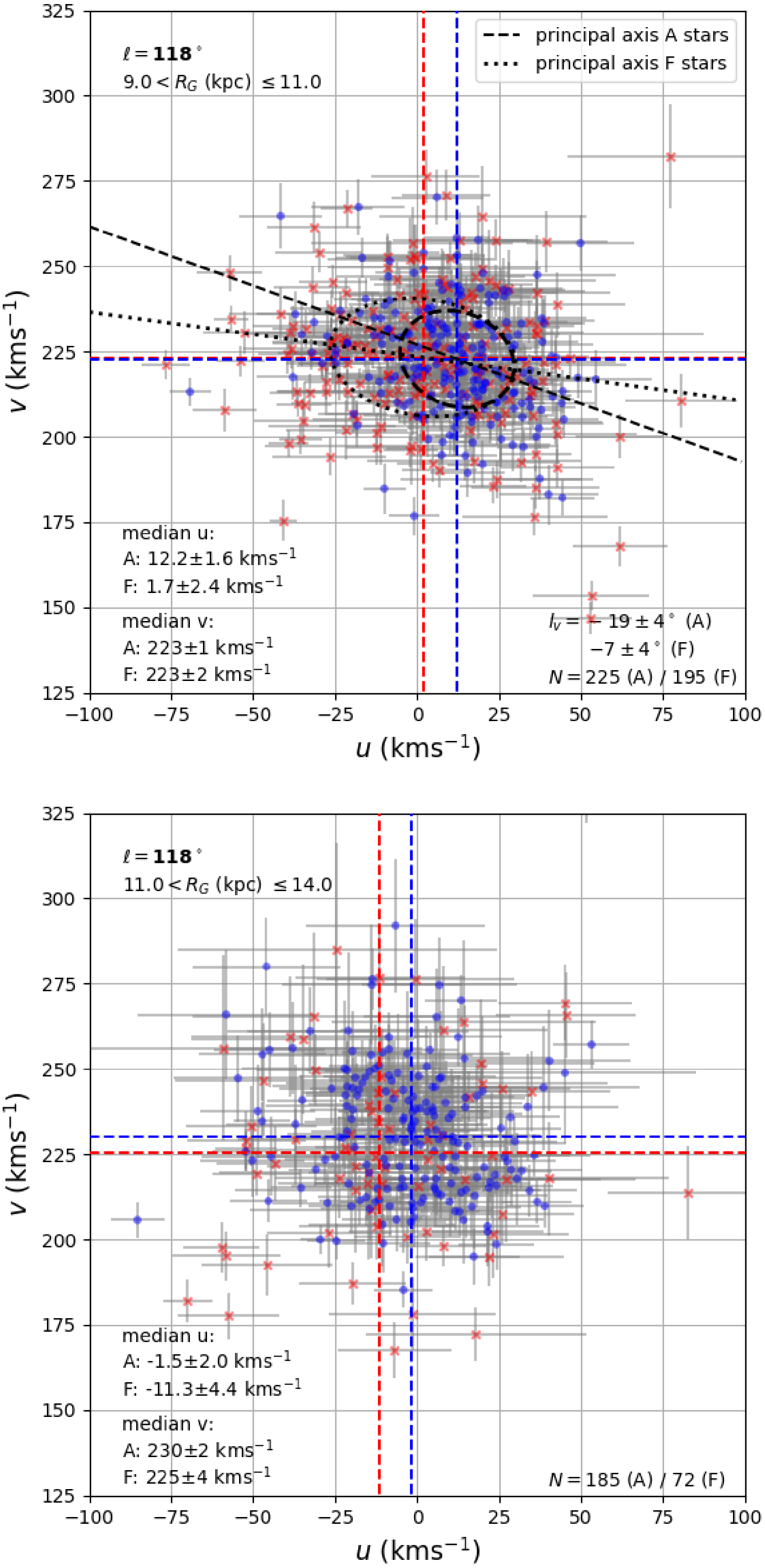

FIGURE 6.16: *The $\ell = 118^\circ$ objects in the u-v plane, split into two distance ranges: an inner region $9 < R_G$ (kpc) ≤ 11 (top), and an outer region $11 < R_G$ (kpc) ≤ 14 (bottom). Blue circles represent A stars and red crosses represent F stars. The blue (red) dashed lines show the median u and v values for A (F) stars. The black dashed (dotted) lines show the velocity ellipsoid and its major axis, defining the vertex deviation, for the A (F) stars.*

of perturbation from a spiral arm would be smaller for the F stars than for the A stars, because larger velocity dispersion helps to stabilise against kinematic perturbation (Toomre, 1964). The A stars should then be more strongly perturbed in both of our analysed distance regions, since they are younger and have smaller velocity dispersion.

However, this is in contrast to the result in the outer R_G region at $\ell = 118^\circ$, where the median u value for the F stars is $-11.3\,\mathrm{km\,s^{-1}}$, compared to $-1.5\,\mathrm{km\,s^{-1}}$ for the A stars. It is not clear why the two spectral-type groups should exhibit this behaviour. We conclude that whilst the offset in the inner region can be easily understood in terms of kinematic perturbation, the outer region cannot. Nevertheless, both stellar groups exhibit a positive (inward) radial motion inside $R_G = 11\,\mathrm{kpc}$, while outwards motion is the norm beyond this radius.

6.4.2 Asymmetric drift

The measured azimuthal velocity trend $v(R_G)$ is not, in fact, a direct measurement of the rotation curve of the Galaxy. It is actually a combination of the rotation curve and the asymmetric drift of the tracers used. Asymmetric drift is the tendency for the mean azimuthal velocity of a stellar population to drift behind that of a similar group moving on perfectly circular orbits. To demonstrate how this arises, consider a group of stars in the vicinity the Sun. The stars move on epicycles around their guiding centres at $R_G = R_g$ (see Figure 6.17), and have radial velocity dispersion σ_u. Stars with guiding centres at $R_g < R_0$ that are close to R_0 in their epicycle will have $v < v_0$. Stars with guiding centres at $R_g > R_0$ that are close to R_0 in their epicycle will have $v > v_0$. Since the stellar density profile declines exponentially with R_G, there will be more stars with $R_g < R_0$, and hence the distribution of v of the group of stars will be skewed to smaller values, i.e. they drift behind. The amount of asymmetric drift is proportional to σ_u. In principle, to measure the rotation curve, a correction for this asymmetric drift should be applied. However as we demonstrate next, the asymmetric drift of our A stars and F stars are similar, and measurements from the literature suggest the magnitude is small.

A slight lag in azimuthal velocity of F stars compared to A stars would not be surprising, since they are older and hence have been subject to larger kinematic scatter and have had more time to build up asymmetric drift. For our sample, the median v values (horizontal dashed lines) are consistent to within 1σ in all panels in both sightlines, except for the $\ell = 178^\circ$ outer region where the F stars lag the A stars by $12\,\mathrm{km\,s^{-1}}$. This is the least populated distance bin with only

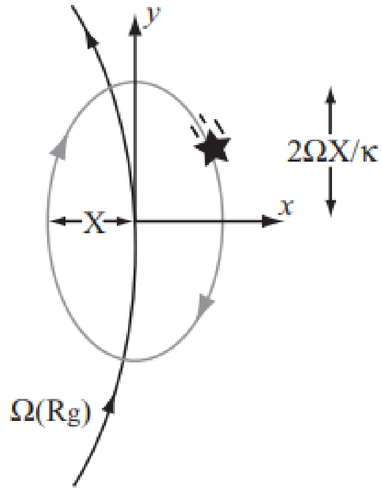

FIGURE 6.17: *Figure 3.9 from Sparke and Gallagher (2007) showing a star moving on an elliptical epicycle around its guiding centre at $x = 0$, $y = 0$, which moves around the Galactic center with angular speed $\Omega(R_g)$.*

24 F stars, and hence the result is accompanied by significant error. Hence, our results provide no sign of a measurable difference in asymmetric drift between A and F stars.

Asymmetric drift, v_a, in young stars is small, but the exact magnitude expected for A and F stars is not well known. Dehnen and Binney (1998) use Hipparcos data to study the kinematics of main sequence stars as a function of $B-V$ colour. Figure 10.12 of Binney and Merrifield (1998) shows the v_a values of their sample. For late-A stars with $B-V \sim 0.2$, they find $v_a = 4-5\,\mathrm{km\,s}$, and for early-F stars with $B-V \sim 0.4$, they find $v_a = 5-6\,\mathrm{km\,s^{-1}}$. Robin et al. (2017) model the asymmetric drift as a function of R_G and Z, and similarly find for stars younger than 1 Gyr the asymmetric drift is $\lesssim 3\,\mathrm{km\,s^{-1}}$ in the plane of the disk, increasing by just $\sim 1\,\mathrm{km\,s^{-1}}$ for stars aged $1-2$ Gyr. Kawata et al. (2019) apply an axisymmetric disk model to 218 Galactic Cepheids - young objects like those in our sample - and find negligible asymmetric drift of $0.28\pm0.2\,\mathrm{km\,s^{-1}}$ at R_0. Clearly the consistent theme from previous work is that A/F star asymmetric drift is small and will not significantly affect our measured rotation curve. Hence, we make no corrections to our observed $v(R_G)$ trend, allowing it to be interpreted as a close approximation to a measured rotation curve.

6.4.3 Vertex deviation

The velocity ellipsoid describes the shape and orientation of the 3D distribution of stellar velocities. In our analysis we have resolved the velocities into the Galactocentic components, (u, v,

w), and hence can obtain values for their dispersion, (σ_u, σ_v, σ_w), to form the velocity ellipsoid. However, it is not a given that these Galactocentric components are the principal axes of the velocity ellipsoid – the velocity ellipsoid may not be exactly aligned with the Galactic centre. The angle at which the major axis of the velocity ellipsoid in the $u-v$ plane is aligned, with respect to the Galactocentric radial velocity direction, is known as the vertex deviation. The vertex deviation is found to be largest in young stars (Mihalas and Binney, 1981; Dehnen and Binney, 1998), indicating the misalignment perhaps originates from the perturbed kinematics at the site of formation, for example the velocity field of the gas in a spiral arm. In this Section, we analyse the vertex deviations of the two spectral-type groups in our sample in order to make comparisons with previous studies.

For the distance ranges with comparable numbers of A and F stars ($R_G = 10-13\,\mathrm{kpc}$ at $\ell = 178^\circ$ and $R_G = 9-11\,\mathrm{kpc}$ at $\ell = 118^\circ$, i.e. the top panels of Figures 6.15 and 6.16) we calculate the vertex deviation for the two spectral groups. The vertex deviation, l_v, is given by

$$l_v = 0.5\tan^{-1}\left(\frac{2\sigma_{uv}^2}{\sigma_u^2-\sigma_v^2}\right) \tag{6.8}$$

where σ_u and σ_v are the velocity dispersions in the u and v velocity components (see Table 6.1), and $\sigma_{uv}^2 = \overline{(u-\bar{u})(v-\bar{v})}$, with the superposed bar representing the mean. Following Vorobyov and Theis (2006) and to account for possible large deviations, we assign to angular quadrants via

$$l_v = \begin{cases} l_v & \sigma_u^2 > \sigma_v^2 \\ l_v + sign(\sigma_{uv}^2)\frac{\pi}{2} & \sigma_u^2 < \sigma_v^2 \end{cases} \tag{6.9}$$

We determine the vertex deviation and its uncertainty for the A and F samples using Monte Carlo simulations, drawing each u and v value from a gaussian distribution with spread determined by their individual errors, and calculating l_v with this drawn sample. We do this 1000 times, and take the mean and standard deviation of the resulting distribution as the measured vertex deviation and its corresponding uncertainty. The left panels of Figures 6.15 and 6.16 show the velocity ellipsoid and principal axis drawn for A stars and F stars. The vertex deviations and velocity dispersions perpendicular to the major axis, σ_1, are detailed in Table 6.1, along with the ratio of the minor to major axis dispersions, σ_2/σ_1.

At $\ell = 118^\circ$ the vertex deviations are $-19\pm4^\circ$ for the A stars and $-7\pm4^\circ$ for the F stars. The ratio of velocity dispersion of the minor and major axes is 0.77 for the A stars and 0.60 for the F stars, implying the ellipsoids are well-defined. At $\ell = 178^\circ$ we see a large difference in the

Sightline & distance	**A/F**	σ_u **(kms^{-1})**	σ_v/σ_u	σ_1 **(kms^{-1})**	σ_2/σ_1	l_v **(deg)**
178°	A	21.0 ± 1.4	0.74 ± 0.06	21.7 ± 1.8	0.63 ± 0.06	-10 ± 3
$10 < R_G$ (kpc) ≤ 13	F	29.3 ± 3.4	0.73 ± 0.10	26.8 ± 2.5	0.91 ± 0.11	-49 ± 17
118°	A	16.1 ± 0.8	0.95 ± 0.06	17.8 ± 0.8	0.77 ± 0.04	-19 ± 4
$9 < R_G$ (kpc) ≤ 11	F	29.0 ± 2.2	0.60 ± 0.05	28.5 ± 1.7	0.60 ± 0.05	-7 ± 4

TABLE 6.1: *Velocity dispersions and vertex deviations for the A and F stars at $R_G = 10 - 13$ kpc at $\ell = 178°$ and $R_G = 9 - 11$ kpc at $\ell = 118°$. σ_u and σ_v are dispersions along the Galactocentric radial and azimuthal directions, and σ_1 and σ_2 are dispersions along the principal axes of the velocity ellipsoid.*

vertex deviation of the F stars compared to the A stars. For the A stars, l_v is $-10 \pm 3°$, whereas for the F stars it is $-49 \pm 17°$. However the F star vertex deviation has significant uncertainty and the ellipsoid is ill-defined with $\sigma_2 = 0.91\sigma_1$.

The magnitudes of our measured vertex deviations in the better-sampled $\ell = 118°$ sightline are comparable with those from Dehnen and Binney (1998), who use Hipparcos data of the Solar neighbourhood to determine the vertex deviation of late-F stars (with $B - V \sim 0.5$) to be $\sim 10°$, rising to $\sim 30°$ for early-A stars (with $B - V \sim 0.05$). Note, however, that the sign of our result is opposite. Roca-Fàbrega et al. (2014) show that the sign of the vertex deviation changes when moving either across a spiral arm, or across a main resonance of the spiral arms (e.g. the corotation radius, CR, or outer Lindblad resonance, OLR). In the two distance ranges over which l_v is calculated, the majority of the stars lie beyond where a spiral arm is believed to be located (Reid et al., 2014). The sign of our measured vertex deviation is potentially a response to this. To test this, a larger sample size on the near-side (far-side) of the Perseus (Outer) Arm is required.

Dehnen and Binney (1998) measured the ratio of velocity dispersion σ_2/σ_1 to be approximately 0.6 for F and A stars in the Solar neighbourhood. Our measurements are roughly equal or larger than this, shown in Table 6.1. From epicyclic theory, for an axisymmetric galaxy with a flat rotation curve, this ratio would be 0.5 (Binney and Tremaine, 2008). Our measurements that deviate from this value indicate our Galaxy is either, or both, non-axisymmetric and without a flat rotation curve. This is unsurprising since we know our Galaxy hosts non-axisymmetries such as spiral arms or the bar, and we have measured a rising azimuthal velocity trend at $\ell = 118°$.

6.5 Discussion

The perturbation of stellar kinematics is an effect of a non-axisymmetric Galactic potential. It is well known that the Milky Way hosts a central bar and spiral structure, and hence the potential departs from axisymmetry. It is then to be expected that we find structure in the observed velocity profiles. In order to fully explain our results the effects of all non-axisymmetric perturbers should be considered simultaneously, but as stated in Minchev and Famaey (2010), the individual effects of these perturbers do not add up linearly. However, we cautiously proceed to examine our results and discuss possible explanations for our findings.

6.5.1 The central bar

The central bar perturbs the velocity field near its natural resonances (Contopoulos and Papayannopoulos, 1980; Dehnen, 2000; Mühlbauer and Dehnen, 2003; Binney and Tremaine, 2008). The general picture is as follows, illustrated in Figure 6.18. Inside the OLR, stellar orbits become elongated perpendicular to the major axis of the bar. Outside the OLR, they become elongated parallel to the bar. The elongation of these orbits result in perturbations of the Galactocentric radial velocity that depend on the radius of the orbit and the angle relative to the bar's major axis, ϕ_b. The perturbations are strongest close to the radius of the OLR, and are modulated by $\sin 2\phi_b$ resulting in the radial gradient being strongest at e.g. $\phi_b = 45^\circ$. The bar pattern speed, and consequently the location of the OLR, continues to be debated (e.g. Portail et al., 2015; Sormani et al., 2015), with estimates ranging between $R_G \sim 6$ and $\sim 12\,\mathrm{kpc}$.

Mühlbauer and Dehnen (2003) (hereafter MD03) modelled the effect of the Galactic bar on the outer disk, locating the OLR at $0.92R_0$. They found that the magnitude of the measured radial perturbation in the dominant $m = 2$ mode is dependent on the radial velocity dispersion of the population, and hence stellar age. The signature is more pronounced for younger stars thanks to less radial smoothing (see Figure 6.19). Across the OLR, a sharp step-like feature is predicted in the perturbation as the sign of u switches from negative to positive with a total amplitude of $10-15\,\mathrm{km\,s^{-1}}$ for younger populations. With increasing R_G beyond the OLR, this perturbation dies away until, in MD03's model, it is negligible at $\sim 1.4R_0$ (or $R_G \sim 11.5$ kpc). The magnitude of perturbation scales with the strength of the bar potential. Perturbations from higher order modes such as $m = 4$ are also expected, but their magnitude of effect is considerably smaller – as recently confirmed by Hunt and Bovy (2018) who explored a range of bar models.

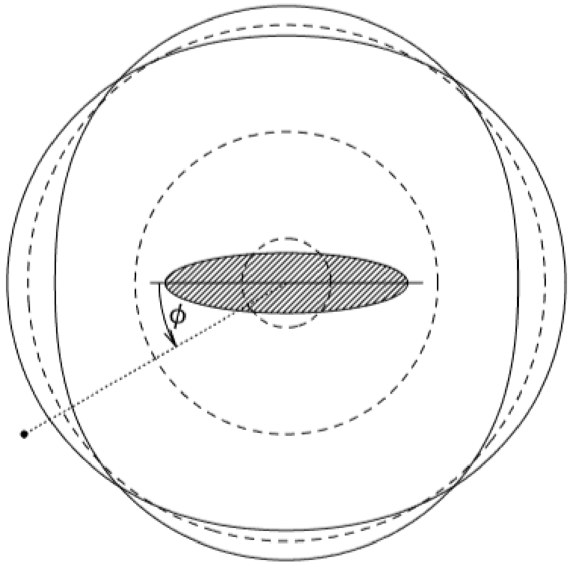

FIGURE 6.18: *Figure 1 of Dehnen (2000): Closed orbits (solid curves) just inside and outside the OLR of a rotating central bar (hatched ellipse). The circles (dashed curves) depict the positions of the inner Lindblad resonance (ILR), CR, and OLR (from inside out) for circular orbits. Note the change of the orbits orientation at the OLR, resulting in the crossing of closed orbits at four azimuths. A possible position of the Sun is shown as filled circle. The bar angle is indicated for the case of a clockwise-rotating bar.*

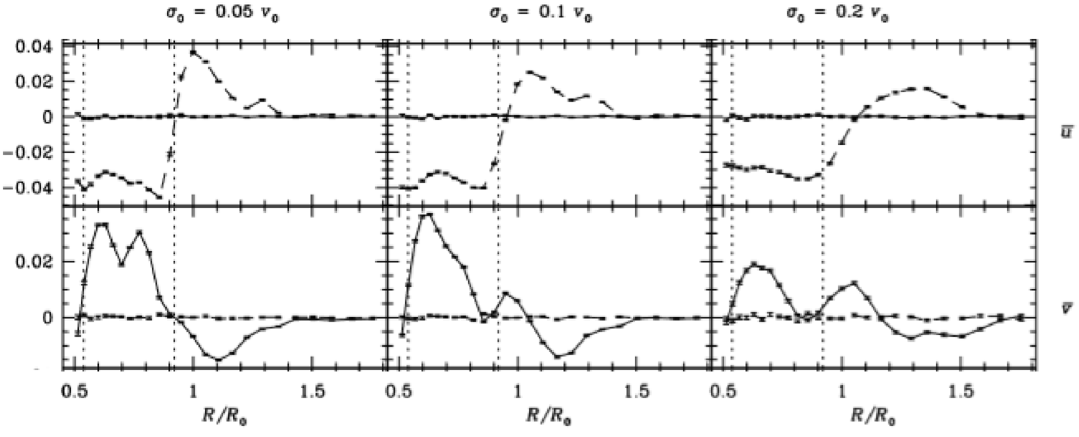

FIGURE 6.19: *Figure 4 of Mühlbauer and Dehnen (2003): $m = 2$ Fourier cosine (solid) and sine (dashed) components, plotted against radius. OLR and CR are at $0.92R_0$ and $0.53R_0$ respectively (dashed vertical lines). Results for models with initial $\sigma_0 = 0.05v_0, 0.1v_0$ and $0.2v_0$ are shown in the left, middle and right panels, respectively. Velocities are given in units of v_0.*

At $\ell = 118°$, ϕ_b ranges from $\sim 0 - 15°$ (for a bar oriented at $\phi = 30°$, see Figure 1.3) whereas $\phi_b \sim 30°$ at $\ell = 178°$. Since bar perturbation is strongest at $\phi_b = 45°$, a weaker signal is expected at $\ell = 118°$ than at $\ell = 178°$. However, comparing our $u(R_G)$ profiles, the overall amplitude of change in u at $\ell = 118°$ is greater than at $\ell = 178°$. Additionally, there is no clear evidence of the sign switch toward more positive u signalling the OLR, and so the data do not inform us about the location of the OLR. We have to conclude bar perturbation is not the dominant factor shaping the observed radial velocity profiles.

6.5.2 Spiral structure

Spiral arms also give rise to non-axisymmetric perturbation. As already discussed in Section 4.6, the scale of perturbation expected depends on the model adopted for the creation of the spiral arms. Monari et al. (2016), who favour the density wave theory, find Galactocentric radial velocity perturbations of order $\pm 5\,\mathrm{km\,s^{-1}}$ within and between the arms (see Figure 6.20). This is observationally supported by Grosbøl and Carraro (2018), who use B and A type stars in the Galactic centre direction to measure radial perturbations of $3 - 4\,\mathrm{km\,s^{-1}}$, and although they focus on density wave theory, their results can not exclude a transient perturbation.

Examining our results at $\ell = 178°$, the wiggles in the mean trend of u in Figure 6.9 do not correlate with the location of spiral arms (black arrows), and seem to have a wavelength too short to link to spiral arm perturbations expected from spiral density wave theory. These bumps could be noise due to low-number statistics. At $\ell = 118°$ (Figure 6.10) we see a small bump in the trend at $10 - 11$ kpc, slightly further out than the Perseus Arm, and also possibly at $12 - 13$ kpc, close to the Outer Arm, but it is difficult to determine if these are real features or if again, they are noise. We arrived at similar conclusions in our comparison of the radial velocity trends with a spiral arm simulation in Section 4.6.

Studies favouring the transient winding arm view predict a change in the velocity field across spiral arms. The general picture of a spiral arm in its mid-life phase is that, on the trailing side of the arm, stars rotate more slowly and move radially outwards, whereas stars on the leading side rotate faster and move radially inwards (Grand et al., 2012; Kawata et al., 2014). Grand et al. (2016) consider the transient winding arm model and find the radial perturbation of young stars (< 3 Gyr) to be considerably stronger than those predicted from density wave theory, at up to $\pm 20\,\mathrm{km\,s^{-1}}$ across the loci of the arm. They find the azimuthal perturbation to be of order $\sim 10\,\mathrm{km\,s^{-1}}$. Figure 6.21 shows their results. Baba et al. (2018) (hereafter B18) use

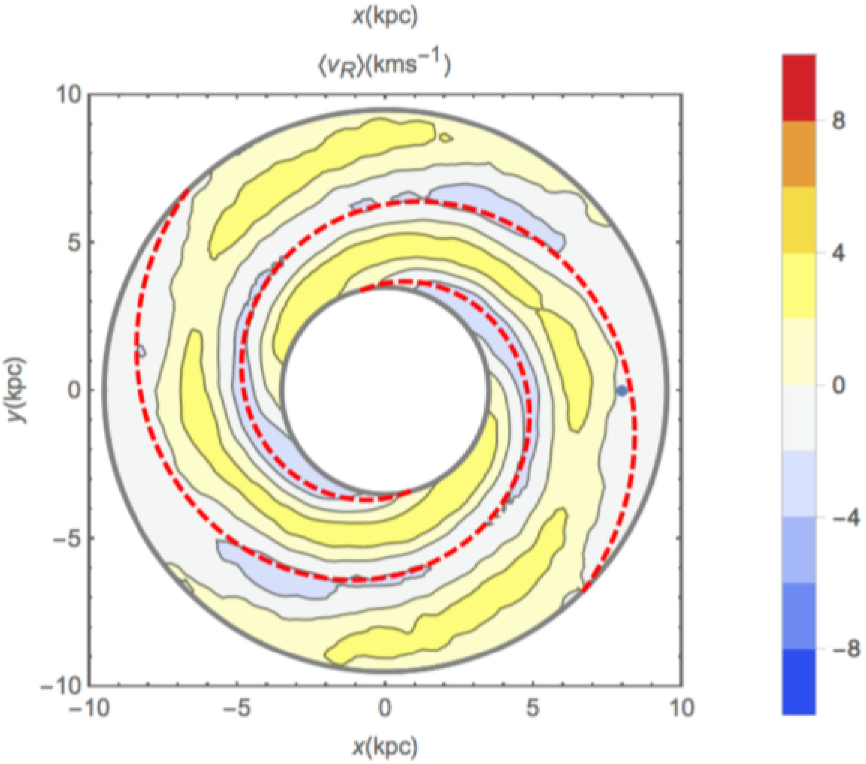

FIGURE 6.20: *Figure 1 of Monari et al. (2016): average radial speed obtained from the spiral arm simulation. The dashed red curves represent the loci of the arms.*

Cepheids with Gaia DR1 data to confirm a velocity field that changes on crossing the Perseus Arm. However, they measure the trailing side to be rotating faster and moving inward toward the Galactic centre compared to the leading side - i.e. of opposite sense to a transient arm in its mid-life phase. They attribute this pattern to the arm being in the disruption phase.

In order to test whether there is a difference in the velocity field on either side of an arm, as predicted from transient winding arm theory, we follow the concept of B18 and compare median u and v values within $0.2-1.5$ kpc of the locus of the Outer Arm (as determined by Reid et al., 2014). We restrict our analysis to the Outer Arm since we have comparable sample sizes for the two (leading & trailing) sides in both sightlines. Our results are summarised in Table 6.2. In our sightlines the trailing side of the arm has a smaller R_G than the leading.

The median u and v values are consistent within 1σ errors across the Outer Arm at $\ell = 178°$, going against expectations of transient winding arm theory. However, there is a significant difference in median u values and v values on either side of the Arm at $\ell = 118°$. The leading side is rotating faster than the trailing side. At the same time, the arm is migrating radially outwards on the whole, but the leading side is moving faster and hence the Arm appears to be

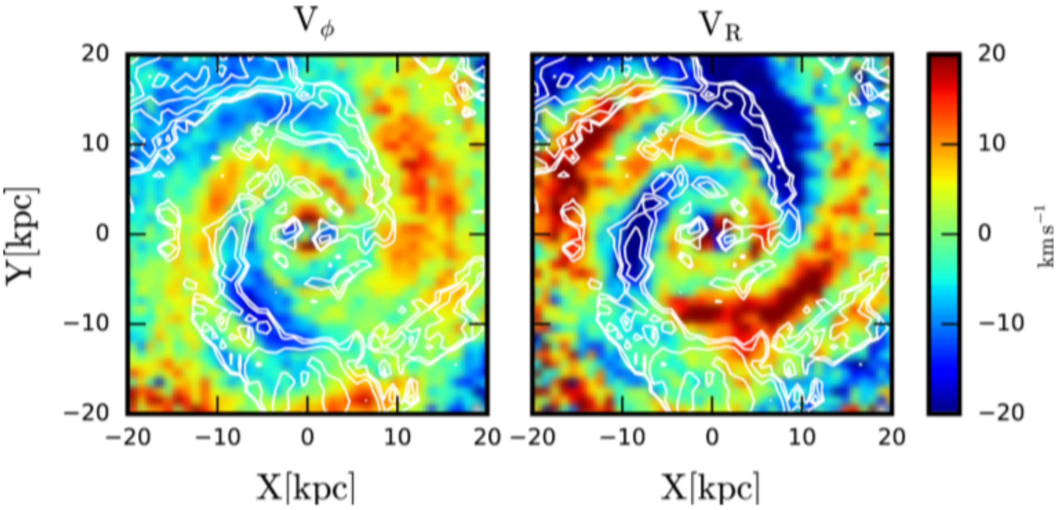

FIGURE 6.21: *Figure 1 of Grand et al. (2016): Face-on maps of the azimuthal (left) and radial (right) peculiar velocity fields. Positive velocities are in the direction of rotation (azimuthal) and the galactic anticentre (radial). Overdensity contours of the mass distribution are indicated by the contours. The azimuthal peculiar velocity field is systematically slower (faster) on the trailing (leading) edge of the spiral, whereas the radial peculiar velocity points outward (inward) on the trailing (leading) edge.*

		u	v	N
$\ell = 178°$	Trailing	-9.3 ± 3.2	217 ± 3	94
	Leading	-11.8 ± 4.7	213 ± 5	35
$\ell = 118°$	Trailing	-0.6 ± 2.3	227 ± 2	169
	Leading	-11.7 ± 3.5	243 ± 3	61

TABLE 6.2: *Median u and v values ($km\,s^{-1}$) for the trailing side and leading side of the Outer Arm at $\ell = 178°$ (top rows) and $\ell = 118°$ (bottom rows) . The number of objects in each subsample is also shown.*

expanding in this sightline. This points to a combination of u and v perturbations that do not fit consistently with the mid-life stage of the transient winding arm model.

6.5.3 Satellites and the warp

Perturbations of vertical velocities can arise due to the passage of a satellite galaxy through the Galactic disk. Gómez et al. (2013) simulate the vertical density waves induced by the Sagittarius dwarf galaxy, and find vertical velocity perturbations of up to 8 $km\,s^{-1}$ in the outer disk. Antoja et al. (2018) explore the vertical phase-space of more than 6 million Gaia DR2 stars and reveal a spiral-like distribution which could be caused by the latest passage of the Sagittarius dwarf galaxy, between 300 and 900 Myr ago. Additionally, large-scale systematic vertical velocities are expected due to the warp in the anticentre region. Poggio et al. (2018) confirm this using

Gaia DR2 kinematics of both upper main sequence stars and giants, measuring an increase in vertical velocity of $5-6\,\mathrm{km\,s^{-1}}$ over $R_G = 8-14\,\mathrm{kpc}$ (i.e. $dw/dR_G \sim 1\,\mathrm{km\,s^{-1}\,kpc^{-1}}$).

As noted in Section 6.3.3, we observe a statistically significant positive gradient of $dw/dR_G = 1.03 \pm 0.13\,\mathrm{km\,s^{-1}\,kpc^{-1}}$ at $\ell = 178^\circ$. This is in good agreement with the gradient measured in Poggio et al. (2018) due to the warp. The kinematic response to the warp is expected to be strongest in the anticentre direction, and hence it is unsurprising that we measure a steeper gradient at $\ell = 178^\circ$ than at $\ell = 118^\circ$. The oscillations observed in vertical velocity at $\ell = 178^\circ$ may be a kinematic signature from a satellite crossing the plane of the Milky Way, such as the Sagittarius dwarf galaxy as discussed in Gómez et al. (2013). It is expected that perturbations of this type present as mainly radially-dependent perturbations throughout the disk (see Figure 5 of Gómez et al., 2013). However, we do not observe obviously correlated perturbations in the $\ell = 118^\circ$ sightline, which somewhat complicates the picture.

The consideration of observed Galactocentric trends has offered no obvious explanations in terms of kinematic perturbers. As we mentioned before, in order to fully understand the complex non-axisymmetric kinematics of our Galaxy, all dynamic processes must be considered in unison. However, doing so relies heavily on knowledge of global kinematics, such as the rotation curve.

Chapter 7

Looking ahead

In this Chapter, we look at extending our MCMC method of stellar parameter determination and radial velocity measurement, with the aim of creating a legacy tool that can be used in the future on spectroscopy from e.g. WEAVE. We introduce Parallel Tempering MCMC, a method designed to deal with multi-modal posteriors, and compare our re-computed parameters for the HectoSpec sample with those determined in Chapter 3, finding some reduction of the occasional and troublesome $T_{\rm eff}$ degeneracy. We also test this method on WEAVE spectra, simulated for an operational rehearsal. This demonstrates that the fit quality achieved is good in the CaT domain, if more challenging at blue wavelengths.

7.1 Parallel Tempering MCMC

The MCMC method used to determine stellar parameters ($T_{\rm eff}$, $\log g$ and $v\sin i$) and measure radial velocities was described in Section 3.1.4. This method uses a likelihood function that, in certain cases, is multi-modal. This multi-modality arises due to a degeneracy where the Paschen line profiles of cooler stars are very similar to that of a higher temperature star, with the addition of line broadening effects from surface gravity and rotation. We described this in Section 3.2.1. In the case of multi-modality, the MCMC walkers can become stuck at a local maximum, and hence fail to find the global maximum which should provide the best template match. This situation is usually betrayed in our results by large asymmetric $T_{\rm eff}$ errors, which we removed from further analysis (see Figure 3.8). 85 objects with $|\sigma(T_{\rm eff})| > 1000\,{\rm K}$ were removed from our original sample. However, if the majority of the walkers become stuck in the local maximum, the resulting 1σ error could be artificially small, and the object would remain in our sample with an inappropriate $T_{\rm eff}$ measurement. It should be possible to break this Paschen line degeneracy due to the presence of more prominent CaT lines in the cooler objects, providing the necessary information to distinguish between the hotter and cooler solutions. In other words, a global maximum does exist and it is a matter of making sure it is found.

A modification of the MCMC fitting technique has been proposed that can deal with multi-modal posteriors. It is known as 'Parallel Tempering' (Earl and Deem, 2005). Parallel Tempering MCMC (PTMCMC) works by running N_t MCMC simulations in parallel, raising the likelihood in the i^{th} simulation to a power of $1/t_i$, where t_i is the 'temperature'. This acts to broaden the likelihood, such that as $t \to \infty$, the posterior becomes the prior (flat in our case). Hence, walkers in the high temperature simulation can easily explore the entire parameter space. The positions of the walkers in each parallel simulation are occasionally swapped with those at another temperature, ensuring the walkers in the $t_0 = 1$ simulation can sample the entire multi-modal posterior. It is the results of the $t_0 = 1$ simulation, whose likelihood is unchanged i.e. raised to the power of 1, that we are ultimately interested in, once the right local maximum has been identified.

7.1.1 Re-computing HectoSpec parameters

We re-computed stellar parameters and radial velocities of our HectoSpec sample using the PTMCMC method[1]. By comparing these with our measurements from the original MCMC method, we could quantify the impact of the temperature degeneracy on our kinematic results. We implemented PTMCMC using the 'PTEMCEE' PYTHON package[2]. We chose to use 5 temperatures, each with 200 walkers and 2000 steps, after an initial burn-in of 250 steps. The temperatures are spread between $1 < t_i < \infty$, with the spacing between temperatures initially determined and progressively adapted by the PTEMCEE implementation to achieve a uniform rate of exchange of walker positions between neighbouring temperatures (Vousden et al., 2015). The best combination of number of temperatures, walkers and steps used was determined experimentally on simulated data (see Section 7.1.2). Since there are 5 simulations running in parallel, the computing time is increased by this amount compared to the original MCMC algorithm, taking $\sim$ 1 hr per object. However use of process parallelisation on a cluster machine allows multiple objects to be run simultaneously.

---

[1] see the Appendix for the code

[2] `https://github.com/willvousden/ptemcee`

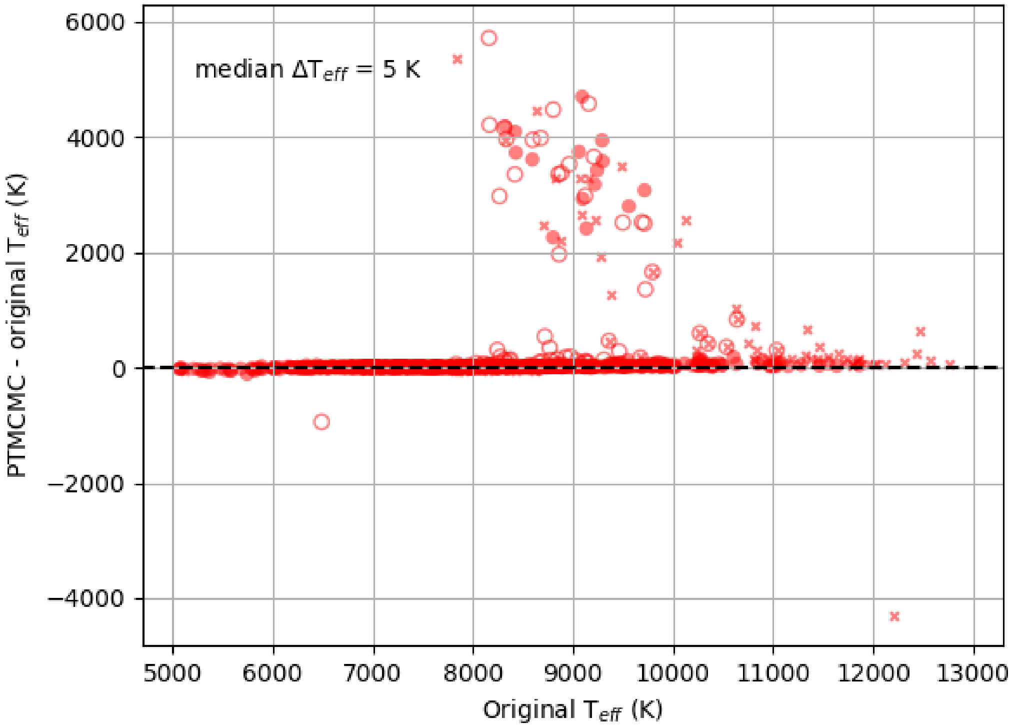

FIGURE 7.1: *The difference between $T_{\rm eff}$ measurements using the PTMCMC method and the original MCMC method, as a function of the original MCMC $T_{\rm eff}$ measurement. Crosses represent objects that were removed from our original sample due to $|\sigma(T_{\rm eff})| > 1000$ K (see Section 3.2.1). Empty circles represent objects that have PTMCMC $|\sigma(T_{\rm eff})| > 1000$ K, and so circles with crosses inside are those with $|\sigma(T_{\rm eff})| > 1000$ in both methods. The black dashed line shows the median difference.*

Figure 7.1 show the difference between the $T_{\rm eff}$ measurements using the PTMCMC method and those from the original MCMC method. The crosses represent objects that were removed from our original sample due to $|\sigma(T_{\rm eff})| > 1000$ K (see Section 3.2.1). Empty circles represent objects that have PTMCMC $|\sigma(T_{\rm eff})| > 1000$ K, and so circles with crosses inside are those with $|\sigma(T_{\rm eff})| > 1000$ K in both methods. Filled circles are those with $|\sigma(T_{\rm eff})| < 1000$ K in both methods. The black dashed line shows the median difference. The differences are generally very small – the median difference is just 5 K.

The collection of objects where the temperature change is $\sim 2000 - 5000$ K have suffered from the Paschen line profile degeneracy. For these objects, the original MCMC method returns $T_{\rm eff}$ of $8000 - 10000$ K, whereas the PTMCMC method returns a hotter temperature of $11000 - 14000$ K. This group consists of 51 objects, which makes up just 4% of the total sample. 16 of these objects were excluded from our analysis in the previous Chapters (cross symbols) due to their large original $T_{\rm eff}$ errors. The remaining 35 that weren't removed from the original sample

	MCMC	**PTMCMC**
$T_{\rm eff}$ (K)	150	130
$\log g$	0.09 (A) 0.14 (F)	0.08 (A) 0.14 (F)
$v \sin i$ (km s^{-1})	21	18
RV (km s^{-1})	6.8 (A) 4.4 (F)	6.2 (A) 4.0 (F)

TABLE 7.1: *Comparison of the median uncertainties of the stellar parameters and RVs as determined from the MCMC method and PTMCMC method.*

probably had artificially small 1σ uncertainties due to the majority of walkers being stuck at the local maximum.

The PTMCMC method should avoid these artificially small uncertainties since the walkers have the freedom to explore the entire parameter space, and so the PTMCMC uncertainties are more realistic and informative. Figure 7.2 is analogous to Figure 3.8, but this time showing the uncertainties in $T_{\rm eff}$, $\log g$ and RV as returned by the PTMCMC method. The general trends of uncertainty with temperature are the same as the original method, although their sizes are slightly reduced. Table 7.1 compares the median uncertainties of the stellar parameters and RVs, as determined using the MCMC method and the PTMCMC method. The empty circles in Figure 7.2 are those with $|\sigma(T_{\rm eff})| > 1000$ K – there are 64 of them, compared to 85 for the original MCMC method. Of the 85 with large original $T_{\rm eff}$ errors, 77 of them have reduced errors (< 1000 K) as determined by PTMCMC. Consequently, the majority of those with large PTMCMC errors are those that had small original errors, and we show below why these large errors are warranted.

Out of the 51 objects with large $T_{\rm eff}$ difference in Figure 7.1, 21 have a large uncertainty in the PTMCMC measurement (empty circles). Figures 7.3 and 7.4 show two examples of these. The top panels show the best-fit template from the original MCMC method, and the bottom from the PTMCMC method. In both cases, the original MCMC method returned small (< 1000 K) uncertainty in $T_{\rm eff}$, and so were not removed from our sample, but the PTMCMC returns large (> 1000 K) uncertainty in $T_{\rm eff}$. These large uncertainties are a reflection of the ambiguity of the spectrum.

The two fits in Figure 7.3 are extremely similar, demonstrating the Paschen line profile degeneracy. The original MCMC method returns $T_{\rm eff} = 8862\pm^{333}_{191}$ K, $\log g = 3.78\pm^{0.07}_{0.07}$, $v \sin i = 192\pm^{25}_{28}$ km s^{-1} and RV$= -89.3\pm^{7.3}_{7.0}$, whereas PTMCMC returns $T_{\rm eff} = 10825\pm^{333}_{1995}$ K, $\log g = 3.82\pm^{0.05}_{0.06}$, $v \sin i = 152\pm^{43}_{31}$ km s^{-1} and RV$= -93.4\pm^{6.7}_{6.6}$. And yet, despite the clearly discrepant parameters, the template fits are almost indistinguishable. It is then understandable that the

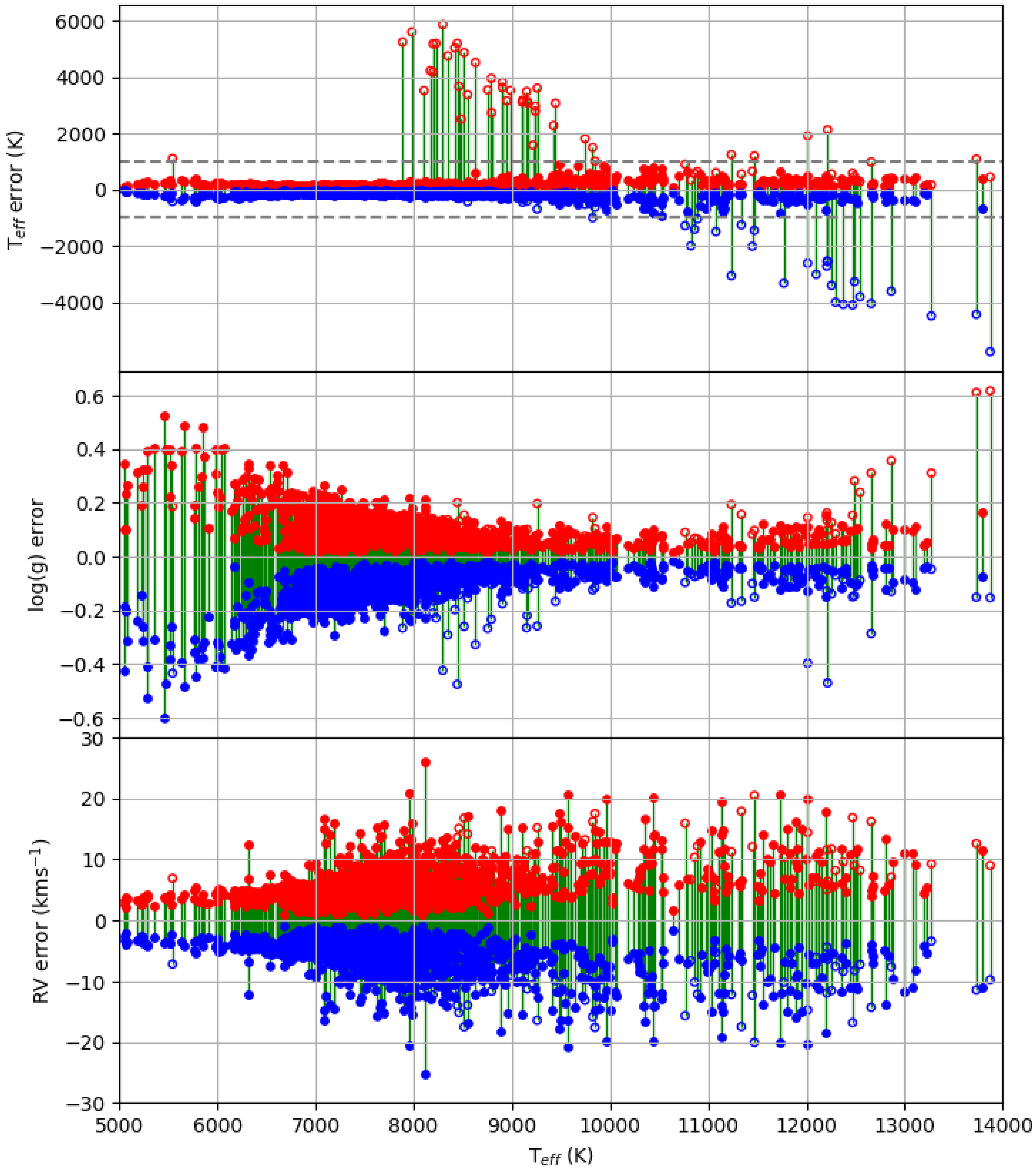

FIGURE 7.2: *Analogous to Figure 3.8 but for the uncertainties returned by the PTMCMC method. Those with* $|\sigma(T_{\rm eff}) > 1000\,K$ *have not been removed here, but are still picked out by empty circles.*

PTMCMC method should return a large $T_{\rm eff}$ uncertainty in this case, and that the uncertainty returned by the original method was unrealistically small.

In Figure 7.4, the fit from the original MCMC method is bad near the Paschen line at $\sim 8600 \AA$, whereas the PTMCMC fit is better for that line, but is not so good for the two included CaT lines. Cases such as these could be explained by binarity – a mix of two objects of different temperatures may produce a combination of line depths that cannot be fit with single-star templates. This is an aspect of our method that could be improved in future. We comment on this in Section 7.1.3.2.

The $\log g$ differences are shown in Figure 7.5. The differences are generally very small, with a median of just 0.005 dex. The group of objects with large $T_{\rm eff}$ difference are those that have larger $\log g$ differences. For these, the PTMCMC method returns a smaller $\log g$ compared to the original MCMC measurement. The story is very similar for the $v \sin i$ and RV measurements (see Figure 7.6). The median difference in $v \sin i$ is just $-2\,{\rm km\,s^{-1}}$, and in RV is $-0.10\,{\rm km\,s^{-1}}$. The PTMCMC method returns smaller $v \sin i$ and RV values for the group that have larger $T_{\rm eff}$ differences.

The main impact of using the PTMCMC method, in place of the original method, on our HectoSpec sample is on a very small (4%) group of objects that suffer from the degeneracy of Paschen line profiles. The PTMCMC method returns hotter temperatures for this group, along with smaller $\log g$, $v \sin i$ and RV values. For the objects in question, the higher $T_{\rm eff}$ clearly makes a better spectral match in the majority of cases. Figure 7.7 shows an example of this, where the PTMCMC fit (bottom panel) is clearly a better match to the HectoSpec spectrum than the original MCMC fit (top panel). In the cases where ambiguity rightly remains, such as those shown in Figures 7.3 and 7.4, the new fits carry increased uncertainties.

The different $T_{\rm eff}$ and $\log g$ values returned result in distance changes. Figure 7.8 shows the difference between the distances, determined as described in Section 3.3, via the PTMCMC and original MCMC methods. The difference is typically small, with a median of only -0.13 kpc. This is smaller than the typical distance error of 0.5 kpc for the PTMCMC method, and 0.6 kpc in the original method. The general reduction of parameter uncertainties in the PTMCMC method has reduced the typical distance error. The group with large $T_{\rm eff}$ differences return larger distances, as expected for their raised temperatures and reduced $\log g$, with the difference ranging between approximately $2-7$ kpc. However, since the remaining 96% of the sample have negligible difference in their stellar parameters and distances, we expect that using the PTMCMC

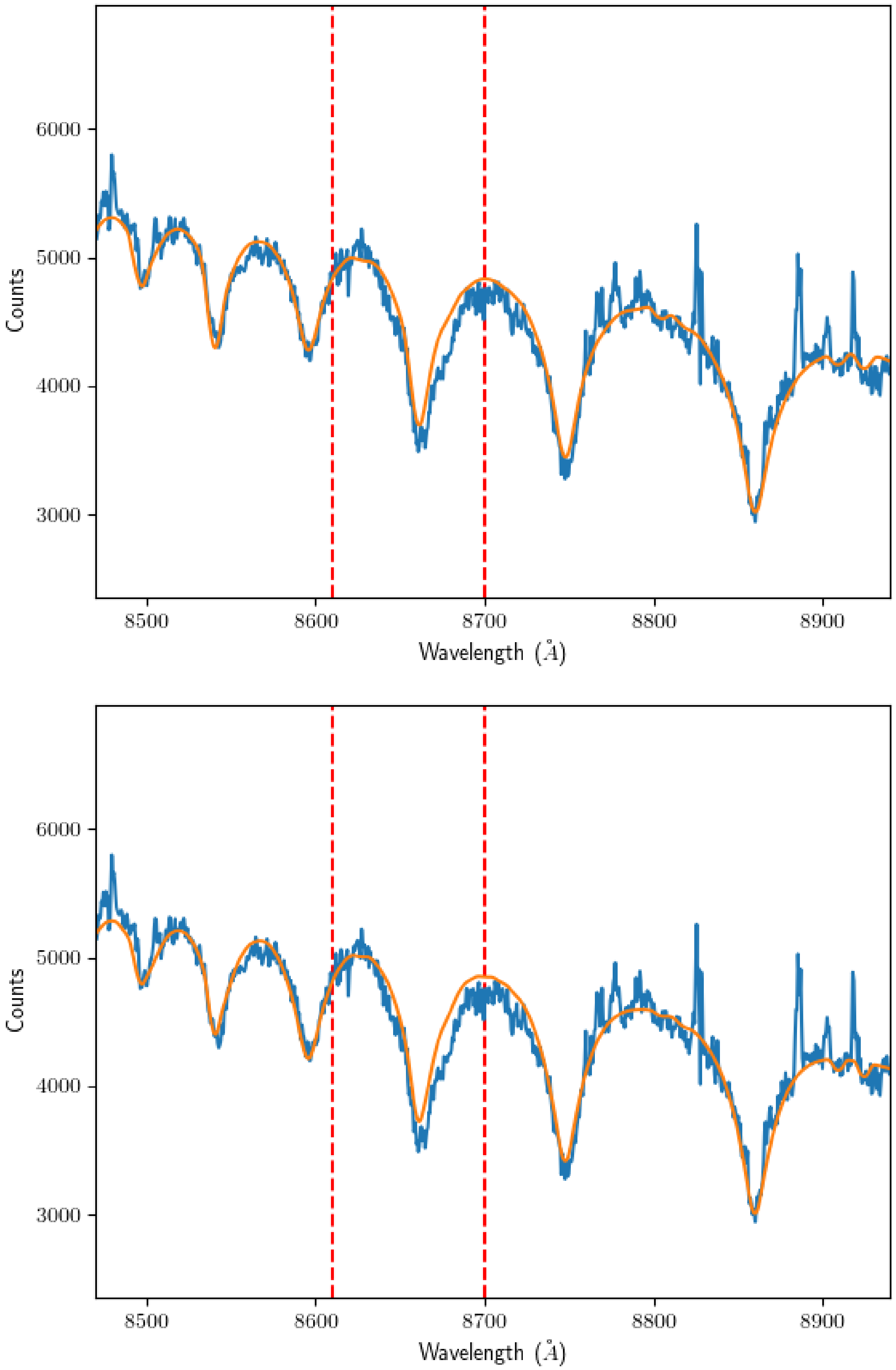

FIGURE 7.3: *A HectoSpec spectrum (blue line) of one of the objects suffering from the Paschen line profile degeneracy, with best-fit template (orange line) from the original MCMC method (top panel) and PTMCMC method (bottom panel). The two fits are almost indistinguishable, despite their very different parameters. The original MCMC fit has parameters:* $T_{\rm eff} = 8862\pm^{333}_{191}$ *K*, $\log g = 3.78\pm^{0.07}_{0.07}$, $v \sin i = 192\pm^{25}_{28}$ *km* s^{-1} *and RV*$= -89.3\pm^{7.3}_{7.0}$, *whereas the PTMCMC fit has parmeters:* $T_{\rm eff} = 10825\pm^{333}_{1995}$ *K*, $\log g = 3.82\pm^{0.05}_{0.06}$, $v \sin i = 152\pm^{43}_{31}$ *km* s^{-1}, *and RV*$= -93.4\pm^{6.7}_{6.6}$.

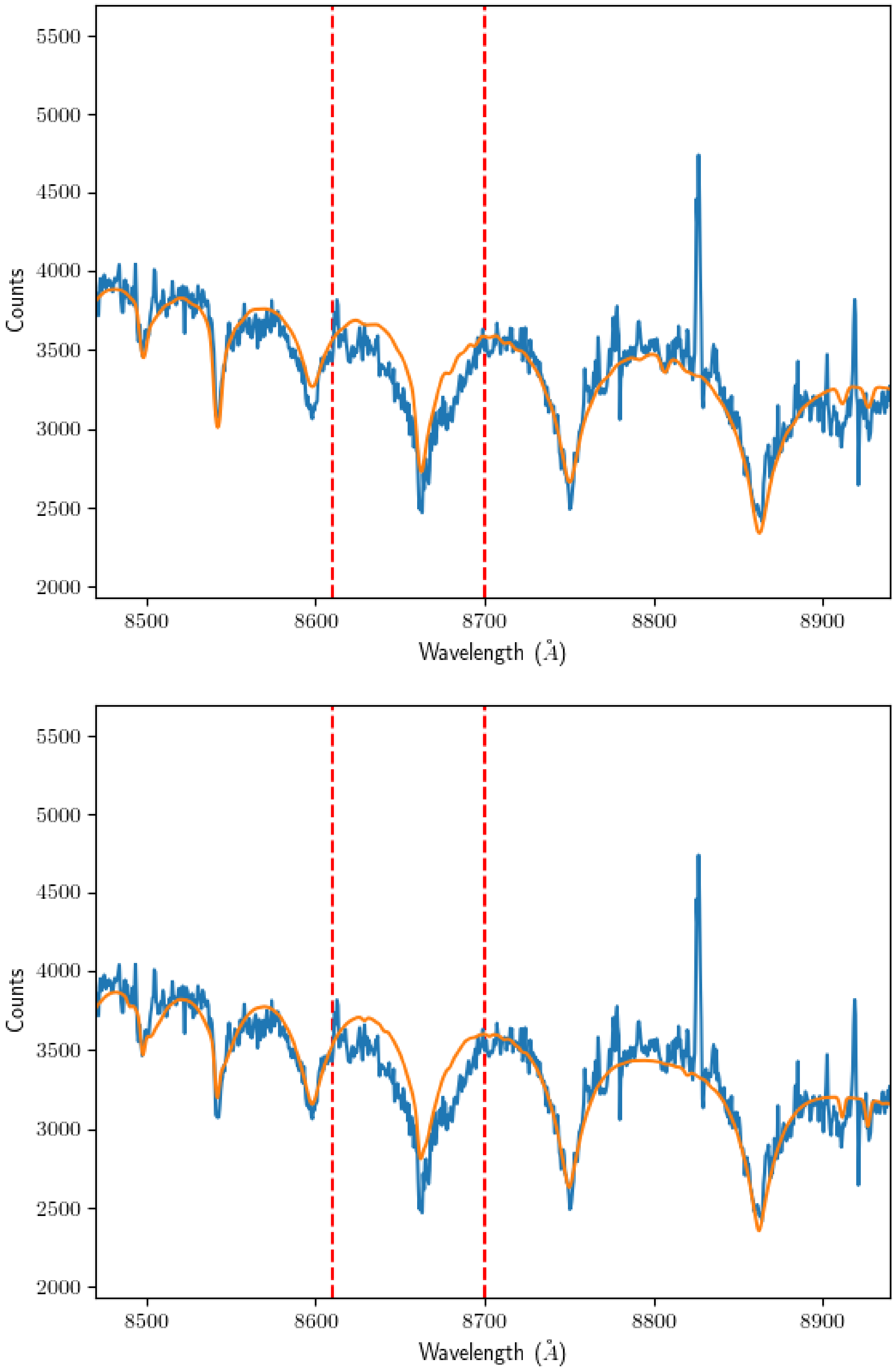

FIGURE 7.4: *A HectoSpec spectrum (blue line) of one of the objects suffering from the Paschen line profile degeneracy, with best-fit template (orange line) from the original MCMC method (top panel) and PTMCMC method (bottom panel). The two fits both have their downfalls, possibly explained by a binary star? The original MCMC fit has parameters:* $T_{\mathrm{eff}} = 8598\pm^{189}_{236}$ *K,* $\log g = 4.09\pm^{0.07}_{0.11}$, $v \sin i = 111\pm^{23}_{24}$ *km* s^{-1} *and RV=* $-4.3\pm^{6.7}_{7.0}$, *whereas the PTMCMC fit has parmeters:* $T_{\mathrm{eff}} = 12545\pm^{280}_{3802}$ *K,* $\log g = 3.79\pm^{0.24}_{0.09}$, $v \sin i = 42\pm^{52}_{29}$ *km* s^{-1}, *and RV=* $-11.8\pm^{8.2}_{7.2}$.

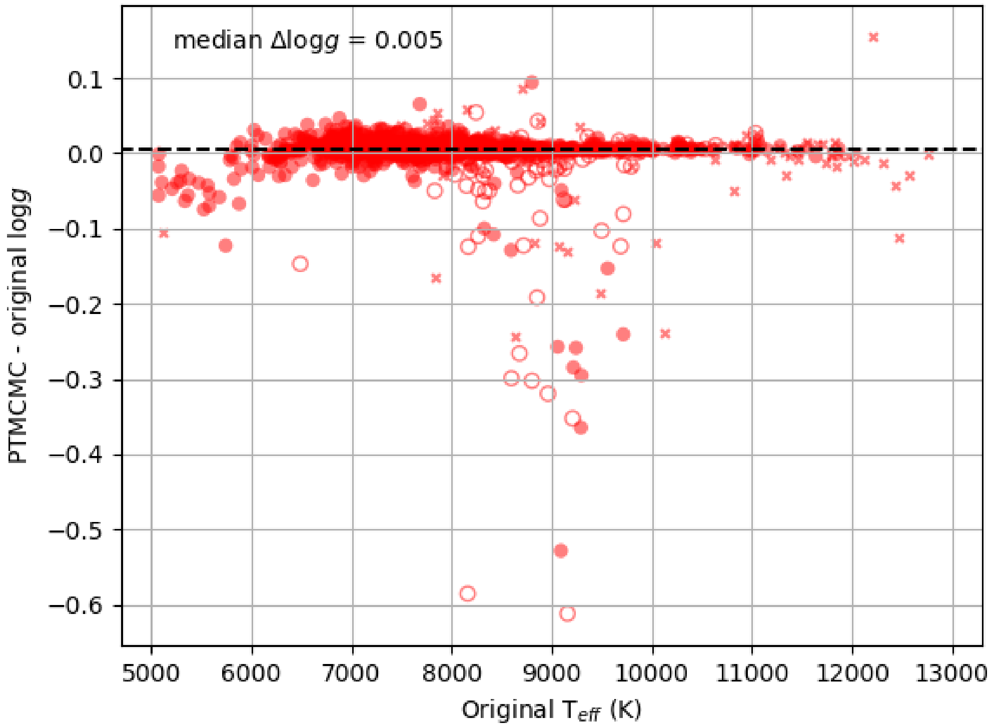

FIGURE 7.5: *Same as Figure 7.1 but for* $\log g$.

measurements for the HectoSpec sample will have no significant impact on the resulting kinematics, such as the Galactocentric velocity trends that we measured in Chapter 6.

To test this, we have recalculated the $u(R_G)$, $v(R_G)$, $w(R_G)$ trends using the PTMCMC parameters. Figures 7.9-7.11 show these trends compared to those computed with the MCMC parameters (as presented in Chapter 6). The trends are indeed very similar, and our analysis remains unchanged. The only case where there is perhaps a notable difference is in the $w(R_G)$ trend at 178°, where the gradient is reduced. The variation of wiggles in the comparison of trends indicates that the wiggles are predominantly noise. Overall, the redetermination of stellar parameters and radial velocities using the PTMCMC method has little impact on the resulting kinematics, especially those in the Galactic plane.

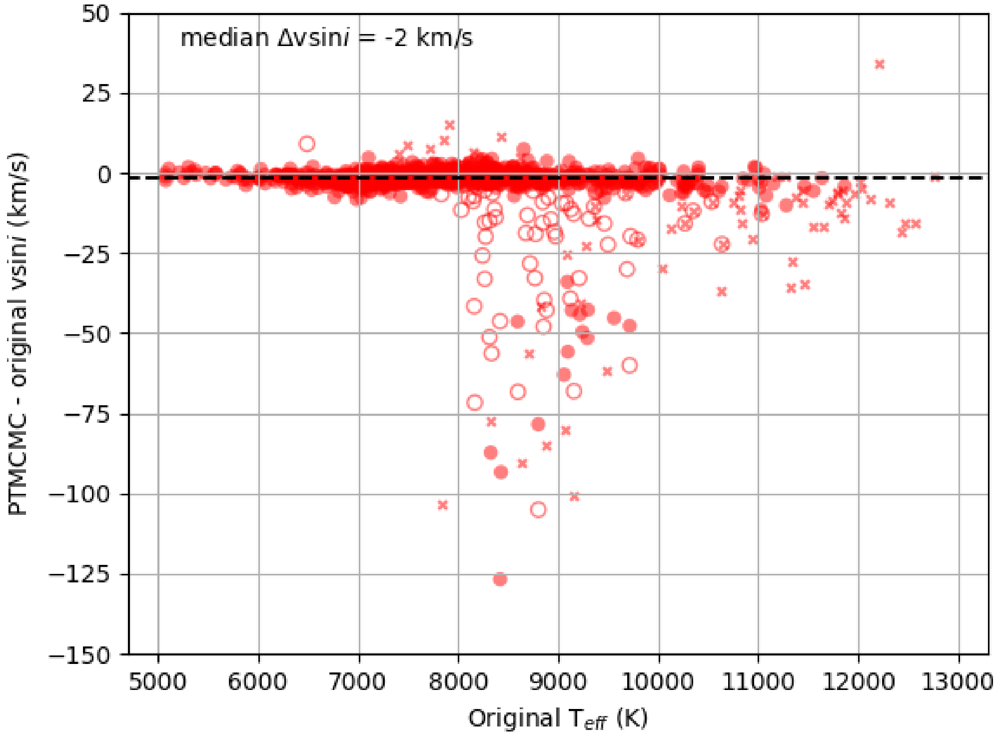

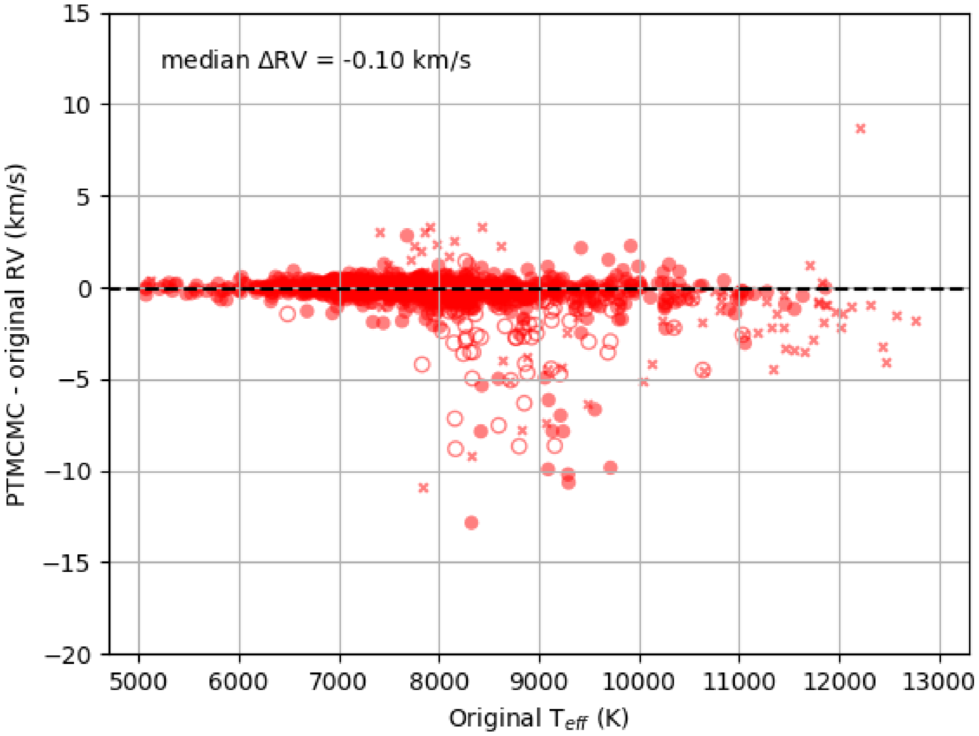

FIGURE 7.6: *Same as Figure 7.1 but for* $v \sin i$ *(top panel) and RV (bottom panel).*

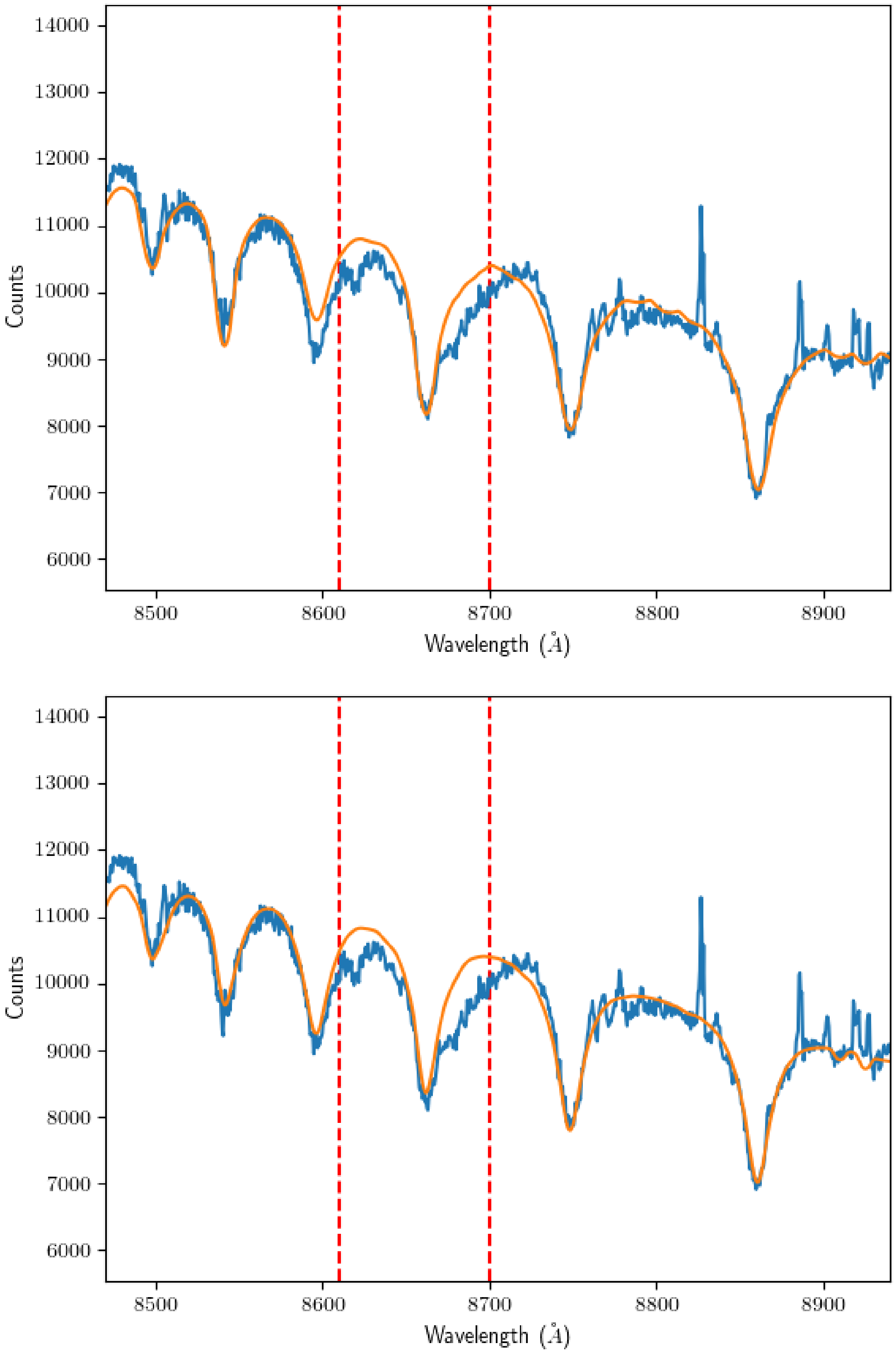

FIGURE 7.7: *A HectoSpec spectrum (blue line) of one of the objects suffering from the Paschen line profile degeneracy, with best-fit template (orange line) from the original MCMC method (top panel) and PTMCMC method (bottom panel). The PTMCMC fit is clearly superior. The original MCMC fit has parameters:* $T_{\rm eff} = 7842\pm^{5258}_{71}$ *K,* $\log g = 3.61\pm^{0.08}_{0.14}$*,* $v\sin i = 266\pm^{15}_{92}$ *km s*$^{-1}$ *and RV*$= -67.3\pm^{5.8}_{8.6}$*, whereas the PTMCMC fit has parmeters:* $T_{\rm eff} = 13195\pm^{141}_{135}$ *K,* $\log g = 3.44\pm^{0.04}_{0.04}$*,* $v\sin i = 163\pm^{19}_{19}$ *km s*$^{-1}$*, and RV*$= -78.1\pm^{4.4}_{4.2}$*.*

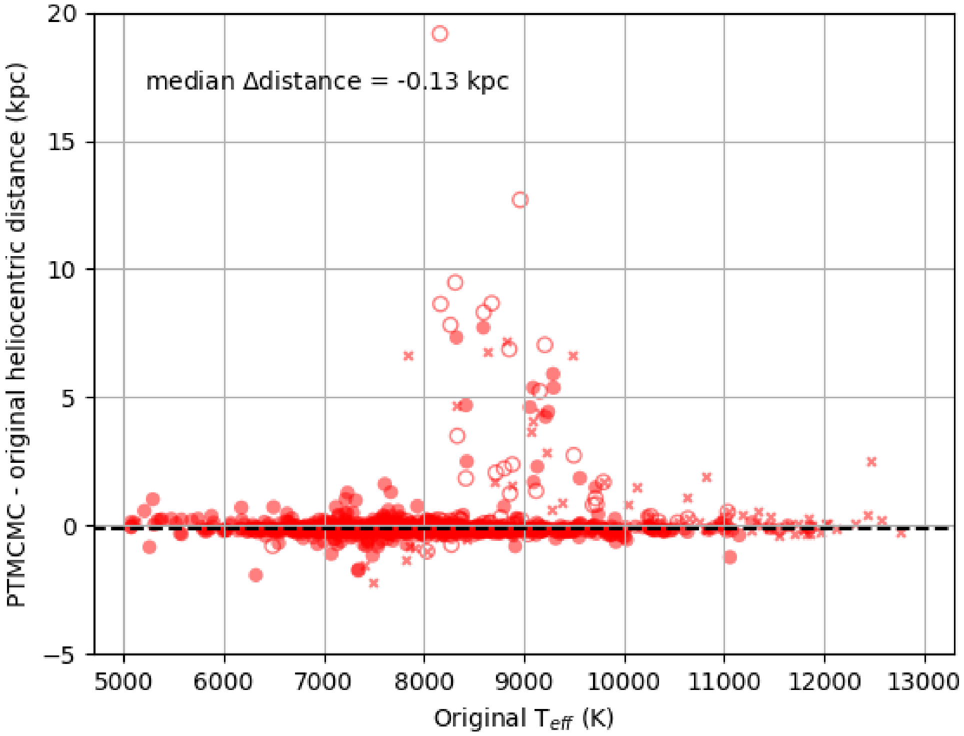

FIGURE 7.8: *Same as Figure 7.1 but for distance.*

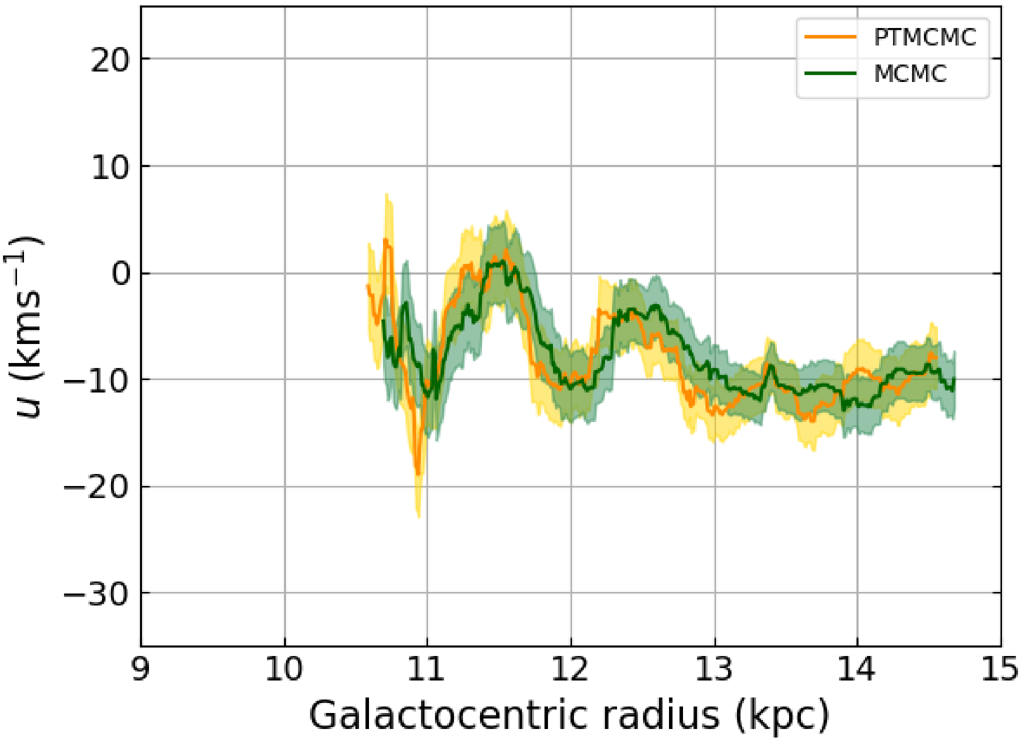

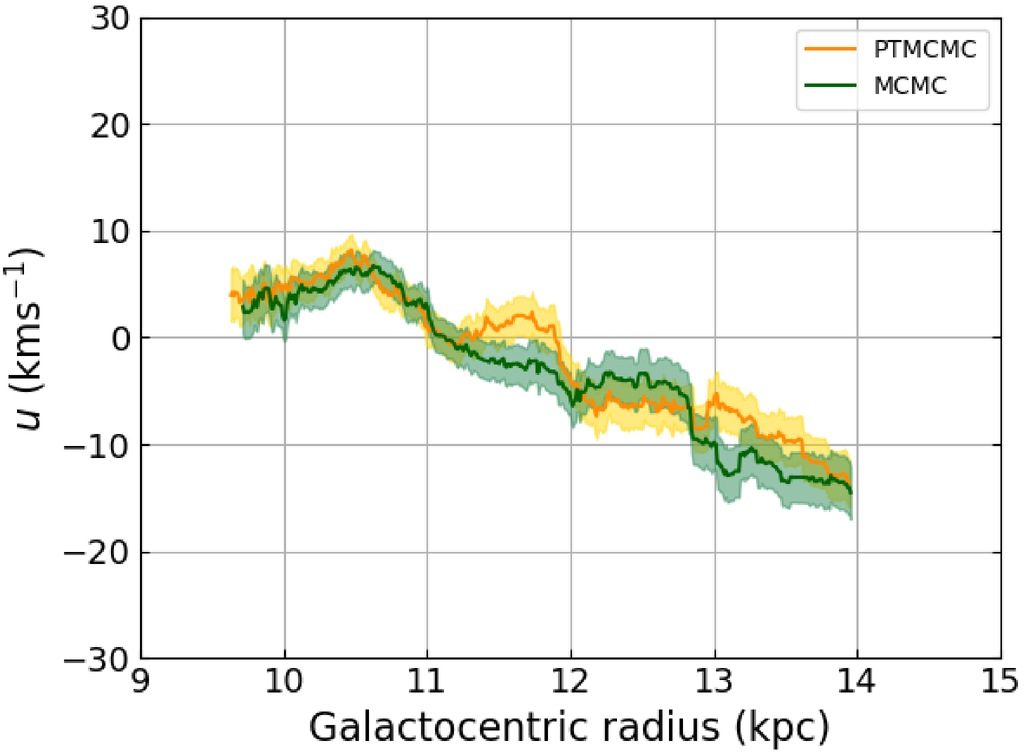

FIGURE 7.9: *Comparison of the $u(R_G)$ trends obtained using the PTMCMC parameters (orange line) and MCMC parameters (green line), for $\ell = 178^\circ$ (top) and $\ell = 118^\circ$ (bottom).*

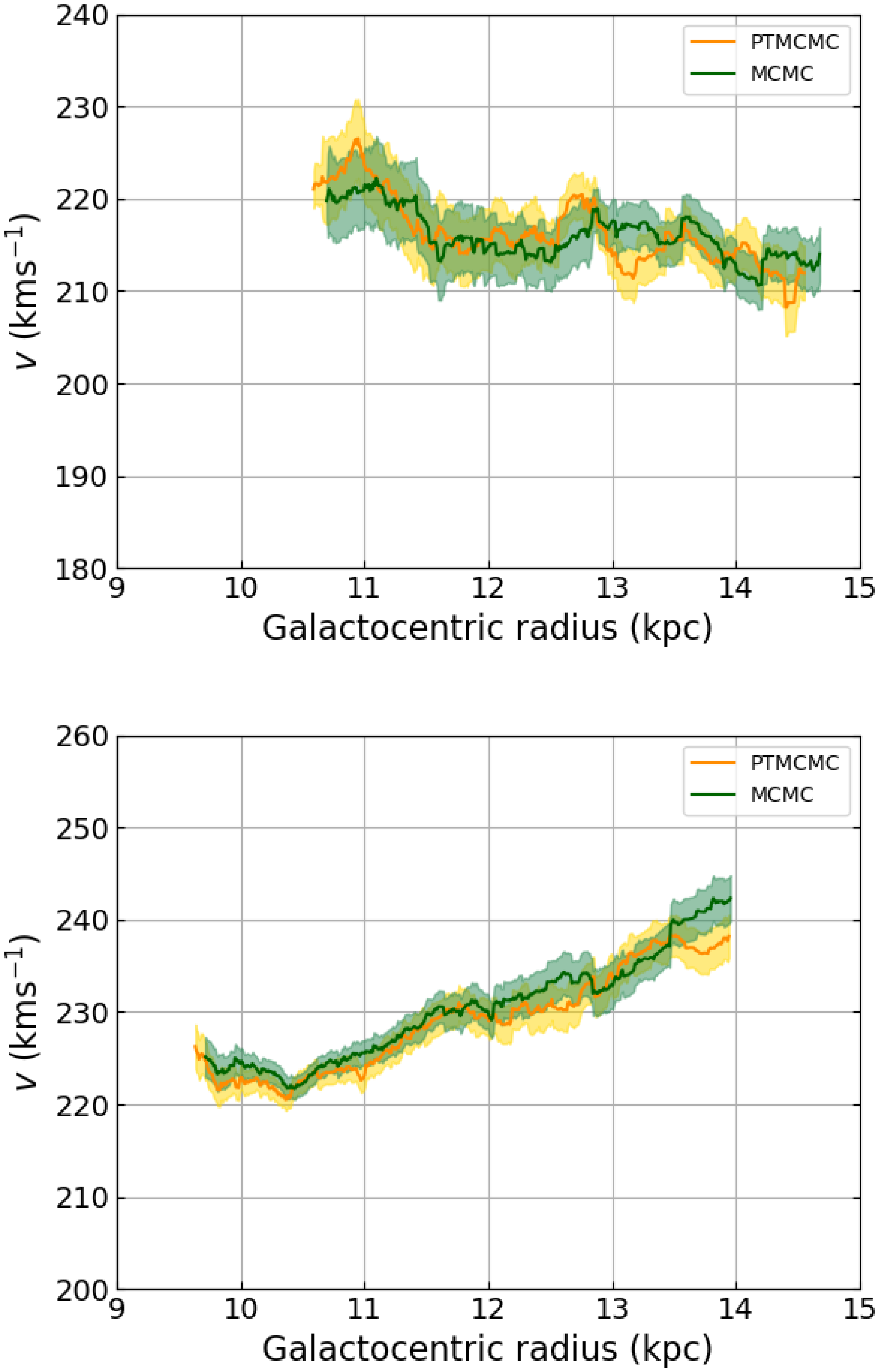

FIGURE 7.10: *Comparison of the $v(R_G)$ trends obtained using the PTMCMC parameters (orange line) and MCMC parameters (green line), for $\ell = 178°$ (top) and $\ell = 118°$ (bottom).*

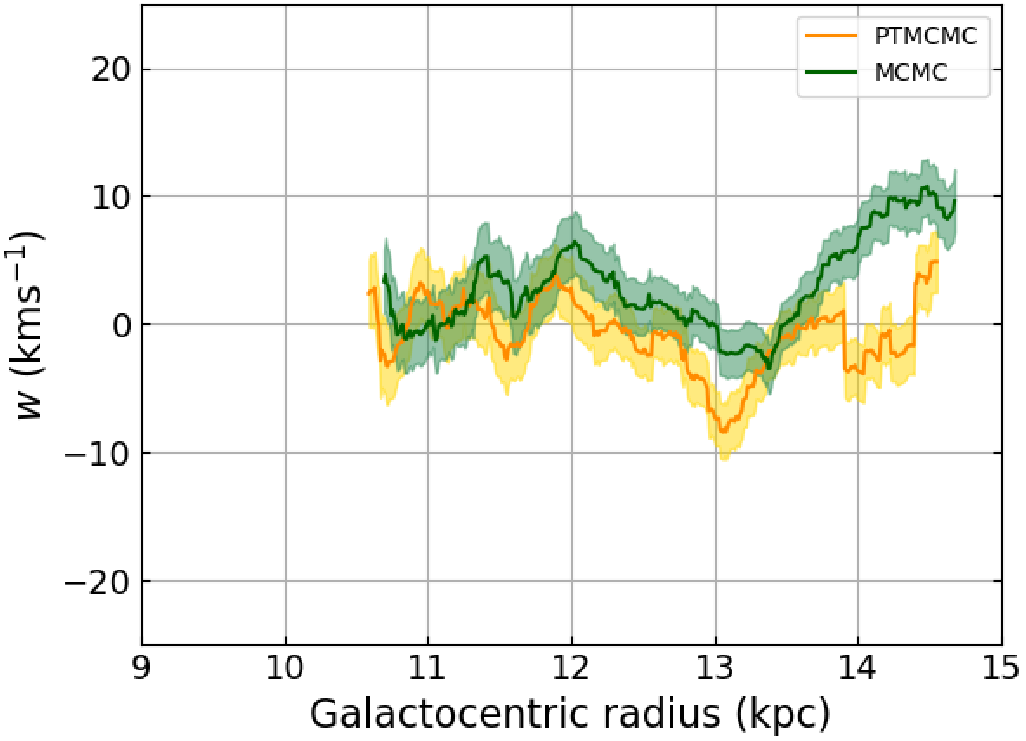

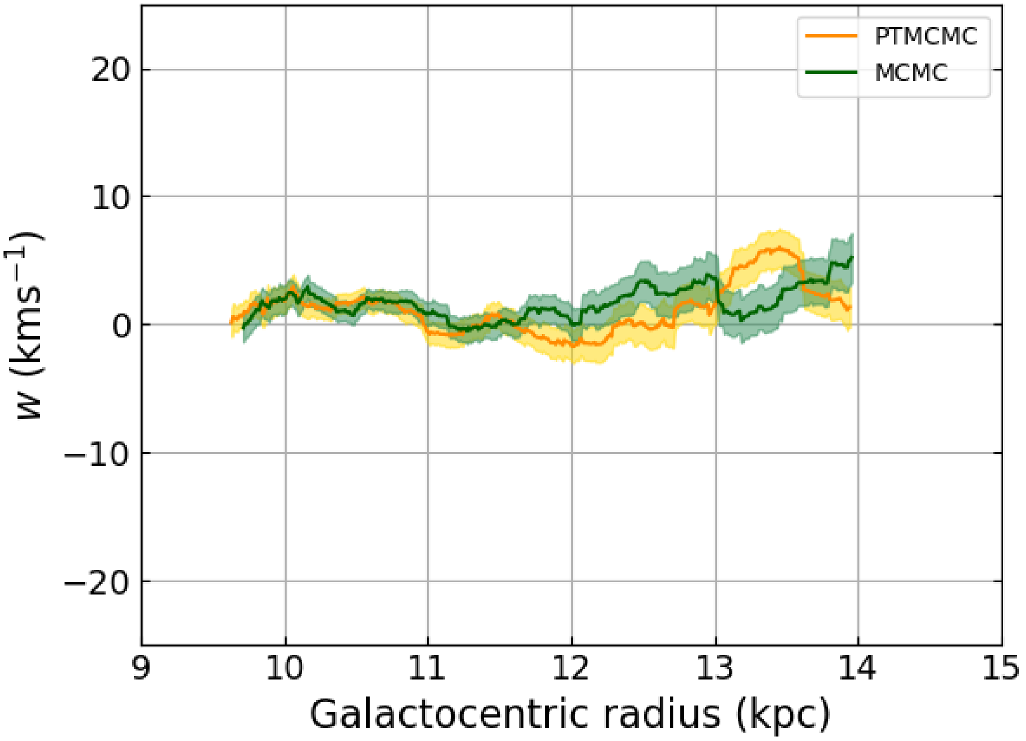

FIGURE 7.11: *Comparison of the $w(R_G)$ trends obtained using the PTMCMC parameters (orange line) and MCMC parameters (green line), for $\ell = 178°$ (top) and $\ell = 118°$ (bottom).*

7.1.2 Testing PTMCMC fitting with WEAVE simulated spectra

WEAVE is a multi-object spectrograph in construction for the 4.2 m William Herschel Telescope (WHT), located at the Observatorio del Roque de los Muchachos in the Canary Islands. It will allow for up to ~ 950 optical spectra to be taken in a single exposure, covering a 2° diameter field of view. It also has the capability to perform integral-field spectroscopy. The fibre-fed spectrograph has both a red arm and a blue arm, and offers spectroscopy in low and high resolutions of $R \sim 5000$ and 20000.

With operations expected to begin in the Spring of 2020, the spectra to be obtained are aimed at complementing data from the ongoing Gaia mission. In particular, the Stellar, Circumstellar and Interstellar Physics (SCIP) survey for WEAVE, of which I am a science team member, will provide radial velocities of photometrically-selected OBA stars, completing the kinematics provided by Gaia astrometry. The methods employed in this work to measure A-type stellar parameters and radial velocities will enable the analysis of Galactocentric velocity trends, including the rotation curve, via WEAVE spectroscopy.

In preparation for the start of WEAVE operations, a number of operational rehearsals have been performed. The third, OpR3, provided full spectroscopic simulations with the aim of testing the quality of the data output as a function of source brightness and observing conditions, and the recovery of the desired parameters using the WEAVE Advanced Processing System (APS) pipeline. In this, the whole observing process is simulated, with artificial images constructed using up to ~ 950 spectra and taking into account sky background and shot noise. The artificial images are passed through the WEAVE pipeline to produce extracted 1D wavelength and flux calibrated (simulated) spectra. The simulated spectra provide an opportunity to test our method of measuring stellar parameters and radial velocities by comparison with known inputs, and also to compare our measurements with those from the APS pipeline. We present the results of these comparisons in this Section.

The WEAVE-like simulated spectra that we analyse here consist of > 1500 low-resolution blue and red spectra of single stars. The set of simulated spectra have the following properties, with roughly the same number of objects in each combination:

- T_{eff}: 7000, 9000, 11000, or 15000 K
- $\log g$: 3.5, 4.0, 4.5

- $v\sin i$: 50, 100, 150 $\mathrm{km\,s^{-1}}$
- RV: 50 $\mathrm{km\,s^{-1}}$
- extinction A_V: 2 or 6
- Solar metallicity

The blue spectra cover the wavelength range $3676\,\text{Å} < \lambda < 6088\,\text{Å}$ and have a resolution ranging between $4500 \lesssim R \lesssim 6000$ over the wavelength range analysed, and the red cover $5772\,\text{Å} < \lambda < 9594\,\text{Å}$ and have a resolution of $6750 \lesssim R \lesssim 7250$ over the wavelength range analysed. Both have wavelength sampling of 0.25 Å.

The template grid we use in our PTMCMC method spans the following parameter space:

- $T_{\rm eff}$: $5000 - 18000$ K
- $\log g$: $2.5 - 5.0$ ($3.0 - 5.0$ for $T_{\rm eff} > 15000$ K)
- $v\sin i$: $0 - 300\,\mathrm{km\,s^{-1}}$
- Solar metallicity

These templates are from the same set as those described in Section 3.1.2. They have been smoothed and rebinned to approximately match the resolution and sampling of the simulated spectra. The FWHM adopted for the simulated spectra are 1.3 Å in the CaT region, and 0.84 Å in the blue region, and these are constant across the wavelengths examined.

The templates used in the PTMCMC method actually form the basis of the simulated spectra. They are used as input for the simulations, which are then exposed to observational and instrumental effects. This test therefore has a slight advantage relative to APS in the fact that there is a template that is an exact match to each input spectrum, which would not be the case when analysing real spectra.

We use the PTMCMC method described in Section 7.1. For the CaT region, we use 5 temperatures, 200 walkers, 2000 steps and a 250 step burn-in. For the blue region, we use 8 temperatures, 200 walkers, 2000 steps and a 250 step burn-in, increasing to 5000 steps for the hottest objects with $T_{\rm eff} = 11000, 15000$ K. These values were determined experimentally. We used this method on both the red region ($8470 - 8920$ Å), which includes the three CaT lines and six Paschen lines, and the blue region ($4000 - 4600$ Å) which includes two Balmer lines.

We multiply the output flux by the calibration function, which reflects the response of the instrument as determined by (simulated) white dwarf calibrators. All WEAVE fields will contain white dwarfs that will be used for calibrations. This means that the calibration function will be available in the real survey data in order to correct for the instrument and CCD response. Multiplication by the calibration function is done since without it the results in the CaT region, whilst overall very satisfactory, showed small offsets in the $T_{\rm eff}$ measurements relative to the input values. We believe these offsets were likely a response to how the continuum changes with different $\log g$ values at different temperatures. For this instrument, a linear mapping function is not optimal, especially in the case of the hottest objects which returned $T_{\rm eff}$ values that were too hot by up to 1000 K. By using the calibration function, the non-linear instrumental response was eliminated, and the offsets went away.

We first present the results determined using the CaT region.

7.1.2.1 Results using the CaT region

The difference between the measured and input $T_{\rm eff}$ values is shown in the top panel of Figure 7.12. The bottom panel shows this difference as a function of i magnitude, coloured by the 1σ uncertainty. The PTMCMC recovers the temperature satisfactorily in almost all cases, with a median difference of -11 K. A gaussian fit to the peak in the upper panel returns a mean of 4 K with a standard deviation of 43 K. There is a small tail to negative $\Delta T_{\rm eff}$ values, showing there is a tendency to measure temperatures that are slightly too cool. Of the ~ 1500 spectra analysed, 94% have a fractional difference $\Delta T_{\rm eff}/T_{\rm eff} < 10\%$, and 92% have $\Delta T_{\rm eff}/T_{\rm eff} < 5\%$.

The bottom panel reveals that the objects with measurement that are very different to the input value ($\Delta T_{\rm eff} \sim 6000$ K) are fainter objects. In 9% of cases, the difference between the measured and input $T_{\rm eff}$ is > 500 K. It is generally the case that their measurements are accompanied by suitably large error. In approximately 50% of cases, the $T_{\rm eff}$ measurement is consistent with the input value within 1σ uncertainty, rising to 77% within 2σ, and 88% within 3σ. Figure 7.13 shows $\Delta T_{\rm eff}$ as a function of input $T_{\rm eff}$, coloured by input $\log g$. This reveals that the temperature recovery is very good for the objects with $T_{\rm eff} \leq 11000$ K, but those with larger $\Delta T_{\rm eff}$ are hot objects with $T_{\rm eff} = 15000$ K. 32% of the 15000 K objects have a temperature too cool by over 500 K. In these cases, the apparent magnitudes are towards the fainter end, with 94% having $i = 16.4$ or fainter.

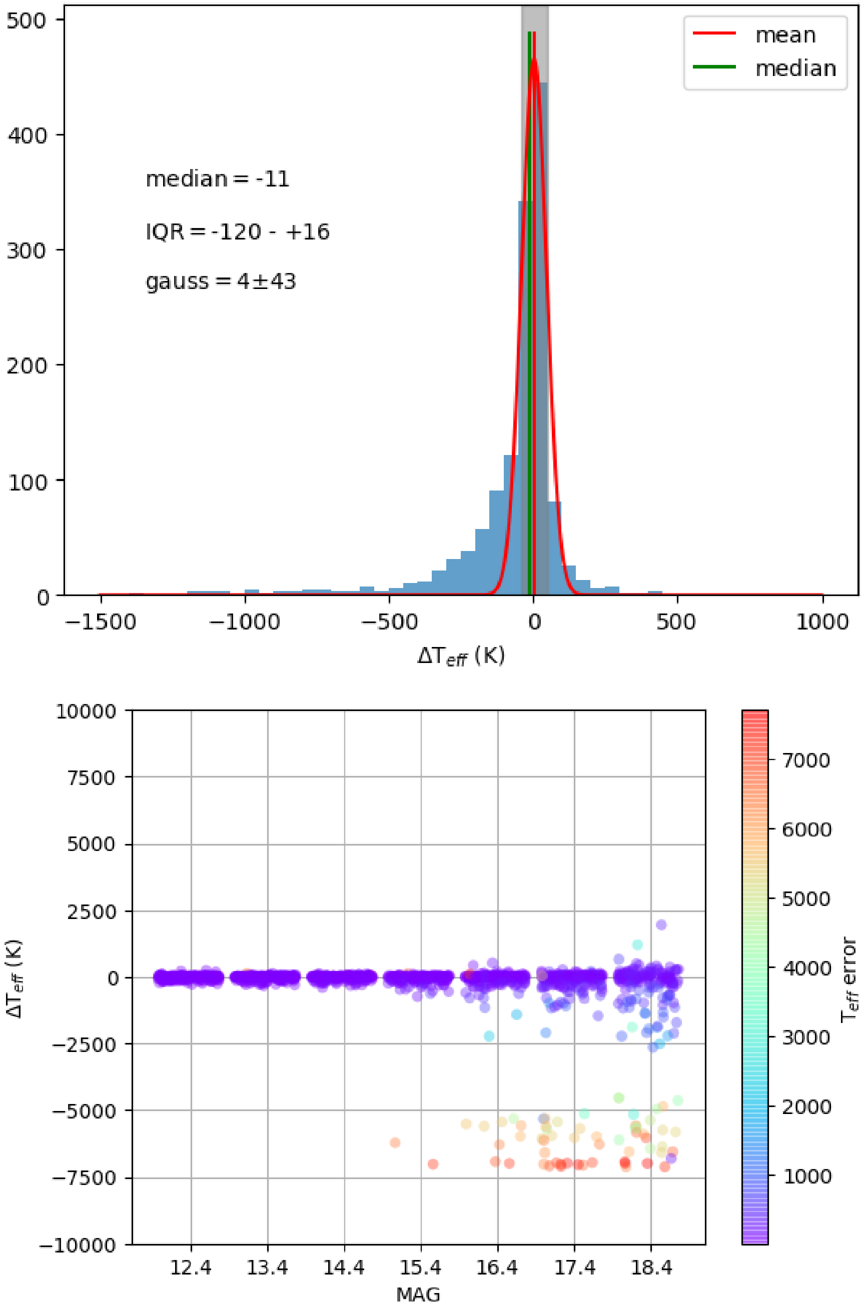

FIGURE 7.12: *Output - input* T_{eff} *(top), and as a function of apparent i magnitude (bottom) from the analysis of the CaT region. The apparent magnitudes have had a random number between* ±0.4 *added for visual clarity. The x ticks represent the true input values. The colour indicates the error on the measured* T_{eff}, *where objects with a negative output - input difference display the positive error, and vice versa.*

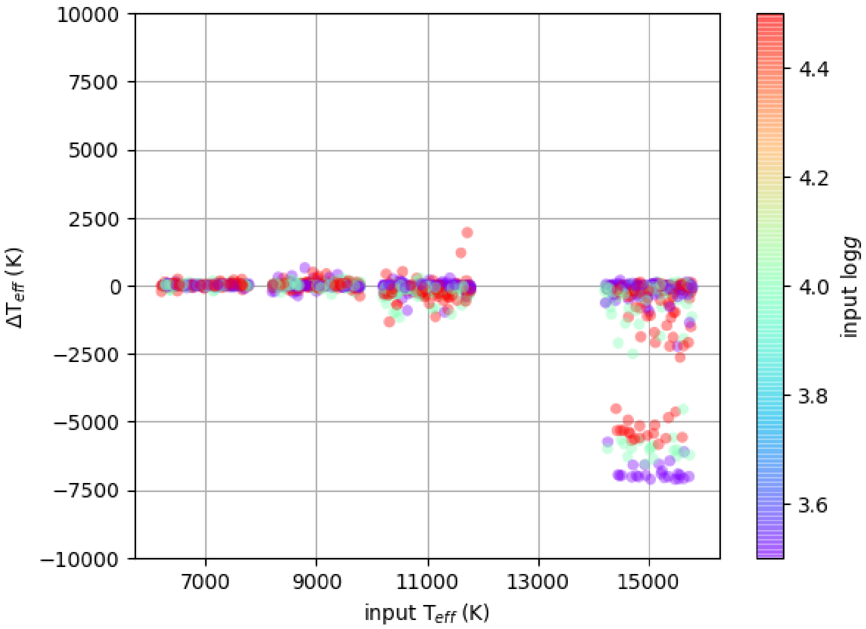

FIGURE 7.13: *Output - input $T_{\rm eff}$ as a function of input $T_{\rm eff}$ from the analysis of the CaT region. The x-axis values have had a random number between* ±800 *added for visual clarity. The x ticks represent the true input values. The colour indicates the input* $\log g$ *value.*

Figure 7.14 shows the differences between the $\log g$ values. The recovered values are very close to the input values. The mean and median differences are just 0.01. The standard deviation of the values is 0.02. Those with larger differences are generally fainter objects, and are accompanied by larger uncertainty. In approximately 60% of cases, the $\log g$ measurement is consistent with the input value within 1σ uncertainty, rising to 81% within 2σ, and 89% within 3σ. Figure 7.15 shows the $\log g$ differences as a function of input $T_{\rm eff}$, coloured by input $\log g$. The hot objects ($T_{\rm eff} = 15000$ K) that have large $\Delta T_{\rm eff}$ values also have large $\Delta \log g$ values, in the sense that the $\log g$ measurement is too large by up to 1.0 dex, likely compensating for the incorrect $T_{\rm eff}$ measurement. Disregarding these obviously erroneous objects momentarily, in general the $\Delta \log g$ is larger for the coolest objects, reflecting the increasing difficulty of $\log g$ determination with decreasing temperature.

Figure 7.16 shows the differences between the $v \sin i$ values. The median difference is $2\,{\rm km\,s^{-1}}$, and the mean and standard deviation of the gaussian fit to the peak are $1\,{\rm km\,s^{-1}}$ and $3\,{\rm km\,s^{-1}}$ respectively. For the faintest objects, there is a tendancy for the $v \sin i$ measurement to be too large. These objects with larger differences to the tune of $\Delta v \sin i > 50\,{\rm km\,s^{-1}}$ mostly consist of the small group of hot objects that also have large $T_{\rm eff}$ and $\log g$ differences (see Figure 7.17). In approximately 54% of cases, the $v \sin i$ measurement is consistent with the input value within 1σ uncertainty, rising to 80% within 2σ, and 90% within 3σ.

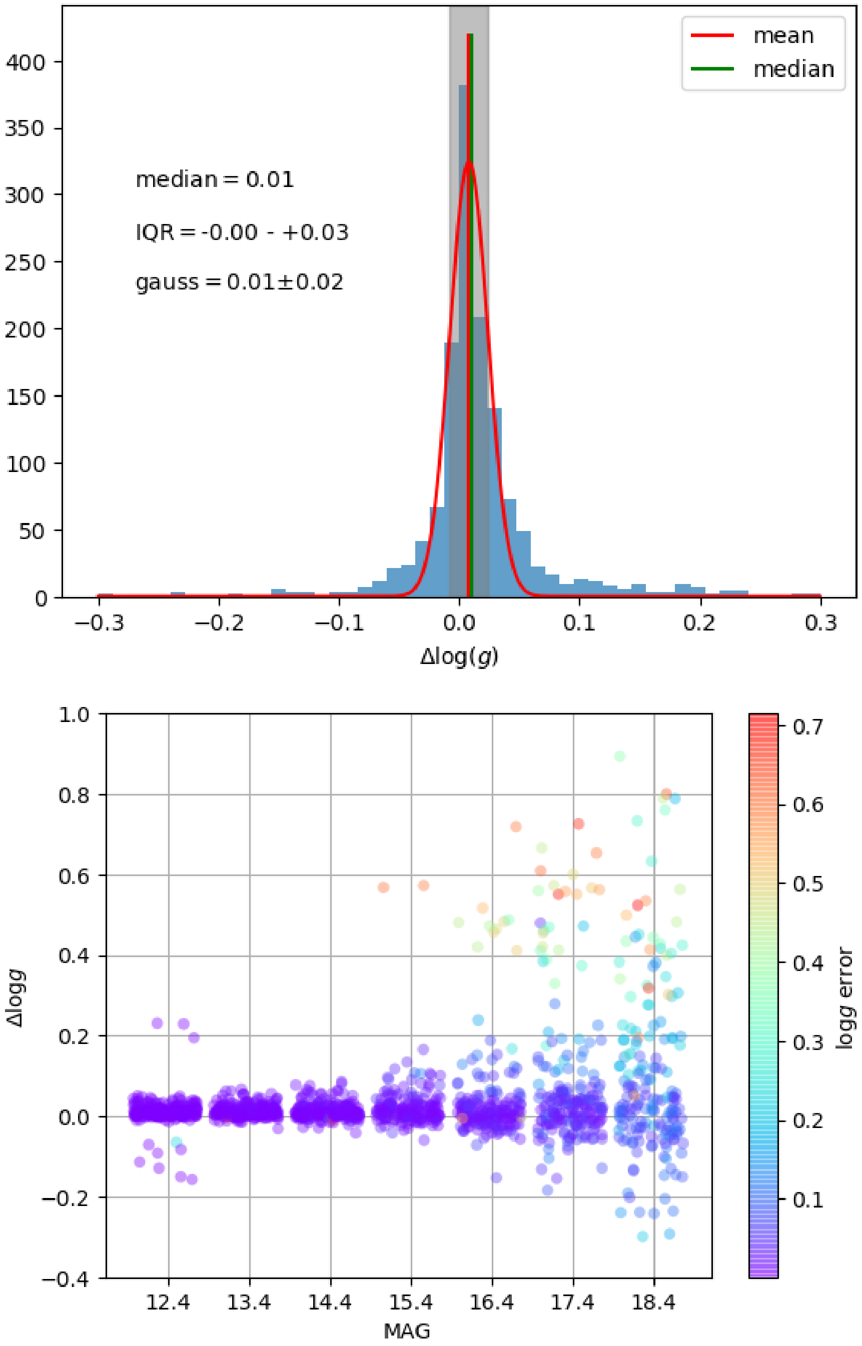

FIGURE 7.14: *Output - input* $\log g$ *(top), and as a function of apparent i magnitude (bottom) from the analysis of the CaT region. The apparent magnitudes have had a random number between* ± 0.4 *added for visual clarity. The x ticks represent the true input values. The colour indicates the error on the measured* $\log g$*, where objects with a negative output - input difference display the positive error, and vice versa.*

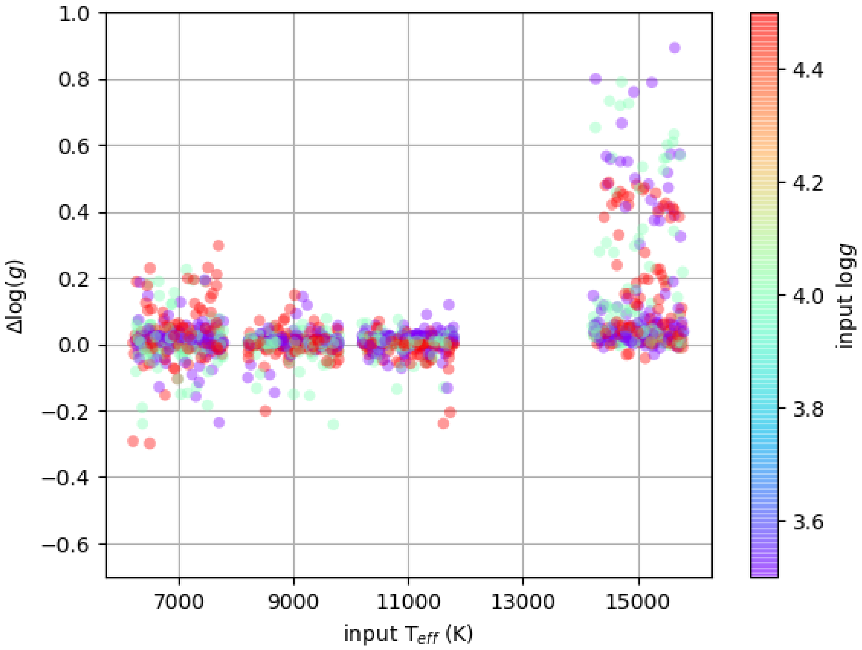

FIGURE 7.15: *Output - input* $\log g$ *as a function of input* $T_{\rm eff}$ *from the analysis of the CaT region. The x-axis values have had a random number between* ± 800 *added for visual clarity. The x ticks represent the true input values. The colour indicates the input* $\log g$ *value.*

The differences in the RV values are shown in Figure 7.18. The PTMCMC method recovers the RVs very well, with mean and standard deviation of the differences of just $0.3\,{\rm km\,s^{-1}}$ and $1.2\,{\rm km\,s^{-1}}$ respectively. Furthermore, there is no sign of bias in that the differences are symmetric. Figure 7.19 shows the differences as a function of input $T_{\rm eff}$, coloured by input $\log g$. There is no bias in ΔRV with $T_{\rm eff}$ or $\log g$, but the spread increases slightly for the hotter temperatures, reflecting the decreasing strength of the sharp CaT lines with increasing temperature. In approximately 50% of cases, the RV measurement is consistent with the input value within 1σ uncertainty, rising to 79% within 2σ, and 89% within 3σ.

To conclude, the PTMCMC method using the CaT region of the spectrum recovers all the input parameters ($T_{\rm eff}$, $\log g$, $v\sin i$, RV) to a satisfactory level. Figure 7.20 show two examples of OpR3 simulated spectra with their PTMCMC fits. The median, mean and standard deviations of the differences between measurement and input values for each parameter are summarised in Table 7.2. It was necessary to use the flux that was calibrated to account for the instrumental and CCD response in order to reduce systematic errors that otherwise arose with use of the non-calibrated flux. Overall, the PTMCMC method is well suited to the needs of stellar parameter recovery and radial velocity measurement, and will be used in the future to analyse WEAVE survey products.

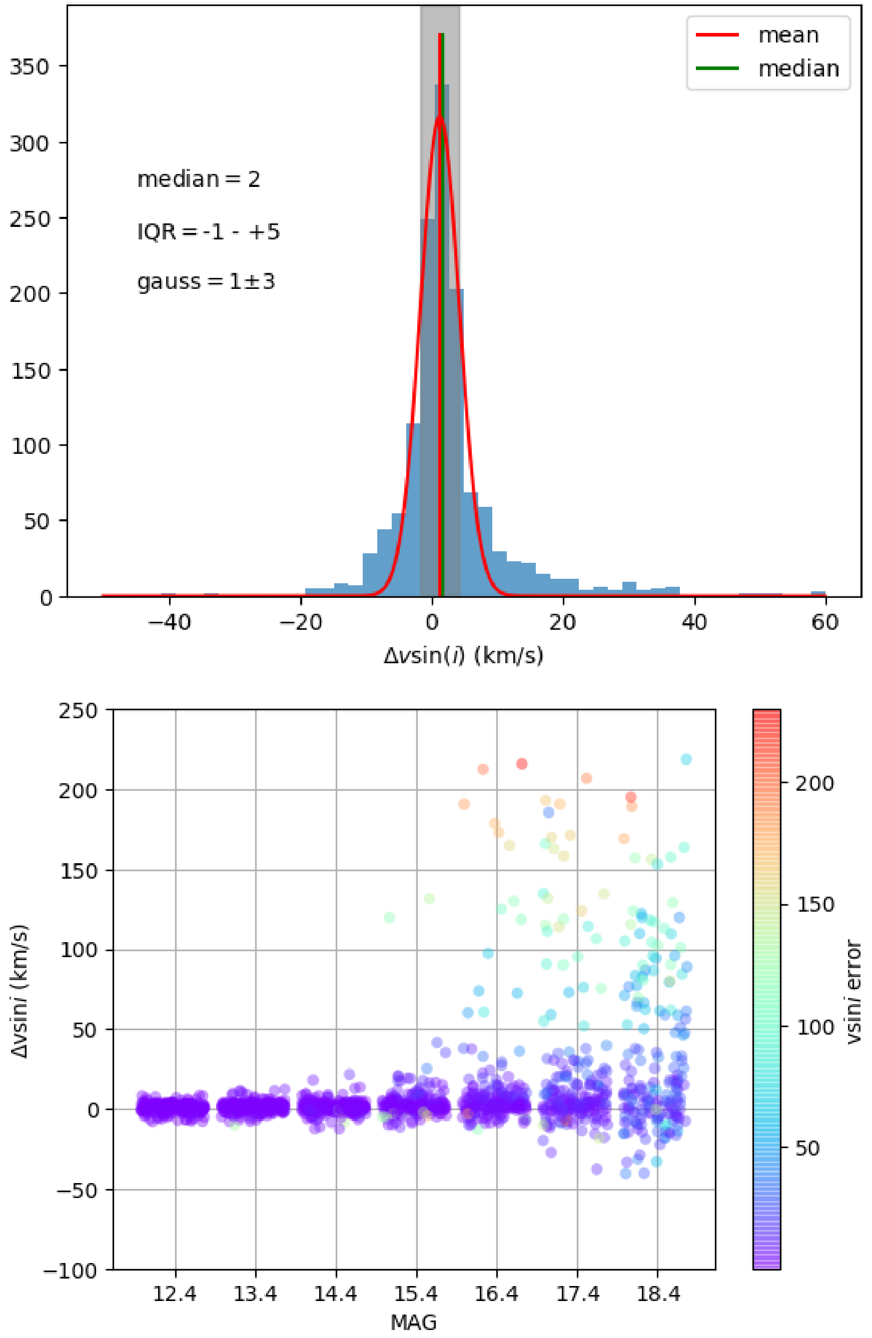

FIGURE 7.16: *Output - input* $v\sin i$ *(top), and as a function of apparent i magnitude (bottom) from the analysis of the CaT region. The apparent magnitudes have had a random number between* ±0.4 *added for visual clarity. The x ticks represent the true input values. The colour indicates the error on the measured* $v\sin i$*, where objects with a negative output - input difference display the positive error, and vice versa.*

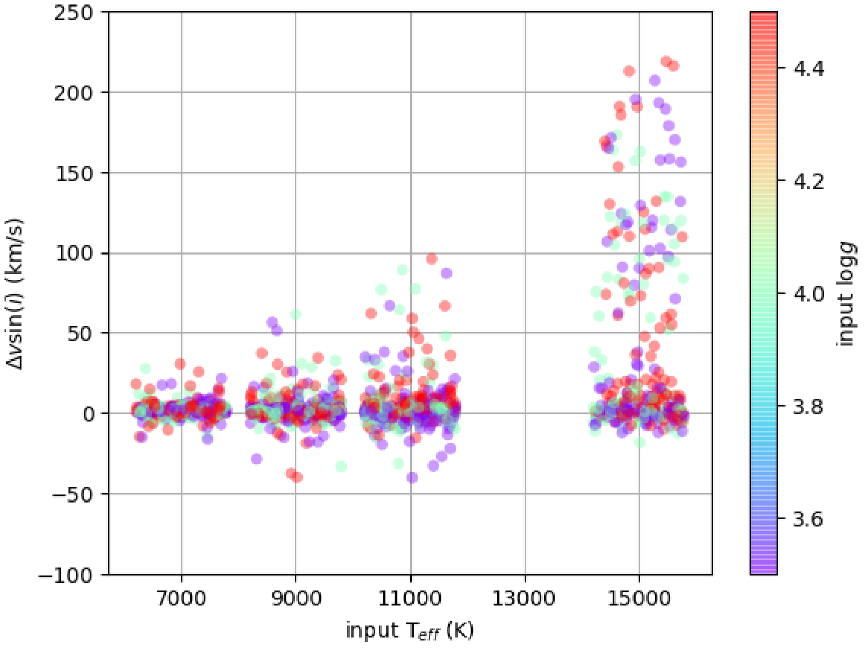

FIGURE 7.17: *Output - input* $v\sin i$ *as a function of input* $T_{\rm eff}$ *from the analysis of the CaT region. The x-axis values have had a random number between* ±800 *added for visual clarity. The x ticks represent the true input values. The colour indicates the input* $\log g$ *value.*

	Median	**Mean**	**Standard deviation**
$T_{\rm eff}$ (K)	-11	$+4$	43
$\log g$	$+0.01$	$+0.01$	0.02
$v\sin i$ (km s^{-1})	$+2$	$+1$	3
RV (km s^{-1})	$+0.4$	$+0.3$	1.2

TABLE 7.2: *Summary of differences between measured parameters and input values.*

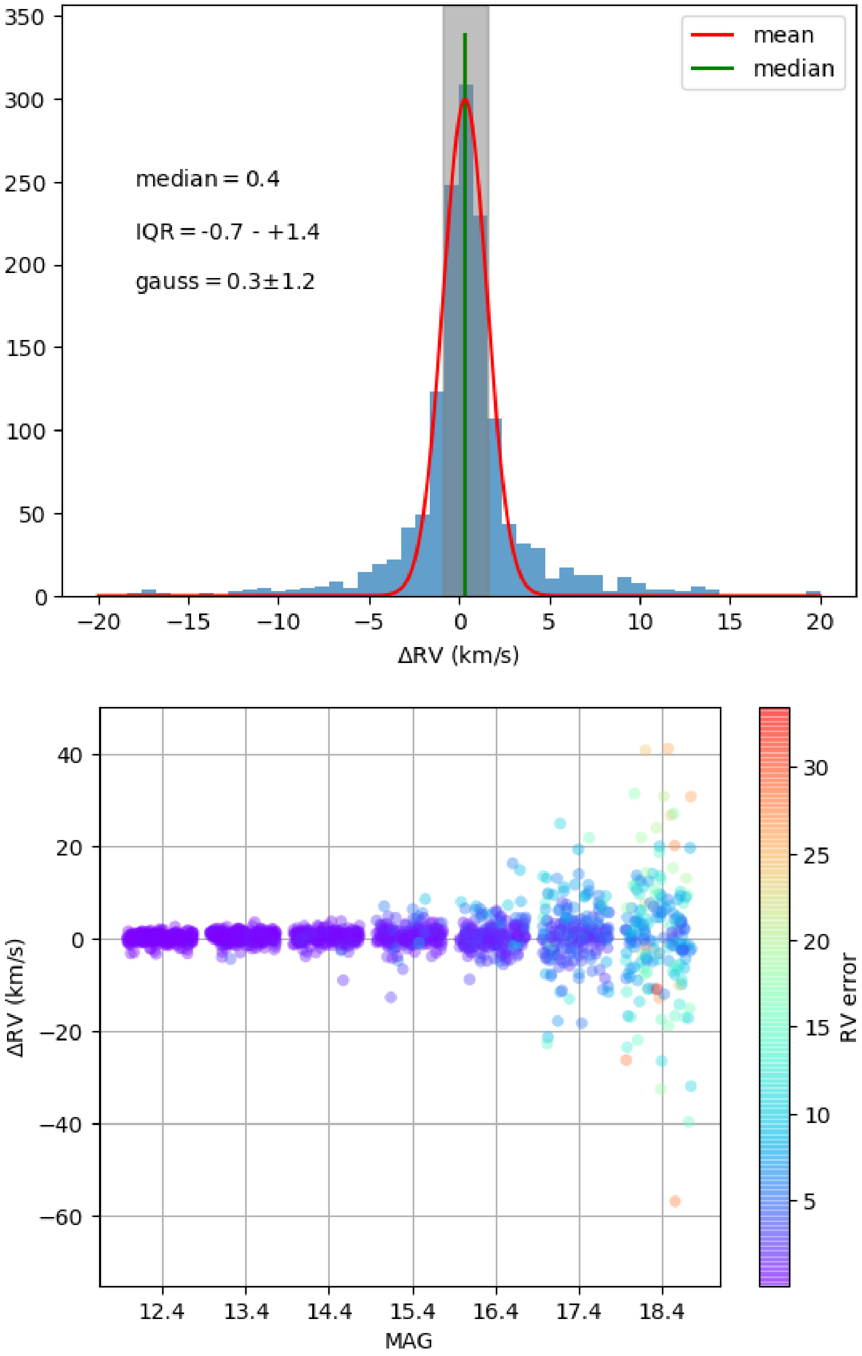

FIGURE 7.18: *Output - input RV (top), and as a function of apparent i magnitude (bottom) from the analysis of the CaT region. The apparent magnitudes have had a random number between* ±0.4 *added for visual clarity. The x ticks represent the true input values. The colour indicates the error on the measured RV, where objects with a negative output - input difference display the positive error, and vice versa.*

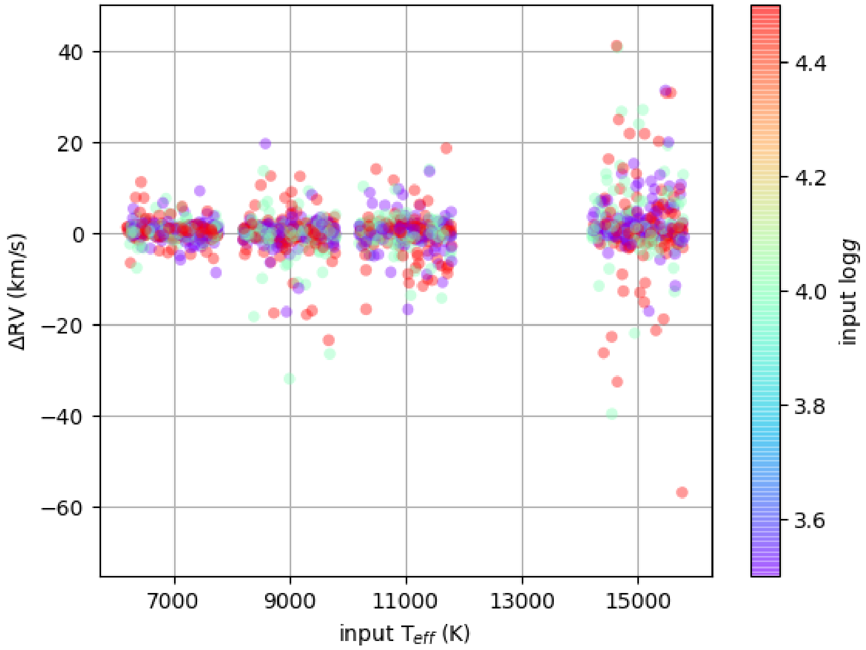

FIGURE 7.19: *Output - input RV as a function of input T_{eff} from the analysis of the CaT region. The x-axis values have had a random number between* ± 800 *added for visual clarity. The x ticks represent the true input values. The colour indicates the input* $\log g$ *value.*

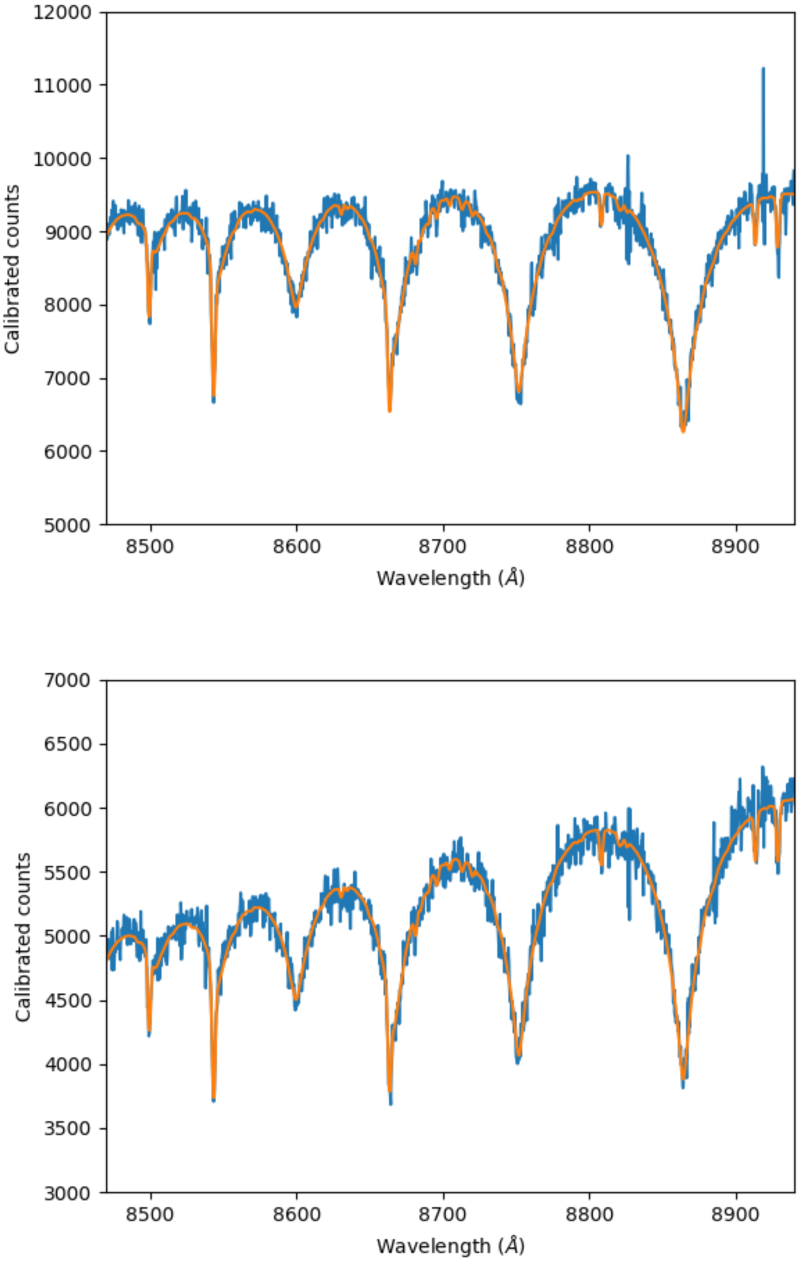

FIGURE 7.20: *Two examples of OpR3 simulated spectra with their PTMCMC fits. Both have input parameters* $T_{\mathrm{eff}} = 9000\,K$, $\log g = 4.0$, $v \sin i = 50\,km\,s^{-1}$, *and* $RV = 50\,km\,s^{-1}$. *The top has apparent magnitude* $i = 15.4$ *and* $A_V = 2$, *and the bottom has* $i = 16.4$ *and* $A_V = 6$. *The measured parameters for the top are:* $T_{\mathrm{eff}} = 9034\pm^{45}_{41}\,K$, $\log g = 4.02\pm^{0.01}_{0.01}$, $v \sin i = 52\pm^{3}_{4}\,km\,s^{-1}$, *and* $RV = 50.5\pm^{1.0}_{1.0}\,km\,s^{-1}$. *The measured parameters for the bottom are:* $T_{\mathrm{eff}} = 8989\pm^{48}_{45}\,K$, $\log g = 4.00\pm^{0.01}_{0.01}$, $v \sin i = 53\pm^{4}_{4}\,km\,s^{-1}$, *and* $RV = 50.7\pm^{1.2}_{1.3}\,km\,s^{-1}$.

7.1.2.2 Comparison of CaT region results with APS

Here we compare our measured T_{eff}, $\log g$ and radial velocity values of the OpR3 simulated spectra to those from the APS pipeline that WEAVE data will pass through by default. The APS pipeline currently returns two sets of values by using two different methods. The first is based on an algorithm known as FERRE[3] (Allende Prieto et al., 2006). The second we refer to as 'RVS', and is described in Koposov et al. (2011). Both methods are based on a χ^2 minimisation between the observed spectrum and a set of templates. A point of difference is that our PTMCMC method uses the same templates as were input to the simulation. To perform a more fair comparison science verification data will be needed. We do not compare $v \sin i$ measurements, since the ferre method does not fit a $v \sin i$ parameter, and there is an issue with the RVS $v \sin i$ values piling up at the edges of their grid.

Figure 7.21 compares the T_{eff} results from the PTMCMC method (black) to the ferre APS results (red) and the RVS APS results (blue). The PTMCMC method more accurately and precisely returns the input T_{eff} than either APS method. A similar comparison is shown in Figure 7.22 for the $\log g$ values. Both the APS methods return $\log g$ values that are systematically larger than the input value by $\sim 0.5 - 1.0$, whereas our PTMCMC is successful in recovering the input value. This may suggest a discrepancy between the template sets used in the APS methods and the template set we use here/in the simulated spectra. On the other hand, since the APS pipelines either do not fit, or unsatifactorily fit, for a $v \sin i$ parameter, this could well interfere with the $\log g$ recovery since both parameters work to broaden the spectral lines.

Figure 7.23 compares the RV measurements from the PTMCMC method and the APS methods. While all 3 methods return fairly accurate results, the spread of differences for our PTMCMC method is slightly reduced compared to the APS methods.

We conclude that for B/A-type stars, our PTMCMC method does a better job at recovering the three compared stellar parameters, in particular $\log g$ where the APS results show a large systematic offset. However further comparison should be done against science verification data, which will remove the advantage of the PTMCMC being based on the same underlying templates as the simulated spectra.

---

[3] Details can be found here `http://hebe.as.utexas.edu/ferre/`

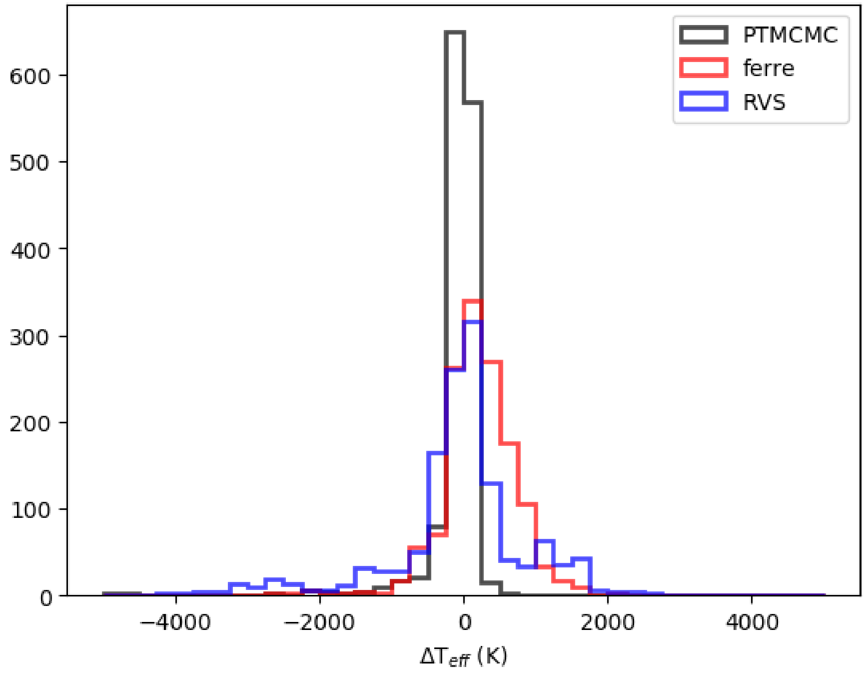

FIGURE 7.21: *Comparison of output - input* T_{eff} *PTMCMC results (black) with APS ferre results (red) and rvs results (blue), from the analysis of the CaT region.*

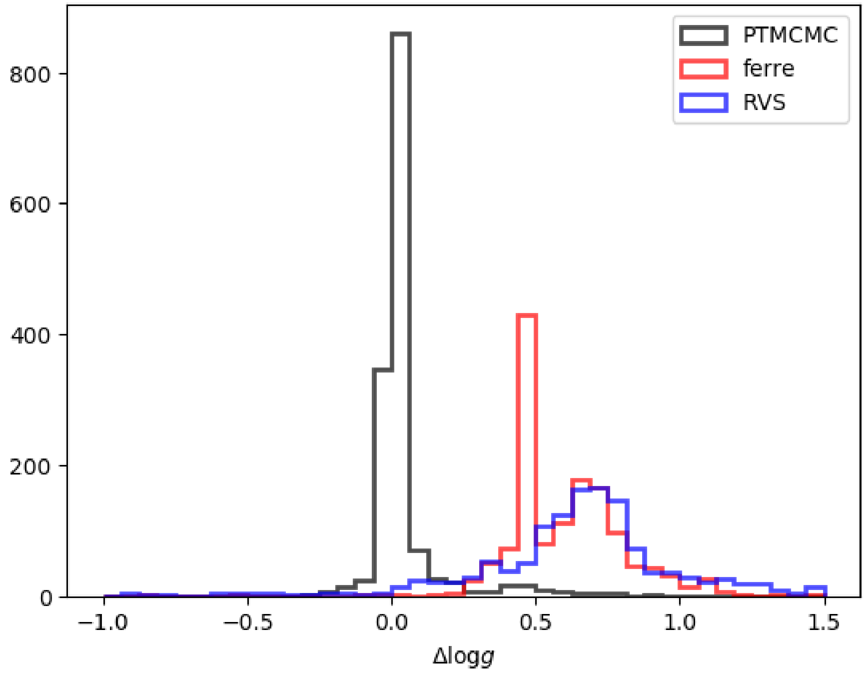

FIGURE 7.22: *Comparison of output - input* $\log g$ *PTMCMC results (black) with APS ferre results (red) and rvs results (blue), from the analysis of the CaT region.*

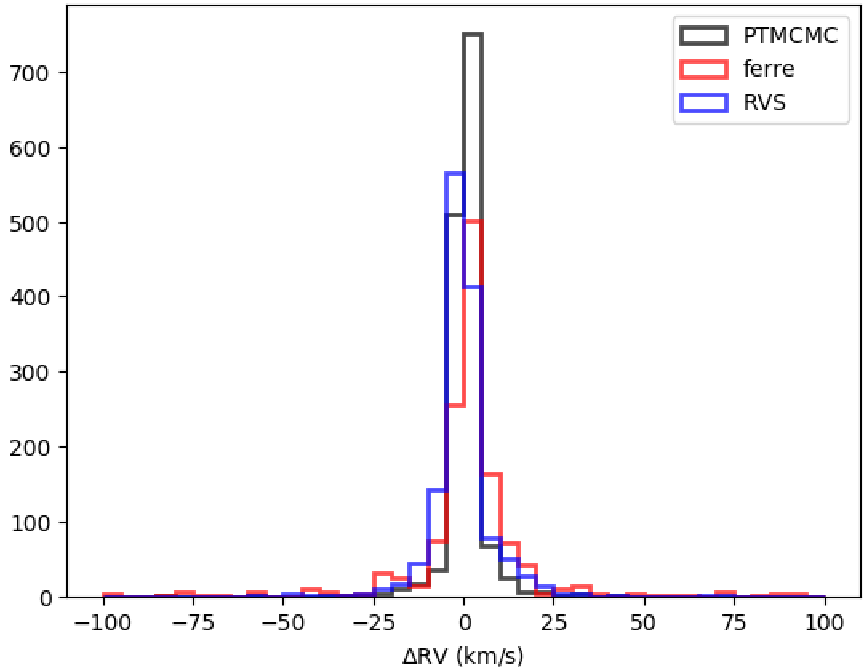

FIGURE 7.23: *Comparison of output - input RV PTMCMC results (black) with APS ferre results (red) and rvs results (blue), from the analysis of the CaT region.*

7.1.2.3 Results using the blue wavelength range

The recovery of parameters using the blue region is less sucessful than using the CaT region. The top panel of Figure 7.24 shows the $\Delta T_{\rm eff}$ values, and the bottom panel shows these as a function of the median square root of counts of the spectra. Figure 7.25 shows the differences as a function of input $T_{\rm eff}$. The PTMCMC routine struggles to recover the $T_{\rm eff}$ value for spectra with low counts, and for the hottest objects ($T_{\rm eff} \geq 11000\,$K). The story is similar for the $\log g$ and $v \sin i$ parameters. Reassuringly, the RV is recovered well for all objects, including the hottest, that have $\sqrt{counts}$ larger than ~ 10. For the cooler objects ($T_{\rm eff} \leq 9000\,$K), the median differences are $\Delta T_{\rm eff} = 9\,$K, $\Delta \log g = 0.12$, $\Delta v \sin i = 9\,$km s^{-1}, ΔRV$= 2.2\,$km s^{-1}.

In the case of the hot objects, we find that those with badly recovered parameters often do not converge to a single solution in the 5000 steps that are used. A convergence test would be useful for these objects, allowing them to run until they do (if ever) converge. This is mentioned again in Section 7.1.3.1.

Throughout this work (except for part of Section 5.1) the focus has been on the CaT region. It is not surprising then that the PTMCMC method, which was tailored to the CaT region, returns

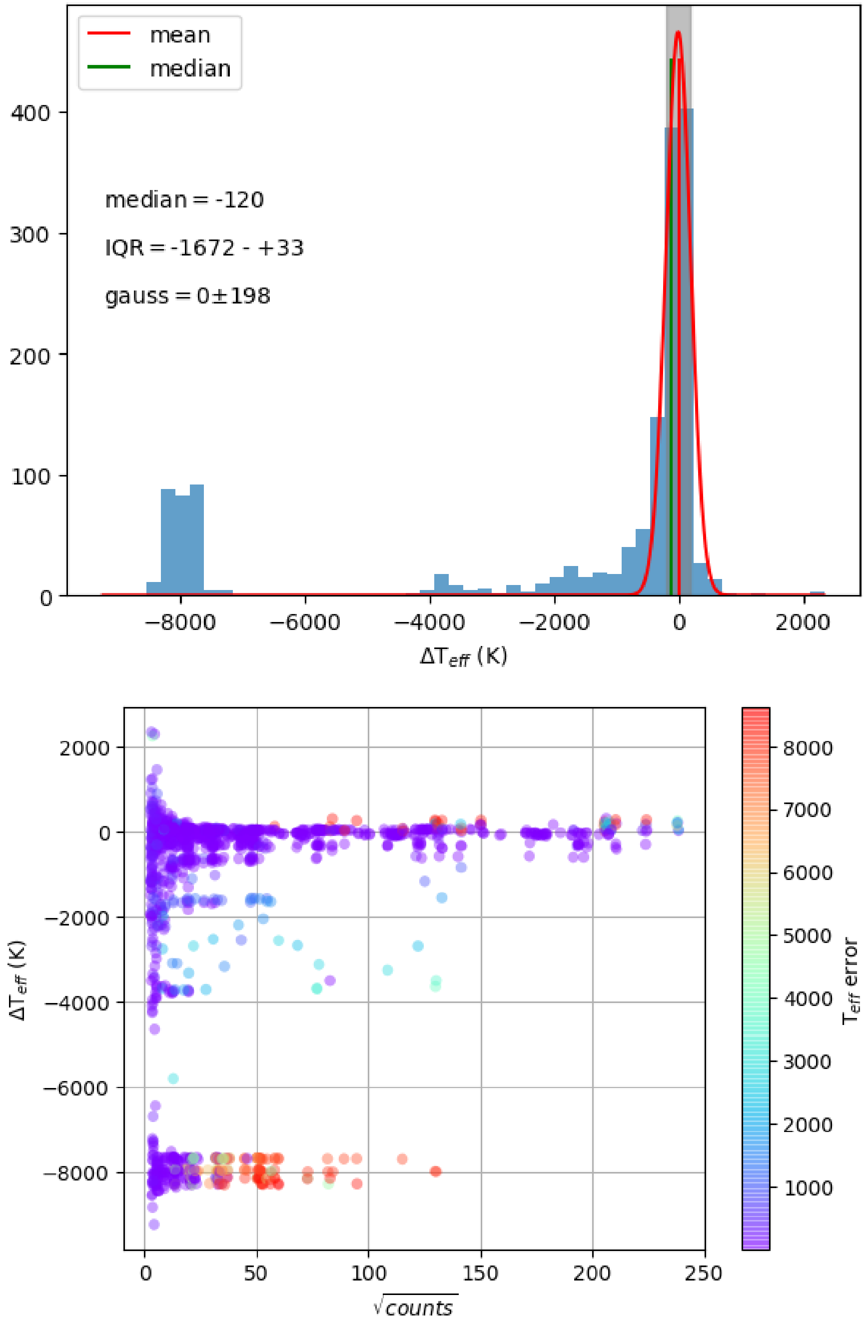

FIGURE 7.24: *Output - input* T_{eff} *(top), and as a function of* $\sqrt{counts}$ *(bottom), from the analysis of the blue region. The colour indicates the error on the measured* T_{eff}*, where objects with a negative output - input difference display the positive error, and vice versa.*

better results for the CaT than for the blue. With more time, the PTMCMC method may be developed to improve current performances in the blue.

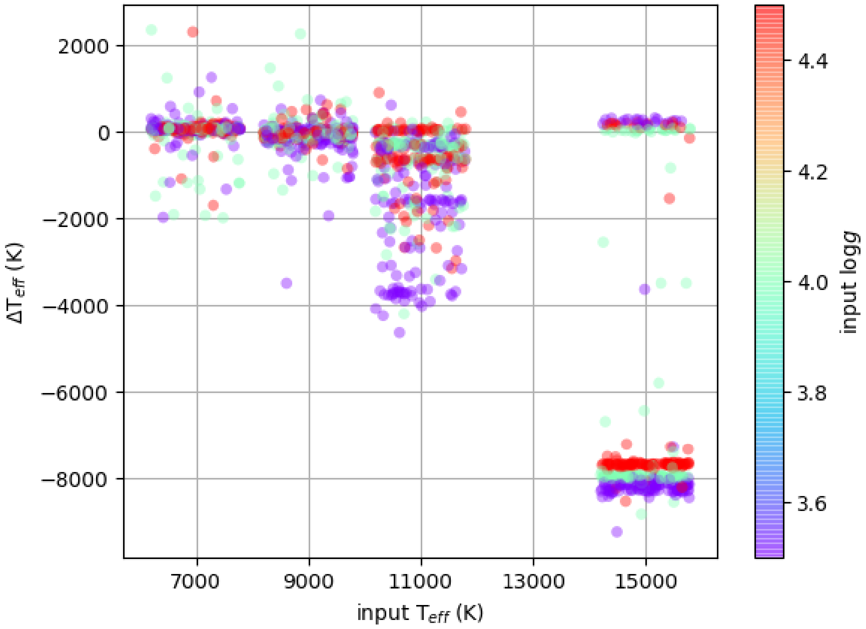

FIGURE 7.25: *Output - input T_{eff} as a function of input T_{eff} from the analysis of the blue region. The x-axis values have had a random number between* ±800 *added for visual clarity. The x ticks represent the true input values. The colour indicates the input* $\log g$ *value.*

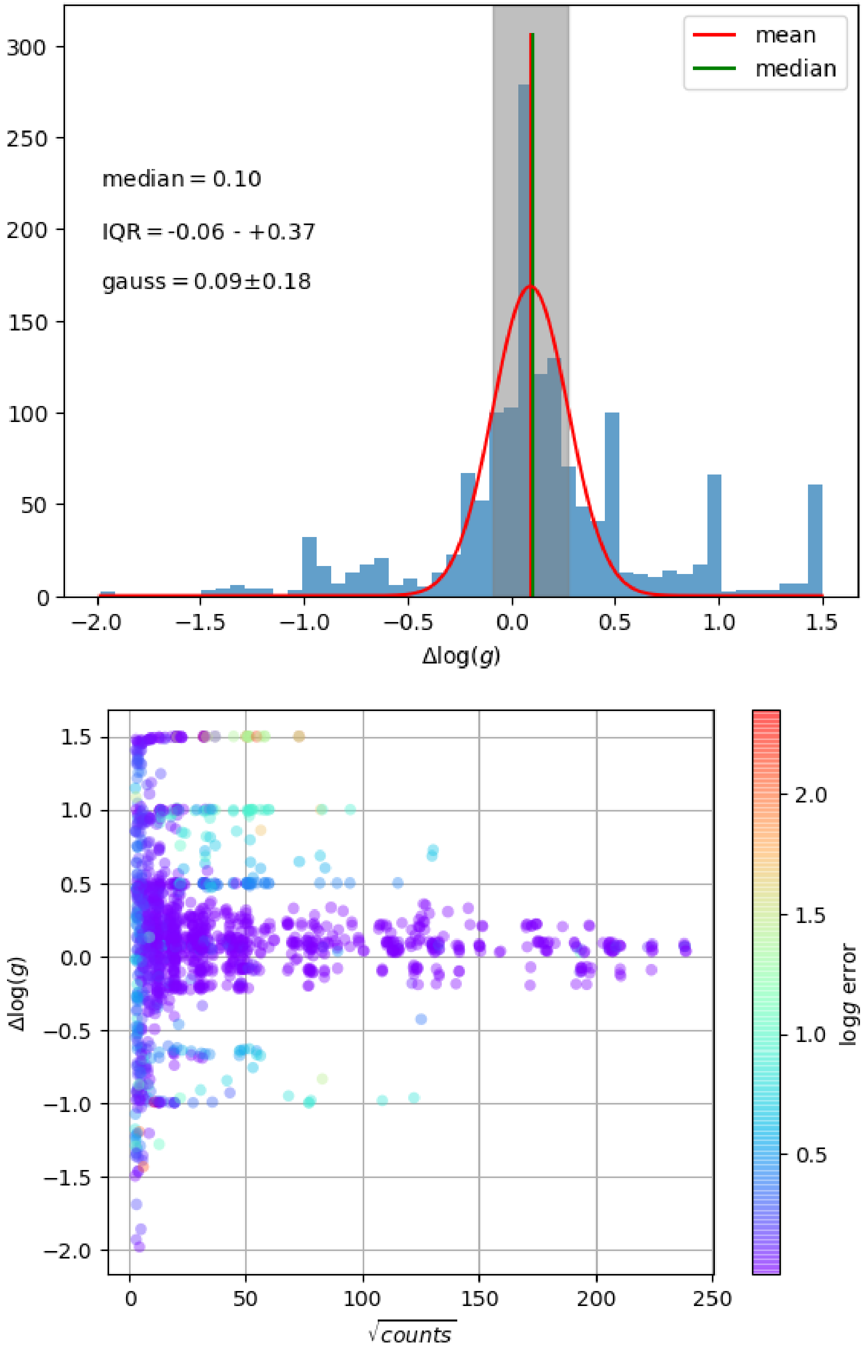

FIGURE 7.26: *Output - input* $\log g$ *(top), and as a function of* $\sqrt{counts}$ *(bottom), from the analysis of the blue region. The colour indicates the error on the measured* $\log g$*, where objects with a negative output - input difference display the positive error, and vice versa.*

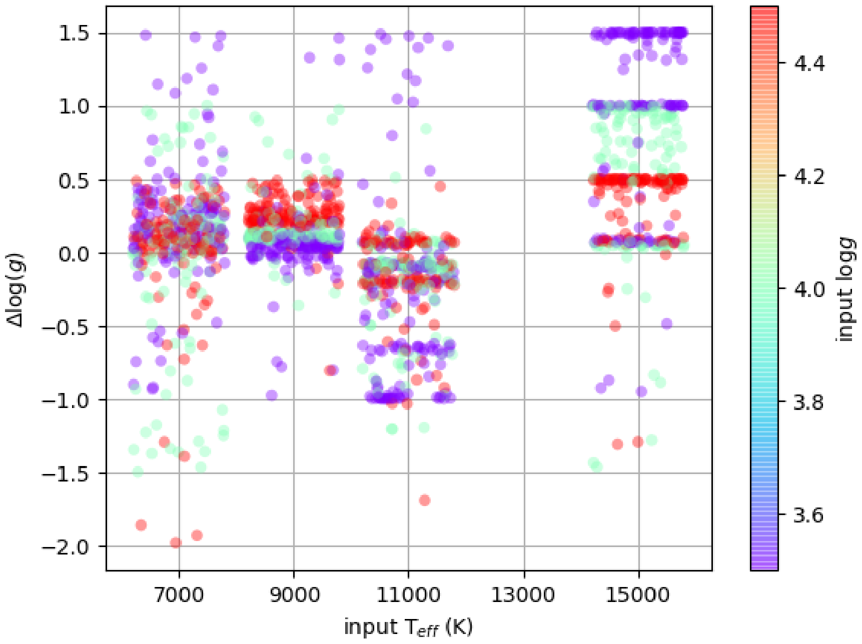

FIGURE 7.27: *Output - input* $\log g$ *as a function of input* $T_{\rm eff}$ *from the analysis of the blue region. The x-axis values have had a random number between* ±800 *added for visual clarity. The x ticks represent the true input values. The colour indicates the input* $\log g$ *value.*

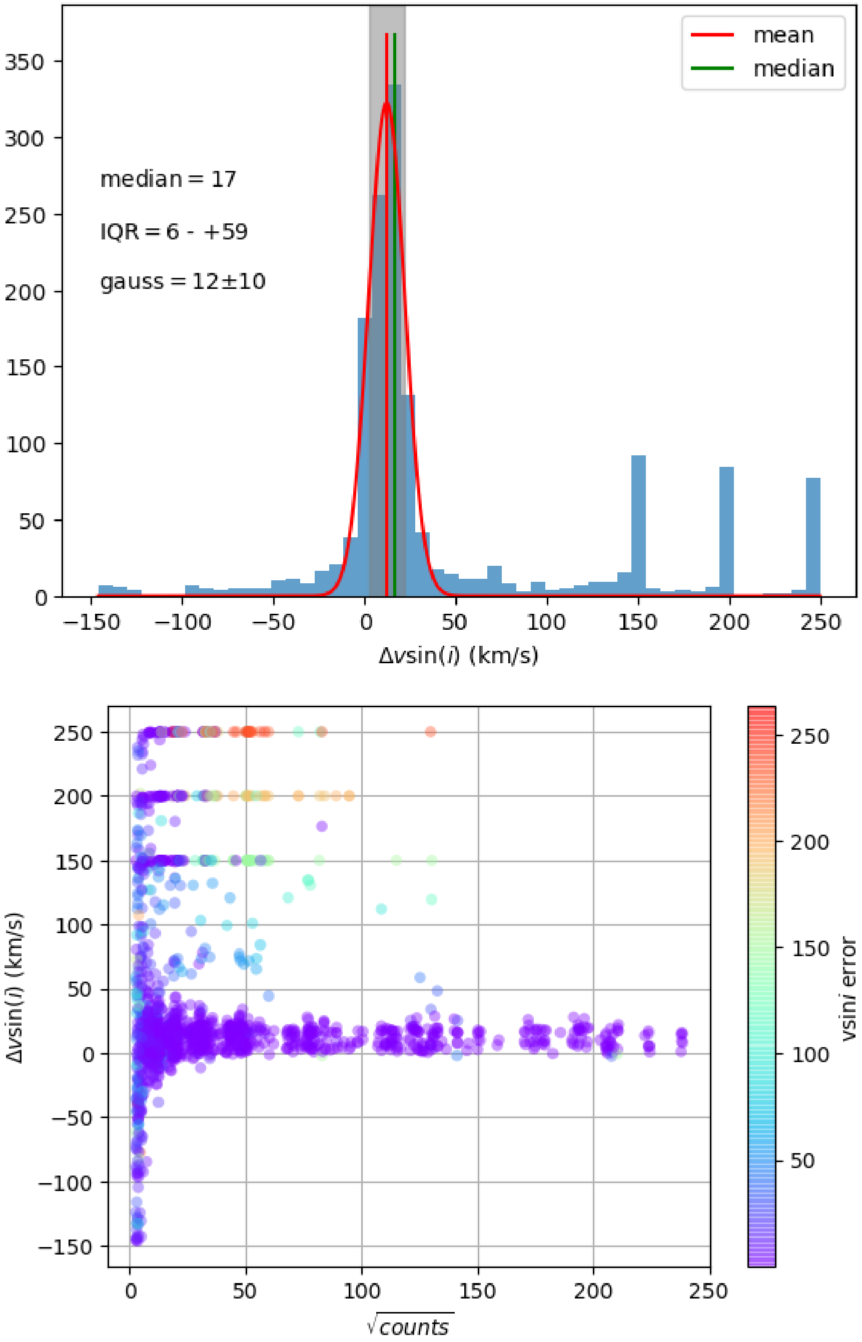

FIGURE 7.28: *Output - input $v \sin i$ (top), and as a function of $\sqrt{counts}$ (bottom), from the analysis of the blue region. The colour indicates the error on the measured $v \sin i$, where objects with a negative output - input difference display the positive error, and vice versa.*

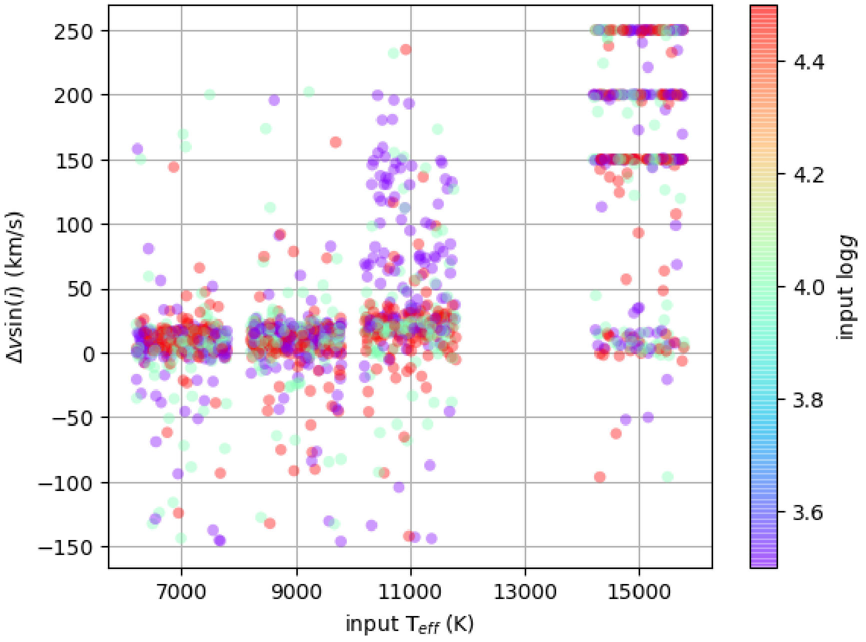

FIGURE 7.29: *Output - input* $v\sin i$ *as a function of input* T_{eff} *from the analysis of the blue region. The x-axis values have had a random number between* ±800 *added for visual clarity. The x ticks represent the true input values. The colour indicates the input* $\log g$ *value.*

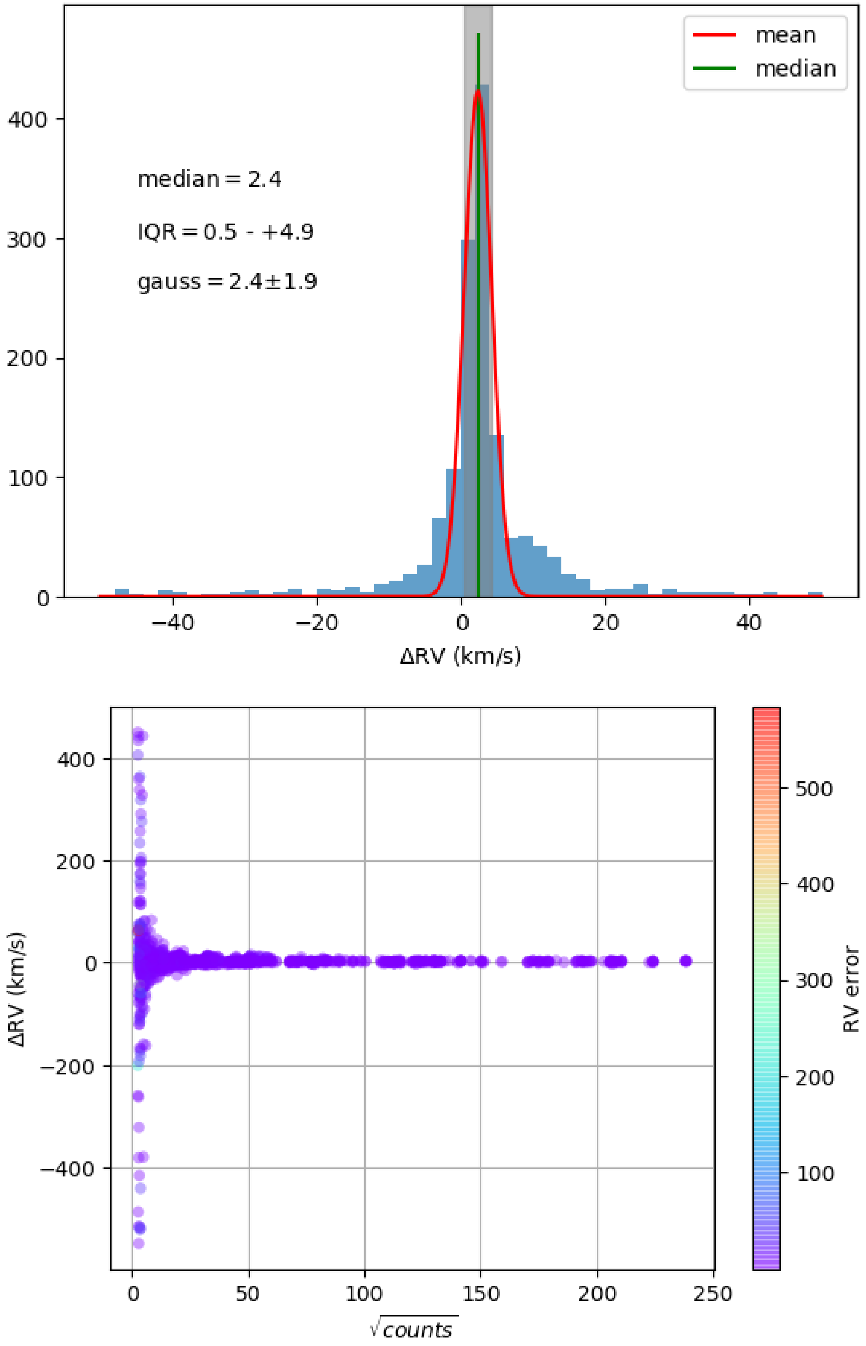

FIGURE 7.30: *Output - input RV (top), and as a function of* $\sqrt{counts}$ *(bottom), from the analysis of the blue region. The colour indicates the error on the measured RV, where objects with a negative output - input difference display the positive error, and vice versa.*

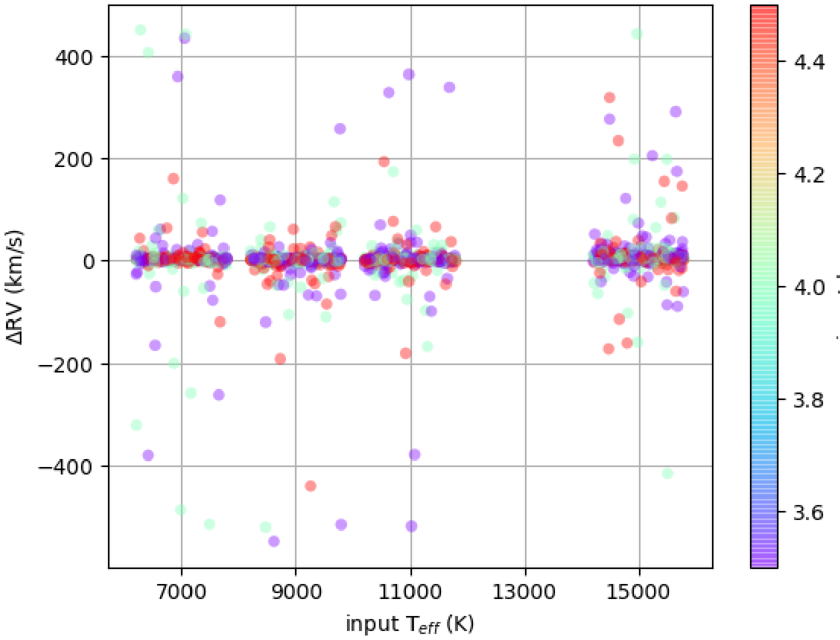

FIGURE 7.31: *Output - input RV as a function of input* $T_{\rm eff}$ *from the analysis of the blue region. The x-axis values have had a random number between* ±800 *added for visual clarity. The x ticks represent the true input values. The colour indicates the input* $\log g$ *value.*

7.1.3 Future improvements to the PTMCMC method

There are a few further improvements that, given more time, could be implemented to improve the PTMCMC method and broaden its potential. We mention these briefly here.

7.1.3.1 Automatic convergence testing

Mathematical testing for convergence of the MCMC walkers is not trivial. In the MCMC methods used in this work, we have tackled this by simply allowing the walkers to run for many steps, and eyeball inspection of the paths of the walkers reveal they usually converge within this limit. However, there are cases where convergence takes significantly longer, and alternatively where they converge very quickly. An automated test for convergence could be integrated into the MCMC algorithm, bringing the process to an end after the walkers have converged. This would save on computing time in the cases where the walkers converge quickly, and would allow for more reliable results in the cases where the walkers converge more slowly. An upper limit on the number of steps could remain in place to avoid the process running for extremely long times.

7.1.3.2 Binary stars

The template set that we use only consists of single star spectra. Since a large proportion of stars are believed to be in binary (or larger) systems, this is an issue. Whether the spectrum of a binary system is resolved or not, there will likely be some effect on the spectral lines. For instance, at inadequate spectral resolution, the lines may still appear broadened due to the binary orbital motions. With our current treatment, this could lead to erroneous stellar parameters and radial velocity measurements. Our method could be adapted to better deal with binary stars by allowing for the combination of different stellar templates within the grid. Alternatively, we could add templates of binary stars to the grid. Both of these suggestions would significantly increase the computing expense, however, and add to the number of free parameters.

Chapter 8

Summary

In this work the kinematics of the outer Galactic disk has been probed with the use of A stars, which are particularly effective, and F stars. The use of these relatively early-type stars is an alternative to the tracers commonly used in previous studies. In the past there has been a tendency to use ISM gas tracers or, in the case of stellar tracers, clump giants.

The particularly influential works of Brand and Blitz (1993) used HII regions to sample the outer disk kinematics over a wide range of longitudes $90^\circ < \ell < 270^\circ$ and out to $R_G = 17\,\mathrm{kpc}$. They find that the Galactic rotation curve is gently rising, and their results show evidence of a velocity anomaly around the Perseus region. Other studies that make use of ISM gas tracers include the works of Reid et al. (2014) who use masers, and Bobylev et al. (2016) who use star clusters. However, the inherent low spatial frequency of ISM gas tracers outside the Solar Circle means the outer disk kinematics remain unsettled.

The frequency of stars is much higher than ISM gas tracers at large radii, and so studies have turned to these in an effort to delve further in the disk. A somewhat obvious choice is to use clump giants, whose fairly constant luminosity, independent of age, allows them to serve as a standard candle (Castellani et al., 1992). However, clump giants are on average relatively old, with ages typically exceeding 1 Gyr. They therefore will have been subject to large amounts of kinematic scatter and built up significant asymmetric drift. This is a major drawback, especially in the quest to determine the Galactic rotation curve.

This work has shown that A-type especially and F-type stars can be used effectively as probes of outer Galactic disk kinematics. These young stellar tracers offer the advantage of reduced kinematic scatter and asymmetric drift as compared to the clump giants, and can provide a much denser sampling in the outer disk than offered by ISM gas tracers. Their bright absolute magnitudes means they can be detected out to great distances. Those used here provide sampling at a useful density out to $R_G \sim 15\,\mathrm{kpc}$. Large samples of these stars can be efficiently selected from the IPHAS $r-i$, $r-H\alpha$ plane. For example in this work, 81% of those selected as candidate A stars had T_{eff} measured to be between $7500-10000\,\mathrm{K}$ (typical of A stars), and 78% of those selected as candidate F stars had T_{eff} measured to be between $6000-7500\,\mathrm{K}$ (typical of F stars).

The two sightlines that are used to probe the outer disk kinematics here are located in the Galactic plane and at $\ell = 118°$ and $\ell = 178°$. Without Gaia DR2 proper motions at the time, the former was chosen in order to sample the radial velocity trend with distance that arises due to the differential Galactic rotation, and the latter was chosen as a control to reveal information about systematic bias and kinematic scatter. Radial velocities and extinction-corrected spectro-photometric distances were computed for the sample of > 1300 A and F stars with aid of MCMC parameter fitting.

The radial velocity trend with distance in the anticentre control sightline (Figure 4.1) revealed the method was indeed working well, with the observed trend remaining relatively flat and near zero as expected. A slight offset in mean RV of $3.5\,\mathrm{km\,s^{-1}}$ suggested a small bias may be present, if indeed the stars do have zero radial motion on average. The magnitude of kinematic scatter was in line with previous studies with the addition of binary orbital motions (see Table 4.1).

The trend observed at $\ell = 118°$, on the other hand, showed strong deviation from that expected from a flat or slowly rising rotation law (Figure 4.3). In particular, there is a lack of the most negative radial velocities expected from these laws in the most distant region of our sampling. At this sightline, and by assuming the stellar orbits are on average circular, the radial velocity trend could be converted to a rotation curve with use of Equation 1.6 . The measured rotation curve (Figure 4.4) is sharply rising, increasing by $\sim 30\,\mathrm{km\,s^{-1}}$ over the range $11-14\,\mathrm{kpc}$. This is remarkably similar to the longitude-averaged rotation curve measured in Huang et al. (2016) using clump giants.

With the release of Gaia DR2 astrometry in April 2018, parallaxes and proper motion measurements for the A and F stars became available. However, this release did not provide the standard of parallax required in order to make the spectro-photometric distances redundant. Significant global systematic errors of up to 0.1 mas, along with random errors of percentage uncertainty between $20-100\%$, rendered the DR2 parallaxes of our sample futile. With this level of uncertainty, methods used to invert the parallax to obtain a distance are dominated by their chosen prior (Bailer-Jones et al., 2018). The parallaxes are at present little use beyond 2 kpc, and it is beyond this that is of interest here. On the other hand, the proper motion precision is generally very good (see Figure 6.6), and combined with the already-measured radial velocities and spectro-photometric distances, full space motions of the A and F stars were obtained.

On conversion of the full space motions to a Galactocentric frame, the Galactocentric radial, u, azimuthal, v, and vertical, w, velocity trends were constructed. Whereas the rotation curve derived using only radial velocity data required the assumption of circular orbits, i.e. $u = 0\,\mathrm{km\,s^{-1}}$, having full space motions negates the need for this assumption. In fact, at $\ell = 118^\circ$ in particular, the observed radial motion is far from $u = 0\,\mathrm{km\,s^{-1}}$ (Figure 6.10), and this results in a rotation curve that is flatter than that from radial velocity data alone (Figure 6.12). The rotation curve incorporating proper motion data increases by just under $20\,\mathrm{km\,s^{-1}}$ over the range $11-14$ kpc, whereas it increases by $30\,\mathrm{km\,s^{-1}}$ when only radial velocity data is used. Clearly the assumption of zero radial motion of stars, as is done for example in López-Corredoira (2014), can have a strong impact on the measured rotation curve, and caution must be taken where there is a lack of information. In the case of ISM gas tracers, radial motion is likely not an issue since the expectation is that the gas largely follows rotation, but there is an issue in their velocities in part being controlled by spiral shocks.

A and F stars, as younger objects, will experience a larger kinematic response to perturbation than relatively older objects such as clump giants. This means that the velocity trends observed will contain information about both the global dynamics of the Galaxy, but also reveal the more intricate motions induced from perturbers such as the spiral arms, central bar, and passing or infalling satellites. The effects from perturbers should be considered in parallel, but this is futile without the underpinning of an accurate model of the global kinematics. Hence, in this work, the detailed form of the observed Galactocentric trends are cautiously considered with specific perturbers in mind.

The Galactocentric velocity trends in the two sightlines offer no conclusive evidence of perturbation from the central bar. This is not particularly surprising given the large Galactocentric distance of our sample. The bumps and wiggles in the u trends are not obviously aligned with current estimates of Perseus and Outer Arm locations, going against predictions from models based on density wave theory (Monari et al., 2016). The A and F star velocities on either side of the Outer Arm do not fit consistently with the mid-life stage of a transient winding arm either (Grand et al., 2016). It is clear that the in-plane velocities at least are extremely complex, and great care along with large amounts of data is required in order to begin to unpick the origin of the detailed structure that exists in the outer disk.

The somewhat hazy understanding of the outer disk kinematics that is observed here is a reflection of the complex dynamics in our Galaxy. Despite there being no obvious explanations in terms of e.g. spiral arm or bar perturbation, the Galactocentric velocity trends have shown great variation with both Galactocentric distance and longitude. Longitude-averaging in kinematic studies smears the substructure that holds crucial information about the clearly non-axisymmetric potential of the Milky Way. The key to understanding the kinematics in the outer disk is to observe it uniformly along the plane.

WEAVE, the multi-object spectrograph in construction for the WHT, is expected to begin operations in the Spring of 2020. The SCIP survey for WEAVE will obtain radial velocities of photometrically-selected OBA stars spanning $20^\circ \lesssim \ell \lesssim 220^\circ$, completing the kinematics provided by Gaia astrometry. The PTMCMC method developed in this work to determine stellar parameters and measure radial velocities will be used to analyse WEAVE survey products. I will package up the software as a pipeline tool in the coming months. The stellar parameters and radial velocities measured with this method will be combined with the photometry and Gaia astrometry to obtain full space motions for the ~ 170000 B/A stars observed by WEAVE. The velocity field of the entire (northern) outer disk will be mapped in higher detail than ever before.

Given the time and opportunity, I would like to have analysed another sightline in the outer disk. The two sightlines examined here have revealed stark differences in their kinematics, and a third would be helpful in filling out the picture. Expanding the probed region to include more dense sampling on either side of the Perseus and Outer Arms would also help to uncover the situation around the spiral arms. The work here has indeed shown that A stars are especially useful for probing the outer Galactic disk kinematics, and their use in the future will help us to understand how our Galaxy is, and came to be, how it is now.

Appendix A

PTMCMC code

```
import numpy as np
from scipy import interpolate
import sys
import matplotlib
from matplotlib import rc, rcParams
rc(’text’, usetex=True)
rcParams[’text.latex.preamble’] = [r"\usepackage{amsmath}",
                                   r"\usepackage{color}"]
matplotlib.use(’Agg’)
import matplotlib.pyplot as plt
import corner
from datetime import datetime
from scipy.stats.mstats import mquantiles
from multiprocessing import Pool
from ptemcee import Sampler as PTSampler
import pickle
import os

startTime = datetime.now()
os.system("taskset -p 0xff %d" % os.getpid())

templatedirectory = ’/home/amy/MCMC_smoothed0.95_nodib/templates/’
templatefile = templatedirectory + ’atSS03550-t005000g3.00-vrot000res010000-met
    +0.0-micr2.0s48_LR_smoothed_rebinned’
flux_data_directory = ’/home/amy/MCMC_smoothed0.95_nodib/’

targetdirectory = ’/home/amy/MCMC_smoothed0.95_nodib/PTMCMC/targets/’
target_list_file = ’/home/amy/MCMC_smoothed0.95_nodib/PTMCMC/ca2000-list’
noisespec_directory = ’/home/amy/MCMC_smoothed0.95_nodib/PTMCMC/targets/
    noisespecs/’

write_directory = ’/home/amy/MCMC_smoothed0.95_nodib/PTMCMC/’
```

```
templatewavelength = np.loadtxt(templatefile, unpack=True, usecols=[0], skiprows
    =1)

rvmin = -500.0
rvmax = 500.0
drvstep = 0.1
c = 299792.458

#LIMITS OF TEMPLATE GRID
Teff = np.arange(5000, 15500, 500)
logg = np.array([3.0, 3.5, 4.0, 4.5, 5.0])
vsini = np.array([0, 50, 100, 150, 200, 250, 300])
drv = np.arange(rvmin, rvmax, drvstep)

slopes = np.arange(-1.0e-5, 1.0e-5, 1.0e-10)
intercepts = np.arange(-1.0e-1, 1.0e-1, 1.0e-6)

# WAVELENGTH REGIONS TO INCLUDE
left = [8470, 8610]
right = [8700, 8940]
lines = [left, right]

normalised_flux_data = np.load(flux_data_directory + 'all_temps_smoothed0.95.npy'
    )
ipo = interpolate.RegularGridInterpolator((Teff, logg, vsini),
    normalised_flux_data, method='linear')

def model(X):
        i, j, k, l, m, n = X
        templateflux = ipo([i, j, k])[0]
        fi = interpolate.interp1d(templatewavelength*(1.0 + l/c), templateflux)
        return fi(wavelength)

def lnprior(X):
        i, j, k, l, m, n = X
        if (5000 <= i) & (i <= 15000) & (3.0 <= j) & (j <= 5.0) & (0 <= k) & (k
    <= 300) & (rvmin <= l) & (l <= rvmax) & (m >= -1.0e-5) & (m <= 1.0e-5) & (n
    >= -1.0e-1) & (n <= 1.0e-1):
                return 0.0
        else:
                return -np.inf

def lnlike(X, flux, noisespec):
        i, j, k, l, m, n = X
        templateflux = model(X)
        z = m, n
        f = np.poly1d(z)
```

```
        return -(np.sum((flux[mask] - (model(X)*f(wavelength))[mask])**2/(2*
    noisespec[mask]**2))/4.3)

# MCMC PARAMETERS
nwalkers=200
ndim=6
burn = 250
runs = 2000
ntemps = 5

with open(target_list_file, 'rb') as fp:
        target_list = pickle.load(fp)

wavelength = np.loadtxt(targetdirectory+target_list[0], skiprows=1, usecols=[0],
    unpack=True)
targetmask = (wavelength > 8470) & (wavelength < 8940)
wavelength = wavelength[targetmask]

mask = np.zeros(len(wavelength), dtype=bool)
for line in lines:
        mask |= (wavelength >= line[0]) & (wavelength <= line[1])

initial = [Teff, logg, vsini, drv, slopes, intercepts]

def mcmc_one(t):

        print t

        if os.path.exists(write_directory + '/results/' + t + '_results'):
                print 'already exists, skipping'
                return

        if os.path.exists(targetdirectory + t) == False:
                print 'spectrum doesnt exist, skipping'
                return

        new_time = datetime.now()

        flux = np.loadtxt(targetdirectory + t, skiprows = 1, unpack=True, usecols
    =[1])
        noisespec = np.loadtxt(noisespec_directory + t + '_noise_spectrum',
    unpack=True, usecols=[1], skiprows=1)
        noisespec = noisespec[targetmask]
        flux = flux[targetmask]

        # INITIALISE WALKER POSITIONS AND MCMC SAMPLER
        pos = [[[np.random.choice(i) for i in initial] for i in range(nwalkers)]
    for i in range(ntemps)]
```

```
    sampler = PTSampler(ntemps=ntemps, nwalkers=nwalkers, dim=ndim, logl=
lnlike, logp=lnprior, Tmax=np.inf, loglargs=[flux, noisespec])

    # RUN MCMC FOR BURN PERIOD THEN RUN PERIOD
    pos, prob, state = sampler.run_mcmc(pos, burn, adapt=True)
    sampler.reset()
    sampler.run_mcmc(pos, runs, adapt=True)

    for m in range(ndim):
            plt.subplot(ndim,1,m+1)
            plt.plot(sampler.chain[0,:,:,m].transpose(), alpha=0.2)

    plt.savefig(write_directory + ’/plots/’ + t + ’_walkers.png’, bbox_inches
=’tight’)
    plt.close()

    samples=sampler.chain[0, :, 1000:, :].reshape((-1, ndim))
    acceptance_list = np.mean(sampler.acceptance_fraction)
    quantiles = mquantiles(samples, prob=[0.16, 0.50, 0.84], axis=0)

    Tefflist = quantiles[1][0]
    Teffminus = quantiles[1][0] - quantiles[0][0]
    Teffplus = quantiles[2][0] - quantiles[1][0]
    logglist = quantiles[1][1]
    loggminus = quantiles[1][1] - quantiles[0][1]
    loggplus = quantiles[2][1] - quantiles[1][1]
    vsinilist = quantiles[1][2]
    vsiniminus = quantiles[1][2] - quantiles[0][2]
    vsiniplus = quantiles[2][2] - quantiles[1][2]
    RV = quantiles[1][3]
    RVminus = quantiles[1][3] - quantiles[0][3]
    RVplus = quantiles[2][3] - quantiles[1][3]
    slope = quantiles[1][4]
    slopeminus = quantiles[1][4] - quantiles[0][4]
    slopeplus = quantiles[2][4] - quantiles[1][4]
    intercept = quantiles[1][5]
    interceptminus = quantiles[1][5] - quantiles[0][5]
    interceptplus = quantiles[2][5] - quantiles[1][5]

    Xp = quantiles[1][0], quantiles[1][1], quantiles[1][2], quantiles[1][3],
quantiles[1][4], quantiles[1][5]
    zp = quantiles[1][4], quantiles[1][5]
    fp = np.poly1d(zp)

    fitp = fp(wavelength)
    plt.plot(wavelength, flux, wavelength, model(Xp) * fitp)
    plt.vlines([lines[0][1], lines[1][0]], flux.min()*0.8, flux.max()*1.2,
colors=’r’, linestyles=’dashed’)
```

```
        plt.xlim(8470, 8940)
        plt.ylim(flux.min()*0.8, flux.max()*1.2)
        plt.xlabel(r'Wavelength ($\AA$)')
        plt.ylabel('Counts')
        plt.savefig(write_directory + '/plots/' + t + '_spectra.png', bbox_inches
    ='tight')
        plt.close()

        plt.plot(wavelength, fitp, wavelength, flux / model(Xp))
        plt.xlim(8470, 8940)
        plt.xlabel(r'Wavelength ($\AA$)')
        plt.ylabel('Counts')
        plt.savefig(write_directory + '/plots/' + t + '_sensitivity_function.png'
    , bbox_inches='tight')
        plt.close()

        tab = open(write_directory + '/results/' + t +  '_results', "a+")
        tab.write(t + " " + np.str(acceptance_list) + " " + np.str(Tefflist) + "
    " + np.str(Teffminus) + " " + np.str(Teffplus) + " " + np.str(logglist) + " "
     + np.str(loggminus) + " " + np.str(loggplus) + " " + np.str(vsinilist) + " "
     + np.str(vsiniminus) + " " + np.str(vsiniplus) + " " + np.str(RV) + " " + np
    .str(RVminus) + " " + np.str(RVplus) + " " + np.str(slope) + " " + np.str(
    slopeminus) + " " + np.str(slopeplus) + " " + np.str(intercept) + " " + np.
    str(interceptminus) + " " + np.str(interceptplus) + "\n")
        tab.close()

        sampler.reset()

        print 'total time: ', datetime.now() - new_time

pool = Pool(processes=32)
it = pool.imap(mcmc_one, target_list)
for i in range(len(target_list)):
        it.next()

print(datetime.now() - startTime)
```

Bibliography

Abuter, R., Amorim, A., Bauboeck, M., et al., 2019. A geometric distance measurement to the Galactic Center black hole with 0.3% uncertainty. *arXiv e-prints*.

Alam, S., Albareti, F.D., Allende Prieto, C., et al., 2015. The eleventh and twelfth data releases of the sloan digital sky survey: Final data from sdss-iii. *ApJS*, 219.

Allende Prieto, C., Beers, T.C., Wilhelm, R., et al., 2006. A Spectroscopic Study of the Ancient Milky Way: F- and G-Type Stars in the Third Data Release of the Sloan Digital Sky Survey. *ApJ*, 636:804.

Ann, H.B. and Park, J.C., 2006. Warped disks in spiral galaxies. *NA*, 11:293.

Antoja, T., Figueras, F., Torra, J., et al., 2010. The Origin of Stellar Moving Groups. *Lecture Notes and Essays in Astrophysics*, 4:13.

Antoja, T., Helmi, A., Romero-Gomez, M., et al., 2018. A dynamically young and perturbed milky way disk. *Nature*, 561:360.

Athanassoula, E., 2005. On the nature of bulges in general and of box/peanut bulges in particular: input from N-body simulations. *MNRAS*, 358:1477.

Athanassoula, E., Rodionov, S.A., and Prantzos, N., 2017. Metallicity-dependent kinematics and morphology of the Milky Way bulge. *MNRAS*, 467:L46.

Baba, J., Kawata, D., Matsunaga, N., et al., 2018. Gaia dr1 evidence of disrupting the perseus arm. *ApJL*, 853.

Baba, J., Saitoh, T.R., and Wada, K., 2013. Dynamics of Non-steady Spiral Arms in Disk Galaxies. *ApJ*, 763:46.

Bailer-Jones, C.A.L., 2015. Estimating Distances from Parallaxes. *PASP*, 127:994.

Bailer-Jones, C.A.L., Rybizki, J., Fouesneau, M., et al., 2018. Estimating distances from parallaxes iv: Distances to 1.33 billion stars in gaia data release 2. *ApJ*.

Battaner, E., Florido, E., and Sanchez-Saavedra, M.L., 1990. Intergalactic magnetic field and galactic WARPS. *A&A*, 236:1.

Bekki, K. and Freeman, K.C., 2003. Formation of ω Centauri from an ancient nucleated dwarf galaxy in the young Galactic disc. *MNRAS*, 346:L11.

Belokurov, V., Zucker, D.B., Evans, N.W., et al., 2006. The Field of Streams: Sagittarius and Its Siblings. *ApJ*, 642(2):L137.

Bensby, T., Oey, M.S., Feltzing, S., et al., 2007. Disentangling the Hercules Stream. *ApJ*, 655:L89.

Binney, J. and Dehnen, W., 1997. The outer rotation curve of the milky way. *MNRAS*, 287.

Binney, J. and Merrifield, M., 1998. *Galactic Astronomy*. Princeton University Press, Princeton, NJ.

Binney, J. and Tremaine, S., 2008. *Galactic Dynamics: Second Edition*. Princeton University Press, Princeton, NJ.

Bird, S.A., Xue, X.X., Liu, C., et al., 2019. Anisotropy of the Milky Way's Stellar Halo Using K Giants from LAMOST and Gaia. *AJ*, 157(3):104.

Bland-Hawthorn, J. and Gerhard, O., 2016. The Galaxy in Context: Structural, Kinematic, and Integrated Properties. *ARAA*, 54:529.

Bobylev, V.V., 2017. Kinematics of the galaxy from Cepheids with proper motions from the Gaia DR1 catalogue. *Astronomy Letters*, 43:152.

Bobylev, V.V. and Bajkova, A.T., 2017. Kinematics of the galaxy from OB stars with proper motions from the Gaia DR1 catalogue. *Astronomy Letters*, 43:159.

Bobylev, V.V., Bajkova, A.T., and Shirokova, K.S., 2016. Galactic kinematics from data on open star clusters from the mwsc catalogue. *Astronomy Letters*, 42:721.

Bosma, A., 1978. *The distribution and kinematics of neutral hydrogen in spiral galaxies of various morphological types*. Ph.D. thesis, PhD Thesis, Groningen Univ., (1978).

Bovy, J., Allende Prieto, C., Beers, T.C., et al., 2012. The Milky Way's Circular-velocity Curve between 4 and 14 kpc from APOGEE data. *ApJ*, 759:131.

Bovy, J. and Hogg, D.W., 2010. The Velocity Distribution of Nearby Stars from Hipparcos Data. II. The Nature of the Low-velocity Moving Groups. *ApJ*, 717:617.

Brand, J. and Blitz, L., 1993. The velocity field of the outer galaxy. *A&A*, 275.

Bressan, A., Marigo, P., Girardi, L., et al., 2012. Parsec: stellar tracks and isochrones with the padova and trieste stellar evolution code. *MNRAS*, 427:127.

Brook, C.B., Stinson, G.S., Gibson, B.K., et al., 2012. Thin disc, thick disc and halo in a simulated galaxy. *MNRAS*, 426:690.

Castellani, V., Chieffi, A., and Straniero, O., 1992. The evolution through h and he burning of galactic cluster stars. *ApJS*, 78:517.

Chabrier, G., 2003. Galactic Stellar and Substellar Initial Mass Function. *PASP*, 115:763.

Chemin, L., Renaud, F., and Soubiran, C., 2015. Incorrect rotation curve of the milky way. *A&A*, 578.

Chen, Y., Bressan, A., Girardi, L., et al., 2015. Parsec evolutionary tracks of massive stars up to 350 msun at metallicities 0.0001 ¡= z ¡= 0.04. *MNRAS*, 452:1068.

Cheng, J.Y., Rockosi, C.M., Morrison, H.L., et al., 2012. Metallicity Gradients in the Milky Way Disk as Observed by the SEGUE Survey. *ApJ*, 746(2):149.

Coelho, P.R.T., 2014. A new library of theoretical stellar spectra with scaled-solar and alpha-enhanced mixtures. *MNRAS*, 440.

Combes, F., Debbasch, F., Friedli, D., et al., 1990. Box and peanut shapes generated by stellar bars. *A&A*, 233:82.

Contopoulos, G. and Papayannopoulos, T., 1980. Orbits in weak and strong bars. *A&A*, 92:33.

Corbelli, E., Lorenzoni, S., Walterbos, R., et al., 2010. A wide-field H I mosaic of Messier 31. II. The disk warp, rotation, and the dark matter halo. *A&A*, 511:A89.

Dalton, G., Trager, S., Abrams, D.C., et al., 2016. Final design and progress of weave: the next generation wide-field spectroscopy facility for the william herschel telescope. *SPIE*, 9908.

Dame, T.M., Hartmann, D., and Thaddeus, P., 2001. The milky way in molecular clouds: A new complete co survey. *ApJ*, 547:792.

Dehnen, W., 2000. The effect of the outer lindblad resonance of the galactic bar on the local stellar velocity distribution. *AJ*, 119:800.

Dehnen, W. and Binney, J.J., 1998. Local stellar kinematics from hipparcos data. *MNRAS*, 298:387.

Dias, W.S. and Lépine, J.R.D., 2005. Direct Determination of the Spiral Pattern Rotation Speed of the Galaxy. *ApJ*, 629:825.

D'Onghia, E., Vogelsberger, M., and Hernquist, L., 2013. Self-perpetuating Spiral Arms in Disk Galaxies. *ApJ*, 766:34.

Drew, J.E., Gonzalez-Solares, E., Greimel, R., et al., 2014. The VST Photometric Hα Survey of the Southern Galactic Plane and Bulge (VPHAS+). *MNRAS*, 440:2036.

Drew, J.E., Greimel, R., Irwin, M.J., et al., 2005. The int photometric hα survey of the northern galactic plane (iphas). *MNRAS*, 362:753.

Drew, J.E., Greimel, R., Irwin, M.J., et al., 2008. Early-a stars from iphas, and their distribution in and around the cyg ob2 association. *MNRAS*, 386:1761.

Drimmel, R. and Spergel, D.N., 2001. Three-dimensional Structure of the Milky Way Disk: The Distribution of Stars and Dust beyond 0.35 R_{solar}. *ApJ*, 556:181.

Drinkwater, M.J., Phillipps, S., Jones, J.B., et al., 2000. The Fornax spectroscopic survey. I. Survey strategy and preliminary results on the redshift distribution of a complete sample of stars and galaxies. *A&A*, 355:900.

Duchêne, G. and Kraus, A., 2013. Stellar multiplicity. *ARAA*, 51:269.

Earl, D.J. and Deem, M.W., 2005. Parallel tempering: Theory, applications, and new perspectives. *Physical Chemistry Chemical Physics (Incorporating Faraday Transactions)*, 7:3910.

Eggen, O.J., Lynden-Bell, D., and Sandage, A.R., 1962. Evidence from the motions of old stars that the Galaxy collapsed. *ApJ*, 136:748.

ESA, editor, 1997. *The HIPPARCOS and TYCHO catalogues. Astrometric and photometric star catalogues derived from the ESA HIPPARCOS Space Astrometry Mission*, volume 1200 of *ESA Special Publication*.

Fabricant, D., Fata, R., Roll, J., et al., 2005. Hectospec, the mmt's 300 optical fiber-fed spectrograph. *PASP*, 117:1411.

Farnhill, H.J., Drew, J.E., Barentsen, G., et al., 2016. Calibrated and completeness-corrected optical stellar density maps of the northern galactic plane. *MNRAS*, 457:642.

Fernández, D., Figueras, F., and Torra, J., 2001. Kinematics of young stars. ii. galactic spiral structure. *A&A*, 372:833.

Fitzpatrick, E.L., 1999. Correcting for the effects of interstellar extinction. *PASP*, 111:63.

Foreman-Mackey, D., Hogg, D.W., Lang, D., et al., 2013. emcee: The mcmc hammer. *PASP*, 125.

Friel, E.D., Janes, K.A., Tavarez, M., et al., 2002. Metallicities of old open clusters. *AJ*, 124:2693.

Fujii, M.S., Baba, J., Saitoh, T.R., et al., 2011. The Dynamics of Spiral Arms in Pure Stellar Disks. *ApJ*, 730:109.

Gaia Collaboration, Brown, A.G.A., Vallenari, A., et al., 2018a. Gaia Data Release 2. Summary of the contents and survey properties. *A&A*, 616:A1.

Gaia Collaboration, Katz, D., Antoja, T., et al., 2018b. Gaia data release 2 - mapping the milky way disc kinematics. *A&A*, 616:A11.

Gaia Collaboration, Prusti, T., de Bruijne, J.H.J., et al., 2016. The Gaia mission. *A&A*, 595:A1.

Gebran, M., Farah, W., Paletou, F., et al., 2016. A new method for the inversion of atmospheric parameters of a/am stars. *A&A*, 589.

Gerhard, O., 2011. Pattern speeds in the Milky Way. *Memorie della Societa Astronomica Italiana Supplementi*, 18:185.

Gilmore, G. and Reid, N., 1983. New light on faint stars. iii - galactic structure towards the south pole and the galactic thick disc. *MNRAS*, 202:1025.

Gómez, F.A., Minchev, I., O'Shea, B.W., et al., 2013. Vertical density waves in the milky way disc induced by the sagittarius dwarf galaxy. *MNRAS*, 429:159.

Goldreich, P. and Lynden-Bell, D., 1965. II. Spiral arms as sheared gravitational instabilities. *MNRAS*, 130:125.

Goodman, A.A., Alves, J., Beaumont, C.N., et al., 2014. The Bones of the Milky Way. *ApJ*, 797:53.

Goodman, J. and Weare, J., 2010. Ensemble samplers with affine invariance. *Communications in Applied Mathematics and Computational Science, Vol. 5, No. 1, p. 65-80, 2010*, 5:65.

Grand, R.J.J., Kawata, D., and Cropper, M., 2012. The dynamics of stars around spiral arms. *MNRAS*, 421:1529.

Grand, R.J.J., Springel, V., Kawata, D., et al., 2016. Spiral-induced velocity and metallicity patterns in a cosmological zoom simulation of a milky way-sized galaxy. *MNRAS*, 460:L94.

Gray, R.O. and Corbally, Christopher, J., 2009. Stellar spectral classification. *Princeton University Press*, page 232.

Grevesse, N. and Sauval, A.J., 1998. Standard Solar Composition. *SSR*, 85:161.

Grosbøl, P. and Carraro, G., 2018. The spiral potential of the milky way. *A&A*.

Hales, A.S., Barlow, M.J., Drew, J.E., et al., 2009. Iphas a-type stars with mid-infrared excesses in spitzer surveys. *ApJ*, 695:75.

Hogg, D.W., Eilers, A.C., and Rix, H.W., 2018. Spectrophotometric parallaxes with linear models: Accurate distances for luminous red-giant stars. *ApJ*.

Honma, M., Kawaguchi, N., and Sasao, T., 2000. Science with VERA: VLBI exploration of radio astrometry. In H.R. Butcher, editor, *Radio Telescopes*, volume 4015 of *SPIE*, pages 624–631.

Honma, M., Nagayama, T., Ando, K., et al., 2012. Fundamental parameters of the milky way galaxy based on vlbi astrometry. *PASJ*, 64.

Huang, Y., Liu, X.W., Yuan, H.B., et al., 2016. The milky way's rotation curve out to 100 kpc and its constraint on the galactic mass distribution. *MNRAS*, 463:2623.

Huang, Y., Liu, X.W., Zhang, H.W., et al., 2015. On the metallicity gradients of the Galactic disk as revealed by LSS-GAC red clump stars. *Research in Astronomy and Astrophysics*, 15:1240.

Hubeny, I. and Lanz, T., 1992. Accelerated complete-linearization method for calculating nlte model stellar atmospheres. *A&A*, 262:501.

Hunt, J.A.S. and Bovy, J., 2018. The 4:1 outer lindblad resonance of a long-slow bar as an explanation for the hercules stream. *MNRAS*, 477:3945.

Hurley, J. and Tout, C.A., 1998. The binary second sequence in cluster colour-magnitude diagrams. *MNRAS*, 300:977.

Jaschek, C. and Jaschek, M., 1990. *The Classification of Stars*.

Julian, W.H. and Toomre, A., 1966. Non-Axisymmetric Responses of Differentially Rotating Disks of Stars. *ApJ*, 146:810.

Jurić, M., Ivezić, v., Brooks, A., et al., 2008. The milky way tomography with sdss. i. stellar number density distribution. *ApJ*, 673:864.

Kalberla, P.M.W., Dedes, L., and Kerp, J.and Haud, U., 2007. Dark matter in the milky way. ii. the hi gas distribution as a tracer of the gravitational potential. *A&A*, 469:511.

Kalberla, P.M.W. and Kerp, J., 2009. The Hi Distribution of the Milky Way. *ARAA*, 47:27.

Kalberla, P.M.W., Kerp, J., Dedes, L., et al., 2014. Does the Stellar Distribution Flare? A Comparison of Stellar Scale Heights with LAB H I Data. *ApJ*, 794:90.

Karim, M.T. and Mamajek, E.E., 2017. Revised geometric estimates of the North Galactic Pole and the Sun's height above the Galactic mid-plane. *MNRAS*, 465(1):472.

Kawata, D., Baba, J., Ciucă, I., et al., 2018. Radial distribution of stellar motions in gaia dr2. *MNRAS*, 479:L108.

Kawata, D., Bovy, J., Matsunaga, N., et al., 2019. Galactic rotation from Cepheids with Gaia DR2 and effects of non-axisymmetry. *MNRAS*, 482:40.

Kawata, D., Hunt, J.A.S., Grand, R.J.J., et al., 2014. Gas and stellar motions and observational signatures of corotating spiral arms. *MNRAS*, 443:2757.

Kerr, F.J., 1957. A Magellanic effect on the galaxy. *AJ*, 62:93.

Kerr, F.J. and Lynden-Bell, D., 1986. Review of galactic constants. *MNRAS*, 221:1023.

King, Charles, I., Brown, W.R., Geller, M.J., et al., 2015. Stellar Velocity Dispersion and Anisotropy of the Milky Way Inner Halo. *ApJ*, 813(2):89.

Koposov, S.E., Gilmore, G., Walker, M.G., et al., 2011. Accurate Stellar Kinematics at Faint Magnitudes: Application to the Boötes I Dwarf Spheroidal Galaxy. *ApJ*, 736:146.

Kroupa, P., 2001. On the variation of the initial mass function. *MNRAS*, 322:231.

Kurucz, R.L., 1992. Atomic and molecular data for opacity calculations. *RMxAA*.

Lemasle, B., François, P., Piersimoni, A., et al., 2008. Galactic abundance gradients from Cepheids. On the iron abundance gradient around 10-12 kpc. *A&A*, 490:613.

Levine, E.S., Blitz, L., and Heiles, C., 2006. The Vertical Structure of the Outer Milky Way H I Disk. *ApJ*, 643:881.

Li, C., Zhao, G., Jia, Y., et al., 2019a. Flare and Warp of Galactic Disk with OB Stars from Gaia DR2. *ApJ*, 871:208.

Li, J., FELLOW, ., Liu, C., et al., 2019b. Detecting the Sagittarius Stream with LAMOST DR4 M Giants and Gaia DR2. *ApJ*, 874:138.

Lin, C.C. and Shu, F.H., 1964. On the Spiral Structure of Disk Galaxies. *ApJ*, 140:646.

Lindegren, L., Hernandez, J., Bombrun, A., et al., 2018. Gaia data release 2: The astrometric solution. *A&A*.

López-Corredoira, M., 2014. Milky way rotation curve from proper motions of red clump giants. *A&A*, 563.

López-Corredoira, M. and Betancort-Rijo, J., 2009. Azimuthal dependence of the density distribution in outer galactic discs accreting intergalactic flows. *A&A*, 493:L9.

López-Corredoira, M., Betancort-Rijo, J., and Beckman, J.E., 2002a. Generation of galactic disc warps due to intergalactic accretion flows onto the disc. *A&A*, 386:169.

López-Corredoira, M., Cabrera-Lavers, A., Garzón, F., et al., 2002b. Old stellar Galactic disc in near-plane regions according to 2MASS: Scales, cut-off, flare and warp. *A&A*, 394:883.

López-Corredoira, M. and González-Fernández, C., 2016. Radial motions in disk stars: Ellipticity or secular flows? *AJ*, 151.

López-Corredoira, M. and Molgó, J., 2014. Flare in the Galactic stellar outer disc detected in SDSS-SEGUE data. *A&A*, 567:A106.

López-Corredoira, M., Cabrera-Lavers, A., and Gerhard, O.E., 2005. A boxy bulge in the milky way. inversion of the stellar statistics equation with 2mass data. *A&A*, 439:107.

Luri, X., Brown, A.G.A., Sarro, L.M., et al., 2018. Gaia data release 2: using gaia parallaxes. *A&A*.

Magnier, E.A., Schlafly, E.F., Finkbeiner, D.P., et al., 2016. Pan-STARRS Photometric and Astrometric Calibration. *arXiv e-prints*.

Maschberger, T., 2013. On the function describing the stellar initial mass function. *MNRAS*, 429:1725.

Matteucci, F. and Francois, P., 1989. Galactic chemical evolution - Abundance gradients of individual elements. *MNRAS*, 239:885.

Mayor, M. and Queloz, D., 1995. A Jupiter-mass companion to a solar-type star. *Nature*, 378:355.

McMillan, P.J., 2017. The mass distribution and gravitational potential of the milky way. *MNRAS*, 465:76.

Merrifield, M.R., Rand, R.J., and Meidt, S.E., 2006. The lifetime of grand design. *MNRAS*, 366:L17.

Mihalas, D. and Binney, J., 1981. *Galactic astronomy: Structure and kinematics /2nd edition/*.

Minchev, I. and Famaey, B., 2010. A new mechanism for radial migration in galactic disks: Spiral-bar resonance overlap. *ApJ*, 722:112.

Monari, G., Famaey, B., and Siebert, A., 2016. Modelling the galactic disc: perturbed distribution functions in the presence of spiral arms. *MNRAS*, 457:2569.

Monari, G., Helmi, A., Antoja, T., et al., 2014. The galactic bar and the large scale velocity gradients in the galactic disk. *A&A*, 569.

Monguió, M., Grosbøl, P., and Figueras, F., 2015. First detection of the field star overdensity in the perseus arm. *A&A*, 577.

Mühlbauer, G. and Dehnen, W., 2003. Kinematic response of the outer stellar disk to a central bar. *A&A*, 401:975.

Naab, T. and Ostriker, J.P., 2006. A simple model for the evolution of disc galaxies: the Milky Way. *MNRAS*, 366:899.

Nakanishi, H., Sakai, N., Kurayama, T., et al., 2015. Outer rotation curve of the Galaxy with VERA. II. Annual parallax and proper motion of the star-forming region IRAS 21379+5106. *PASJ*, 67(4):68.

Noguchi, M., 1999. Early Evolution of Disk Galaxies: Formation of Bulges in Clumpy Young Galactic Disks. *ApJ*, 514:77.

Palacios, A., Gebran, M., Josselin, E., et al., 2010. Pollux: a database of synthetic stellar spectra. *A&A*, 516.

Poggio, E., Drimmel, R., Lattanzi, M.G., et al., 2018. The galactic warp revealed by gaia dr2 kinematics. *MNRAS*.

Poleski, R., 2018. Transformation of the equatorial proper motion to the galactic system.

Portail, M., Wegg, C., Gerhard, O., et al., 2015. Made-to-measure models of the galactic box/-peanut bulge: stellar and total mass in the bulge region. *MNRAS*, 448:713.

Purcell, C.W., Bullock, J.S., Tollerud, E.J., et al., 2011. The Sagittarius impact as an architect of spirality and outer rings in the Milky Way. *Nature*, 477:301.

Ramos, P., Antoja, T., and Figueras, F., 2018. Riding the kinematic waves in the Milky Way disk with Gaia. *A&A*, 619:A72.

Reed, B.C., 1996. Evidence for a Warped Distribution of OB Stars in the Southern Milky Way. *AJ*, 111:804.

Reid, M.J., Dame, T.M., Menten, K.M., et al., 2016. A parallax-based distance estimator for spiral arm sources. *ApJ*, 823.

Reid, M.J., Menten, K.M., Brunthaler, A., et al., 2014. Trigonometric parallaxes of high mass star forming regions: The structure and kinematics of the milky way. *ApJ*, 783.

Rich, R.M., Reitzel, D.B., Howard, C.D., et al., 2007. The Bulge Radial Velocity Assay: Techniques and a Rotation Curve. *ApJl*, 658:L29.

Ridge, N.A., Di Francesco, J., Kirk, H., et al., 2006. The complete survey of star-forming regions: Phase i data. *ApJ*, 131:2921.

Robin, A.C., Bienaymé, O., Fernández-Trincado, J.G., et al., 2017. Kinematics of the local disk from the rave survey and the gaia first data release. *A&A*, 605.

Robin, A.C., Reylé, C., Derrière, S., et al., 2003. A synthetic view on structure and evolution of the milky way. *A&A*, 409:523.

Roca-Fàbrega, S., Antoja, T., Figueras, F., et al., 2014. A novel method to bracket the corotation radius in galaxy discs: vertex deviation maps. *MNRAS*, 440:1950.

Roeser, S., Demleitner, M., and Schilbach, E., 2010. The ppmxl catalog of positions and proper motions on the icrs. combining usno-b1.0 and the two micron all sky survey (2mass). *AJ*, 139:2440.

Roman-Duval, J., Jackson, J.M., Heyer, M., et al., 2009. Kinematic Distances to Molecular Clouds Identified in the Galactic Ring Survey. *ApJ*, 699:1153.

Royer, F., 2014. A-type rotator properties. pages 256–264.

Rubin, V.C., Ford, Jr., W.K., and Thonnard, N., 1978. Extended rotation curves of high-luminosity spiral galaxies. IV - Systematic dynamical properties, SA through SC. *ApJl*, 225:L107.

Ruphy, S., Robin, A.C., Epchtein, N., et al., 1996. New determination of the disc scale length and the radial cutoff in the anticenter with denis data. *A&A*, 313:L21.

Russeil, D., 2003. Star-forming complexes and the spiral structure of our galaxy. *A&A*, 397:133.

Sakai, N., Honma, M., Nakanishi, H., et al., 2013. The outer rotation curve project with VERA: Trigonometric parallax of IRAS 05168+3634. In R. de Grijs, editor, *Advancing the Physics of Cosmic Distances*, volume 289 of *IAU Symposium*, pages 95–98.

Sale, S.E., Drew, J.E., Barentsen, G., et al., 2014. A 3d extinction map of the northern galactic plane based on iphas photometry. *MNRAS*, 443:2907.

Sale, S.E., Drew, J.E., Knigge, C., et al., 2010. The structure of the outer galactic disc as revealed by iphas early a stars. *MNRAS*, 402:713.

Sale, S.E. and Magorrian, J., 2015. Marginal likelihoods of distances and extinctions to stars: computation and compact representation. *MNRAS*, 448:1738.

Sánchez-Saavedra, M.L., Battaner, E., and Florido, E., 1990. Frequency of Warped Spiral Galaxies at Visible Wavelengths. *MNRAS*, 246:458.

Sánchez-Saavedra, M.L., Battaner, E., Guijarro, A., et al., 2003. A catalog of warps in spiral and lenticular galaxies in the Southern hemisphere. *A&A*, 399:457.

Schönrich, R., Binney, J., and Dehnen, W., 2010. Local kinematics and the local standard of rest. *MNRAS*, 403:1761.

Schönrich, R. and Dehnen, W., 2018. Warp, waves, and wrinkles in the milky way. *MNRAS*, 478:3809.

Sellwood, J.A., 2008. Dynamical Evolution of Disk Galaxies. In J.G. Funes and E.M. Corsini, editors, *Formation and Evolution of Galaxy Disks*, volume 396 of *Astronomical Society of the Pacific Conference Series*, pages 341–346.

Sellwood, J.A. and Carlberg, R.G., 1984. Spiral instabilities provoked by accretion and star formation. *ApJ*, 282:61.

Simkin, S.M., 1974. Measurements of velocity dispersions and doppler shifts from digitized optical spectra. *A&A*, 31.

Smith, G. and Drake, J.J., 1987. The wings of the calcium infrared triplet lines in solar-type stars. *A&A*, 181:103.

Snaith, O., Haywood, M., Di Matteo, P., et al., 2015. Reconstructing the star formation history of the Milky Way disc(s) from chemical abundances. *A&A*, 578:A87.

Snaith, O.N., Haywood, M., Di Matteo, P., et al., 2014. The Dominant Epoch of Star Formation in the Milky Way Formed the Thick Disk. *ApJ*, 781:L31.

Sormani, M.C., Binney, J., and Magorrian, J., 2015. Gas flow in barred potentials - iii. effects of varying the quadrupole. *MNRAS*, 454:1818.

Sparke, L.S. and Gallagher, III, J.S., 2007. *Galaxies in the Universe*.

Tian, H.J., Liu, C., Wan, J.C., et al., 2017. Peculiar in-plane velocities in the outer disc of the milky way. *RAA*, 17.

Tonry, J. and Davis, M., 1979. A survey of galaxy redshifts. i - data reduction techniques. *AJ*, 84.

Toomre, A., 1964. On the gravitational stability of a disk of stars. *ApJ*, 139:1217.

Vallenari, A., Pasetto, S., Bertelli, G., et al., 2006. Kinematics and stellar content of the Milky Way populations toward the North Galactic Pole. *A&A*, 451:125.

Veltz, L., Bienaymé, O., Freeman, K.C., et al., 2008. Galactic kinematics with RAVE data. I. The distribution of stars towards the Galactic poles. *A&A*, 480:753.

Vorobyov, E.I. and Theis, C., 2006. Boltzmann moment equation approach for the numerical study of anisotropic stellar discs. *MNRAS*, 373:197.

Vousden, W.D., Farr, W.M., and Mandel, I., 2015. Dynamic temperature selection for parallel tempering in Markov chain Monte Carlo simulations. *MNRAS*, 455(2):1919.

Wegg, C. and Gerhard, O., 2013. Mapping the three-dimensional density of the galactic bulge with vvv red clump stars. *MNRAS*, 435:1874.

Wegg, C., Gerhard, O., and Portail, M., 2015. The structure of the milky way's bar outside the bulge. *MNRAS*, 450:4050.

Weinberg, M.D. and Blitz, L., 2006. A Magellanic Origin for the Warp of the Galaxy. *ApJl*, 641:L33.

Winkel, B., Kerp, J., Flöer, L., et al., 2016. The effelsberg-bonn h i survey: Milky way gas. first data release. *A&A*, 585.

Xiang, M.S., Liu, X.W., Yuan, H.B., et al., 2017. Lamost spectroscopic survey of the galactic anticentre (lss-gac): the second release of value-added catalogues. *MNRAS*, 467:1890.

Yu, J. and Liu, C., 2018. The age-velocity dispersion relation of the Galactic discs from LAMOST-Gaia data. *MNRAS*, 475(1):1093.

Zonoozi, A.H., Mahani, H., and Kroupa, P., 2019. Was the Milky Way a chain galaxy? Using the IGIMF theory to constrain the thin-disc star formation history and mass. *MNRAS*, 483:46.